

# **Design and Detection Process in Chipless RFID Systems Based on a Space-Time-Frequency Technique**

REZA REZAIESARLAK

Dissertation submitted to the faculty of the Virginia Polytechnic Institute and State  
University in partial fulfillment of the requirements for the degree of

Doctor of Philosophy  
in  
Electrical Engineering

Majid Manteghi, Chair  
William A. Davis  
Gary S. Brown  
Jeffrey H. Reed  
Werner E. Kohler

APRIL 27, 2015  
BLACKSBURG, VIRGINIA

Keywords: Antenna, Chipless RFID, Detection, Scattering, Short-time Matrix Pencil Method  
(STMPM), Time-Frequency Analysis, Transient Analysis, Ultra Wideband.

Copyright© 2015 REZA REZAIESARLAK

# **Design and Detection Process in Chipless RFID Systems Based on a Space-Time-Frequency Technique**

Reza Rezaiesarлак

## **ABSTRACT**

Recently, Radio Frequency Identification (RFID) technology has become commonplace in many applications. It is based on storing and remotely retrieving the data embedded on the tags. The tag structure can be chipped or chipless. In chipped tags, an integrated IC attached to the antenna is biased by an onboard battery or interrogating signal. Compared to barcodes, the chipped tags are expensive because of the existence of the chip. That was why chipless RFID tags are demanded as a cheap candidate for chipped RFID tags and barcodes. As its name expresses, the geometry of the tag acts as both modulator and scatterer. As a modulator, it incorporates data into the received electric field launched from the reader antenna and reflects it back to the receiving antenna. The scattered signal from the tag is captured by the antenna and transferred to the reader for the detection process.

By employing the singularity expansion method (SEM) and the characteristic mode theory (CMT), a systematic design process is introduced by which the resonant and radiation characteristics of the tag are monitored in the pole diagram versus structural parameters. The antenna is another component of the system. Taking advantage of ultra-wideband (UWB) technology, it is possible to study the time and frequency domain characteristics of the antenna used in chipless RFID system. A new omni-directional antenna element useful in wideband and UWB systems is presented. Then, a new time-frequency technique, called short-time matrix pencil method (STMPM), is introduced as an efficient approach for analyzing various scattering mechanisms in chipless RFID tags. By studying the performance of STMPM in early-time and late-time responses of the scatterers, the detection process is improved in cases of multiple tags located close to each other. A space-time-frequency algorithm is introduced based on STMPM to detect, identify, and localize multiple multi-bit chipless RFID tags in the reader area. The proposed technique has applications in electromagnetic and acoustic-based detection of targets.

To my parents, Fakhri and Hamid

## **ACKNOWLEDGEMENTS**

First and foremost, I would like to thank my parents and sisters for their invaluable support and sacrifices during my education.

There are so many people who contributed to my educational life. I remember the names of many of them and have forgotten some of them. I am grateful to all of them from my first grade teacher to my PhD advisor. I would like to express my gratitude to my supervisor, Dr. Majid Manteghi, for his wonderful mentorship, encouragement, constructive criticism and discussions, and providing me a friendly scientific atmosphere throughout my PhD studies.

I would like to thank Dr. William A. Davis, Dr. Gary S. Brown, Dr. Jeffrey H. Reed, and Dr. Werner Kohler for serving on my committee. I really appreciate their support, patience and comments in every step of the way, during my PhD education.

Special thanks to my great friends in Blacksburg, especially Hanif Livani, Mohsen Salehi, and Reza Arghandeh for their precious helps and all the fun we had together. In addition, I have to thank my colleagues at Virginia Tech Antenna Group (VTAG), Rodrigues Blanco, Taeyoung Yang and Shyam Manbiar for their precious time, discussions and suggestions.

# TABLE OF CONTENTS

ABSTRACT.....	ii
Dedication.....	iii
ACKNOWLEDGEMENTS.....	iv
TABLE OF CONTENTS.....	v
LIST OF FIGURES.....	vii
LIST OF TABLES.....	xiv
1 INTRODUCTION.....	1
1.1 RFID Systems.....	2
1.2 Passive RFID tags.....	2
1.2.1 Near-field RFID.....	3
1.2.2 Far-field RFID.....	4
1.3 Chipless RFID System.....	6
1.4 Dissertation Outline.....	7
2 Mathematical Representation of Scattered Fields from Chipless RFID Tags [8] (Chapter used with permission of Springer science and business media, 2015).....	10
2.1 Singularity Expansion Method (SEM).....	10
2.1.1 Altes' Model.....	19
2.1.2 SEM-Based Equivalent Circuit of Scatterer.....	23
2.1.3 SEM Representation of Currents on a Dipole.....	26
2.2 Eigenmode Expansion Method.....	29
2.2.1 Example: Eigenmode Expansion of Currents on a Dipole.....	32
2.3 Characteristic Mode Theory.....	33
2.3.1 Mathematical Formulation of the Characteristic Mode Theory.....	35
2.3.2 Characteristic Mode Analysis of Dipole.....	40
3 Design of Chipless RFID Tags [8] (Chapter used with permission of Springer science and business media, 2015).....	42
3.1 Complex Natural Resonance-Based Design of Chipless RFID Tags.....	47
3.2 Design of Chipless RFID Tag Based on Characteristic Mode Theory.....	57
4 UWB Antenna in Chipless RFID Systems.....	69
4.1 Link Equation in Frequency Domain.....	70

4.2	Time-Domain Signal Link Characterization .....	72
4.3	Antenna Effective Length.....	75
4.4	Antenna Characteristics in Time Domain.....	77
4.5	New Antenna Prototype for Wideband and Ultra-wideband Applications.....	82
5	Time-Frequency Techniques for Analyzing Transient Scattered Signal from Targets [8] (Chapter used with permission of Springer science and business media, 2015) .....	100
5.1	Short-Time Fourier Transform (STFT) .....	100
5.1.1	Resolution .....	102
5.2	Wavelet Transform .....	104
5.3	Re-assigned Joint Time-Frequency (RJTF).....	108
5.4	Short-Time Matrix Pencil Method (STMPM) .....	113
5.4.1	Matrix Pencil Method (MPM) [68].....	114
5.4.2	STMPM in Late-Time .....	118
5.4.3	STMPM in Early Time .....	122
5.4.4	Performance of STMPM Against Noise.....	130
5.5	Application of STMPM in Wideband Scattering from Resonant Structures [70].....	134
6	Detection, Identification, and Localization in Chipless RFID Tags [8] (Chapter used with permission of Springer science and business media, 2015).....	139
6.1	Detection of Chipless RFID Tags.....	139
6.2	Space-Time-Frequency Anti-Collision Algorithm for Identifying Chipless RFID Tags [80] .....	143
6.2.1	Space, Time and Frequency Resolutions.....	154
6.3	Separating the Early-Time and Late-Time Responses for Detection, Identification, and Localization of Chipless RFID Tags .....	156
6.4	Measurement Results .....	157
6.5	Localization of Chipless RFID Tag [88].....	162
7	Conclusion and Future Work .....	177
7.1	Summary of Dissertation .....	177
7.2	Suggestions for Future Work .....	179
8	References .....	17785

# LIST OF FIGURES

Figure 1.1 Two passive RFID tags. ....	2
Figure 1.2 Block diagram of near-field passive RFID tag.....	3
Figure 1.3 Far-field communication mechanism in RFID systems. ....	4
Figure 1.4 Gamma-matched antenna. ....	5
Figure 1.5 A 6-stage full-wave rectifier voltage multiplier. ....	5
Figure 1.6 Chipless RFID system. ....	7
Figure 2.13-bit tag illuminated by an incident plane wave.....	11
Figure 2.23-bit tag illuminated partly by an incident plane wave. ....	18
Figure 2.3(a) Transversal and (b) modified filter model of the early-time response.....	20
Figure 2.4 Measurement setup to measure a UWB pulse scattered from a metal object. ....	22
Figure 2.5 Excitation pulse and its derivative with respect to time. ....	23
Figure 2.6 Received electric field from the metal object for different distances (a) $d = 20$ cm, (b) $d = 30$ cm, (c) $d = 100$ cm, and $d = 130$ cm. ....	24
Figure 2.7 Received electric field from the metal plate for $d = 20$ cm and $d = 130$ cm. ....	24
Figure 2.8 (a) A tag illuminated by an incident plane pulse, and (b) SEM-based equivalent circuit of chipless RFID tag ....	26
Figure 2.9 Geometry of the dipole illuminated by an incident field.....	27
Figure 2.10 Pole diagram of the dipole, representing the resonant frequency and damping factor of the CNRs.....	29
Figure 2.11 (a) Real and (b) imaginary parts of the first three natural currents of the dipole.....	29
Figure 2.12 Real and imaginary parts of the first three eigenmodes of the dipole. ....	33
Figure 2.13 Eigenvalues of the characteristic modes versus frequency. ....	40
Figure 2.14 (a) Modal significance and (b) characteristic angle of the characteristic modes versus frequency.....	41
Figure 2.15 First three characteristic modes of the dipole at (a) $f = 130$ MHz, (b) $f = 282$ MHz, (c) $f = 300$ MHz, and $f = 430$ MHz ....	41
Figure 3.1 Schematic view of a surface acoustic wave tag.....	43
Figure 3.2 Dispersive delay structures [40] (With permission, Copyright© 2011 IEEE). ....	44
Figure 3.3 Chipless RFID system based on DDSs [40] (With permission, Copyright© 2011 IEEE).....	44
Figure 3.4 Assigned resonant frequencies for a chipless RFID tag.....	44
Figure 3.5 Spectral-based chipless RFID tags using (a) dipole resonators [43] (Copyright© 2005 IEEE) (b) fractal Hilbert curve [44] (Copyright© 2006 IEEE) (c) slot resonators [45]. (Copyright© 2007 IEEE) (d) Resonant circuitry attached to the transmitting/receiving antennas as a chipless RFID tag [46] (Copyright© 2009 IEEE) (e) chipless RFID tag based on high-impedance surface [47] (Copyright© 2013 IEEE) (f) 24-bit tag using quarter-wavelength slot resonators [42] (With permission, Copyright© 2014 IEEE). ....	46
Figure 3.6 Single-bit tag with structural dimensions. ....	47
Figure 3.7 Current distribution on the tag for different time instances [33] (With permission, Copyright© 2015 IEEE). ....	49
Figure 3.8 (a) Frequency-domain and (b) time-domain backscattered field from the single-bit tag [33] (With permission, Copyright© 2015 IEEE).....	49
Figure 3.9 Pole diagram of the single-bit tag [33] (With permission, Copyright© 2015 IEEE)..	50

Figure 3.10 Current distribution on the tag at (a) $f = 5.54\text{GHz}$ and (b) $8.8\text{ GHz}$ [42] (With permission, Copyright© 2014 IEEE).....	51
Figure 3.11 Resonant frequency of the slot versus $L$ . $W = 0.3\text{mm}$ [42] (With permission, Copyright© 2014 IEEE). .....	51
Figure 3.12 Damping factor of the CNR of the slot versus $d$ for different values of $a$ . $W = 0.3\text{ mm}$ [42] (With permission, Copyright© 2014 IEEE).....	52
Figure 3.13 Damping factor of the CNR of the slot versus $d$ for different values of $a$ . $W = 0.3\text{mm}$ [42] (With permission, Copyright© 2014 IEEE).....	52
Figure 3.14 (a) Resonant frequency and (b) damping factor of the CNR of the tag versus dielectric constant. $A = 10\text{mm}$ , $d = 0.8\text{mm}$ , $t = 0.3\text{mm}$ . .....	54
Figure 3.15 Single-bit tag above a metallic plate. ....	55
Figure 3.16 Percentage variations in the (a) resonant frequency and (b) damping factor of the CNR of the tag versus distant to the metallic plate. $A = 10\text{mm}$ , $d = 0.8\text{mm}$ , $t = 0.3\text{mm}$ .....	56
Figure 3.17 Schematic view of the 24-bit tag [42] (With permission, Copyright© 2014 IEEE). ..	56
Figure 3.18 Radar cross-sections of the 24-bit tags [42] (With permission, Copyright© 2014 IEEE).....	57
Figure 3.19 Single-bit tag illuminated by incident plane wave. ....	58
Figure 3.20 Eigenvalues of the characteristic modes versus frequency. ....	59
Figure 3.21 Modal significances of the characteristic modes versus frequency.....	59
Figure 3.22 Characteristic angle of the characteristic modes versus frequency. ....	60
Figure 3.23 Characteristic modes of the tag at two resonant frequencies [33] (With permission, Copyright© 2015 IEEE). ....	61
Figure 3.24 Variation of the resonant frequencies of the tag versus $d_1$ [33] (With permission, Copyright© 2015 IEEE). ....	62
Figure 3.25 Variation of the resonant frequencies of the tag versus $d_2$ [33] (With permission, Copyright© 2015 IEEE). ....	63
Figure 3.26 Scattered far-field electric field radiated from the tag. $d_1 = 6\text{ mm}$ , $a = 12\text{ mm}$ , $d = 0.8\text{ mm}$ , $W = 0.3\text{ mm}$ [33] (With permission, Copyright© 2015 IEEE).....	63
Figure 3.27 Quality factor of the CNR of the tag versus $d$ [33] (With permission, Copyright© 2015 IEEE).....	64
Figure 3.28 Far-field electric fields radiated from the tag for (a) $d = 0.8\text{ mm}$ and (b) $d = 0.4\text{ mm}$ [33] (With permission, Copyright© 2015 IEEE).....	65
Figure 3.29 Schematic view of the designed 4-bit tag. Units: mm [33] (With permission, Copyright© 2015 IEEE). ....	65
Figure 3.30 The simulated backscattered electric field from 4-bit tags [33] (With permission, Copyright© 2015 IEEE). ....	66
Figure 3.31 Pole diagram of the simulated backscattered fields from the tags [33] (With permission, Copyright© 2015 IEEE).....	66
Figure 3.32 Two 4-bit fabricated tags (a) $d_2 = 3\text{ mm}$ and (b) $d_2 = 7\text{ mm}$ [33] (With permission, Copyright© 2015 IEEE). ....	67
Figure 3.33 Measured RCS of the tags [33] (With permission, Copyright© 2015 IEEE). ....	67
Figure 3.34 Pole diagram of the measured backscattered fields from the tags [33] (With permission, Copyright© 2015 IEEE).....	68
Figure 4.1 FCC mask for outdoor and indoor UWB applications. ....	69
Figure 4.2 Mono-static chipless RFID system.....	71
Figure 4.3 Gain and power considerations in chipless RFID systems.....	72

Figure 4.4 Schematic of the bio-static set-up for measuring the impulse response of the tag.....	73
Figure 4.5 Measurement set-up for measuring transfer function of the antenna. ....	75
Figure 4.6 (a) UWB Monopole disk and (b) Narrowband monopole antenna. ....	77
Figure 4.7 (a) Amplitude and (b) phase of the $S_{21}$ for $\theta = 0$ and $\varphi = 0$ , (c) Amplitude and (d) phase of the antenna effective length in frequency domain, (e) antenna effective length in time domain, and (f) pole-diagram of the antenna.....	78
Figure 4.8 (a) Monopole antenna above a ground plane (b) its reflection coefficient.....	79
Figure 4.9 Radiated $E_{\theta}$ versus the distance from the monopole antenna. ....	80
Figure 4.10 Normalized impulse response of the UWB monopole antenna along with analytic envelope. ....	80
Figure 4.11 Variation of $E_{\theta}$ versus distance from the antenna in (a) near field and (b) far field of the antenna. ....	83
Figure 4.12 Group delay of UWB monopole antenna. ....	84
Figure 4.13 (a) Bowtie antenna as a frequency-independent antenna, (b) a self-complementary antenna, (c) TEM horn as a travelling-wave antenna, and (d) Log-periodic antenna as a multiple resonance antenna. ....	85
Figure 4.14 Two examples of UWB small antennas. ....	85
Figure 4.15 Amplitude of the current along the monopole and its direction at different frequencies. ....	87
Figure 4.16 Radiation gain of the monopole antenna at different frequencies. ....	87
Figure 4.17 Variations of CNRs of the monopole antenna versus (a) antenna length, $L$ and (b) antenna radius, $r$ . ....	88
Figure 4.18 (a) Monopole antenna above a ground plane, (b) its pole diagram for different values of $r_2$ . ....	89
Figure 4.19 (a) Reflection coefficient of the monopole antenna, and (b) time-domain radiated field from the antenna. ....	89
Figure 4.20 Current distribution on the monopole antenna at different resonant frequencies. ....	90
Figure 4.21 Radiation gain of the monopole antenna at different resonant frequencies. (Solid line: $\varphi = 0$ and dashed line: $\varphi = 90^{\circ}$ ).....	91
Figure 4.22 A monopole antenna surrounded by short cylinder as a wideband /UWB element. .	91
Figure 4.23 Reflection coefficient of the antenna for different values of $h$ . ....	92
Figure 4.24 The current distribution on the antenna at three resonant frequencies. ....	93
Figure 4.25 The current distribution on the monopole antenna at its coaxial mode resonance for two different values of $h$ , (b) resonant and radiation modes of current. ....	93
Figure 4.26 Reflection coefficient of the antenna for different values of $s$ . ....	94
Figure 4.27 The gain of the antenna versus elevation angle at different frequencies for $h=8$ mm. ....	94
Figure 4.28 Reflection coefficient of the antenna for two different designs. Design 1: $s = 11$ mm, $W = 2$ mm, $h = 5.5$ mm, $d = 18$ mm, Design 2: $s = 9$ mm, $W = 2$ mm, $h = 5.5$ mm, $d = 18$ mm..	95
Figure 4.29 Gain of the antenna at (a) $f = 4$ GHz, (b) $f = 6$ GHz, (c) $f = 8$ GHz, and (d) $f = 10$ GHz. ....	96
Figure 4.30 (a) The radiation field and (b) normalized radiation field of the antenna in far field. ....	96
Figure 4.31 (a) amplitude and (b) phase of $S_{21}$ between two similar antennas when they are spaced 40 cm far from each other, (c) amplitude and (d) phase of the antenna effective length for $\theta = 90^{\circ}$ and $\varphi = 0^{\circ}$ . ....	97

Figure 4.32 (a) Fabricated tag, and (b ) Antenna connected to the network analyzer. ....	98
Figure 4.33 Measured reflection coefficient of the antenna. ....	98
Figure 4.34 Co- and cross polar radiation pattern of the antenna at (a) $f = 2.7$ GHz, (b) $f = 4.8$ GHz, (c) $f = 6.9$ GHz, and (d) $f = 9$ GHz at xz and yz planes. ....	99
Figure 5.1 Time-domain signal. ....	103
Figure 5.2 Spectrogram of the signal for (a) $\delta = 0.8e-9$ , and (b) $\delta = 4e-9$ ....	103
Figure 5.3 Time and frequency resolutions in wavelet transform. ....	107
Figure 5.4 Wavelet transform of the signal. ....	108
Figure 5.5 Some practical wavelets. ....	109
Figure 5.6 Time-frequency representation of signal by RJTF and $\delta = 0.6e-9$ . ....	113
Figure 5.7 Time-domain signal with moving window. ....	119
Figure 5.8 (a) Time-domain signal, (b) time-frequency, (c) time-damping factor and (d) time-residue diagrams of the signal. ....	120
Figure 5.9 Minimum window length for distinguishing two resonances of the signal versus frequency distance [70] (With permission, Copyright© 2015 IEEE). ....	121
Figure 5.10 Time-frequency representation of the signal by applying (a) STMPM and (b) RJTF. ....	121
Figure 5.11 (a) Signal in time domain, Time-frequency representation of signal for (a) $T_w = 1.1$ ns, $p = 2$ , (b) $T_w = 4$ ns, $p = 2$ , and (c) $T_w = 1.1$ ns, $p = 4$ [70] (With permission, Copyright© 2015 IEEE). ....	122
Figure 5.12 Gaussian pulse and its first derivative with respect to time. ....	124
Figure 5.13 Pole diagram of the Gaussian pulse function. ....	124
Figure 5.14 Four extracted damped sinusoidal modes by applying STMPM to the Gaussian pulse. ....	125
Figure 5.15 Gaussian pulse and reconstruction one from Fourier transform and CNRs. ....	125
Figure 5.16 Pole diagram of the Gaussian pulse for different values of $\tau$ . ....	127
Figure 5.17 Reconstructed pulse signal for (a) $\tau = .5$ ns, $p = 4$ , (b) $\tau = 1$ ns, $p = 4$ , (c) $\tau = 1$ ns, $p = 8$ , (d) $\tau = 1.5$ ns, $p = 4$ . ....	127
Figure 5.18 Pole diagram of the derivative of Gaussian pulse for different values of $\tau$ . ....	128
Figure 5.19 Derivative of the Gaussian pulse and reconstruction one from Fourier transform and CNRs. ....	129
Figure 5.20 Extracted damping factor versus the center of the sliding window for (a) pulse, and (b) its derivative. ....	129
Figure 5.21 (a) Backscattered electric field from the scatterer, (b) pole diagram of the signal for different sliding times, (c) extracted damping factors with respect to the center of the sliding window, (d) backscattered electric field from two scatterers, (e) extracted damping factors with respect to the center of the sliding window, and (f) reconstructed early-time and late-time responses. ....	131
Figure 5.22 (a) Backscattered electric field, (b) Time-frequency diagram, (c) Time-damping factor, and (d) Time-residue diagram of the signal [69] (With permission, Copyright© 2014 IEEE). ....	133
Figure 5.23 (a) Time-damping factor of the signal, (b) Time-residue diagram of the signal for SNR = 15 dB [69] (With permission, Copyright© 2013 IEEE). ....	133
Figure 5.24 Scattering mechanisms in time-frequency analysis. (a) Scattering center. (b) Resonant behavior. (c) Structural dispersion. (d) Material dispersion [70] (With permission, Copyright© 2015 IEEE). ....	135

Figure 5.25 (a) Open-ended circular cavity excited by incident plane wave, (b) Backscattered signal in time domain [70] (With permission, Copyright© 2015 IEEE).	136
Figure 5.26 (a) Time-frequency diagram of the backscattered signal from the cylinder based on (a) STMPM and (b) STFT [70] (With permission, Copyright© 2015 IEEE).	136
Figure 5.27 Time-frequency diagram of the scattered field for $T_w = 1$ ns, $p = 4$ [70] (With permission, Copyright© 2015 IEEE).	137
Figure 5.28 Time-damping factor representation of backscattered signal from cavity.	138
Figure 5.29 Time-frequency diagram of the signal with (a) SNR=10dB, $T_w = 0.8$ ns, $p=2$ and (b) SNR=20dB. $T_w = 0.8$ ns, $p=4$ [70] (With permission, Copyright© 2015 IEEE).	138
Figure 6.1 Single-bit tag illuminated by a plane incident field.	142
Figure 6.2 (a) Scattered electric field from the tag for two different orientations of receiving antenna, (b) Group delay of the scattered field for two different orientations of receiving antenna.	142
Figure 6.3 Multiple chipless RFID tags present in the reader zone [80] (With permission, Copyright© 2014 IEEE).	143
Figure 6.4 Flowchart of the proposed anti-collision algorithm [80] (With permission, Copyright© 2014 IEEE).	146
Figure 6.5 (a) Two single-bit tags and (b) two 2-bit tags spaced by $R$ are illuminated by a plane wave. Units in mm [80] (With permission, Copyright© 2014 IEEE).	147
Figure 6.6 (a) Time-domain backscattered signal from two tags spaced by $R=20$ cm (b) time-frequency representation of the signal by applying STMPM with $T = 0.5$ ns. (c) time-residue diagram of the signal. (d) Separated responses of the tags in frequency-domain [80] (With permission, Copyright© 2014 IEEE).	147
Figure 6.7 (a) Time-frequency and (b) time-residue representation of the signal by applying STMPM with $T= 0.5$ ns. (c) Separated responses of the tags in frequency-domain (d) space-frequency response after SFMPM [80] (With permission, Copyright© 2014 IEEE).	149
Figure 6.8 6.8. Time-residue diagram for different polarizations [80] (With permission, Copyright© 2014 IEEE).	150
Figure 6.9 (a) Time-domain signal (b) frequency-domain response (c) time-frequency diagram after STMPM (d) space-frequency diagram after SFMPM [80] (With permission, Copyright© 2014 IEEE).	150
Figure 6.10 Schematic view of the tags. (a) ID <sub>1</sub> :111, (b) ID <sub>2</sub> : 101[80] (With permission, Copyright© 2014 IEEE).	151
Figure 6.11 Pole diagram of the 3-bit tag [80] (With permission, Copyright© 2014 IEEE).	152
Figure 6.12 (a) Time-domain backscattered signal from two tags spaced by $R=20$ cm (b) frequency-domain response (c) time-frequency representation of the signal by applying STMPM with $T= 0.5$ ns. (d) Time-residue diagram of the signal [80] (With permission, Copyright© 2014 IEEE).	153
Figure 6.13 (a) Time-residue diagram of the backscattered signal (b) separated responses of the tags in frequency-domain [80] (With permission, Copyright© 2014 IEEE).	153
Figure 6.14 Minimum required window length as a function of $\Delta$ for different SNRs [80] (With permission, Copyright© 2014 IEEE).	154
Figure 6.15 6.15. Backscattered signal from two single-bit tags [80] (With permission, Copyright© 2014 IEEE).	155
Figure 6.16 A 4-bit chipless RFID tag located 30 cm away from the antenna.	158

Figure 6.17 Reflection coefficient of the antenna loaded by tag in (a) frequency domain, (b) time domain, (c) Time-damping factor diagram and (d) Time-frequency diagram of the $S_{11}$ .....	158
Figure 6.18 (a) Time domains and (b) Time-damping factor diagrams of the backscattered signal from two tags. ....	159
Figure 6.19 Set-up for the measurement of backscattered signal from two tags [80] (With permission, Copyright© 2014 IEEE).....	160
Figure 6.20 (a) Time-domain backscattered signal from the tags, (b) Time-frequency representation of the backscattered signal [80] (With permission, Copyright© 2014 IEEE). ...	161
Figure 6.21 Time-residue representation of the backscattered signal [80] (With permission, Copyright© 2014 IEEE). ....	161
Figure 6.22 (a) Real and imaginary parts of the measured backscattered signal, (b) Space-frequency diagram of the measured response [80] (With permission, Copyright© 2014 IEEE). .....	162
Figure 6.23 Ranging error versus SNR [88] (With permission, Copyright© 2014 IEEE). ....	164
Figure 6.24 System configuration for localizing chipless RFID tags in the reader area [88] (With permission, Copyright© 2014 IEEE).....	165
Figure 6.25 Flowchart of proposed localization algorithm [88] (With permission, Copyright© 2014 IEEE).....	167
Figure 6.26 Configuration of the 3-bit fabricated tag [88] (With permission, Copyright© 2014 IEEE).....	168
Figure 6.27 Simulated and measured RCS of the tag when the incident electric field is perpendicular to slot length [88] (With permission, Copyright© 2014 IEEE). ....	169
Figure 6.28 Normalized received power at the antenna versus frequency [88] (With permission, Copyright© 2014 IEEE). ....	169
Figure 6.29 Measured time-domain response from the tag for different distances [88] (With permission, Copyright© 2014 IEEE).....	170
Figure 6.30 (a) Frequency-domain, (b) time-domain, (c) time-frequency and (d) time-residue representation of measured backscattered signal from the tag [88] (With permission, Copyright© 2014 IEEE).....	171
Figure 6.31 (a) Real and (b) imaginary parts of the measured backscattered signal from the tag[88] (With permission, Copyright© 2014 IEEE). ....	171
Figure 6.32 Space-frequency diagram of measured backscattered response from the tag for different cases [88] (With permission, Copyright© 2014 IEEE). ....	172
Figure 6.33 (a) Two 2-bit tags illuminated by an incident electric field. (b) Frequency-domain response of the backscattered electric field from two tags, time-domain response from the tags for (c) $\varphi = 0^\circ$ and (d) $\varphi = 30^\circ$ [88] (With permission, Copyright© 2014 IEEE).....	173
Figure 6.34 Space-frequency diagram of the backscattered response from the tags [88] (With permission, Copyright© 2014 IEEE).....	173
Figure 6.35 Simulation set-up in FEKO [88] (With permission, Copyright© 2014 IEEE). ....	174
Figure 6.36 Measurement set-up for localizing the chipless RFID tag [88] (With permission, Copyright© 2014 IEEE). ....	175
Figure 6.37 (a) Measured time-domain signals from the tag located at the center of the unit cell, (b) Position of the tag extracted from the proposed technique compared to real position [88] (With permission, Copyright© 2014 IEEE). ....	175
Figure 6.38 Backscattered signals from two tags at the antenna ports [88] (With permission, Copyright© 2014 IEEE). ....	176

Figure 6.39 (a) Time-frequency response of the received signal at the first antenna, (b) Positions of the tags extracted from the proposed technique compared to real position [88] (With permission, Copyright© 2014 IEEE)..... 176

## LIST OF TABLES

Table 3-1. The resonant frequency, quality factor, and residue of the CNR of the slot for different cases. ....	64
Table 5-1 Percentage error of estimating of real and imaginary parts of the dominant poles of the tag calculated from direct matrix pencil method (MPM) and short-time-matrix-pencil-method (STMPM).....	134

# 1 INTRODUCTION

Today's ever increasing demand for wireless tracking and identification of objects and targets has attracted many people in industry to move toward the application of RFID systems. Compared to Barcodes, the RFID tags can be detected in longer distances and non-line-of-sight view of the reader antenna. It enables the sellers and managers to monitor different objects and personnel remotely. Nowadays, they are widely being used in different applications such as: advertising, transportation systems, passports, animal and human identification, libraries, hospitals and healthcare systems, museums and so on [1].

The concept of radio frequency identification (RFID) is relatively old and back to World War II [2]. Identification, friend or foe (IFF) is an identification system enables the radar to detect the closing target as friendly or not. In fact, it is the first RFID system used in practice. In 1948, the idea of modulation of the reflected signals in time domain was introduced [3]. The device modulated human voice on reflected light signals. In 1963, a breakthrough was happened by introducing the passive RFID transponder developed and patented by Richardson. Later on, inductive coupling between interrogator and tag was used for charging the passive RFID tags by Vinding. Many available chipless RFIDs in the market are working based on the same idea proposed in 1967. In 1975, Koelle, Depp and Feyman at Los Alamos Scientific Laboratory (LASL), introduced the idea of transponder antenna load modulation [4]. In 1980s and 1990s, many companies around the world started commercializing RFID systems in various applications such as transportation and personnel access in United States and Europe. In 1987, first RFID toll-collection system was employed in Alesound, Norway. Because of the widespread use of RFIDs in commercial applications, some organizations such as the International Standards Organization (ISO) and the International Electrotechnical Commission (IEC) conducted some standardization activities [5]. Recent advances in silicon technology enabled the integration and miniaturization of efficient RFID tags [6]. In June 2003, Wall-Mart Inc. introduced the RFID in "the near future" for all its suppliers at the Retail system conference, which led to the release of first EPCglobal standard [5, 7].

## 1.1 RFID Systems

In general, RFID systems can be divided into three classes: active, passive and semi-passive. Active tags need a power supply to power RF communication. This power supply implementation enables active tags to transmit information of longer distances. In passive RFID tags, there is no onboard power supply attached to the tag. Instead, it receives its power from an illuminating electromagnetic field lunched from the reader antenna. Hence, they are usually used in shorter-range communication with smaller data capacity compared to active tags. Figure 1.1 shows some passive RFID tags. These RFID tags are lighter and cheaper than active RFID tags.

Compared to active tags where a battery is directly used for generating RF power, the onboard battery in semi-passive RFID tags are employed only to provide power for supporting enabling circuits, not for generating RF power.

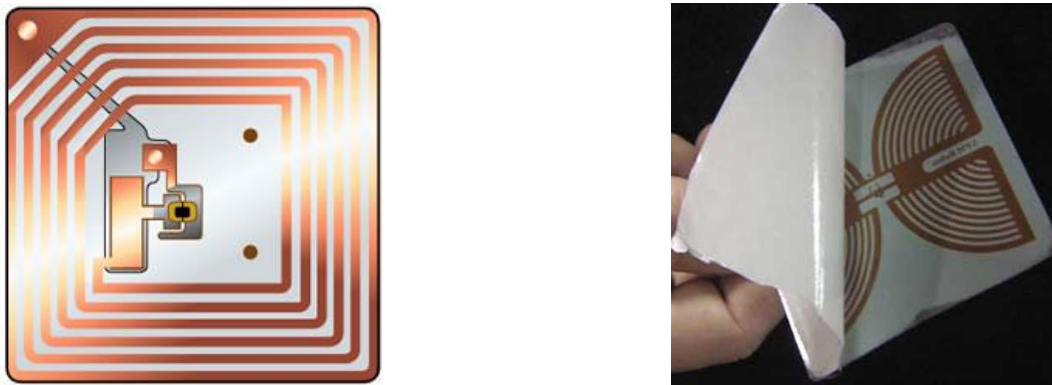


Figure 1.1 Two passive RFID tags.

## 1.2 Passive RFID tags

Because of lower price of passive tags, they are commonly used in identification systems. As mentioned before, passive tags are powered by an interrogating electromagnetic field. The tag introduces modulation on the scattered field, depending on the ID of the illuminated tag. These tags can be categorized by two groups of near-field and far-field tags.

### 1.2.1 Near-field RFID

In near-field RFID systems, the electromagnetic fields radiated from the reader antenna are coupled to the tag by an inductive coupling mechanism. Based on Faraday's principle, a large alternating current on the reader coil generates an alternating magnetic field around the antenna. The time-varying magnetic field can produce a small voltage across the tag if they are located in the reactive near-field of the tag. The voltage is rectified and used for powering the tag chip. The basic block diagram of the near-field RFID is shown in Figure 1.2. The analog front-end includes a limiter, rectifier and regulator. The regulated voltage powers up the digital unit including microcontrollers, Input/output and memory. It also has to meet the communications protocol and generate the required serial data to be transmitted to the reader [8]. Near-field tags are usually designed at low frequencies, commonly 128 KHz (LF) and 13.56 MHz (HF). The most problematic aspect with these tags is the large size of the antenna coils. As another drawback, the power changes with  $1/r^6$  ( $r$  is the distance from antenna) in the near field of the antenna leading to a fast decay of the power with respect to distance. The low data rate is another downside of near-field tags [5, 9].

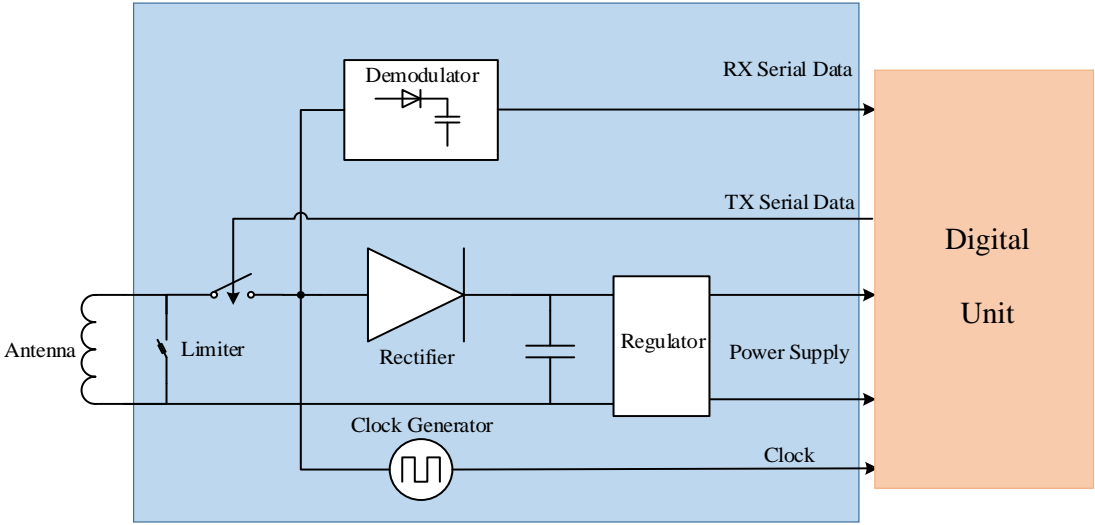


Figure 1.2 Block diagram of near-field passive RFID tag.

### 1.2.2 Far-field RFID

The fields in the far-field of antennas are radiative in nature. Figure 1.3 illustrates the communication mechanism in far-field RFID systems. The antenna illuminates the tag located in its far-field. Part of the incident field is modulated by a mismatching load connected to the antenna. This incorporates some data on the scattered field which can be used for identification purpose. Far-field tags usually operate at higher frequencies, 860-960 MHz (UHF band) or 2.45 GHz (Microwave). Compared to near-field tags, the employed antennas in these tags are smaller. The essential parts of the tag are antenna, voltage multiplier, modulator, and digital unit [6, 10].

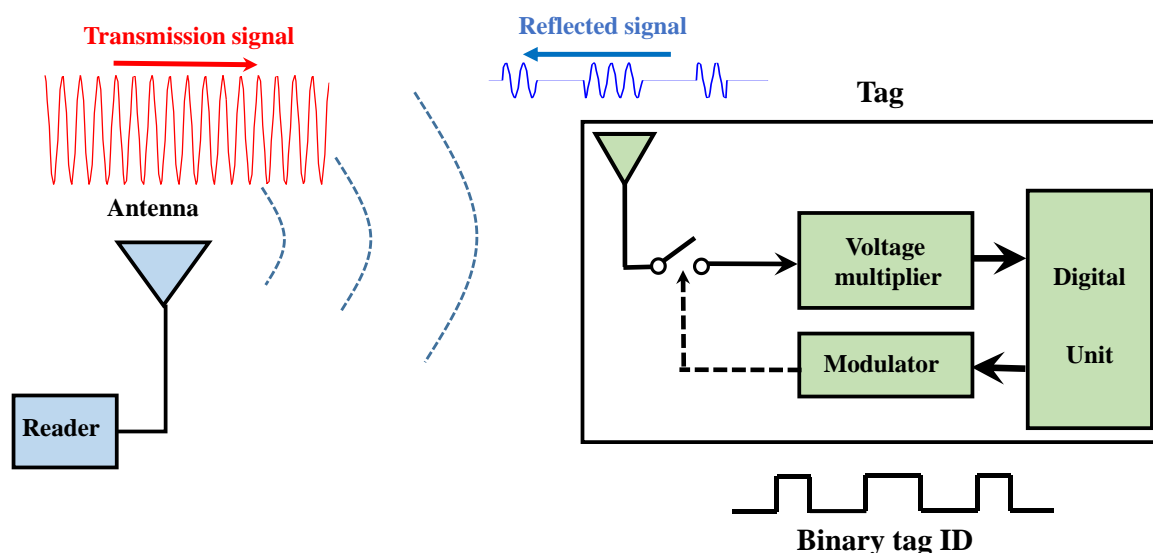


Figure 1.3 Far-field communication mechanism in RFID systems.

**Antenna.** Among various antennas proposed for RFID tags, the Gamma-matched dipole has been used in more UHF tags [8]. As Figure 1.4 shows, the antenna is attached to a chip. By loading the antenna with different impedances, a ASK modulation, based on information stored in the digital unit, is performed on the scattered electric field and reflected back to the reader.

**Voltage-multiplier.** Although higher power transfer efficiency is possible in near-field RFID systems, they are used in short-range communication. In UHF RFID tags, the tag is located in the far-field of the antenna. Based on radar equation, the maximum detectable range of the tag can be written by

$$R_{\max} = \frac{\lambda}{4\pi} \sqrt{\frac{P_{\text{reader}} G_{\text{reader}} G_{\text{tag}}}{P_{\min}}} \quad (1.1)$$

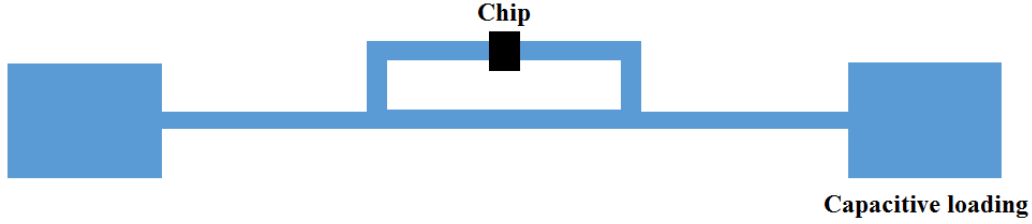


Figure 1.4 Gamma-matched antenna.

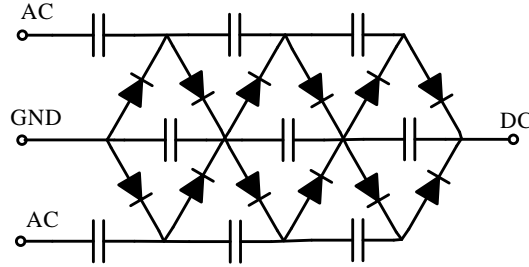


Figure 1.5 A 6-stage full-wave rectifier voltage multiplier.

where  $\lambda$  is the wavelength,  $P_{\text{reader}}$  represents radiated power of the transmitting signal,  $G_{\text{reader}}$  and  $G_{\text{tag}}$  are the gain of the reader antenna and tag antenna, respectively, and  $P_{\text{min}}$  is minimum power required by the tag to turn on. According to FCC regulation [11], the equivalent Isotropically Radiated Power (EIRP) for a reader at ISM band, 902 – 928 MHz, must be less than 4 W. Assuming 0 dB gain for the tag antenna and  $P_{\text{min}} = -15$  dBm, the maximum read range will be  $R_{\text{max}} = 3$  m at 915 MHz by ignoring polarization mismatch. In perfect matching condition between antenna and attached chip, the voltage on the chip port will be 41 mV, which is not sufficient for powering up the tag circuitry. A full-wave rectifier voltage multiplier shown in Figure 1.5 can be used to power up the tag circuitry. The number of stages and type of diodes determines the multiplication constant [8].

**Modulator.** Based on the radar equation, the received power ( $P_r$ ) by the reader antenna is given by

$$P_r = P_{\text{reader}} \frac{G_{\text{reader}} G_{\text{tag}} \lambda^2}{(4\pi)^3 R^4} \sigma_{\text{tag}} \quad (1.2)$$

The radar cross-section (RCS) of the tag,  $\sigma_{tag}$ , depends strongly on the loading of the antenna. Hence, by loading the antenna consistent with the embedded data in the digital memory, the RCS of the tag is changed. The demodulator can be a simple envelope detector which provides required power for digital unit.

**Digital Unit.** The digital unit is responsible for generating various transmit data based on the EPC G2 protocol. It is composed of a few sections including controller, memory, EPROM, clock generator, and so on. The voltage multiplier provides the required power to power up the digital unit [8].

### 1.3 Chipless RFID System

In chipless RFID systems, the tag does not contain any microchip. This reduces the price of the fabrication process of tag in industrial level. In these tags, the structure acts as both scatterer and modulator. The overall configuration of chipless RFID system is depicted in Figure 1.6. Three important parts of the system are tag, antenna and reader. The frequency of operation is UWB range, 3.1-10.6 GHz. The UWB antenna illuminates the reader area. The incident wave interrogates the chipless RFID tags presented in the reader area. The induced currents on the tags depends strongly on the tag geometry and size, polarization, direction and position of the tag relative to the reader antenna. The information on the tag must be aspect-independent and do not change by direction and position of the tag. These parameters are complex natural resonances (CNRs) of the tag. By embedding some resonant circuitry on the tag structure, the CNRs can be used as the ID of the tag. The reflected field is modulated by the tag structure, corresponding to embedded resonant circuitry, and reflects back to the antenna reader. After front-end of the receiver, the received signal is processed in the reader in order to extract the information of the tag. The most important part of the system is the reader and the employed detection algorithm. The received signal by the antenna includes the noise and reflections from background objects (clutter) in addition to the scattered signal from the tags. These interferences introduce some difficulties in extracting the required information from the received signal.

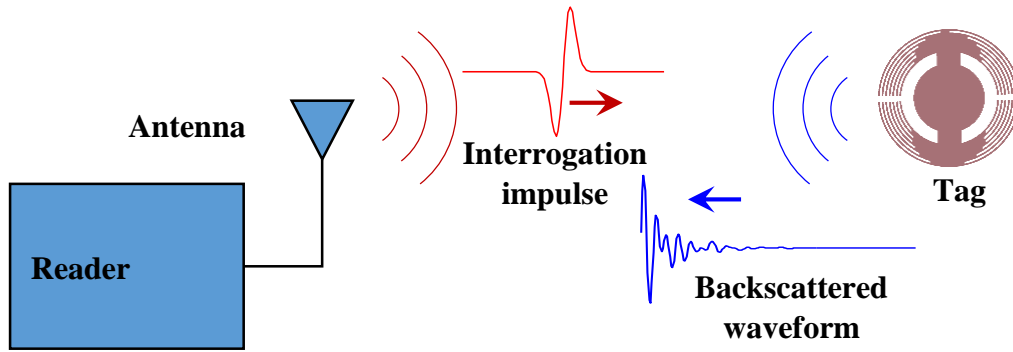


Figure 1.6 Chipless RFID system.

## 1.4 Dissertation Outline

This dissertation addresses three important parts of chipless RFID systems: chipless tag, antenna, and detection technique. Before starting the design and implementation of chipless RFID components, a theoretical background on the scattering mechanism in chipless RFID systems is required. Chapter 2 is devoted to the theory of the singularity expansion method (SEM), the eigenmode expansion method (EEM), and the characteristic mode theory (CMT). After studying the theoretical issues, some important features of the aforementioned methods applicable in the design of chipless RFID systems are addressed.

The theory introduced in chapter 2 is used in the design of chipless RFID tags in chapter 3. Since the tag structure acts as both scatterer and modulator, the radiation and resonant behaviors of the tag are studied versus structural parameters based on SEM and CMT. Taking advantages of SEM and CMT, the resonant frequencies, quality factors, and radiation characteristics of tag are investigated in terms of geometry and dimensions in a pole diagram. This helps the designer to easily assign the resonant frequencies and desired damping factors of the resonators for meeting requirements. These specifications are the read-range of the tag, data density (number of bits), and tag size. In some applications, all aforementioned specifications cannot be satisfied simultaneously and trade-off are needed in the design procedure. As an example, for embedding a high density of data on a small tag, the quality factors of the resonances must be very high. On the other hand, by increasing the quality factor, the radiation fields decrease, leading to a smaller radar cross-section of the tag. Hence, the read-range of the tag becomes shorter. In chipless RFID sensors, the radar cross-section of the tag or equivalently the strength of the received signal is very important.

Systematic design procedures introduced in chapter 3 provide some useful information and insight of the electromagnetic behavior of the tags.

In chapter 4, antenna structures applicable in UWB systems are reviewed. Because of the employment of UWB technology in chipless RFID systems, one needs to study both time-domain and frequency-domain characteristics of UWB antennas. Frequency-domain parameters of antennas are the input impedance and radiation pattern of the antenna. Likewise, the time-domain parameters of the antenna are the dispersion characteristics such as ringing, analytic envelope and group delay of the antenna. After a summary of these parameters, a small omni-directional antenna element useful in wideband and UWB applications is proposed. The time and frequency domain characteristics of the antenna are investigated in more detail in this chapter.

The next chapters of the dissertation are devoted to the detection process in chipless RFID system. In multiple multi-bit tags presented in the reader area, the time, frequency and spatial information of the tags are important in the detection, identification and localization processes, respectively. The accuracy of the employed approach depends strongly on the resolution in time, frequency and space. Since the IDs of the tags are included in the spectral domain of the scattered signal and its location can be obtained from its time-domain response, chapter 5 introduces some time-frequency representations of the received signal. After a review on short-time frequency transform (STFT), wavelet, and re-assigned joint time-frequency (RJTF) techniques, a new time-frequency analysis approach, called short-time matrix pencil method (STMPM) is explored in detail. By addressing the effective parameters of STMPM on resolution in time and frequency, it is applied to some scattered signals from scatterers. It will be shown that various scattering mechanisms such as resonance, scattering center, and dispersion characteristics of the scatterers can be detected in time-frequency representation of the signal. The effect of noise in the calculation of CNRs extracted from matrix pencil method (MPM) is studied and improved by STMPM. Then, the pole diagram and damping factors of the extracted CNRs of the signal are studied when the sliding window is located in the early-time and late-time responses of the scatterer. Finally, an efficient technique is introduced for separating the early-time and late-time responses of the scatterers.

Chapter 6 is dedicated to detection, identification and localization of chipless RFID tags. First, a space-time-frequency algorithm is introduced by which the locations and IDs of the tags are obtained in the reader. Assuming the reader area as a scattering medium, the tags act as the

scattering centers of the media. Based on Altes' model introduced in chapter 2, the scattering centers are calculated by applying NFMPM (dual of SMPM) to the frequency-domain response. In detection process, the number of tags presented in the reader area is obtained. In the cases where the tags are close to each other, the detection process is constrained to the range resolution. The range resolution is proportional to the inverse of the bandwidth of the incident pulse. In chipless RFID systems, the frequency band of operation is in the range of 3.1-10.6 GHz, leading to the resolution of 2 cm. It means that the tags distanced farther than 2 cm can be detected in the reader. In most radar applications, the idea of matched filter is used in the detection process. In chipless RFID systems where the information of the tags are included in the late-time responses, the early-time of the second scatterer might be hidden in the early time of the former illuminated target, which complicates the detection of the tags. This scenario is more complicated when the tags are located in close proximity of each other. By applying STMPM to the time-domain signal and monitoring the poles of the windowed signal in the pole diagram or the zero-crossing points in time-damping factor diagram of the signal, the locations of the tags can be obtained with a better accuracy. After detection of the tags, the identification process is performed by extracting the resonant frequencies of the tags. In circumstances when multiple tags are present in the reader area, an anti-collision algorithm is required in order to assign the extracted CNRs to the presented tags. Using three antennas spaced in the reader area, the positions of the tags can be calculated relative to a reference point. This procedure is called tag localization. Some scenarios are simulated and measured in the laboratory to confirm the validity of the proposed algorithm.

Finally, chapter 7 presents an overall summary, conclusions, contributions and followed by a short discussion and suggestions on the possibilities for future work.

## **2 Mathematical Representation of Scattered Fields from Chipless RFID Tags [8] (Chapter used with permission of Springer science and business media, 2015)**

In scattering scenarios when an incident electric field impinges a scatterer, the scattered fields can be mathematically represented by an inner product of the dyadic Green's function of the structure and equivalent induced currents on the scatterer. The induced currents and equivalently, the scattered fields can be expanded in different ways. In singularity expansion method (SEM), the induced currents are expanded versus the natural resonant modes of the scatterer. The natural modes are defined as the corresponding currents on the scatter surface at complex natural resonances (CNR), the zeroes of the metricized Green's function of the scatterer. Instead, the induced currents can be expanded versus the eigenmodes of the Green's function. Compared to the natural modes of the scatterer which are independent of frequency, the eigenmodes and corresponding eigenvalues of the scatterer are functions of frequency. For some special geometries, the structure is perfectly coincided with a special coordinate system. In such cases, the eigenmodes are in-phase on the scatterer surface. This is not valid for arbitrary shaped geometries. The characteristic modes of the scatterer are defined as the current modes whose corresponding scattered fields are in-phase on the surface of the scatterer. These modes are the eigenmodes of a generalized eigenvalue equation.

In this chapter, after studying the mathematical descriptions and the physical interpretation of the aforementioned current representations, a simple dipole is considered as a scatterer. By employing SEM and using electric-field integral equation (EFIE), the CNRs and corresponding natural modes on the dipole are calculated. As a second method, the eigenmodes and eigenvalues of the dipole are calculated by applying method of moment to the EFIE representation of the scatterer. Finally, the characteristic modes and equivalently, their scattered fields are calculated for different frequencies.

### **2.1 Singularity Expansion Method (SEM)**

As an example, a 3-bit chipless RFID tag shown in Figure 2.1 is illuminated by an incident field ( $\mathbf{E}^{\text{inc}}, \mathbf{H}^{\text{inc}}$ ), launched from a transmitting antenna. The surrounding medium is assumed to be free

space with permittivity  $\epsilon_0$  and permeability  $\mu_0$ . The ID of the tag is set into the resonant frequencies of the structure, which can be embedded into some resonant-based circuitry on the tag. In practical applications, it is beneficial to design the tag on a metallic surface in order to maximize the radiation efficiency of the scatterer. Assuming the induced current on the tag as  $\mathbf{J}$ , the scattered field is obtained from either an electric-field integral equation (EFIE) or a magnetic-field integral equation (MFIE) [12]. Here, the former case is considered for simplicity in formulations. Therefore, the scattered electric field is written in the Laplace domain as [13]

$$\mathbf{E}^s(\mathbf{r};s) = -\mu s \iint_A \left[ \left( \bar{\mathbf{I}} - \frac{1}{k^2} \nabla \nabla \right) G_0(\mathbf{r}, \mathbf{r}'; s) \right] \cdot \mathbf{J}(\mathbf{r}'; s) dS' \quad (2.1)$$

where  $\bar{\mathbf{I}} = \hat{x}\hat{x} + \hat{y}\hat{y} + \hat{z}\hat{z}$ ,  $s = \alpha + j\omega$  is the complex frequency,  $k = s/c$  represents the propagation constant of the fields in the complex frequency domain, and  $A$  is the surface of the tag. The primed and unprimed coordinates represent the source and observation points, respectively. The quantity  $G_0$  is the scalar Green's function in free space.

$$G_0(\mathbf{r}, \mathbf{r}'; s) = \frac{e^{-jk|\mathbf{r}-\mathbf{r}'|}}{4\pi|\mathbf{r}-\mathbf{r}'|} \quad (2.2)$$

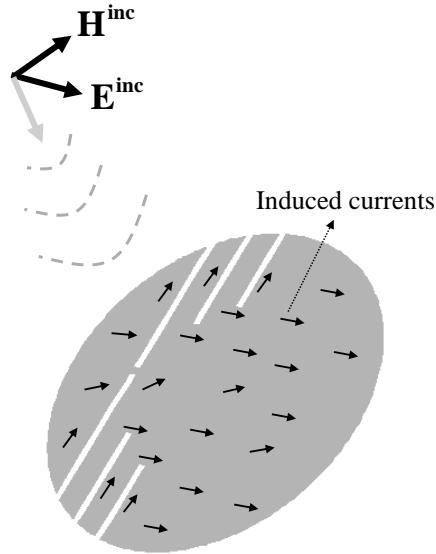


Figure 2.13-bit tag illuminated by an incident plane wave.

where  $G_0$  satisfies the Sommerfeld radiation condition as

$$\lim_{r \rightarrow \infty} r \left( \frac{\partial}{\partial r} + jk \right) G_0(\mathbf{r}, \mathbf{r}'; s) = 0 \quad (2.3)$$

The scattered field in (2.1) can be written as the inner product of the dyadic Green's function and current distribution on the structure as

$$\mathbf{E}^s(\mathbf{r}; s) = \left\langle \tilde{\mathbf{G}}(\mathbf{r}, \mathbf{r}'; s), \mathbf{J}(\mathbf{r}') \right\rangle_{\mathbf{r}'} \quad (2.4)$$

where the dyadic Green's function is defined as

$$\tilde{\mathbf{G}}(\mathbf{r}, \mathbf{r}'; s) = -\mu s \left( \tilde{\mathbf{I}} - \frac{1}{k^2} \nabla \nabla \right) G_0(\mathbf{r}, \mathbf{r}'; s) \quad (2.5)$$

The associated radiation condition for  $\tilde{\mathbf{G}}$  is

$$\lim_{r \rightarrow \infty} r (\nabla \times + jk \hat{r} \times) \tilde{\mathbf{G}}(\mathbf{r}, \mathbf{r}'; s) = \mathbf{0} \quad (2.6)$$

and  $\langle . \rangle$  in (2.4) is defined by

$$\langle \mathbf{A}, \mathbf{B} \rangle_a = \int \mathbf{A} \cdot \mathbf{B} da \quad (2.7)$$

Assuming the tag is a perfect electric conductor (PEC), the boundary condition on the tag surface is given by

$$\hat{t} \cdot (\mathbf{E}^s(\mathbf{r}; s) + \mathbf{E}^{\text{inc}}(\mathbf{r}; s)) = \mathbf{0} \quad \forall \mathbf{r} \in A \quad (2.8)$$

where  $\hat{t}$  denotes the unit vector tangential to the tag surface. As a result, the electric-field integral equation (EFIE) is written by

$$\left\langle \tilde{\mathbf{G}}(\mathbf{r}, \mathbf{r}'), \mathbf{J}(\mathbf{r}') \right\rangle_{\mathbf{r}'} = -\mathbf{E}_t^{\text{inc}}(\mathbf{r}) \quad \forall \mathbf{r} \in A \quad (2.9)$$

It is assumed that the integral in (2.9) is done as a finite-part integral. Subscript  $t$  in (2.9) indicates the tangential components of the fields on the tag surface. The method of moment (MoM) can be used to solve equation (2.9). By discretizing the surface of the tag into  $N$  isolated meshes and applying method of moments (MoM), one can rewrite (2.9) as

$$\Gamma_{mn} \cdot \mathbf{J}_n = \mathbf{I}_n \quad (2.10)$$

The matrix equation in (2.10) should be in some sense an accurate representation of the integral equation in (2.9). One important criterion of such accuracy is the convergence of the solution obtained from (2.9) to the real current distribution as  $N \rightarrow \infty$  [14]. The current distribution on the tag is obtained from

$$\mathbf{J}_n = \Gamma_{mn}^{-1} \cdot \mathbf{I}_n \quad (2.11)$$

According to (2.11), the singularity poles of the tag are the zeroes of the determinant of the coefficient matrix  $\Gamma$  as

$$\det(\Gamma(s_k)) = 0 \quad k=1, 2, 3 \quad (2.12)$$

These singularity poles are the complex natural resonances (CNRs) of the tag at which the current distribution on the tag shows damped oscillating behavior after the incident source field crosses through the tag. The basis of the SEM is that the current distribution is assumed to be an analytic function in the complex  $s$ -plane, except at CNRs such as

$$\mathbf{J}(\mathbf{r}; s) = \sum_{n=-\infty}^{+\infty} \frac{\mathbf{a}_n(\mathbf{r}; s)}{s - s_n} + \mathbf{J}_e(\mathbf{r}; s) \quad (2.13)$$

where  $s_n = \alpha_n + j\omega_n$  is the  $n^{\text{th}}$  CNR of the tag. Since the time-domain response is a real-valued signal, then for simple complex poles and coupling coefficients, one can write

$$s_n = s_{-n}^* \quad (2.14a)$$

$$\mathbf{a}_n(\mathbf{r}; s^*) = [\mathbf{a}_n(\mathbf{r}; s)]^* \quad (2.14b)$$

$$\mathbf{J}_e(\mathbf{r}; s^*) = [\mathbf{J}_e(\mathbf{r}; s)]^* \quad (2.14c)$$

Equation (2.13) needs some more interpretation. According to Mittag-Leffler's theorem [12], an entire function in the  $s$ -plane is required for each pole in the infinite series to guarantee the convergence of the series [15]. This entire function is represented by  $\mathbf{J}_e(\mathbf{r}; s)$  in (2.13). The other important part of the series is the weighting function  $\mathbf{a}_n(\mathbf{r}; s)$ , which is assumed separable in the spectral-spatial form of

$$\mathbf{a}_n(\mathbf{r}; s) = R_n(s) \mathbf{J}_n(\mathbf{r}) \quad (2.15)$$

Here,  $\mathbf{J}_n(\mathbf{r})$  is the natural mode of the tag at the  $n^{\text{th}}$  resonant frequency, and  $R_n(s)$  is the corresponding frequency-dependent residue of the pole. By inserting (2.15) in (2.13), the current distribution close to  $s_n$  is written by

$$\mathbf{J}(\mathbf{r}; s) = \frac{R_n(s) \mathbf{J}_n(\mathbf{r})}{s - s_n} + \mathbf{J}_e(\mathbf{r}; s) \quad (2.16)$$

It will be shown that for class-1 coupling coefficients,  $R_n$  is independent of complex frequency. By expanding  $\vec{\mathbf{G}}$  and the incident source field,  $\mathbf{E}^{\text{inc}}$ , in a power series around  $s = s_n$  as

$$\vec{\mathbf{G}}(\mathbf{r}, \mathbf{r}'; s) = \sum_{m=0}^{\infty} \frac{1}{m!} \left. \frac{\partial^m \vec{\mathbf{G}}(\mathbf{r}, \mathbf{r}'; s)}{\partial s^m} \right|_{s=s_n} (s - s_n)^m \quad (2.17)$$

$$\mathbf{E}_t^{\text{inc}}(\mathbf{r}; s) = \sum_{m=0}^{\infty} \frac{1}{m!} \left. \frac{\partial^m \mathbf{E}_t^{\text{inc}}(\mathbf{r}; s)}{\partial s^m} \right|_{s=s_n} (s - s_n)^m \quad (2.18)$$

and inserting (2.17) and (2.18) in (2.9), one can write

$$\begin{aligned} & \left\langle \vec{\mathbf{G}}(\mathbf{r}, \mathbf{r}'; s_n) + (s - s_n) \left. \frac{\partial \vec{\mathbf{G}}(\mathbf{r}, \mathbf{r}'; s)}{\partial s} \right|_{s=s_n} + \dots, \frac{R_n(s_n) \mathbf{J}_n(\mathbf{r}')}{s - s_n} + \mathbf{J}_e(\mathbf{r}'; s) \right\rangle_{\mathbf{r}'} \\ & = -\mathbf{E}_t^{\text{inc}}(\mathbf{r}; s_n) - (s - s_n) \left. \frac{\partial \mathbf{E}_t^{\text{inc}}(\mathbf{r}; s)}{\partial s} \right|_{s=s_n} - \dots \end{aligned} \quad (2.19)$$

By balancing the two sides of (2.19) according to powers of  $(s - s_n)$ , some important expressions are obtained. The coefficient of the  $(s - s_n)^{-1}$  term at  $s = s_n$  gives

$$\left\langle \vec{\mathbf{G}}(\mathbf{r}, \mathbf{r}'; s_n), \mathbf{J}_n(\mathbf{r}') \right\rangle_{\mathbf{r}'} = \mathbf{0} \quad (2.20)$$

Equation (2.20) provides some important features of the CNRs and corresponding natural modes. By converting (2.20) to matrix form, it is seen that the determinant of the coefficient matrix should be zero at CNRs in order to have nontrivial solutions. As another significant point, these poles are completely dependent upon the dyadic Green's function of the structure and as (2.20) illustrates, they are source-free and aspect-independent parameters of the tag. This is the reason that these parameters are often used in identification applications. For each CNR,  $s_n$ , there is a nontrivial

natural mode,  $\mathbf{J}_n(\mathbf{r})$ , which is the solution of (2.20). Corresponding to (2.20), one can define the coupling factors as the solutions to the following homogenous equation

$$\langle \mathbf{M}_n(\mathbf{r}'), \tilde{\mathbf{G}}(\mathbf{r}, \mathbf{r}'; s_n) \rangle_{\mathbf{r}'} = \mathbf{0} \quad (2.21)$$

By equating the coefficients of  $(s-s_n)^0$  in both sides of (2.19), one has

$$\langle \tilde{\mathbf{G}}(\mathbf{r}, \mathbf{r}'; s_n), \mathbf{J}_e(\mathbf{r}'; s) \rangle_{\mathbf{r}'} + R_n(s_n) \left\langle \left. \frac{\partial \tilde{\mathbf{G}}(\mathbf{r}, \mathbf{r}'; s)}{\partial s} \right|_{s=s_n}, \mathbf{J}_n(\mathbf{r}') \right\rangle_{\mathbf{r}'} = -\mathbf{E}_t^{\text{inc}}(\mathbf{r}; s_n) \quad (2.22)$$

The inner products in the left-hand side of (2.22) are performed on the  $\mathbf{r}'$  parameter. Thus, both sides of the equation are functions of  $\mathbf{r}$ . By taking the inner products of the two sides of (2.22) by  $\mathbf{M}_n(\mathbf{r})$ , the coupling coefficients can be found at resonant frequencies as

$$R_n(s_n) = - \frac{\langle \mathbf{M}_n(\mathbf{r}), \mathbf{E}_t^{\text{inc}}(\mathbf{r}; s_n) \rangle_{\mathbf{r}}}{\left\langle \mathbf{M}_n(\mathbf{r}), \left\langle \left. \frac{\partial \tilde{\mathbf{G}}(\mathbf{r}, \mathbf{r}'; s)}{\partial s} \right|_{s=s_n}, \mathbf{J}_n(\mathbf{r}') \right\rangle_{\mathbf{r}'} \right\rangle_{\mathbf{r}}} \quad (2.23)$$

For electric-field integral equations (EFIE), where symmetric matrices are encountered, the coupling vectors and natural mode vectors are the same [12], so that (2.23) is written by

$$R_n(s_n) = - \frac{\langle \mathbf{J}_n(\mathbf{r}), \mathbf{E}_t^{\text{inc}}(\mathbf{r}; s_n) \rangle_{\mathbf{r}}}{\left\langle \mathbf{J}_n(\mathbf{r}), \left\langle \left. \frac{\partial \tilde{\mathbf{G}}(\mathbf{r}, \mathbf{r}'; s)}{\partial s} \right|_{s=s_n}, \mathbf{J}_n(\mathbf{r}') \right\rangle_{\mathbf{r}'} \right\rangle_{\mathbf{r}}} \quad (2.24)$$

It is seen in (2.24) that the coupling coefficients at resonant frequencies depend on the incident electric field as well as the natural mode distribution at the corresponding resonant frequency. In the cases where  $\langle \mathbf{J}_n(\mathbf{r}), \mathbf{E}_t^{\text{inc}}(\mathbf{r}; s_n) \rangle_{\mathbf{r}} = 0$ , the related mode will not be excited by the incident electric field. The coupling coefficients in (2.24) are just obtained at CNRs of the tag. There is no straightforward way to obtain the entire function added to the resonant response of the scatterer in (2.13). Mathematically, this is necessary to guarantee convergence of the series. However, more explanation is needed in order to understand the physical concepts behind the theory of SEM. As the equation (2.24) shows, the coupling coefficients at the resonant frequencies of the structure

depend on the natural modes, dyadic Green's function of the structure, and incident field at those frequencies. For other complex frequencies,  $s$ , different representations can be chosen as the coupling coefficient, which affects the entire function added to the series. In the late-time response of the scatterer, we have just the damped sinusoids corresponding to the CNRs of the tag. Hence, the entire-function contribution comes into the early-time response, which rises and falls faster than the late-time signals. In order to cover other complex frequencies, different coupling coefficients have been introduced, where class 1 and class 2 representations are most common in literature [12]. For a class 1 representation, which is the simplest one, the coupling coefficients of the natural modes are defined as

$$\begin{aligned}
R_n^{(1)}(s) &= e^{(s_n - s)t_0} R_n(s_n) \\
&= -e^{(s_n - s)t_0} \frac{\left\langle \mathbf{J}_n(\mathbf{r}), \mathbf{E}_t^{\text{inc}}(\mathbf{r}; s_n) \right\rangle_{\mathbf{r}}}{\left\langle \mathbf{J}_n(\mathbf{r}), \left\langle \frac{\partial \tilde{\mathbf{G}}(\mathbf{r}, \mathbf{r}'; s)}{\partial s} \Big|_{s=s_n}, \mathbf{J}_n(\mathbf{r}') \right\rangle_{\mathbf{r}'} \right\rangle_{\mathbf{r}}}
\end{aligned} \tag{2.25}$$

By inserting (2.25) in the series part in (2.13), the time-domain response is given by

$$\mathbf{j}(\mathbf{r}; t) = U(t - t_0) \text{Re} \left[ \sum_{n=1}^{\infty} R_n \mathbf{j}_n(\mathbf{r}) e^{s_n t} \right] + \mathbf{j}_e(\mathbf{r}; t) \tag{2.26}$$

where  $U(\cdot)$  is the Heaviside step function defined as

$$U(t - t_0) = \begin{cases} 1 & t \geq t_0 \\ 0 & t < t_0 \end{cases} \tag{2.27}$$

and the inverse Laplace transform is defined as

$$\mathbf{j}(\mathbf{r}; t) = \int_{Br} e^{st} \mathbf{J}(\mathbf{r}; s) ds \tag{2.28}$$

which causality ensured by having the Bromwich integration contour  $Br$  passing above all singularities in the  $s$ -plane. Turn-on time might be the time at which the incident wave is first applied anywhere on the tag. Although class 1 form of the coupling is more useful in the analytical-based formulation of SEM, it shows some convergence issues in earlier times of the response in

numerical calculations [16]. For computational purposes, the class 2 form is more efficient. In this form, the frequency dependency of the coupling coefficients is held in the incident electric field as

$$R_n^{(2)}(s) = - \frac{\left\langle \mathbf{J}_n(\mathbf{r}), e^{(s_n-s)t_0} \mathbf{E}_t^{\text{inc}}(\mathbf{r}; s) \right\rangle_{\mathbf{r}}}{\left\langle \mathbf{J}_n(\mathbf{r}), \left\langle \frac{\partial \tilde{\mathbf{G}}(\mathbf{r}, \mathbf{r}'; s)}{\partial s} \Big|_{s=s_n}, \mathbf{J}_n(\mathbf{r}') \right\rangle_{\mathbf{r}'} \right\rangle_{\mathbf{r}}} \quad (2.29)$$

The effect of these coupling coefficients on the current distribution can be better illustrated in the time domain. For more simplicity, the following incident electric field is considered.

$$\mathbf{E}_t^{\text{inc}}(\mathbf{r}; s) = \mathbf{E}_0 e^{-\frac{s}{c} \hat{\mathbf{r}} \cdot \mathbf{r}} \quad (2.30)$$

where the vector  $\hat{\mathbf{r}}$  is the propagation vector,  $\mathbf{E}_0$  includes the polarization vector and amplitude of the incident wave, and  $c$  is the speed of light in free space. By inserting (2.29) and (2.30) in (2.23), the current distribution in the Laplace domain is written as

$$\mathbf{J}(\mathbf{r}; s) = \sum_{n=-\infty}^{\infty} \frac{\left\langle \mathbf{J}_n(\mathbf{r}), \mathbf{E}_0 e^{(s_n-s)t_0 - \frac{s}{c} \hat{\mathbf{r}} \cdot \mathbf{r}} \right\rangle_{\mathbf{r}} \mathbf{J}_n(\mathbf{r})}{(s-s_n) \left\langle \mathbf{J}_n(\mathbf{r}), \left\langle \frac{\partial \tilde{\mathbf{G}}(\mathbf{r}, \mathbf{r}'; s)}{\partial s} \Big|_{s=s_n}, \mathbf{J}_n(\mathbf{r}') \right\rangle_{\mathbf{r}'} \right\rangle_{\mathbf{r}}} + \mathbf{J}_e(\mathbf{r}; s) \quad (2.31)$$

By applying the inverse Laplace transform defined in (2.28) to (2.31), the current distribution in time domain is written as

$$\mathbf{j}(\mathbf{r}; t) = 2 \sum_{n=1}^{\infty} \text{Re} \left( \frac{\left\langle \mathbf{J}_n(\mathbf{r}), \mathbf{E}_0 e^{-\frac{s_n}{c} \hat{\mathbf{r}} \cdot \mathbf{r}} U\left(t-t_0 - \frac{\hat{\mathbf{r}} \cdot \mathbf{r}}{c}\right) \right\rangle_{\mathbf{r}} \mathbf{J}_n(\mathbf{r})}{\left\langle \mathbf{J}_n(\mathbf{r}), \left\langle \frac{\partial \tilde{\mathbf{G}}(\mathbf{r}, \mathbf{r}'; s)}{\partial s} \Big|_{s=s_n}, \mathbf{J}_n(\mathbf{r}') \right\rangle_{\mathbf{r}'} \right\rangle_{\mathbf{r}}} e^{s_n t} \right) + \mathbf{j}_e(\mathbf{r}; t) \quad (2.32)$$

The convergence difficulties in the class 1 form of coupling coefficients are alleviated in the class 2 representation, where a time-varying region of integration covers that part of the object surface, which has already been illuminated by the incident field [16]. When the incident wave completely passes through the tag, both class 1 and class 2 representations are similar. For better illustration,

Figure 2.2 shows the region of integration at  $t = t_0$  on the surface of the tag for class 2 coupling coefficients when the incident plane wave passes through a part of the tag.

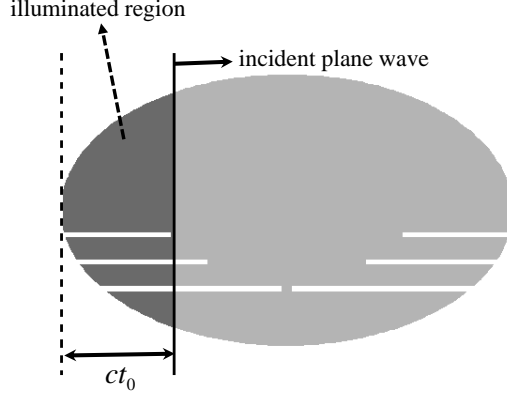


Figure 2.23-bit tag illuminated partly by an incident plane wave.

By representing the current distribution on the tag as the summation over the natural modes in the late-time response accompanying an entire function as the early-time response, the scattered field is obtained from the integral equation in (2.4) as

$$\begin{aligned} \mathbf{E}^s(\mathbf{r}; s) &= \left\langle \tilde{\mathbf{G}}(\mathbf{r}, \mathbf{r}'; s), \sum_n \frac{R_n(s) \mathbf{J}_n(\mathbf{r}')}{s - s_n} + \mathbf{J}_e(\mathbf{r}'; s) \right\rangle_{\mathbf{r}'} \\ &= \sum_n \frac{\left\langle \tilde{\mathbf{G}}(\mathbf{r}, \mathbf{r}'; s), \mathbf{J}_n(s) R_n(s) \right\rangle_{\mathbf{r}'}}{s - s_n} + \left\langle \tilde{\mathbf{G}}(\mathbf{r}, \mathbf{r}'; s), \mathbf{J}_e(\mathbf{r}'; s) \right\rangle_{\mathbf{r}'} \end{aligned} \quad (2.33)$$

The radiated field close to the  $n^{\text{th}}$  CNR is written by

$$\mathbf{E}^s(\mathbf{r}; s) = \left\langle -\mu s \left( \tilde{\mathbf{I}} - \frac{1}{k^2} \nabla \nabla \right) G_0(\mathbf{r}, \mathbf{r}'; s), \frac{R_n(s) \mathbf{J}_n(\mathbf{r}')}{s - s_n} + \mathbf{J}_e(\mathbf{r}'; s) \right\rangle_{\mathbf{r}'} \quad (2.34)$$

In the far field, the field in (2.34) can be approximated by

$$\begin{aligned} \mathbf{E}_n(\mathbf{r}; s) &= \left\langle -\mu s (\tilde{\mathbf{I}} - \hat{r} \hat{r}) G_0(\mathbf{r}, \mathbf{r}'), \frac{R_n(s) \mathbf{J}_n(\mathbf{r}')}{s - s_n} \right\rangle_{\mathbf{r}', s=s_n} - \left\langle \mu s (\tilde{\mathbf{I}} - \hat{r} \hat{r}) G_0(\mathbf{r}, \mathbf{r}'), \mathbf{J}_e(\mathbf{r}'; s) \right\rangle_{\mathbf{r}'} \\ &= \left\langle -\mu s (\tilde{\mathbf{I}} - \hat{r} \hat{r}) \frac{e^{-jk(r-r'\cdot\hat{r})}}{4\pi r}, \frac{R_n(s) \mathbf{J}_n(\mathbf{r}')}{s - s_n} \right\rangle_{\mathbf{r}', s=s_n} - \left\langle \mu s (\tilde{\mathbf{I}} - \hat{r} \hat{r}) \frac{e^{-jk(r-r'\cdot\hat{r})}}{4\pi r}, \mathbf{J}_e(\mathbf{r}'; s) \right\rangle_{\mathbf{r}'} \end{aligned} \quad (2.35)$$

As (2.35) expresses, in the far-field region, the scattered fields in the time domain are approximately proportional to the first derivative of the current distributions on the tag. In contrast, in the near field, the field distribution is mostly affected by the spatial derivatives of the currents. By applying the inverse Laplace transform to the scattered field in (2.33), the fields in the time domain are written as

$$e^s(\mathbf{r};t) = U(t-t_0) \sum_n |R_n| e^{-\alpha_n t} \cos(\omega_n t + \phi_n) + e_e(\mathbf{r};t) \quad (2.36)$$

where the class 1 form of coupling coefficients is assumed in (2.36). According to (2.36), the scattered field from a tag is affected by two different phenomena. Early-time response, which is depicted by  $e_e(r;t)$  in (2.36), is affected by the specular reflections from the scattering centers of the tag. The early-time response is followed by the series of damped sinusoidals with some weighting coefficients. The CNRs of the tag, shown by  $s_n = \alpha_n + j\omega_n$ , are aspect-independent parameters of the tag, not dependent on the direction, polarization, or distance to the tag's observation point. For this reason, they are well-suited to be used as the tag's ID.

### 2.1.1 Altes' Model

Though the late-time response of the tag can be compactly cast into a series-form formulation, it is not as easy to predict the behavior of the early-time impulse response. This is because it depends on the spatial variations of the scatterer and observation point. Based on (2.33), the early-time response is formulated by

$$\mathbf{E}_e(r;s) = \left\langle -\mu s \left( \tilde{\mathbf{I}} - \frac{1}{k^2} \nabla \nabla \right) G_0(\mathbf{r}, \mathbf{r}'; s), \mathbf{J}_e(\mathbf{r}'; s) \right\rangle \quad (2.37)$$

where the first part of the dyadic Green's function is more pronounced in the far zone and the second term is dominant in the near zone of the scatterer. Because of the fast variations of the early-time currents, the scattered field includes pulse-shape impulses reflected from the scattering centers of the tag. Assuming a scatterer containing  $M$  scattering centers is illuminated by an incident plane wave with pulse function  $p(t)$ , the backscattered signal in the early time can be modeled as the summation of the delayed pulses from the scattering centers as [17]

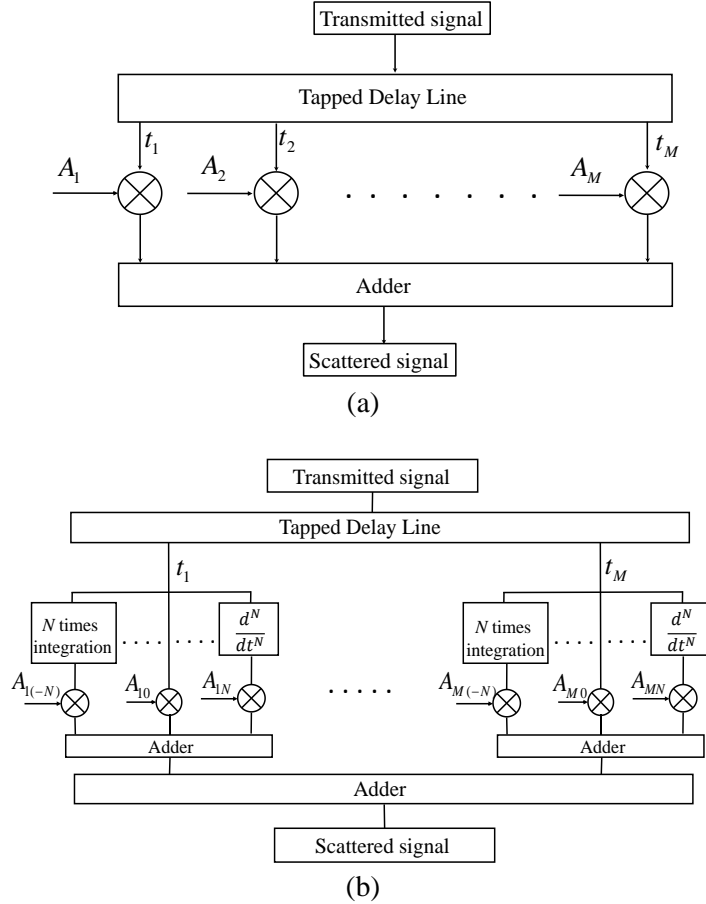


Figure 2.3(a) Transversal and (b) modified filter model of the early-time response.

$$e_e(r;t) = \sum_{m=1}^M A_m p(t-t_m) \quad (2.38)$$

where  $A_m$  and  $t_m$  are the amplitude and time delay related to the  $m^{\text{th}}$  scattering center. This early-time representation is modeled in Figure 2.3a as a tapped delay line ( $t_1, t_2, \dots, t_M$ ) with  $M$  multipliers and an adder. Based on physical optics approximations, some functions other than impulses must be added to the series in (2.38) in order to completely model the early-time response of the scatterer. The model seen in Figure 2.3a, which includes the parallel combinations of the integrators and differentiators, can be described with the well-accepted model in Figure 2.3b by assuming that some of the delay differences  $t_{m+1}-t_m$  are very small compared to the smallest wavelength of the impinging signal. If two neighboring scattering centers have opposite signs, and their delay difference ( $d= t_{m+1}-t_m$ ) is very small,  $d \ll 1$ , one can write

$$A_m(p(t-t_{m+1})-p(t-t_m)) \propto \left. \frac{dp(t)}{dt} \right|_{t=t_m} \quad (2.39)$$

This component is proportional to the differentiated signal at  $t = t_m$ . Similarly, weighting factors can result in a return component as

$$[p(t) + p(t+d) + \dots + p(t+kd)] \propto \int_0^{kd} p(t) dt \quad (2.40)$$

In order to perfectly model the early-time response of the scatterer, one must consider both the integrators and differentiators in the model, in addition to the replica of the incident pulse. This model is formulated as the convolution of the incident pulse with the impulse responses of the scattering centers.

$$e_e(r;t) = p(t) * \sum_{m=1}^M \sum_{n=-\infty}^{+\infty} A_{mn} \delta^{(n)}(r;t-t_m) \quad (2.41)$$

In (2.41), the impulse response of the  $m^{\text{th}}$  scattering center is summed over the integrals and derivatives of the Dirac-delta function. Here, the negative and positive values of  $n$  refer to the  $n^{\text{th}}$  integral and derivative of the delta function with respect to time. In the Laplace domain, the early-time response is written by

$$\begin{aligned} E_e(r;s) &= \sum_{m=1}^M \sum_{n=-\infty}^{+\infty} A_{mn} s^n P(r;s) e^{st_m} \\ &= \sum_{m=1}^M \sum_{n=-\infty}^{+\infty} B_{mn}(r;s) e^{st_m} \end{aligned} \quad (2.42)$$

where

$$B_{mn} = A_{mn} s^n P(r;s) \quad (2.43)$$

For scattering from edges, fractional  $n = \pm 0.5$  must be considered in  $B_{mn}$  [18]. By comparing (2.42) with (2.36), it is inferred that there is a duality between early-time response in the Laplace domain and late-time response in the time domain. In the former, the response is expanded over the exponential functions of delay times, while in the latter, the time-domain response is expanded versus exponential functions of complex resonances of the tags. This duality will be helpful in the identification process of chipless RFID tags, presented in Chapter 6.

In simple scatterers such as chipless RFID tags, the reflection from the first illuminated part of the tag is strong enough to be considered as the early-time response of the tag. But in the complex scatterers such as an airplane, the impulse responses of the multiple scattering centers of the target should be considered in the response. Therefore, the early-time response from the simple scatterers can accurately be approximated by just one term of the series shown in (2.42). This part is strongly dependent on the polarization and direction of the incident electric field. This is because of the dependency of the scattering centers on the polarization and direction of the incident wave. Additionally, the shape of the early-time response changes from the near field of the scatterer to its far field. In the near field, the scattered field is mostly similar to the incident pulse, but in the far field, the scattered field is limited to the first time-derivative of the incident field [19], [20]. As an example, the scattered field from a rectangular metal plane with size of 15 cm×15 cm illuminated by an incident pulse is considered. The measurement set-up is shown in Figure 2.4. A rectangular metal plane is located 60 cm above an optical table. A TEM horn antenna is connected to a digital sampling oscilloscope in order to calculate the backscattered signal from the tag at different distances. Another measurement without the presence of the metal is performed and the results are subtracted from the earlier signal to cancel the effects of background objects. Time averaging is applied to the received pulses in order to improve the signal-to-noise ratio (SNR). The excitation pulse and its derivative with respect to time are shown in Figure 2.5. In Figure 2.6, the backscattered signal from the plate is shown when it is located at four different distances  $d = 20$  cm, 30 cm, 1 m and 1.3 m away from the antenna aperture.

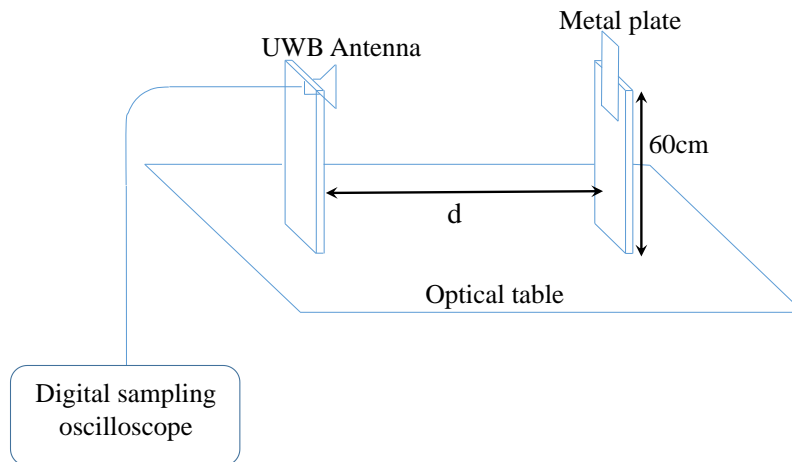


Figure 2.4 Measurement setup to measure a UWB pulse scattered from a metal object.

In the cases where  $d = 20$  cm and 30 cm, the observation point is in the near-field of the scatterer and as can be seen, the scattered signal is similar to the incident pulse. In these two cases, the scattered signal is followed by a tail, which is related to the impulse response of the antenna. By locating the plate and the antenna in the far- field of each other, the scattered signal inclines to the first derivative of the incident pulse. By increasing the distance between the antenna and scatterer, the amplitude of the scattered signal decreases. In Figure 2.7, the normalized responses are plotted for  $d = 20$  cm and  $d = 130$  cm. According to the results, the scattered field is similar to the incident field in the near-field and similar to the first derivative of the incident pulse in the far-field of the scatterer.

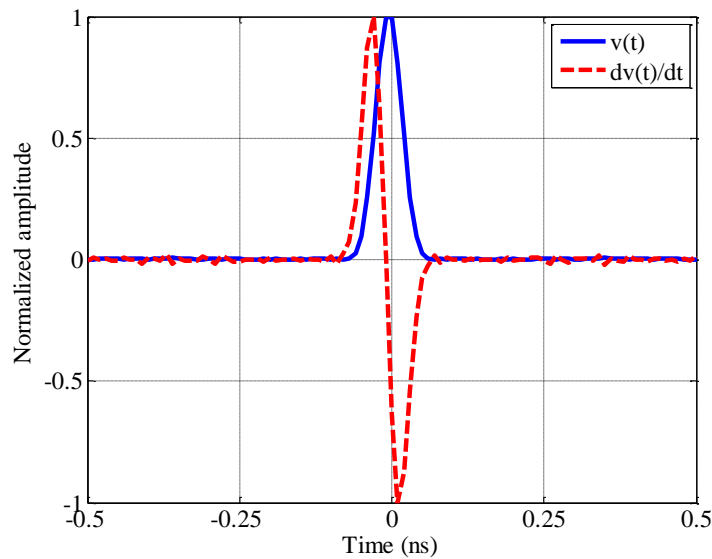


Figure 2.5 Excitation pulse and its derivative with respect to time.

### 2.1.2 SEM-Based Equivalent Circuit of Scatterer

In previous chapters, the mathematical representation of the scattering modes was studied. The early-time response of the scatterer was formulated in (2.41) by the time convolution of the incident pulse with the summation over localized impulse responses of the scattering centers of the tag. Based on the wavefront representation [21-23], the interactions between the local resonances in the early time generate global resonances. According to the singularity expansion method, these global resonances are modeled in the time domain as the summation over damped sinusoids corresponding to the complex natural resonances of the scatterer with some weighting residues as the coupling coefficients. Although the CNRs are aspect-independent, depending only on the geometry and material of the scatterer, the coupling coefficients are strongly aspect-

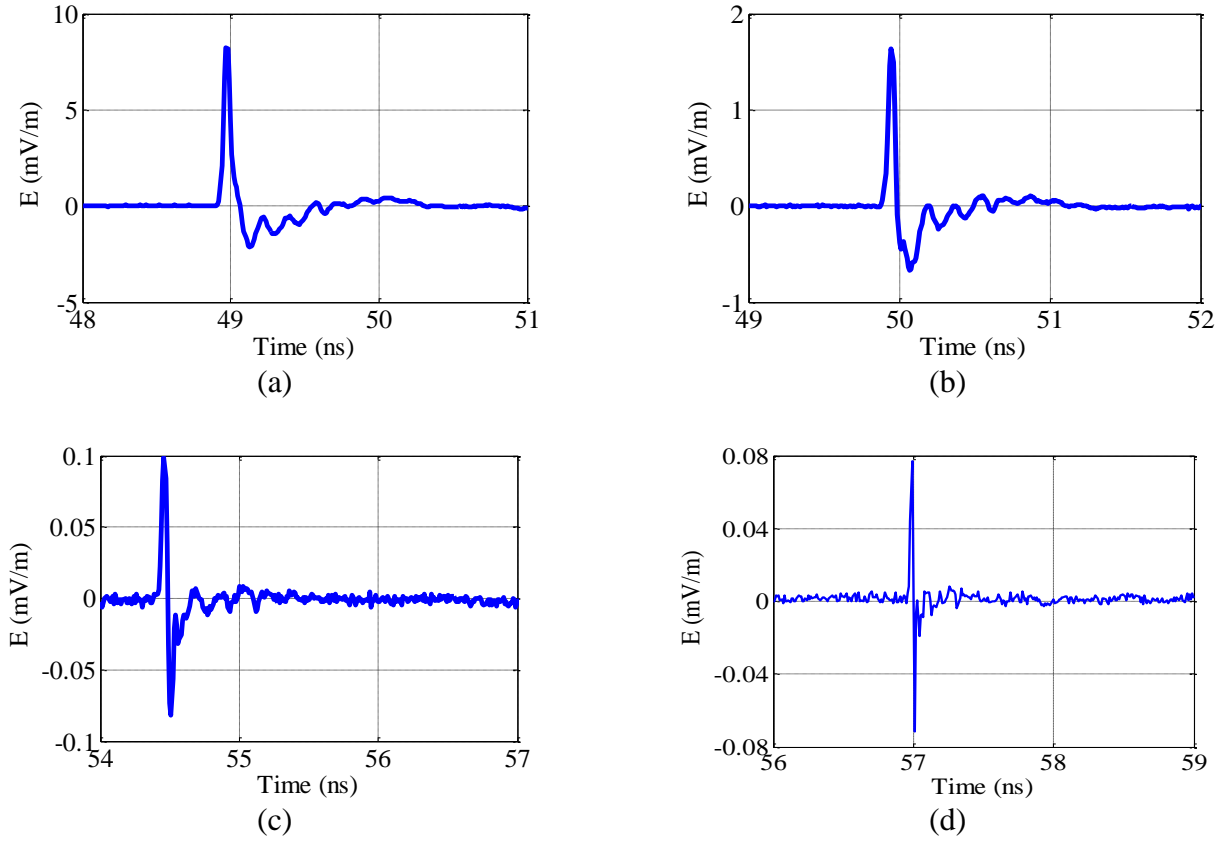


Figure 2.6 Received electric field from the metal object for different distances (a)  $d = 20$  cm, (b)  $d = 30$  cm, (c)  $d = 100$  cm, and  $d = 130$  cm.

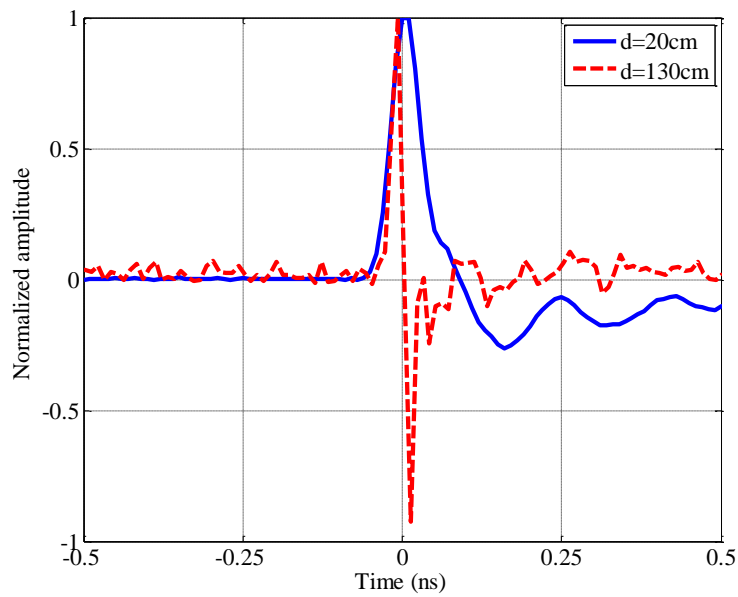


Figure 2.7 Received electric field from the metal plate for  $d = 20$  cm and  $d = 130$  cm.

dependent. In the scattering analysis, it is usually more desirable to model the scattering process with an equivalent-circuit representation. This equivalent circuit is helpful in the design process of the scatterer. In order to consider the effects of polarization in the scattering process, a general situation, shown in Figure 2.8a, is assumed. Assuming the incident and scattered electric fields as  $E^{\text{inc}}$  and  $E^{\text{s}}$  with polarization vectors  $\hat{a}_{\text{inc}}$  and  $\hat{a}_s$ , the scattering transfer function of the tag is defined as

$$H_t(\hat{a}_{\text{inc}}, \hat{a}_s; s) = \frac{E^{\text{s}}(r; s)}{E^{\text{inc}}(r; s)} \quad (2.44)$$

Assuming the incident electric field as a Dirac-delta function, the transfer function of the tag is related to the scattered electric field. The equivalent circuit of the scatterer is depicted in Figure 2.8b. The input and output voltages are defined at the transmitting and receiving antenna ports, respectively. The incident field is coupled to the CNRs by coupling coefficients  $n_{\text{inc}}^{(i)}$   $i=1, 2, \dots, N$ , which depend on the direction and polarization of the incident electric field. Each CNR is represented by a parallel RLC circuit in series with a delay line, which models the turn-on times of the CNRs. The excited natural current modes are coupled to the scattered field with coupling coefficients  $n_s^{(i)}$   $i=1, 2, \dots, N$ . The quantity  $Z_e$  represents the early-time response of the tag, which is aspect-dependent. The transfer function of the tag as defined in (2.44) is converted to the ratio of output to input voltages. With some mathematical manipulation, the transfer function can easily be written as

$$\begin{aligned} H(s) &= H_e(s) + H_1(s) \\ &= H_e(s) + \sum_{n=1}^N \left[ \frac{A_n}{s - s_n} + \frac{A_n^*}{s - s_n^*} \right] \end{aligned} \quad (2.45)$$

The first term is the early-time part and the second term, including the complex natural resonances, is the late-time part. Although in reality,  $N$  is infinity, for numerical computations,  $N$  is usually truncated to a finite value.

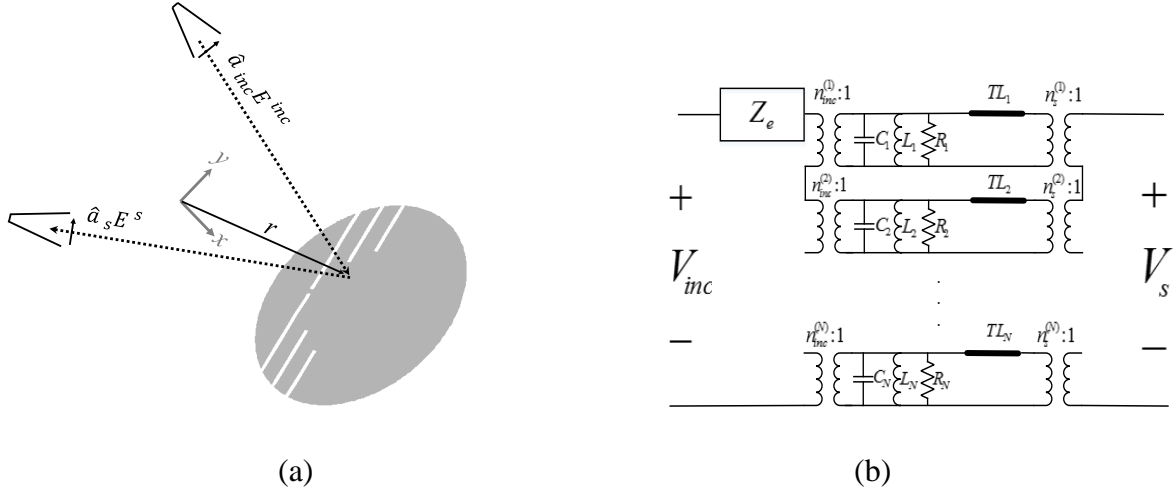


Figure 2.8 (a) A tag illuminated by an incident plane pulse, and (b) SEM-based equivalent circuit of chipless RFID tag

### 2.1.3 SEM Representation of Currents on a Dipole

In this section, scattered fields from a dipole are formulated based on the SEM in order to illustrate the application of the SEM in numerical computations [24]. A single dipole of length  $L = 1\text{m}$  is aligned with the  $z$ -axis (Figure 2.9) and illuminated by an incident plane wave propagating in the direction forming an angle  $\theta$  with the  $z$ -axis. The incident wave is assumed to be a step function, striking the scatterer at  $t = 0$ . By formulating the current distribution using the SEM, it is possible to obtain the current distribution and scattered fields in the time domain. By neglecting the effects of the end caps on the wire and  $\varphi$  variations of the currents on the wire, a Pocklington equation can be written for the axially-directed current on the dipole. Assuming  $s = \alpha + j\omega$ , the Pocklington equation is written as [24]

$$-s\varepsilon_0 E_t^{\text{inc}}(z, s) = \int_{-L/2}^{L/2} I(z', s) \left( \frac{\partial^2}{\partial z^2} - \frac{s^2}{c^2} \right) K(z, z'; s) dz' \quad (2.46)$$

where  $E_t^{\text{inc}}$  is the tangential component of the incident electric field along the dipole and the kernel  $K$  is given by

$$K(z, z'; s) = \frac{1}{2\pi a} \int_0^{2\pi} \frac{\exp(-sR/c)}{4\pi R} a d\phi \quad (2.47)$$

Here,  $a$  is the radius of the wire and

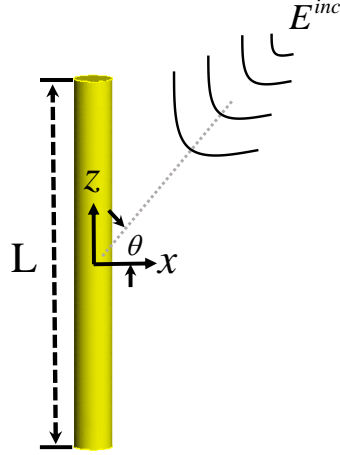


Figure 2.9 Geometry of the dipole illuminated by an incident field.

$$R = \left[ (z - z')^2 + 4a^2 \sin^2(\phi/2) \right]^{1/2} \quad (2.48)$$

The incident tangential electric field along the dipole is written by

$$E_t^{inc}(z, s) = E^{inc}(s) \cos(\theta) \exp\left(\frac{sz \sin(\theta)}{c}\right) \quad (2.49)$$

For the step-function incident wave, we have

$$E^{inc}(s) = \frac{E_0}{s} \quad (2.50)$$

By discretizing the length of the dipole into  $N$  segments, the integral equation in (2.46) is converted to the equation

$$[Z][I] = [V] \quad (2.51)$$

where  $[Z]$  is an  $N \times N$  matrix referred to as the system impedance matrix,  $[I]$  is an  $N \times 1$  response vector and  $[V]$  is an  $N \times 1$  vector corresponding to the incident field. According to (2.20), at CNRs of the scatterer, the following equation holds

$$[Z(s_n)][I(s_n)] = 0 \quad (2.52)$$

The CNRs of the dipole are obtained from

$$\Delta(s_n) = \det(Z(s_n)) = 0 \quad (2.53)$$

The CNRs can be calculated by employing different searching algorithms. One easy way is to expand  $\Delta(s)$  in a complex Taylor series about  $s_n$  as

$$\Delta(s_n) = \Delta(s_0) + \Delta'(s_0)(s - s_0) + \dots = 0 \quad (2.54)$$

Keeping the first two terms of the series, the CNR,  $s_n$ , is obtained from

$$s_n = s_0 - \frac{\Delta(s_0)}{\Delta'(s_0)} \quad (2.55)$$

where  $s_0$  is the initial guess of the resonant frequency. More accurate values for  $s_n$  can be obtained by repeating this procedure. Figure 2.10 shows the pole diagram of the dipole. It is seen that the poles,  $s_n = \alpha_n + j\omega_n$ , are located in different layers in the  $s$ -plane. The poles situated in the first layer are more dominant in the time-domain response because they have lower damping factors than those located in the further layers. The natural current modes on the dipole are the solutions of equation (2.52).

$$[I] = [Z]^{-1} [V] = \frac{[Y]}{\Delta(s)} [V] \quad (2.56)$$

In Figure 2.11, the real and imaginary parts of the first three modes of the dipole located in the first layer are depicted. By possessing the natural modes and CNRs of the dipole, the current distribution can be cast to the form

$$[I] = [Z]^{-1} [V] = \frac{[Y]}{\Delta(s)} [V] \quad (2.57)$$

where  $R_n$  is the residue of the  $n^{\text{th}}$  pole, obtained from (2.24). The time-domain response is obtained by applying an inverse Laplace transform along the appropriate Bromwich contour.

$$[i(t)] = \sum_n R_n \exp(s_n t) [J_n] \quad (2.58)$$

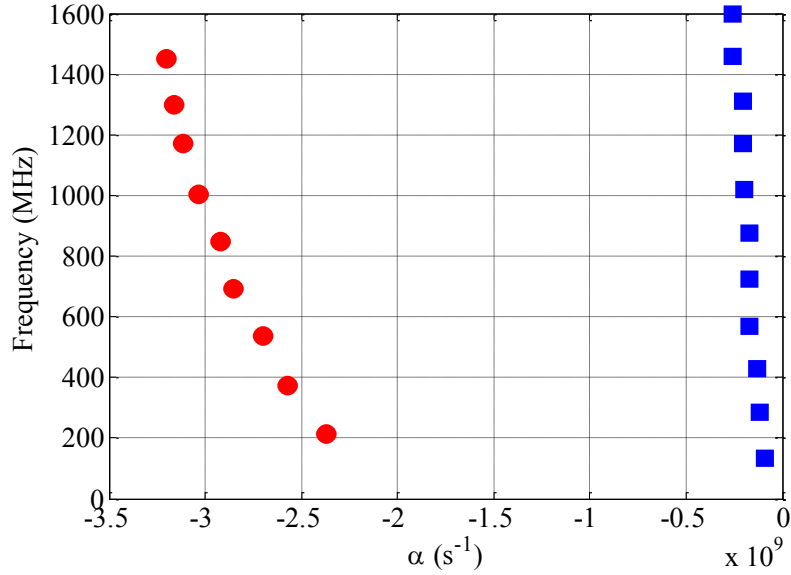


Figure 2.10 Pole diagram of the dipole, representing the resonant frequency and damping factor of the CNRs.

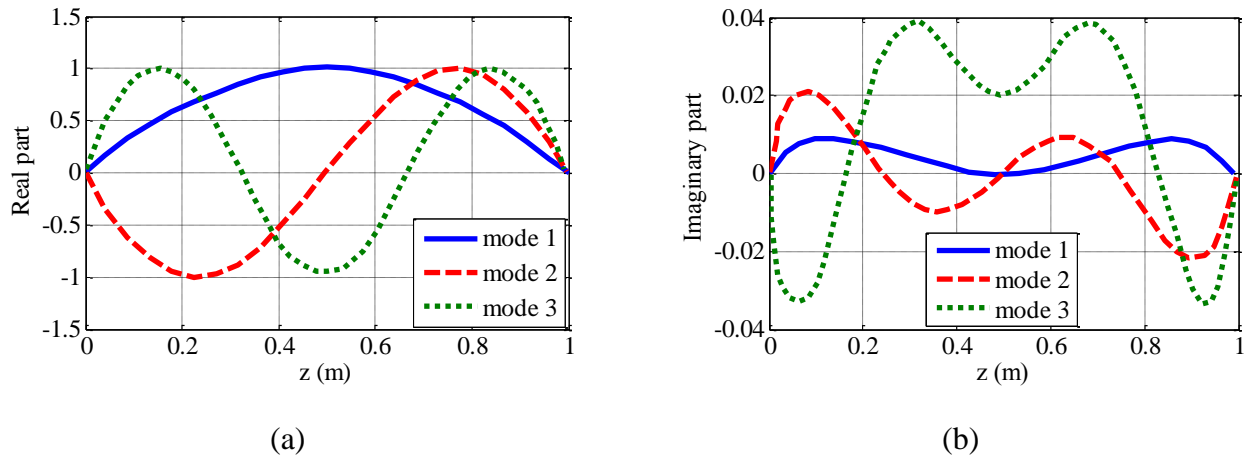


Figure 2.11 (a) Real and (b) imaginary parts of the first three natural currents of the dipole.

## 2.2 Eigenmode Expansion Method

Returning to scattering from the chipless tag shown in Figure 2.1, the incident electric field induces a current distribution on the tag, which can be calculated by applying boundary conditions on the tag surface as

$$\langle \tilde{\mathbf{G}}(\mathbf{r}, \mathbf{r}'; s), \mathbf{J}(\mathbf{r}') \rangle_{\mathbf{r}'} = -\mathbf{E}_t^{\text{inc}}(\mathbf{r}; s) \quad \forall \mathbf{r} \in A \quad (2.59)$$

where  $\hat{\mathbf{G}}$  in the following formulations is the electric-type dyadic Green's function and  $A$  represents the surface of the tag. The eigenvalue equation associated with (2.59) is written by

$$\langle \tilde{\mathbf{G}}(\mathbf{r}, \mathbf{r}'; s), \mathbf{J}_n(\mathbf{r}'; s) \rangle_{\mathbf{r}'} = \lambda_n(s) \mathbf{J}_n(\mathbf{r}; s) \quad \forall \mathbf{r} \in A \quad (2.60)$$

where  $\mathbf{J}_n(\mathbf{r}; s)$  and  $\lambda_n(s)$  are  $n^{\text{th}}$  eigenmode and eigenvalue of  $\tilde{\mathbf{G}}$ , respectively. By applying the method of moment (MoM), the integral equation in (2.59) is converted to the following matrix equation

$$\mathbf{\Gamma}(s) \cdot \mathbf{J}(s) = \mathbf{I}_e(s) \quad (2.61)$$

and the eigenvalue equation corresponding to (2.61) is written by

$$\mathbf{\Gamma}(s) \cdot \mathbf{J}_n(s) = \lambda_n(s) \mathbf{J}_n(s) \quad (2.62)$$

In order to have nontrivial solutions, the determinant of the coefficient matrix must be zero as

$$C = \det(\mathbf{\Gamma}(s) - \lambda_n(s) \mathbf{I}) = 0 \quad (2.63)$$

$C$ , is called the characteristic equation and  $\mathbf{I}$ , is a unit matrix. Assuming  $\mathbf{\Gamma}$  to be a square matrix of rank  $N$ , one can write

$$\det(\mathbf{\Gamma}(s)) = \prod_{n=1}^N \lambda_n(s) \quad (2.64)$$

The eigenvalues may or may not all be distinct. It is clearly seen from (2.63) and (2.64) that the CNRs of the scatterer are the zeroes of the eigenvalues. Each eigenvalue may contain an infinite number of CNRs. For each square matrix, two sets of eigenmodes, right-side and left-side, are defined. In (2.62), the right-side eigenmodes are introduced, which are represented by  $\mathbf{J}_n^{\text{R}}$  in the following. The left-side Eigenmodes are defined as [25]

$$\mathbf{J}_n^{\text{L}}(s) \cdot \mathbf{\Gamma}(s) = \lambda_n(s) \mathbf{J}_n^{\text{L}}(s) \quad (2.65)$$

The orthogonality and bi-orthogonality relations between eigenmodes can be summarized as

$$\mathbf{J}_n^L(s) \cdot \mathbf{J}_m^L(s) = \delta_{mn} \quad (2.66a)$$

$$\mathbf{J}_n^R(s) \cdot \mathbf{J}_m^R(s) = \delta_{mn} \quad (2.66b)$$

$$\mathbf{J}_n^L(s) \cdot \mathbf{J}_m^R(s) = \delta_{mn} \quad (2.66c)$$

where

$$\delta_{mn} = \begin{cases} 0 & m \neq n \\ 1 & m = n \end{cases}$$

The current distribution and incident electric field in (2.62) can be expanded versus the eigenmodes as

$$\mathbf{J}(s) = \sum_{n=1} a_n \mathbf{J}_n^R(s) \quad (2.67)$$

$$\mathbf{I}_e = \sum_{n=1} b_n \mathbf{J}_n^R(s) \quad (2.68)$$

Substituting (2.67) into (2.63) and using (2.68), one arrives at

$$\begin{aligned} \sum_{n=1} a_n \Gamma(s) \cdot \mathbf{J}_n^{(R)}(s) &= \sum_{n=1} a_n \lambda_n(s) \mathbf{J}_n^{(R)}(s) \\ &= \mathbf{I}_e(s) \end{aligned} \quad (2.69)$$

By taking an inner product of the two sides of (2.69) with  $\mathbf{J}_n^{(L)}(s)$  and using the orthogonality relation in (2.66), one can write

$$a_n = \frac{1}{\lambda_n(s)} \cdot \frac{\mathbf{J}_n^{(L)}(s) \cdot \mathbf{I}(s)}{\mathbf{J}_n^{(L)}(s) \cdot \mathbf{J}_n^{(R)}(s)} \quad (2.70)$$

Therefore, the current distribution on the tag is written by

$$\mathbf{J}(s) = \sum_{n=1} \frac{1}{\lambda_n(s)} \cdot \frac{\mathbf{J}_n^{(L)}(s) \cdot \mathbf{I}(s)}{\mathbf{J}_n^{(L)}(s) \cdot \mathbf{J}_n^{(R)}(s)} \mathbf{J}_n^{(R)}(s) \quad (2.71)$$

By defining the normalized dyadic functions as

$$\mathbf{d}_n(s) = \frac{\mathbf{J}_n^{(R)}(s)\mathbf{J}_n^{(L)}(s)}{\mathbf{J}_n^{(R)}(s) \cdot \mathbf{J}_n^{(L)}} \quad (2.72)$$

the current distribution in (1.71) can be expressed by

$$\mathbf{J}(s) = \sum_n \frac{1}{\lambda_n(s)} \mathbf{d}_n(s) \cdot \mathbf{I}(s) \quad (2.73)$$

By comparing (2.61) and (2.73), one can write

$$\Gamma^{-1} = \sum_n \frac{1}{\lambda_n(s)} \mathbf{d}_n(s) \quad (2.74)$$

It shows that the singularity poles of the scatterer are the zeroes of the Eigenvalues. Similarly,

$$\Gamma = \sum_n \lambda_n(s) \mathbf{d}_n(s) \quad (2.75)$$

Therefore,

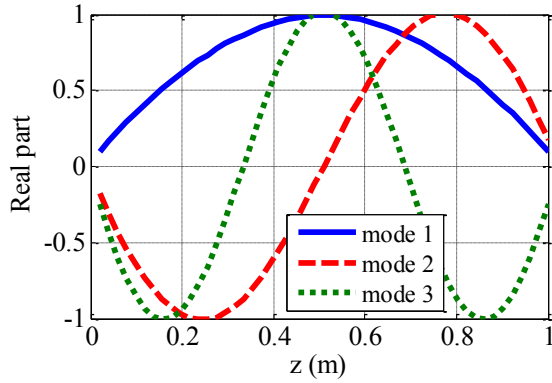
$$\begin{aligned} (\Gamma(s))^{-1} \cdot \Gamma(s) &= \sum_n \mathbf{d}_n \\ &= \boldsymbol{\delta} \end{aligned} \quad (2.76)$$

In some scattering problems, the geometry of the scatterer is perfectly matched to a specific coordinate system. As an example, when the incident electric field illuminates a perfectly electric conducting (PEC) sphere or an infinite cylinder, the scattered fields or equivalently the induced currents on the scatterer can be easily expanded versus the eigenmodes of the structures. For arbitrary geometries, which are not necessarily compatible with any specific coordinate system, the numerical evolution of the eigenmode equation (2.62) can be used in order to find the eigenmodes, eigenvalues and, consequently, the complex natural resonances of the scatterer.

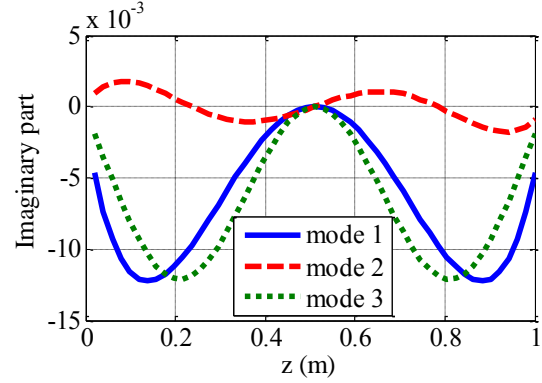
### 2.2.1 Example: Eigenmode Expansion of Currents on a Dipole

Assuming the dipole seen in Figure 2.9, the eigenmodes and eigenvalues of the dyadic Green's function of the scatterer can be calculated from (2.62). The real and imaginary parts of the first

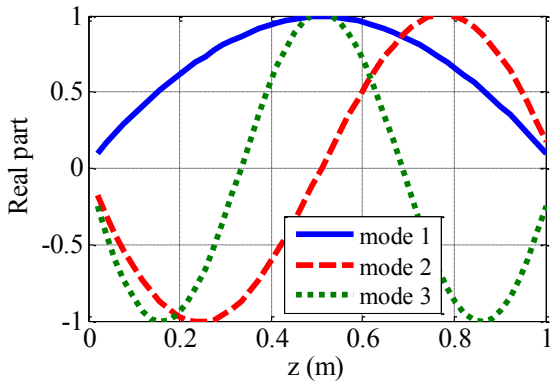
three eigenmodes of impedance matrix of the dipole are represented in Figure 2.12 at frequencies  $f = 133$  MHz and  $f = 400$  MHz. Compared to the real part of the eigenmodes, the imaginary part changes significantly by frequency.



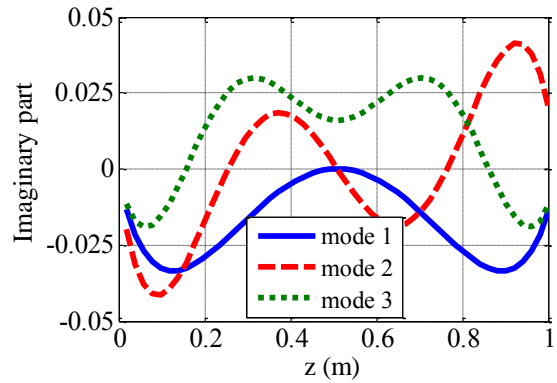
(a) Real part at  $f = 133$  MHz



(b) Imaginary part at  $f = 133$  MHz



(c) Real part at  $f = 400$  MHz



(d) Imaginary part at  $f = 400$  MHz

Figure 2.12 Real and imaginary parts of the first three eigenmodes of the dipole.

### 2.3 Characteristic Mode Theory

For structures whose geometry coincides perfectly with a special coordinate system, the eigenmodes of the structure are in-phase on the surface of the scatterer. As an example, assuming a perfectly conducting sphere of radius  $a$  is illuminated by an incident plane wave, the scattered fields can be written by

$$\begin{Bmatrix} \mathbf{E} \\ \mathbf{H} \end{Bmatrix} = \sum_{m,n} \begin{Bmatrix} \mathbf{A}_{mn} \\ \mathbf{B}_{mn} \end{Bmatrix} h_n^{(2)}(\beta_r r) P_n^m(\cos(\theta)) e^{-jn\phi} \quad (2.77)$$

where  $h_n^{(2)}$  is the second kind spherical Hankel function and  $P_n^m$  represents the associated Legendre function of first kind,  $\theta$  is the angle measured from  $z$ -axis and  $\phi$  is the angle measured from  $xz$ -plane. Since the sphere is assumed as PEC, the induced currents on its surface can be obtained from

$$\mathbf{J} = \hat{\mathbf{n}} \times \mathbf{H} \quad (2.78)$$

Fields in (2.77) satisfy the following Maxwell equation as

$$\nabla \times \nabla \times \begin{Bmatrix} \mathbf{E} \\ \mathbf{H} \end{Bmatrix} = k_0^2 \begin{Bmatrix} \mathbf{E} \\ \mathbf{H} \end{Bmatrix} \quad (2.79)$$

which can be written as three separate eigenvalue equation. The induced currents and the scattered fields in (2.77) and (2.78) are in-phase on the surface of the sphere. The same result is seen for cylindrical mode expansion around an infinitely long cylinder located along the  $z$ -axis. In such special cases where the geometry of the structure is perfectly matched to a special coordinate system, the boundary conditions can be easily satisfied on just one spatial component of the fields. The idea of characteristic modes is how to expand the currents and fields versus the basis functions (or characteristic modes) which are in-phase on the scatterer surface. This theory was first introduced by Garbacz in 1971 for conducting bodies of arbitrary shapes [26]. His proposed approach was based on diagonalizing the scattering matrix of the scatterers. He presented a new class of eigenmodes on a scatterer that are real and their corresponding scattered fields have constant phase over the surface of the body. Although the proposed method was used in some cases, its implementation was not easy for an arbitrarily-shaped scatterer. In [27], Harrington proposed an alternative viewpoint for diagonalizing an operator. This technique relates the current distribution to the tangential electric field on the body. He defined a particular weighted eigenvalue equation, which gives the same eigenmodes defined by Garbacz, but with a simpler approach. Ever since, this proposed technique has been widely employed in the design and modeling of antennas and scatterers [28-33]. Similar to natural resonant modes, the characteristic modes are independent of source fields and depend only on the geometry and shape of a scatterer.

### 2.3.1 Mathematical Formulation of the Characteristic Mode Theory

Referring to Figure 2.1, it is assumed that an incident plane wave illuminates the scatterer. The first step in formulating the eigenvalue equation, which defines the characteristic modes of the tag, is the application of the electric-field integral equation (EFIE) on the tag surface as

$$\begin{aligned}\mathcal{L}(J) &= \left\langle \vec{\mathbf{G}}(\mathbf{r}, \mathbf{r}'; s), \mathbf{J}(\mathbf{r}') \right\rangle_{\mathbf{r}'} \\ &= -\mathbf{E}_t^{\text{inc}}(\mathbf{r}; s)\end{aligned}\quad (2.80)$$

where  $\vec{\mathbf{G}}$  is defined in (2.5) and the integration is performed over the surface of the tag. Since the operator  $\mathcal{L}(\cdot)$  in (2.80) has the dimensions of impedance, it is more convenient to introduce the notation

$$\mathcal{Z}(\mathbf{J}) = \mathcal{L}(\mathbf{J}) \quad (2.81)$$

where  $\mathcal{Z}$  is a symmetric operator as

$$\langle B, \mathcal{Z}(C) \rangle = \langle \mathcal{Z}(B), C \rangle \quad (2.82)$$

One can write  $\mathcal{Z}$  in terms of its real and imaginary components

$$\mathcal{Z} = \mathcal{R} + j\mathcal{X} \quad (2.83)$$

where  $\mathcal{R} = \frac{1}{2}(\mathcal{Z} + \mathcal{Z}^*)$  and  $\mathcal{X} = \frac{1}{2j}(\mathcal{Z} - \mathcal{Z}^*)$ . Since the radiated power from a current distribution  $\mathbf{J}$  on the tag is given by

$$P = \langle \mathbf{J}^*, \mathcal{R}(\mathbf{J}) \rangle \quad (2.84)$$

it follows that  $\mathcal{R}$  is positive semi-definite. The starting step in defining the characteristic modes of the tag is the following eigenvalue equation

$$\mathcal{Z}(\mathbf{J}_n) = \gamma_n \mathcal{M}(\mathbf{J}_n) \quad (2.85)$$

where  $\gamma_n$  and  $\mathbf{J}_n$  are the  $n^{\text{th}}$  eigenvalue and eigenmode of the equation and  $\mathcal{M}$  is a weighting operator. Choosing  $\mathcal{M} = \mathcal{R}$  ensures orthogonality of the radiation patterns of the current modes in the far zone. Introducing

$$\gamma_n = 1 + j\lambda_n \quad (2.86)$$

into (2.85), the eigenvalue equation is converted to

$$\mathcal{X}(\mathbf{J}_n) = \lambda_n \mathcal{R}(\mathbf{J}_n) \quad (2.87)$$

Since  $\mathcal{R}$  and  $\mathcal{X}$  are real symmetric operators, both the eigenvalues  $\lambda_n$  and the corresponding characteristic modes,  $\mathbf{J}_n$ , must be real. In addition, the eigenmodes satisfy the orthogonality relationships

$$\langle \mathbf{J}_m, \mathcal{R}(\mathbf{J}_n) \rangle = \delta_{mn} \quad (2.88a)$$

$$\langle \mathbf{J}_m, \mathcal{X}(\mathbf{J}_n) \rangle = \lambda_n \delta_{mn} \quad (2.88b)$$

$$\langle \mathbf{J}_m, \mathcal{Z}(\mathbf{J}_n) \rangle = (1 + j\lambda_n) \delta_{mn} \quad (2.88c)$$

where

$$\delta_{mn} = \begin{cases} 1 & m = n \\ 0 & m \neq n \end{cases}$$

The electric and magnetic fields produced by an eigenmode  $\mathbf{J}_n$  on the surface of the tag are called characteristic fields, and are referred to as  $(\mathbf{E}_n, \mathbf{H}_n)$ . One important property of the characteristic fields is their orthogonality in the far zone. Based on Poynting's Theorem, the mutual power coupling between the current modes  $\mathbf{J}_n$  and  $\mathbf{J}_m$  distributed on the surface of the tag can be written as follows

$$\begin{aligned} P_{mn} &= \langle \mathbf{J}_m^*, \mathcal{Z}(\mathbf{J}_n) \rangle \\ &= \langle \mathbf{J}_m^*, \mathcal{R}(\mathbf{J}_n) \rangle + j \langle \mathbf{J}_m^*, \mathcal{X}(\mathbf{J}_n) \rangle \\ &= \int_{S'} \mathbf{E}_m \times \mathbf{H}_n^* \cdot d\mathbf{s} + j\omega \iiint_{v'} (\mu \mathbf{H}_m \cdot \mathbf{H}_n^* - \varepsilon \mathbf{E}_m \cdot \mathbf{E}_n^*) dv \end{aligned} \quad (2.89)$$

Here,  $S'$  is any surface enclosing the tag and  $v'$  is the region enclosed by  $S'$ . According to the orthogonality relations in (2.88), we have

$$P_{mn} = (1 + j\lambda_n) \delta_{mn} \quad (2.90)$$

If  $S'$  is chosen to be a sphere at infinity, then the characteristic fields in the far zone can be expressed by

$$\begin{aligned}\mathbf{E}_n &= -\eta \hat{r} \times \mathbf{H}_n \\ &= \frac{-j\omega\mu}{4\pi r} e^{-jkr} \mathbf{F}_n(\theta, \phi)\end{aligned}\quad (2.91)$$

where  $\eta = \sqrt{\mu/\varepsilon}$  is the intrinsic impedance of space,  $\hat{r}$  is the unit radial vector perpendicular to  $S'$ ,  $(\theta, \varphi)$  are the angular coordinates of the position on  $S'$  and  $\mathbf{F}_n$  is the pattern of the field. Inserting the far-zone fields in (2.89), the real and imaginary parts of the radiated power can easily be separated as

$$\int_{S'} \mathbf{E}_m \times \mathbf{H}_n^* \cdot d\mathbf{s} = \delta_{mn} \quad (2.92)$$

$$\omega \iiint_{V'} (\mu \mathbf{H}_m \cdot \mathbf{H}_n^* - \varepsilon \mathbf{E}_m \cdot \mathbf{E}_n^*) dv = \lambda_n \delta_{mn} \quad (2.93)$$

Relation (2.92) expresses the orthogonality of the characteristic fields in the far-zone region. For a single characteristic mode, (2.93) is written by

$$\omega \iiint_{V'} (\mu \mathbf{H}_n \cdot \mathbf{H}_n^* - \varepsilon \mathbf{E}_n \cdot \mathbf{E}_n^*) dv = \lambda_n \quad (2.94)$$

From (2.94), it is seen that at resonant frequencies where the electric and magnetic energies are equal, the corresponding eigenvalues are zero. At frequencies where  $\lambda_n > 0$ , the fields are inductive and for  $\lambda_n < 0$ , the fields are capacitive. According to (2.87), at resonant frequencies, we have

$$\mathcal{X}(\mathbf{J}_n) = 0 \quad (2.95)$$

By applying MoM and converting equation (2.95) into matrix equation, the determinant of the reactance matrix should be zero at the resonant frequencies of the structure in order to have nontrivial solutions.

The current distribution on the tag can be expanded in terms of the characteristic current modes as

$$\mathbf{J} = \sum_{n=1} a_n \mathbf{J}_n \quad (2.96)$$

where  $\mathbf{J}_n$  is the  $n^{\text{th}}$  characteristic mode and  $a_n$  is the unknown coefficient in the expansion series. Substituting (2.96) in (2.80) and considering the linearity of the operator, we have

$$\sum_n a_n \mathcal{Z}(\mathbf{J}_n) = -\mathbf{E}_t^{\text{inc}} \quad (2.97)$$

By taking an inner product of the two sides of (2.97) with  $\mathbf{J}_m$  and using the orthogonality relations in (2.88), one can write

$$a_n = -\frac{\langle \mathbf{E}_t^{\text{inc}}, \mathbf{J}_n \rangle}{\langle \mathbf{J}_n, \mathcal{Z}(\mathbf{J}_n) \rangle} = -\frac{\langle \mathbf{E}_t^{\text{inc}}, \mathbf{J}_n \rangle}{1 + j\lambda_n} \quad (2.98)$$

It is seen that the unknown coefficients are strongly dependent on the coupling between the characteristic modes and the incident electric field. By substituting (2.97) in (2.95), the current distribution on the tag is given by

$$\begin{aligned} \mathbf{J} &= -\sum_{n=1} \frac{\langle \mathbf{E}_t^{\text{inc}}, \mathbf{J}_n \rangle}{1 + j\lambda_n} \mathbf{J}_n \\ &= -\sum_{n=1} \frac{V_n}{1 + j\lambda_n} \mathbf{J}_n \end{aligned} \quad (2.99)$$

where

$$V_n = \langle \mathbf{E}_t^{\text{inc}}, \mathbf{J}_n \rangle \quad (2.100)$$

is the coupling coefficient between  $n^{\text{th}}$  characteristic mode and incident electric field. The electric and magnetic fields scattered from the tag can be written by

$$\mathbf{E} = -\sum_{n=1} \frac{V_n}{1 + j\lambda_n} \mathbf{E}_n \quad (2.101)$$

$$\mathbf{H} = -\sum_{n=1} \frac{V_n}{1 + j\lambda_n} \mathbf{H}_n \quad (2.102)$$

The variation of eigenvalues, current distribution, and corresponding fields versus frequency provides some useful information about the scattering properties of the tag structure. The modal expansion of the current in (2.99) is inversely dependent on the eigenvalues as

$$MS_n = \left| \frac{1}{1 + j\lambda_n} \right| \quad (2.103)$$

This parameter is called the modal significance. This parameter depends only upon the geometry and dimensions of the tag, and does not vary with the incident excitation. Another parameter, which is very useful in calculating the quality factor of the scatterer at resonant frequencies, is the characteristic angle defined as

$$\alpha_n = 180^\circ - \tan^{-1}(\lambda_n) \quad (2.104)$$

This parameter models the phase angle between a characteristic current,  $\mathbf{J}_n$ , and the associated characteristic field,  $\mathbf{E}_n$ . It is clear from (2.103) and (2.104) that at the resonant frequencies of the tag, the characteristic angle is equal to zero and the modal significance has a maximum value of one. These parameters are very useful in calculating the quality factor of the tag response at resonant frequencies. In computing the radiating bandwidth of the modes, we need to know the frequencies at which the radiated power is half of that at resonant frequencies. From (2.103), at the frequencies where  $\lambda_n = 1$  or  $\lambda_n = -1$ , the corresponding modal significance is 0.707, and the corresponding characteristic angles are  $135^\circ$  and  $225^\circ$ . Labelling these frequencies  $f_L$  and  $f_H$ , the quality factor of the characteristic mode at resonant frequency can be calculated from the expression

$$Q \approx \frac{f_0}{f_H - f_L} \quad (2.105)$$

This approximation is only valid for high-Q resonators. There have been numerous formulae for calculating the quality factor of a scatterer. In our application where we try to implement resonators with high quality factor, all the proposed formulae give approximately the same results with slight variations. Another simple formula useful in calculating the quality factor of the resonators embedded on chipless RFID tags is given by the expression

$$Q_n = \frac{\omega}{2} \frac{d\lambda_n}{d\omega} \quad (2.106)$$

which was proposed by Harrington [34].

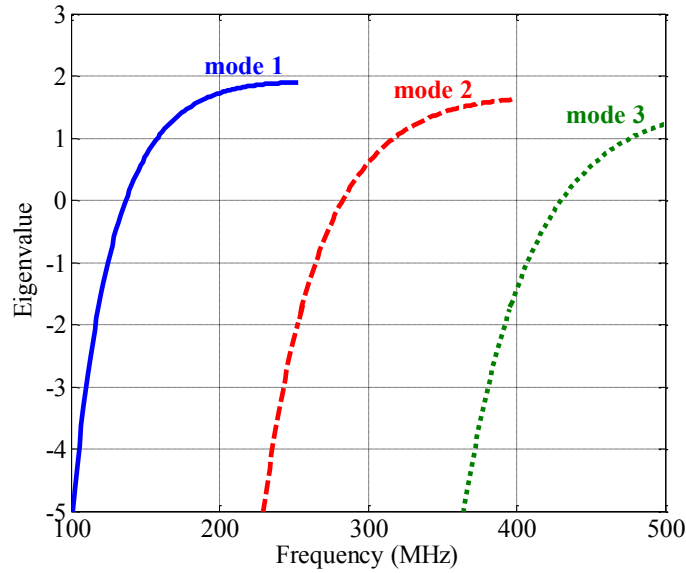
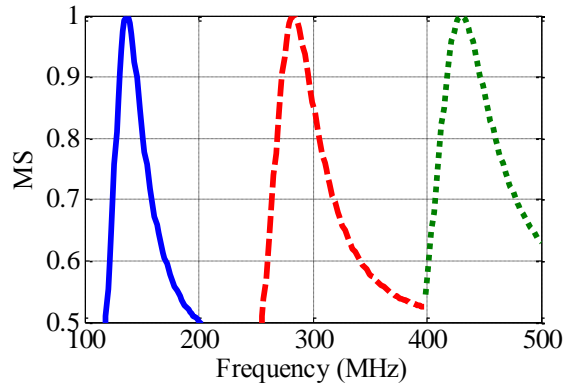


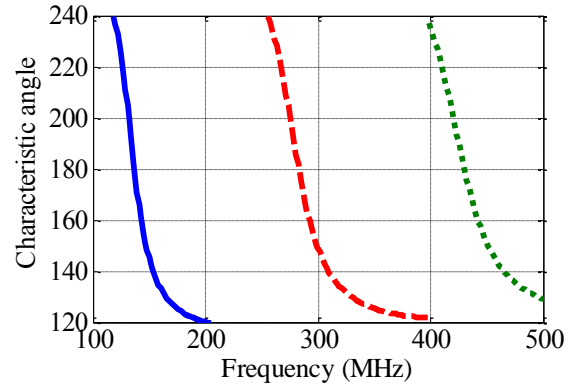
Figure 2.13 Eigenvalues of the characteristic modes versus frequency.

### 2.3.2 Characteristic Mode Analysis of Dipole

Assuming the dipole of length  $L = 1$  m seen in Figure 2.9, the variations of eigenvalues of the dipole are shown in Figures 2.13. The first three resonant frequencies of the dipole are located at  $f_1 = 133$  MHz,  $f_2 = 282$  MHz and  $f_3 = 430$  MHz at which the corresponding eigenvalues are zero. The mode is capacitive at frequencies lower than its corresponding resonant frequency and is inductive at frequencies above it. According to Figure 2.14a, the modal significance is equal to 1 at the resonant frequencies of the dipole. The quality factor of the dipole at the resonant frequencies are equal to  $Q_1 = 4.3$ ,  $Q_2 = 5.34$  and  $Q_3 = 6.2$ . The characteristic angle of the characteristic modes is equal to  $180^\circ$  at the resonant frequencies, as Figure 2.14b shows. The first three characteristic modes of the dipole are shown in Figure 2.15 at resonant frequencies. The characteristic modes are sorted based on their corresponding eigenvalues. The actual current on the dipole is the summation of the characteristic modes weighted by coupling coefficients, which depend on the incident electric field.

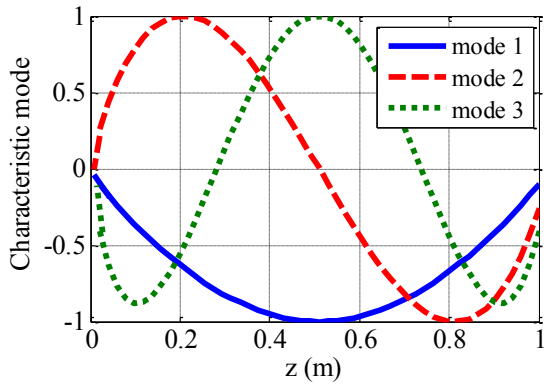


(a)

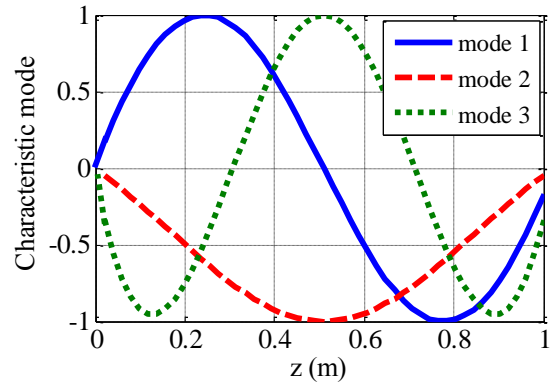


(b)

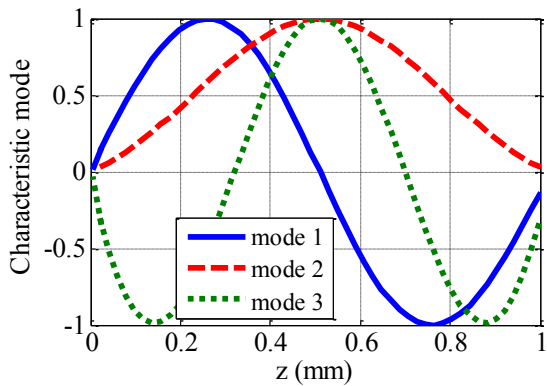
Figure 2.14 (a) Modal significance and (b) characteristic angle of the characteristic modes versus frequency.



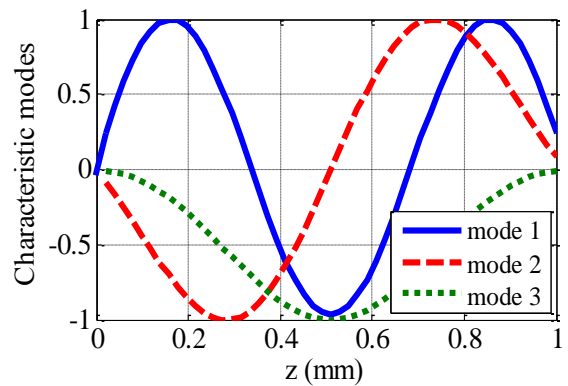
(a)



(b)



(c)



(d)

Figure 2.15 First three characteristic modes of the dipole at (a)  $f = 130$  MHz, (b)  $f = 282$  MHz, (c)  $f = 300$  MHz, and  $f = 430$  MHz

### **3 Design of Chipless RFID Tags [8] (Chapter used with permission of Springer science and business media, 2015)**

One key element of a chipless RFID system is the tag. Since it is chipless, it acts both as the scatterer and encoder. As the scatterer, it needs to reradiate the incident field as much as possible in order to maximize signal-to-noise ratio (SNR) in the reader. As the encoder, it needs to encode a high density of data on the backscattered signal. There are some challenges in attaining all desired characteristics of the tag as the scatterer and encoder altogether. Although many designs have been proposed as chipless RFID tags, they can be categorized into two general groups [35].

In the first group, called time-domain reflectometry-based (TDR) design, the tag includes some discontinuities along a long transmission line. The positions of the discontinuities encode the data by a train of pulses shifted corresponding to the positions of the discontinuities. Surface acoustic wave (SAW) tags are an example of this category. The schematic view of a SAW RFID tag is shown in Figure 3.1. It includes an antenna, piezoelectric surface, and multiple reflectors which encode the data on the signal [36]. The incident electromagnetic pulse received by the antenna is converted to the acoustic wave through the piezoelectric substrate. The SAW is affected by a number of reflectors, which create a number of shifted pulses corresponding to the positions of the reflectors. Although SAW tags are nowadays used in some commercial applications, there are still some issues to be addressed to make them compatible for RFID applications. Reduction in size and loss, and increase in data capacity and reading range are some of these issues. Additionally, due to the costly process of making the SAW and attaching it to the antenna, this type of RFID tag is more expensive than the silicon-based tags [37]. The same idea was employed by utilizing delay line instead of piezoelectric substrate, incorporated by some discontinuities instead of reflectors [38, 39]. In [40], a chipless RFID tag based on group delay engineered dispersive delay structures is proposed. The tag employs transmission-type all-pass dispersive delay structures (DDSs, shown in Figure 3.2) to assign the pulse position modulation (PPM) code onto the interrogating signal. The proposed chipless RFID system based on DDSs is shown in Figure 3.3. The interrogating signal includes three pulses modulated with three different frequencies. Depending on the frequency of the incident pulse, the structure introduces the required phase shift corresponding to bits 0 or 1. As an example, the pulses can be positioned in the first half or the second half of a bit interval to encode a bit 0 or a bit 1, respectively.

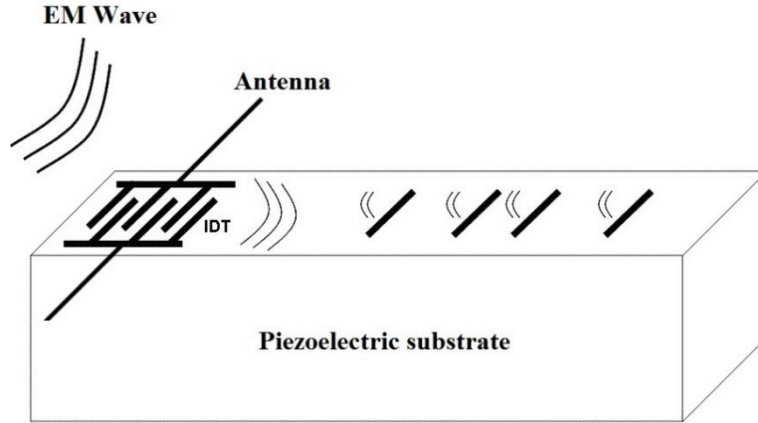


Figure 3.1 Schematic view of a surface acoustic wave tag.

In practical applications, TDR-based tags are loaded with an antenna, which increases the size. In addition, the long transmission line included in these structure introduces some loss in the transmission path of the signal.

In the second group of chipless RFID tags, which is called spectral-based tags, the ID of the tag is incorporated into the spectral response of the scattered signal. In these designs, the frequency band of operation is divided into  $N$  sections, corresponding to  $N$  bits. According to Figure 3.4, the presence and absence of resonance at each section of the frequency band is associated with bits 1 and 0, respectively. By increasing the number of bits on the tag, the couplings between the resonances are increased [41]. Hence, by removing a specific resonance, the couplings between the other resonators are changed and as a result, the resonant frequencies of the other resonances are altered. Therefore, we need to increase the quality factor of the resonator in order to decrease the coupling between them [42].

The first spectral-based design is shown in Figure 3.5a. It is an 11-bit tag including 11 dipoles, each corresponding to one bit [43]. In order to decrease the coupling between the dipoles, they are placed far from each other, which increases the size of the tag. Another drawback of the tag is the low quality factor of the dipoles, which is not suitable for high density of data. In 2006, a chipless RFID tag based on the fractal Hilbert curve was proposed [44]. The configuration of the proposed tag is depicted in Figure 3.5b. From an electromagnetic point of view, such a curve provides a structure that can resonate at a wavelength much longer than its physical size. For high densities of data where we need to pack the resonances into a limited frequency band, this structure involves some difficulties in the fabrication process.

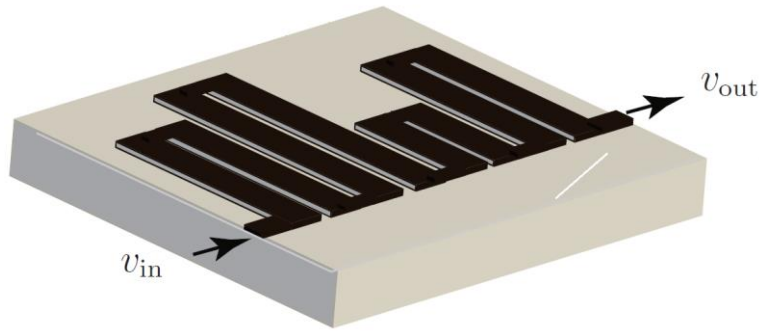


Figure 3.2 Dispersive delay structures [40] (With permission, Copyright© 2011 IEEE).

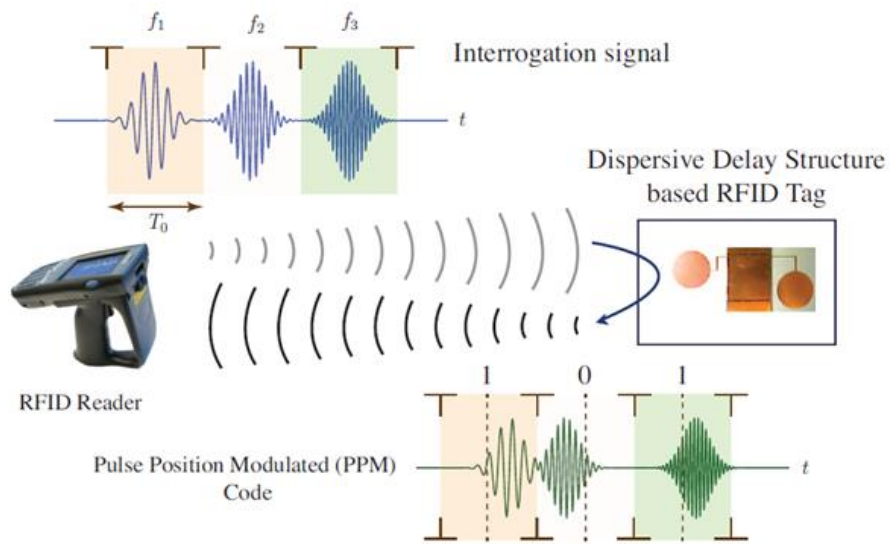


Figure 3.3 Chipless RFID system based on DDSs [40] (With permission, Copyright© 2011 IEEE).

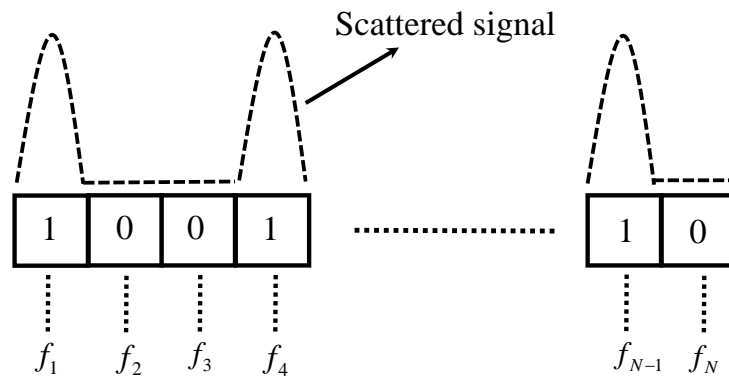


Figure 3.4 Assigned resonant frequencies for a chipless RFID tag.

In 2007, a simple structure based on the slot resonator was proposed [45]. By inserting quarter-wavelength slot resonators on a metallic plane as seen in Figure 3.5c, the ID of the tag is adjusted by the resonant frequencies of the slots. Later on, this structure was used as a basis for designing compact multi-bit chipless RFID tags. Figure 3.5d shows another chipless RFID tag in which a receiving antenna is attached to a resonant circuitry that encodes data on the signal and then transmits the encoded signal through a transmitting antenna [46]. The antennas are placed in different polarizations for transmitting and receiving purposes. Compared to the spectral-based chipless RFID tags in which the structure acts both as the scatterer and encoder, the tag shown in Figure 3.5d has larger size with higher loss. Hence, this design is not suitable for compact chipless RFID tags. Figure 3.5e shows a chipless RFID tag designed based on high impedance surfaces. In this tag, by employing a multi-resonant HIS unit cell, several bits can be stored in the structure [47]. The states “total reflection” and “total absorption” encode bits 0 and 1, respectively. The ground plane of the microstrip participates in the resonant mechanism of the structure, which makes the tag bulky in some applications. The 24-bit tag represented in Figure 3.5f contains 24 quarter-wavelength slots, each resonating at the specified frequency [42].

Besides all aforementioned designs proposed as chipless RFID tags, there is a need for a systematic design, which includes all effective structural parameters in the design process. As the encoder, we need to consider the quality factor and resonant frequency tunability of the embedded resonators. As the scatterer, the residue of the poles and radar cross section of the tag and their dependency on polarization and direction should be considered in the design process. In this chapter, two design approaches based on singularity expansion method (SEM) and characteristic mode theory (CMT) are presented. First, complex natural resonance-based design of chipless RFID tags is introduced. By monitoring the effects of structural dimensions on the damping factor and resonant frequency of the resonators, the process of encoding the data onto the tag is presented. In the following, another design process of the tag based on the theory of characteristic modes is introduced, which provides the resonant frequency, quality factor, and additionally the intensity of the characteristic fields in the far-zone region [48]. Although the design procedure is general and can be used for any arbitrary resonant-based structure, the quarter-wavelength slot resonators is used as the resonant circuitry in the presented design procedure. This structure exhibits some desired features compared to other proposed resonant structures [42, 49]. Its low profile, ease of fabrication, and lightness are the important features of the proposed tag.

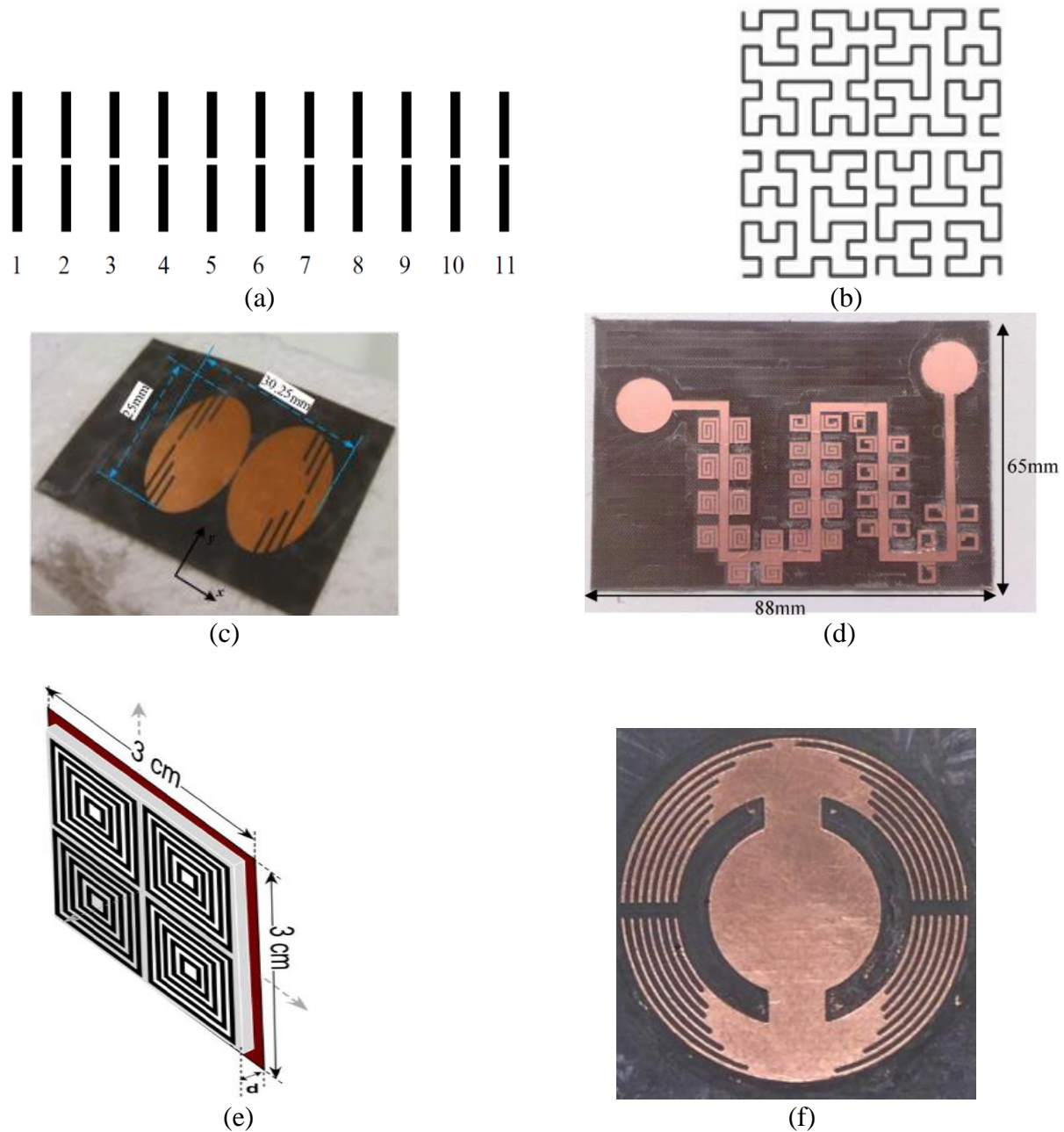


Figure 3.5 Spectral-based chipless RFID tags using (a) dipole resonators [43] (Copyright© 2005 IEEE) (b) fractal Hilbert curve [44] (Copyright© 2006 IEEE) (c) slot resonators [45]. (Copyright© 2007 IEEE) (d) Resonant circuitry attached to the transmitting/receiving antennas as a chipless RFID tag [46] (Copyright© 2009 IEEE) (e) chipless RFID tag based on high-impedance surface [47] (Copyright© 2013 IEEE) (f) 24-bit tag using quarter-wavelength slot resonators [42] (With permission, Copyright© 2014 IEEE).

### 3.1 Complex Natural Resonance-Based Design of Chipless RFID Tags

As mentioned in Chapter 2, the impulse response of the tag can be written as the summation over the CNRs combined with an entire-domain function including the early-time response of the tag as

$$H(s) = \sum_{n=-\infty}^{+\infty} \frac{R_n}{s - s_n} + H_e(s) \quad (3.1)$$

As mentioned before, the residues ( $R_n$ ) and entire-domain function ( $H_e(\cdot)$ ) depend strongly on the polarization and direction of the transmitting and receiving antennas, while the CNRs of the tag ( $s_n$ ) are aspect-independent. Although the series includes an infinite number of poles, we consider just  $N$  fundamental high-Q CNRs of the tag, which are excited strongly by the incident electric field. A single-bit scheme of the tag is shown in Figure 3.6 with its structural dimensions.

In order to perceive an intuitive description of the scattering modes, the tag shown in Figure 3.6 is illuminated by a  $y$ -polarized electric field propagating in the  $x$ -direction. The current distribution on the tag is illustrated in Figure 3.7 at different time instances. At  $t=0.02\text{ns}$ , the impinging wave hits the leading edge of the tag. The current on the tag at  $t=0.04\text{ns}$  is shown in Figure 3.7b. At this time, the incident wave illuminates part of the tag and as the figure shows the induced current is strongly dependent on the source field. At  $t = 0.06 \text{ ns}$ , the incident field crosses through the tag and afterward the current distribution can be written by the summation over the natural modes of the tag. Although each scatterer has infinite CNRs, the dominant resonances

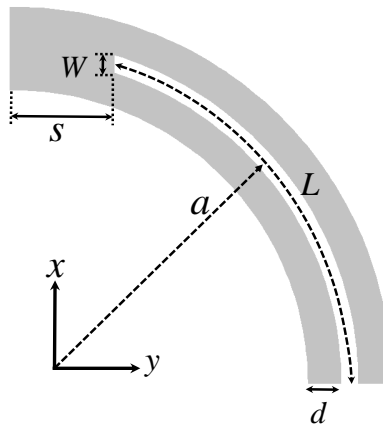


Figure 3.6 Single-bit tag with structural dimensions.

excited by the incident field are related to the fundamental resonant frequency of the slot and metal parts. According to the current distribution at  $t = 0.4$  ns and  $t = 0.6$  ns, it is explicitly seen that the current distribution on the tag is the summation of the natural currents related to the fundamental resonance of the slot and metal. At  $t = 0.4$ ns, the current is dominated by the natural modes related to the slot and metal resonant frequencies. At  $t = 0.6$ ns and thereafter, the slot's fundamental natural mode is more dominant, because it has a low damping factor compared to other CNRs of the tag.

Assuming  $W = 0.3$  mm,  $S = 3$  mm,  $d = 0.8$  mm, and  $L = 12.6$  mm, the time-domain and frequency-domain backscattered field from the tag are depicted in Figure 3.8. The incident electric field is polarized in the  $y$ -direction and propagates in the  $z$ -direction. As the frequency-domain response of the backscattered field shows, two excited resonant frequencies of the structure are located at  $f = 5.54$  GHz and  $f = 8.35$  GHz. The pole diagram of the tag is shown in Figure 3.9. It depicts the resonant frequencies of the tag versus their corresponding damping factors. The residues of the poles are depicted beside them. The high-Q resonance at  $f = 5.54$ GHz is related to the fundamental frequency of the slot resonator, and the low-Q resonant frequency at  $f = 8.35$ GHz is associated with the metallic part of the tag. Although the CNR of the slot has a lower damping factor than the CNR of the metal, its residue is five times weaker. Since the fundamental resonant frequency of the slot is used in encoding the data onto the tag, the resonant frequency of the metal should be considered in the design procedure and distinguished in the applied detection technique. In Figure 3.10, the current distribution on the tag is shown for two resonant frequencies. As it shows, at the resonant frequency of the slot, the current on the arms of the slot are in opposite directions while at  $f = 8.35$ GHz, which corresponds to the half-wavelength resonance of the metal, the current on the arms is mostly in the same direction. Based on these current distributions, it can be inferred that the resonant frequency of the slot is mostly sensitive to the slot length  $L$  and that the resonant frequency of the metal can be changed by  $L+S$ . In practical applications, the fundamental CNR of the slot rather than the metal is used for encoding the data onto the tag because of its higher quality factor. In Figure 3.11, the resonant frequency of the slot is plotted versus slot length for two different values of  $d$ . As can be seen, increasing the slot length shifts down its resonant frequency. In addition, for larger values of  $d$ , as a result of slightly increasing the electrical length of the slot, its resonant frequency decreases. Therefore, the resonant frequency can be easily adjusted by the slot length ( $L$ ). Another important parameter to be considered in the

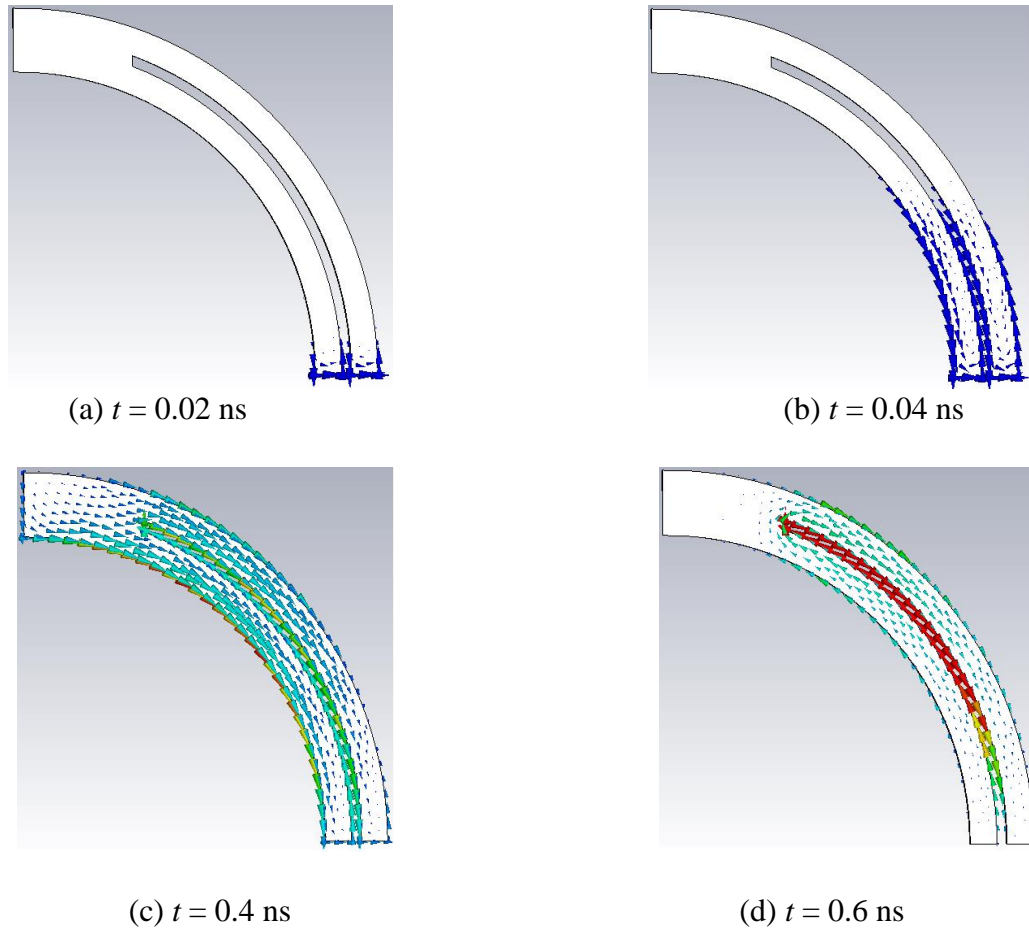


Figure 3.7 Current distribution on the tag for different time instances [33] (With permission, Copyright© 2015 IEEE).

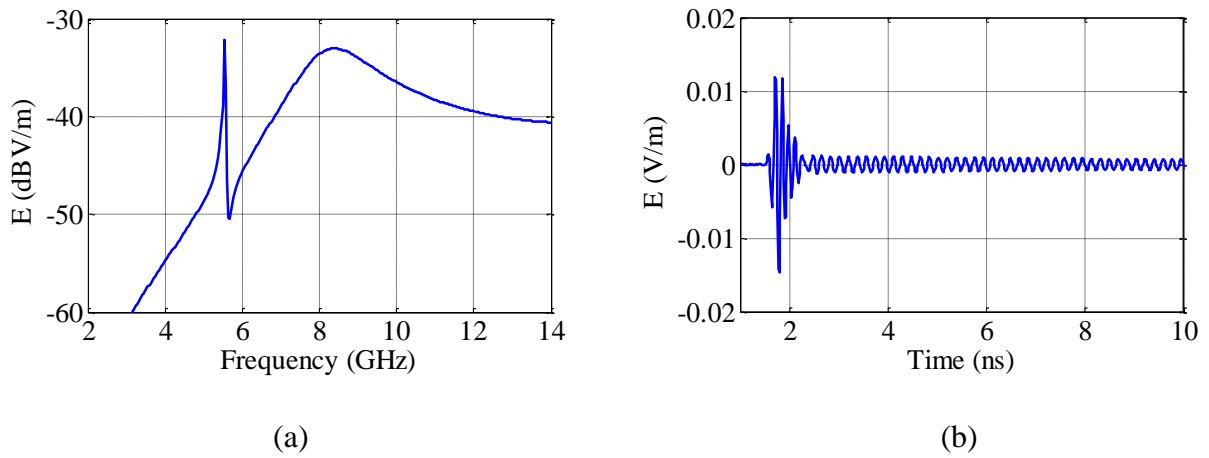


Figure 3.8 (a) Frequency-domain and (b) time-domain backscattered field from the single-bit tag [33] (With permission, Copyright© 2015 IEEE).

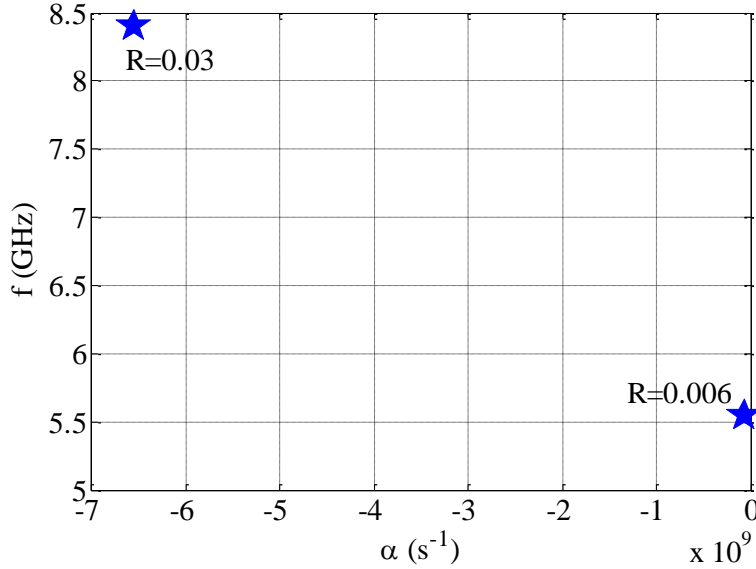


Figure 3.9 Pole diagram of the single-bit tag [33] (With permission, Copyright© 2015 IEEE).

design procedure is the damping factor of the resonances. In order to incorporate more resonant frequencies into a relatively narrow frequency band, it is necessary to design the poles with low damping factors or equivalently high quality factors. In Figure 3.12, the damping factor of the slot's fundamental CNR is plotted versus the width of slot ( $W$ ). As it shows, by increasing the slot width and consequently increasing the parasitic fields at the open-ended edge of the slot, its damping factor slightly increases. Due to the limitation in prototyping of slots with widths below 0.2mm, this parameter cannot be used effectively to lower the damping factor of the slot resonator. Assuming slot width of  $W = 0.2\text{mm}$ , the damping factor of the slot is depicted in Figure 3.13 in terms of  $d$ . As it shows, by decreasing  $d$ , the damping factor is significantly decreased. According to the current distribution on the tag as seen in Figure 3.10a, by decreasing  $d$ , the currents on the edges of the resonator are placed closer to each other and as a result, backscattered radiation decreases drastically. By reducing the radiated power, according to the definition of the quality factor

$$Q = \omega \frac{E_{\text{stored}}}{P_{\text{radiation}}} \quad (3.2)$$

the quality factor of the resonator increases which leads to a lower damping factor at that resonant frequency. The quantities  $\omega$ ,  $E_{\text{stored}}$ , and  $P_{\text{radiation}}$  are the radian frequency, stored energy around the tag, and radiation power from the tag, respectively. By decreasing the radiation fields the radar

cross-section (RCS) of the tag is decreased, which makes the identification process of the tag more challenging especially in the presence of noise and clutter.

Assuming a single-bit tag as seen in Figure 3.6, the late-time response corresponding to fundamental resonance can be written by

$$s(t) = \text{Re}^{-\alpha_0 t} \cos(\omega_0 t + \phi_0) \quad (3.3)$$

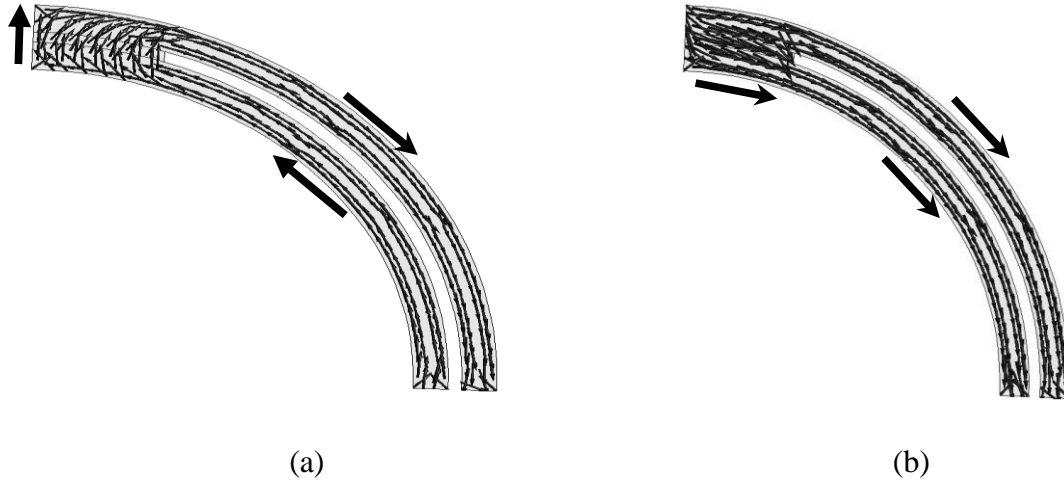


Figure 3.10 Current distribution on the tag at (a)  $f = 5.54\text{GHz}$  and (b)  $8.8\text{ GHz}$  [42] (With permission, Copyright© 2014 IEEE).

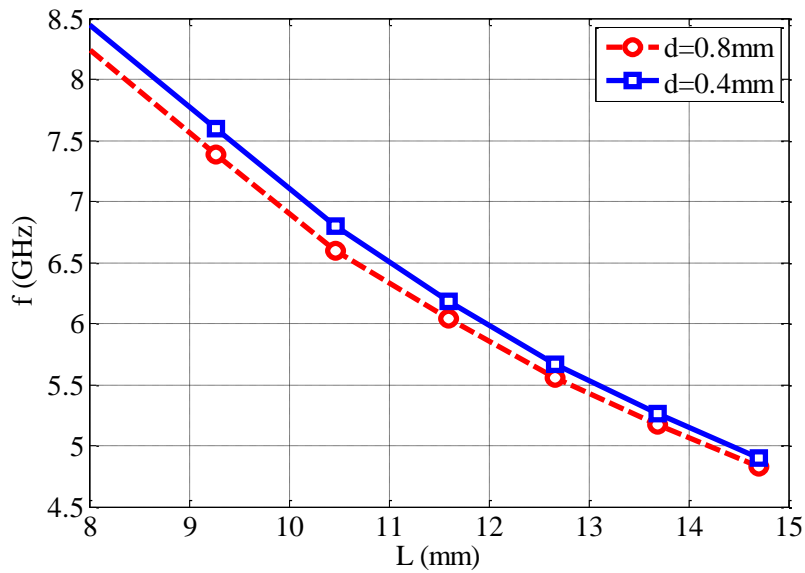


Figure 3.11 Resonant frequency of the slot versus  $L$ .  $W = 0.3\text{mm}$  [42] (With permission, Copyright© 2014 IEEE).

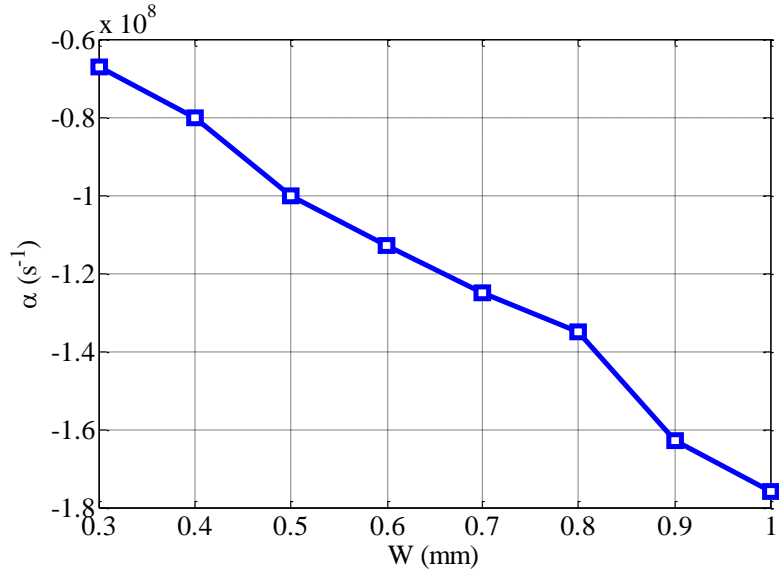


Figure 3.12 Damping factor of the CNR of the slot versus  $d$  for different values of  $a$ .  $W = 0.3$  mm [42] (With permission, Copyright© 2014 IEEE).

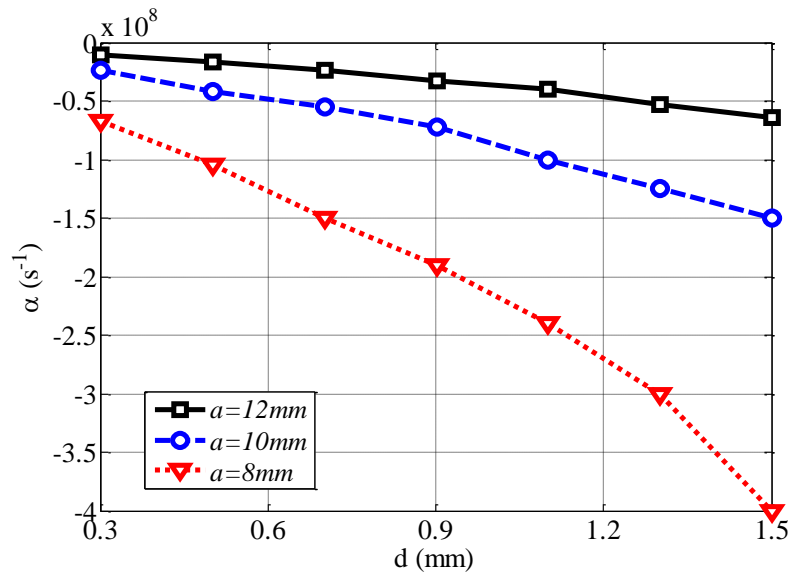


Figure 3.13 Damping factor of the CNR of the slot versus  $d$  for different values of  $a$ .  $W = 0.3$ mm [42] (With permission, Copyright© 2014 IEEE).

where  $R$  and  $\varphi_0$  are the amplitude and phase of the signal resonating at the radian resonant frequency of  $\omega_0$  and attenuating with damping factor  $\alpha_0$ . The energy of the signal is defined by

$$\begin{aligned}
E_s &= \int_{t=0}^{+\infty} s^2(t) dt \\
&= \frac{R^2}{4\alpha_0} + \frac{R^2\alpha_0}{4(\alpha_0^2 + \omega_0^2)} e^{\frac{-2\alpha_0 t_0}{\omega_0}}
\end{aligned} \tag{3.4}$$

For the CNRs with low damping factor as  $\omega_0 \gg \alpha$ , assuming  $\varphi_0=0$ , the energy of the signal in (3.4) is summarized as

$$E_s = \frac{R^2}{4\alpha_0} \tag{3.5}$$

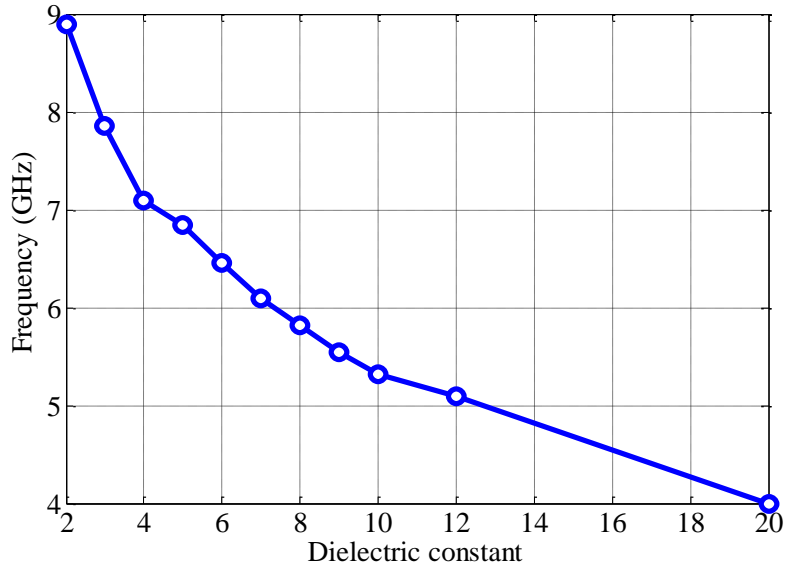
It is seen that the energy of the single-pole signal is proportional to the square of its amplitude and inverse of its damping factor, when its damping factor is much smaller than radial frequency. For this reason, it is crucial in the identification process of the scattered signal from chipless RFID tag to use resonances with a low damping factor.

In practical application, the tag structure is usually designed on a thin dielectric substrate. Because of the existence of the lossy dielectric, both the resonant frequency and damping factor of the CNRs change. In Figure 3.14, the variation of the CNRs versus dielectric constant of the substrate is shown. The thickness of the substrate is assumed 0.7874 mm and the dimensions of the structure are  $a = 10\text{mm}$ ,  $d = 0.8\text{mm}$ ,  $W = 0.3\text{mm}$ . As it shows by increasing the dielectric constant of the lossless substrate, the resonant frequency and the damping factor of the CNR decrease. Based on the scaling relationship, when a tag is located in a lossy dielectric with dielectric constant  $\varepsilon$  and conductivity  $\delta$  [50],

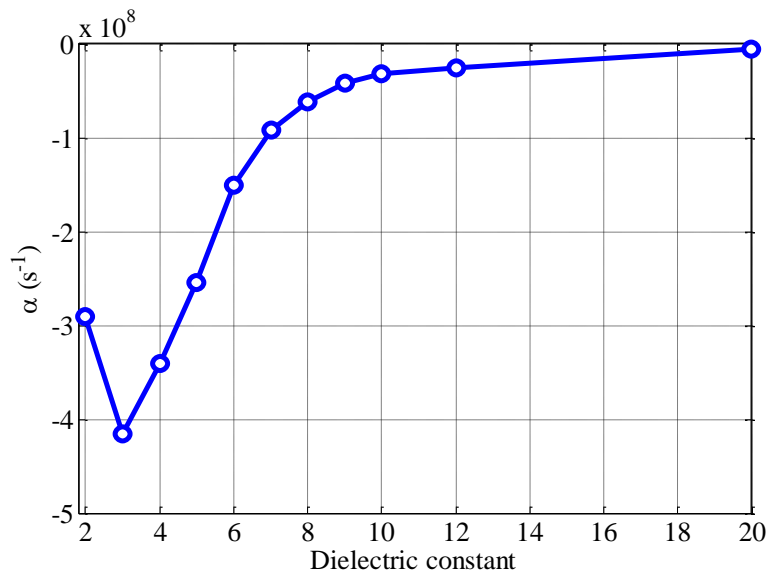
$$s_n = -\frac{\delta}{2\varepsilon} + \sqrt{\left(\frac{\delta}{2\varepsilon}\right)^2 + \left(\frac{s_n^{\text{fs}}}{\varepsilon}\right)^2} \tag{3.6}$$

where  $s_n^{\text{fs}}$  and  $s_n$  are the  $n^{\text{th}}$ -CNR of the tag in free space and in the lossy dielectric. In the case where the tag is located on the dielectric substrate from one side, neglecting the loss of the dielectric, we have

$$s_n = \frac{s_n^{\text{fs}}}{\sqrt{\varepsilon_{\text{eff}}}} \tag{3.7}$$



(a)



(b)

Figure 3.14 (a) Resonant frequency and (b) damping factor of the CNR of the tag versus dielectric constant.  $A = 10\text{mm}$ ,  $d = 0.8\text{mm}$ ,  $t = 0.3\text{mm}$ .

According to (3.7), the damping factor and resonant frequency of the tag attached to the dielectric substrate decrease by increasing the dielectric constant of the substrate (according to Figures 3.13 and 3.14). As the Figure 3.14 shows, when the dielectric constant of the substrate is between 2 and 3, the damping factor of the CNR increases. In this region, the resonant frequency of the slot is

close to the resonant frequency of the metal. Therefore, the coupling effect between these two resonant mechanisms increases the damping factor of the slot's CNR.

Another important parameter in chipless RFID tags is the sensitivity of the CNRs to background objects in the environment. For this purpose, a single-bit chipless RFID tag is assumed above a metallic plate as the Figure 3.15 shows. The percentage variations of the resonant frequency and damping factor in terms of the distance between tag and plate are illustrated in Figure 3.16. According to the figures, as a result of coupling, the damping factor of the pole is much more sensitive to the environmental objects than the resonant frequency. This is the reason why the damping factor of the poles is not usually used in the identification process. The single-bit tag seen in Figure 3.6 can be used in the design of multi-bit chipless RFID tags. The coupling between resonances plays a critical role in the design of chipless RFID tags. The presence and absence of a resonance at a specific resonant frequency represents bit 1 or 0, respectively. Therefore, the structure should be designed in such a way that by nulling one resonant frequency, the resonant frequencies of the other resonators do not change.

A 24-bit tag shown in Figure 3.17 is designed based on the quarter-wavelength slot resonators on a Rogers RT/Duroid®/5870 ( $\epsilon_r = 2.2$ ) with a thickness of 0.78mm. The lengths of the slots are tuned in order to adjust the resonant frequencies of the slots according to the ID of the tag. By filling the slot surface with metal or inserting some stubs along the slot, the corresponding bit is

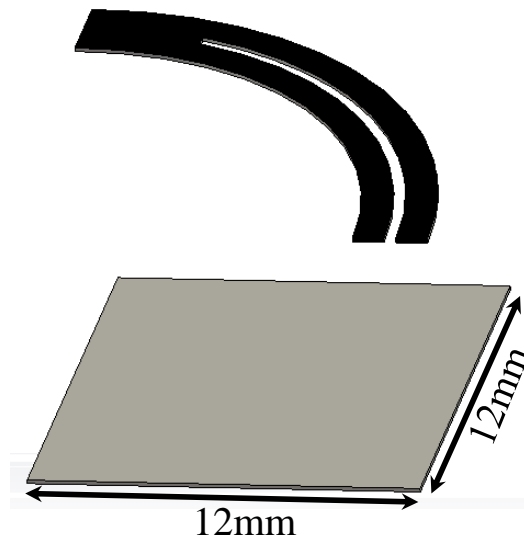


Figure 3.15 Single-bit tag above a metallic plate.

nulled. Therefore,  $2^{24}$  tags with unique IDs can be encoded with 24 slots. As an example, in the second tag, the second and fifth bits of the tag are nulled by inserting some stubs along the slot. The radar cross-sections of the tags are depicted in Figure 3.18. It is seen that the second and fifth bits of the tag are nulled without any considerable change in the positions of the other resonances.

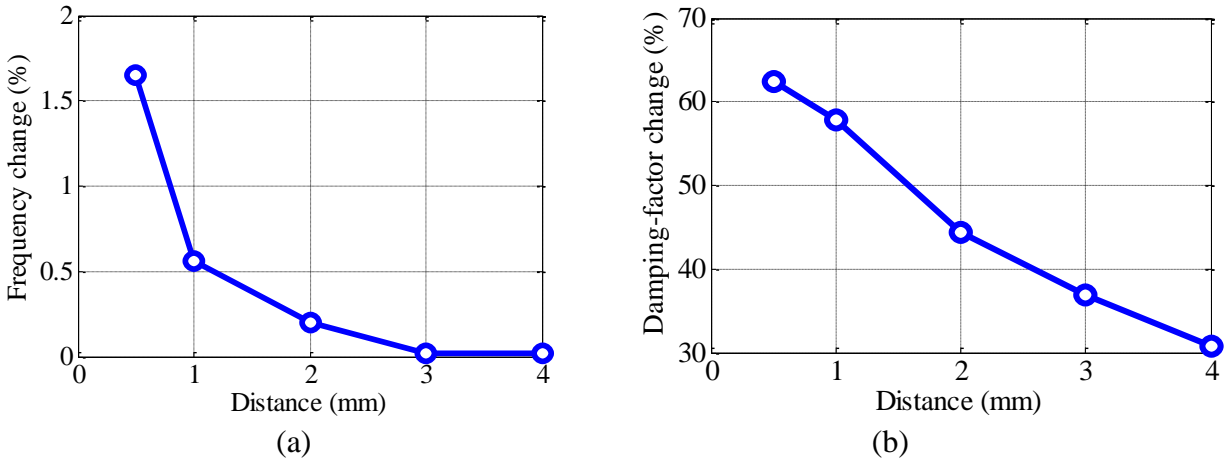


Figure 3.16 Percentage variations in the (a) resonant frequency and (b) damping factor of the CNR of the tag versus distant to the metallic plate.  $A = 10\text{mm}$ ,  $d = 0.8\text{mm}$ ,  $t = 0.3\text{mm}$ .

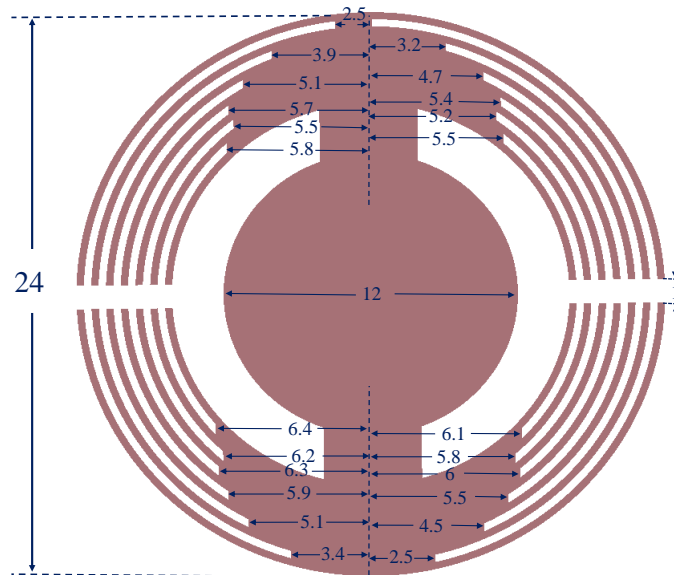


Figure 3.17 Schematic view of the 24-bit tag [42] (With permission, Copyright© 2014 IEEE).

## 3.2 Design of Chipless RFID Tag Based on Characteristic Mode Theory

In the previous section, the effects of various structural dimensions of the tag on the CNRs were studied. The scattered field radiated from the natural current mode depends strongly on its distribution on the tag surface. We need to calculate the CNRs and corresponding natural modes on the tag by employing some numerical techniques such as method of moment (MoM). Another approach for monitoring the effects of structural parameters on the scattered response is characteristic mode theory (CMT). As mentioned in Chapter 2, by decomposing the current distribution on the tag into its characteristic modes, the resonant and radiation characteristics of the tag can be studied easily at each frequency. In some commercial software such as FEKO, the characteristic modes of the structure and the variations of the eigenvalues, modal significances, and radiated power can be easily monitored versus frequency. This insight is useful in the design of chipless RFID tags.

A single-bit tag with the dimensions shown in Figure 3.19 is considered. Two parameters  $d_1$  and  $d_2$  are shown in Figure 3.19, which are initialized at the y-axis in order to study the effects of the metal and slot resonances more accurately. The eigenvalues of the first two characteristic modes of the tag are illustrated in Figure 3.20 versus frequency for  $d = .8$  mm,  $W = 0.3$  mm,  $d_1 = 3.5$  mm,  $d_2 = 0$ ,  $a = 10$  mm, and  $L = 12.1$  mm.

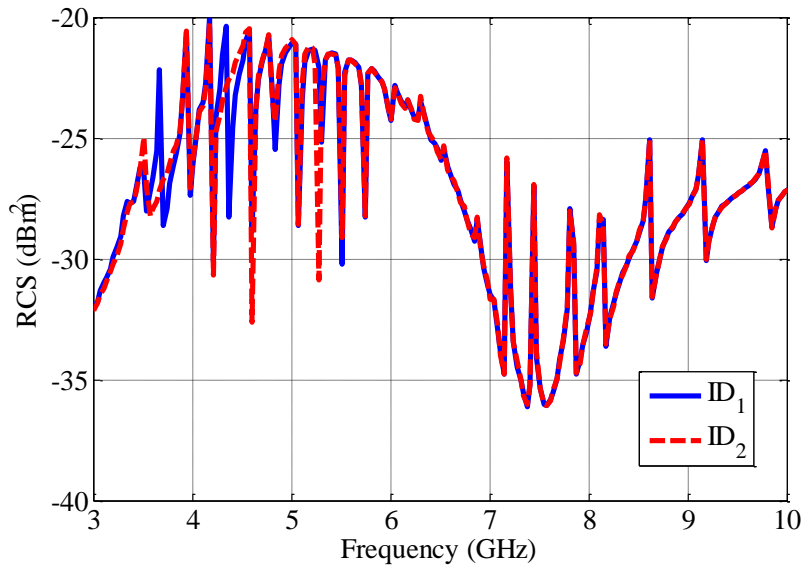


Figure 3.18 Radar cross-sections of the 24-bit tags [42] (With permission, Copyright© 2014 IEEE).

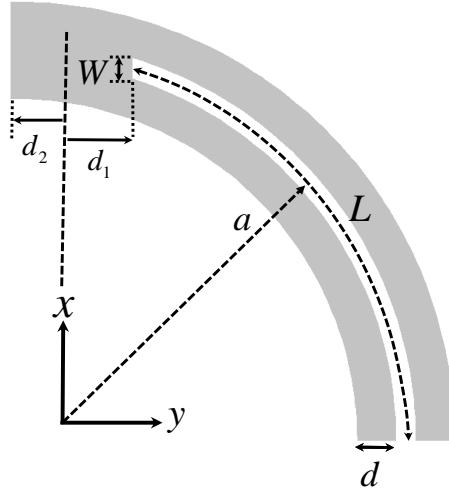


Figure 3.19 Single-bit tag illuminated by incident plane wave.

The resonant frequencies of the tag are the frequencies at which the eigenvalues are equal to zero. In this case, the resonant frequencies of the tag in the 3-10GHz band are located at  $f_1 = 5.7\text{GHz}$  and  $f_2 = 8.6\text{GHz}$ . Figure 3.21 illustrates the modal significances of the characteristic modes, which are calculated from

$$MS_n = \left| \frac{1}{1 + j\lambda_n} \right| \quad (3.8)$$

According to Figure 3.21, the first resonance of the tag has a much higher quality factor than the second. For high-Q resonances which are usually used in the design of chipless RFID tags, the quality factor of the CNRs can be calculated from the modal significance (MS) of the modes. Assuming  $f_L$  and  $f_H$  as the frequencies at which the MS is 0.707, the quality factor can be calculated from

$$Q \approx \frac{f_0}{f_H - f_L} \quad (3.9)$$

where  $f_0$  is the resonant frequency of the tag. The quality factor of the resonances can also be calculated from the characteristic angles of the modes. The characteristic angle of a characteristic mode is obtained from

$$\alpha_n = 180^\circ - \tan^{-1}(\lambda_n) \quad (3.10)$$

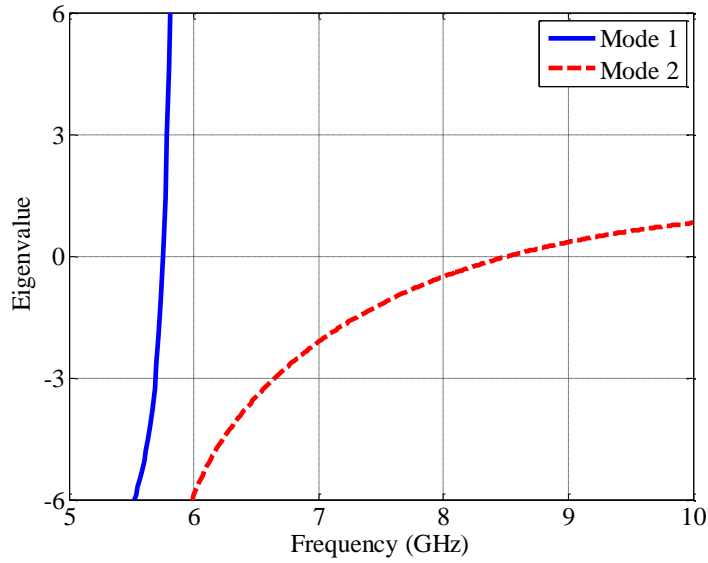


Figure 3.20 Eigenvalues of the characteristic modes versus frequency.

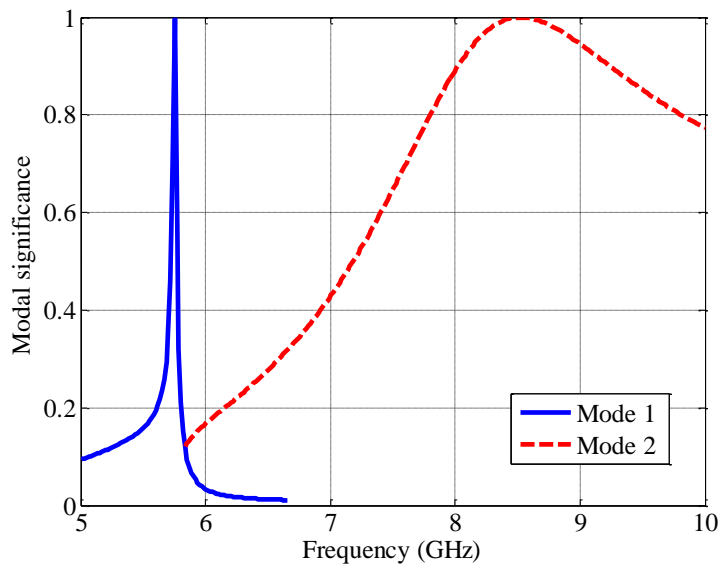


Figure 3.21 Modal significances of the characteristic modes versus frequency.

As can be seen from (3.10), the characteristic angle is  $180^\circ$  at the resonant frequency and is  $135^\circ$  and  $225^\circ$  at  $f_L$  and  $f_H$ , respectively. The characteristic angles of the modes are shown in Figure 3.22 versus frequency. The first resonant frequency at  $f_1 = 5.7$  GHz is corresponding to the quarter-wavelength resonant of the slot and the resonant frequency at  $f_2 = 8.6$  GHz is related to the half-wavelength resonance of the metal.

The first two characteristic modes of the tag at two resonant frequencies are depicted in Figure 3.23. As the figures show, the currents on the arms of the slots oppose each other at  $f = 5.7$  GHz which is associated to the slot's resonance. The first characteristic mode of the tag at  $f = 8.6$  GHz agrees with the current distribution at the half-wavelength resonance of the tag, while it is not the same for the second characteristic mode. The actual current on the tag is the superposition of the characteristic modes weighted with coefficients proportional to the coupling coefficients and modal significances.

Taking advantage of the characteristic mode theory (CMT) in the design procedure, the variations of the resonant frequency and quality factor of the CNRs and field intensity can be monitored easily. According to the current modes, it is seen that the resonant frequency of the slot is dependent strongly upon the slot length and the resonance of the metal is proportional to the metal length. Knowing this, two parameters  $d_1$  and  $d_2$  shown in Figure 3.19 are used to change the lengths of the slot and metal on the tag structure. In Figure 3.24, the variations of the first and second resonant frequencies of the tag are shown versus  $d_1$ . It is seen that by increasing  $d_1$  and consequently decreasing the slot length, its resonant frequency increases without considerable change in the resonant frequency of the metal. Figure 3.25 shows the variations of the resonant frequencies of the slot and metal versus  $d_2$ . By altering  $d_2$ , the resonant frequency of the metal changes without considerable variations in the resonant frequency of the slot. It is very useful in

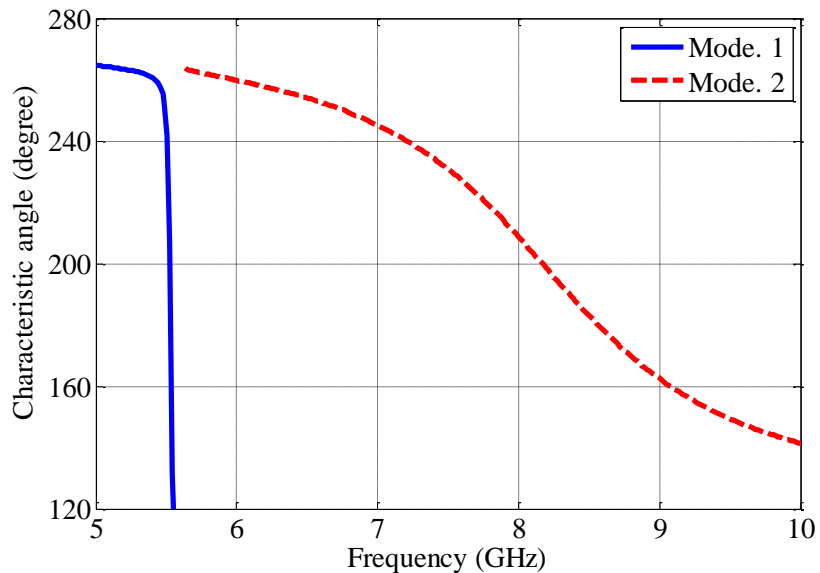


Figure 3.22 Characteristic angle of the characteristic modes versus frequency.

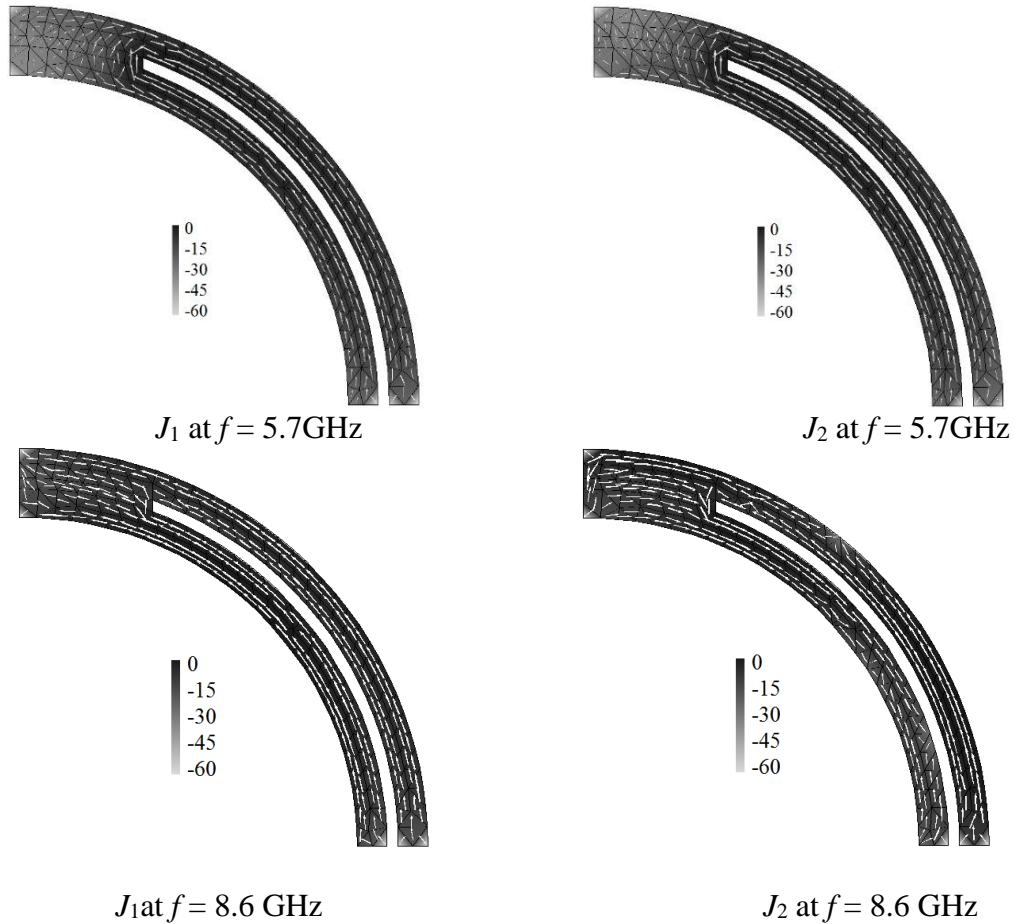


Figure 3.23 Characteristic modes of the tag at two resonant frequencies [33] (With permission, Copyright© 2015 IEEE).

the design of the tag to be able to tune the resonant frequencies of the structure separately. Since the resonance of the slot is usually utilized for encoding the ID onto the tag, it is necessary to place the resonance of the metal outside the frequency band of operation or to distinguish it from the slot resonances in the detection process. When the resonant frequency of the slot is located close to the resonant frequency of the metal, by increasing the coupling between these two resonant frequencies the quality factor of the slot resonator decreases. In Figure 3.26, the backscattered response from the single-bit tag with dimensions  $d_1 = 6$  mm,  $a = 12$  mm,  $d = 0.8$  mm,  $W = 0.3$  mm is shown for three different values of  $d_2$ . By keeping the value of  $d_1 = 6$ mm and changing  $d_2$ , the resonant frequency of the slot changes, but not the metal's resonant frequency. The quality factor of the CNRs of the tag is shown in Table 1 for three cases. It is seen that in the second case where the resonant frequencies are located in close proximity to each other, the quality factor of the slot's CNR decreases more than 10 times. The quantity  $R$  in the table is the residue of the corresponding

CNR of the tag in the late time. In the second case, the slot's CNR has higher residue, which is very important in the detection process. Based on (3.3), the energy of the CNR is directly proportional to the square of the residue and inversely to the damping factor of the CNR. In Chapter 5, the effects of residue and damping factor on detection of a signal in the presence of noise will be shown. In some applications such as chipless RFID sensors where few bits are used in the sensing process in the lossy media, the strength of the late-time response is critical in the detection of a signal. In tags with high density of data, a low damping factor is desirable, decreasing the coupling between resonators. As mentioned before, the quality factor of the resonances of the tag can be controlled by  $d$ . The variation of the quality factor of the slot is shown in Figure 3.27 versus  $d$ . By increasing the arm width  $d$ , the quality factor of the slot's resonance decreases, which agrees with the discussion in section 3.2. By decreasing  $d$  and increasing the quality factor of the CNR, more energy is localized in the reactive near-field of the tag, which leads to a decrease in the radiation from the tag. Therefore, the RCS of the tag decreases. As an example, the far-field radiation pattern of the tag is seen in Figure 3.28 for  $d = 0.8$  mm and  $d = 0.4$  mm. The maximum radiation intensity of the far-zone electric field is 330uV/m for  $d = 0.8$  mm, compared to 84uV/m for  $d = 0.4$ mm. By following the aforementioned design procedure and monitoring the effects of

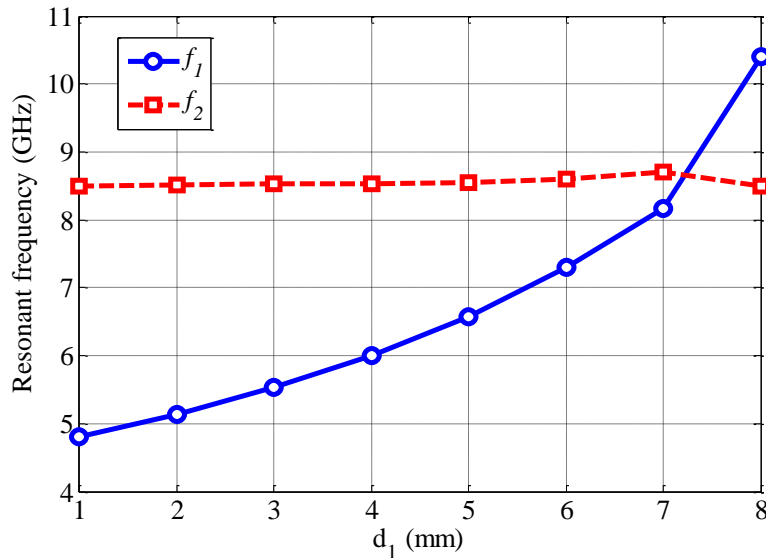


Figure 3.24 Variation of the resonant frequencies of the tag versus  $d_1$  [33] (With permission, Copyright© 2015 IEEE).

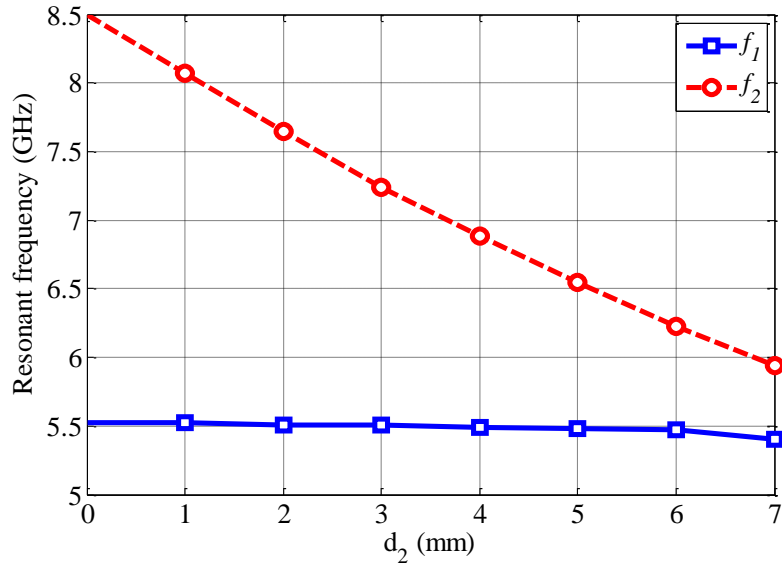


Figure 3.25 Variation of the resonant frequencies of the tag versus  $d_2$  [33] (With permission, Copyright© 2015 IEEE).

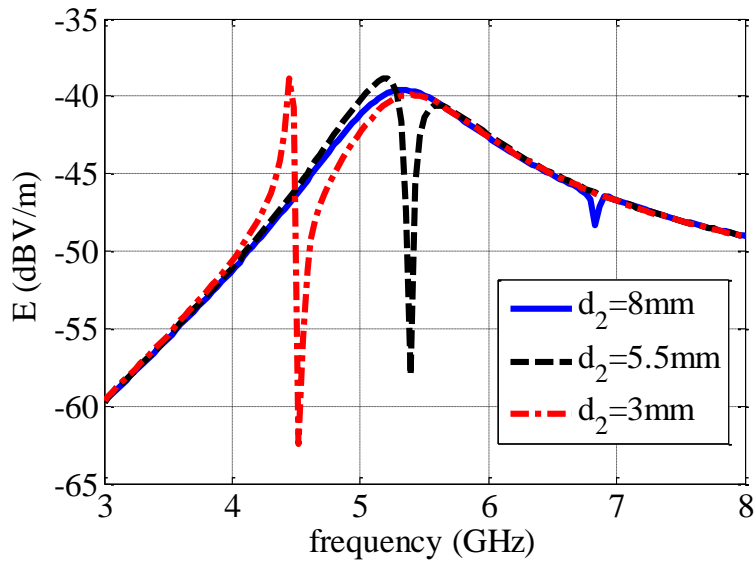


Figure 3.26 Scattered far-field electric field radiated from the tag.  $d_1 = 6$  mm,  $a = 12$  mm,  $d = 0.8$  mm,  $W = 0.3$  mm [33] (With permission, Copyright© 2015 IEEE).

Table 3-1. The resonant frequency, quality factor, and residue of the CNR of the slot for different cases [33] (With permission, Copyright© 2015 IEEE).

$d_2(\text{mm})$	$Q_{\text{slot}}$	$Q_{\text{metal}}$	$(R)$	$f_{\text{slot}}(\text{GHz})$	$f_{\text{metal}}(\text{GHz})$
8	115	4.12	1.2	6.8	5.4
5.5	11.3	6	5	5.2	5.7
3	446	4.12	0.2	4.4	5.4

structural dimensions on the resonant frequency, quality factor, and intensity of the backscattered field from the tag, two 4-bit tags are designed. The schematic view of the tag is shown in Figure 3.29. The slot resonators embedded on the metallic plane are used for encoding the data. Two different cases of  $d_2 = 3 \text{ mm}$  and  $d_2 = 7 \text{ mm}$  are considered. By illuminating the tag with an incident plane wave polarized in the  $x$ -direction and propagating in the  $z$ -direction, the backscattered response from the tag is shown in Figure 3.30 for two values of  $d_2$ . The pole diagram of the tag is depicted in Figure 3.31 for two different cases. The resonance of the metal is located out of the frequency band of the slot's resonances for  $d_2 = 3 \text{ mm}$ . By increasing  $d_2$  sufficiently, the resonance of the metal can be within the frequency band of the slot's resonances. In this case, the damping factor of the slot's resonances increases as a result of coupling, which leads to a lower quality factor. This must be avoided in the design of the tags with high density of data in order to pack many resonant frequencies in a narrow frequency band. Two fabricated tags are shown in Figure

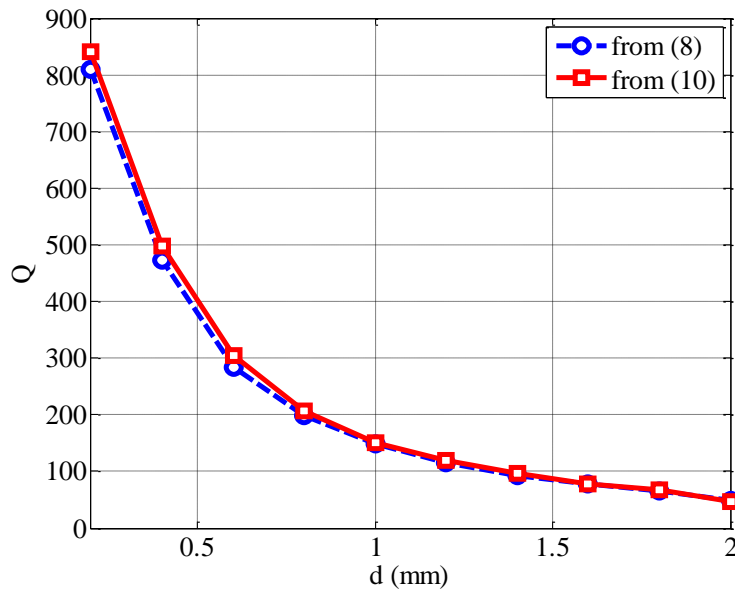


Figure 3.27 Quality factor of the CNR of the tag versus  $d$  [33] (With permission, Copyright© 2015 IEEE).

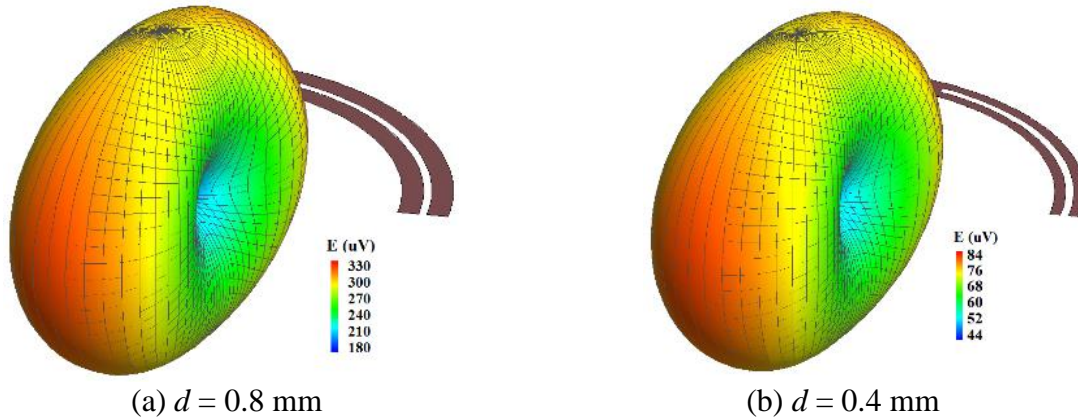


Figure 3.28 Far-field electric fields radiated from the tag for (a)  $d = 0.8$  mm and (b)  $d = 0.4$  mm [33] (With permission, Copyright© 2015 IEEE).

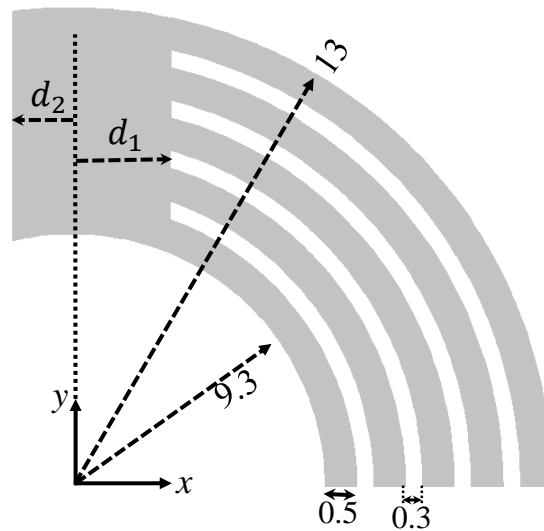


Figure 3.29 Schematic view of the designed 4-bit tag. Units: mm [33] (With permission, Copyright© 2015 IEEE).

3.32. The tags were designed on a Rogers RT/Duroid®/3003 ( $\epsilon_r=3$ ) with a thickness of 0.7874mm. Assuming the incident electric field directed in  $x$  and propagating in  $z$ , the measured backscattered electric field from the tags is depicted in Figure 3.33. Although the data are incorporated as four resonant frequencies of the slots, five resonant frequencies are seen in the backscattered signal from the tags. In these circumstances, the resonant frequency of the metal shall be distinguished from the slot resonances in the detection process of the tag. The pole diagram of the tags is shown

in Figure 34 based on the measured backscattered signal. It is seen that the CNRs of the tags calculated from the measurement data are in good agreement with the simulation results.

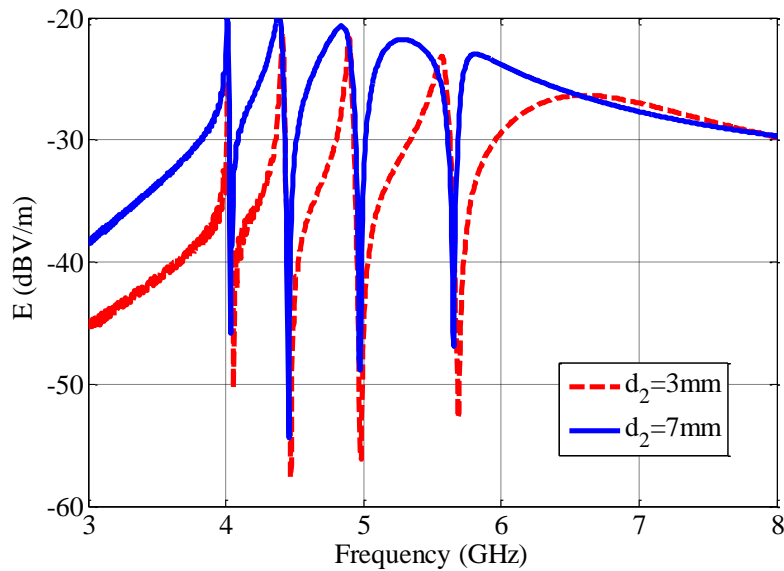


Figure 3.30 The simulated backscattered electric field from 4-bit tags [33] (With permission, Copyright© 2015 IEEE).

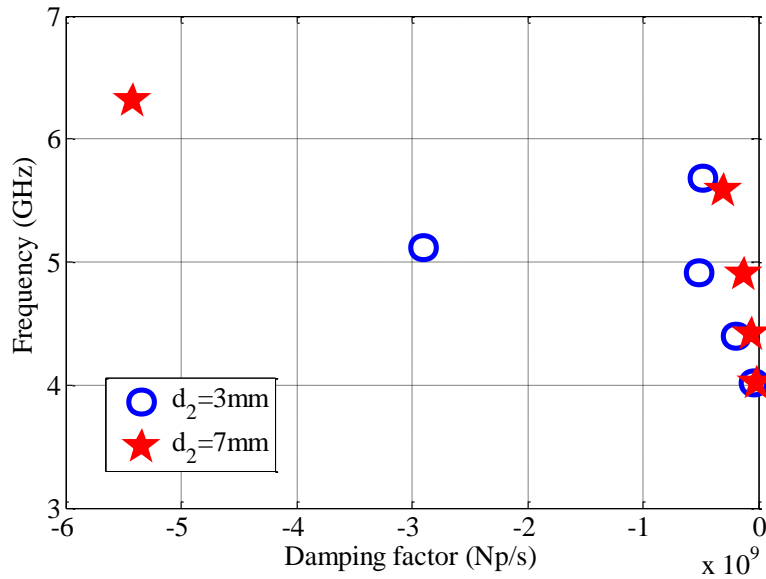


Figure 3.31 Pole diagram of the simulated backscattered fields from the tags [33] (With permission, Copyright© 2015 IEEE).



Figure 3.32 Two 4-bit fabricated tags (a)  $d_2 = 3$  mm and (b)  $d_2 = 7$  mm [33] (With permission, Copyright© 2015 IEEE).

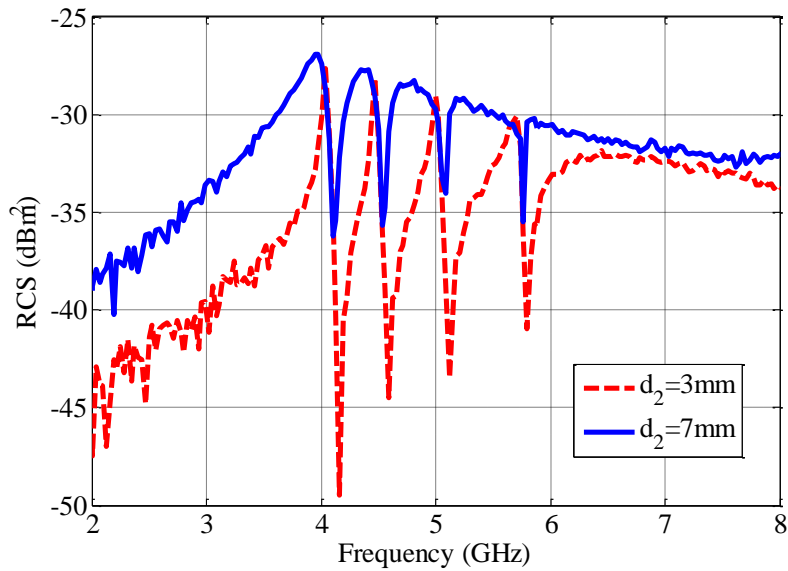


Figure 3.33 Measured RCS of the tags [33] (With permission, Copyright© 2015 IEEE).

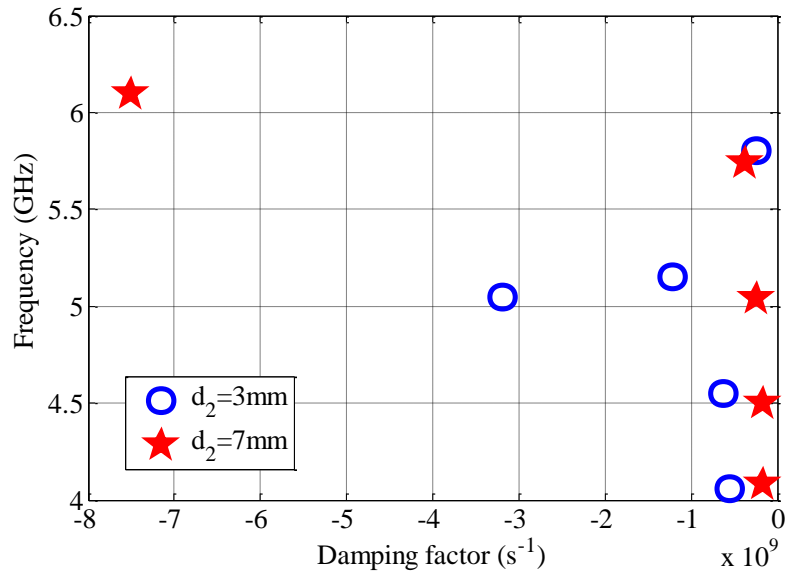


Figure 3.34 Pole diagram of the measured backscattered fields from the tags [33] (With permission, Copyright© 2015 IEEE).

## 4 UWB Antenna in Chipless RFID Systems

This chapter is devoted to the scattering process in chipless RFID systems. When an antenna illuminates a scatterer, the backscattered signal received by the antenna is analyzed in the reader to extract the required information of the scatterer. Therefore, the interaction between antenna and scatterer plays an important role in the detection process of data. The antenna needs to cover a wide range of frequencies and its frequency response strongly affects the received signal. Different antenna types can be used for this purpose providing some pros and cons. Since the location and ID of the tag are calculated based on time-domain and frequency-domain signals, respectively, both time and frequency domain properties of antenna must be considered in the systematic design of chipless RFIDs [51].

The United States of America was the first country to release a regulatory framework for the use of UWB technology. This framework defines UWB transmitters as: “An intentional radiator that, at any point in time, has a fractional bandwidth equal to or greater than 0.2 or has a UWB bandwidth equal to or greater than 500 MHz, regardless of the fractional bandwidth” [11]. The available spectrum for unlicensed UWB communications is between 3.1 GHz to 10.6 GHz with a maximum power emission limit of -41.3 dBm/MHz. The FCC mask for outdoor and indoor UWB applications in USA is shown in Figure 4.1. Assuming the FCC regulation, some attentions must be drawn in the design process of chipless RFID systems. According to the radar equation in the

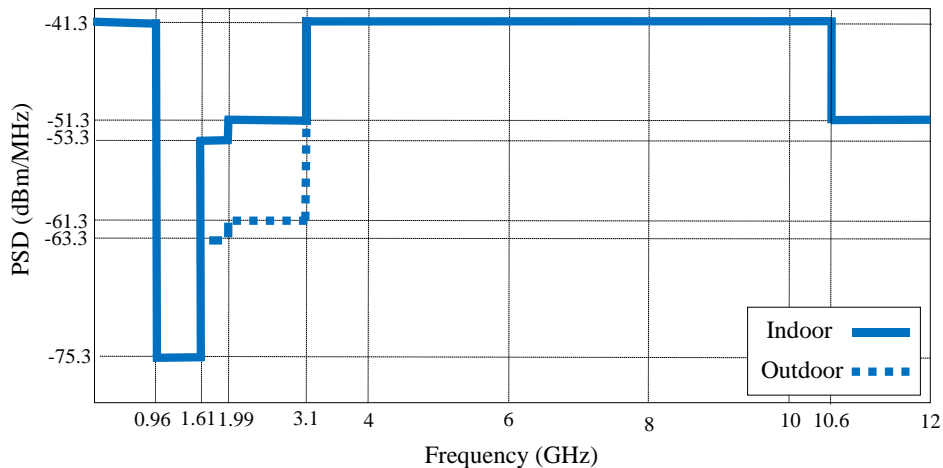


Figure 4.1 FCC mask for outdoor and indoor UWB applications.

frequency domain, the power of received signal depends on the transmitted power, path loss, radar cross section (RCS) of the tag, and antenna gains. Since these parameters are frequency-dependent, one needs to study their frequency dependency in the desired frequency band of operation.

In this chapter, first a mathematical representation of the scattering process in between the antenna and scatterer is presented and then, some important parameters of the antenna in time domain are reviewed. Various UWB antennas are studied in summary and finally, a new antenna element applicable in wideband and UWB is introduced.

## 4.1 Link Equation in Frequency Domain

As mentioned, the received signal by the antenna is a function of many parameters. Assuming a mono-static case seen in Figure 4.2 and based on the radar budget equation, the power of the received signal can be written as

$$P_r(f) = \frac{P_t(f) \cdot G_a(f) \cdot G_a(f) \cdot \lambda^2(f)}{(4\pi)^3 R^4} \cdot \delta(f) \quad (4.1)$$

where  $R$  is the read-range distance from the scatterer to the antenna,  $P_t$  and  $G_a$  are the power of the transmitted signal and antenna gain respectively,  $\lambda$  is the wavelength and  $\delta(f)$  represents the radar cross-section (RCS) of the scatterer. All these parameters are frequency-dependent. It is assumed that the antenna and scatterer are located in the far field of each other. High-gain antennas concentrate energy into a narrower solid angle than omni-directional ones and are usually used so as to reduce the effects of the interferences and background objects in the scattering media. In contrast, the omni-directional antennas can receive signal from any direction. These antennas have relatively lower gain and a wider field of view. Regulatory constrains require transmitted power to be decreased when using a high-gain antenna in order to meet the same maximum radiated emission limit shown in Figure 4.1. Since the regulatory limits are defined in terms of equivalent isotropically radiated power (EIRP),  $P_t \cdot G_a$ , the transmitted signal is engineered based on the antenna gain to meet the FCC constrains for short-rang UWB applications. The term  $\lambda^2/(4\pi)^3 R^4$  is referred as roundtrip path loss. The frequency dependency of the path loss comes from the definition of the antenna gain and antenna effective aperture in the frequency domain as [52, 53]

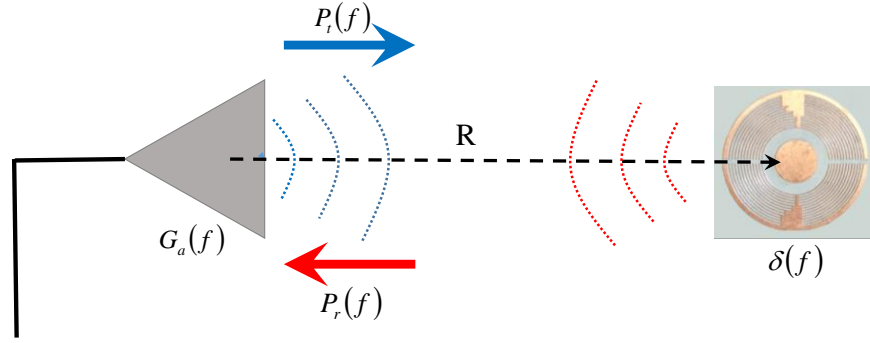
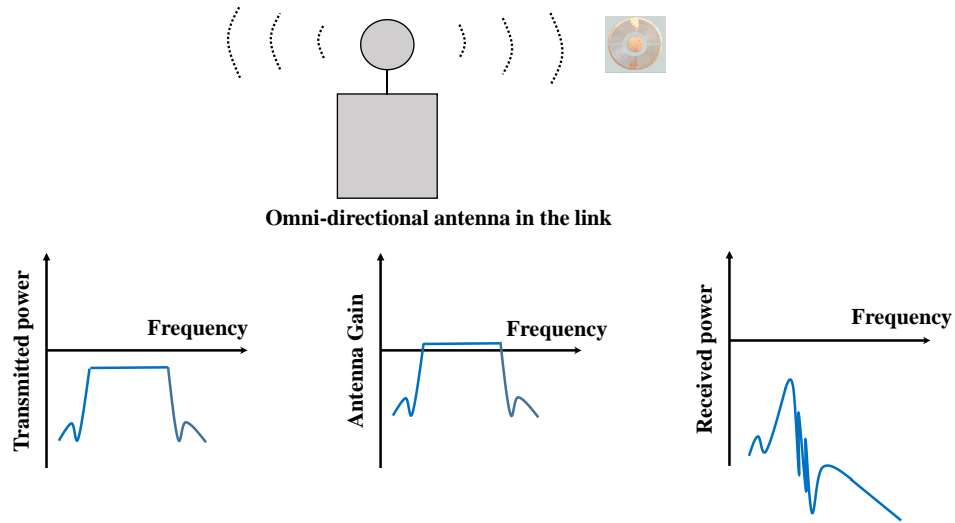


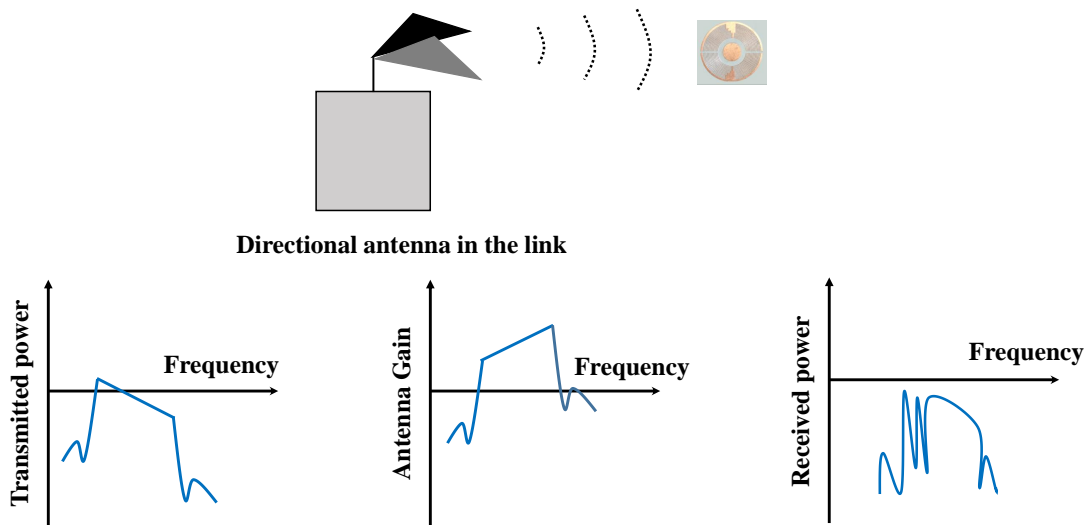
Figure 4.2 Mono-static chipless RFID system.

$$G_a(f) = \frac{4\pi A_{eff}(f)}{\lambda^2} \quad (4.2)$$

For large directive antennas, the effective aperture is comparable to the physical area of the antenna. For omnidirectional small antennas, the effective aperture may be significantly larger than the physical area of the antenna. It means that although a very small antenna may have negligible RCS, it is an effective receiver or radiator. Two groups of antennas as constant-gain and constant-aperture are considered here [52]. In omni-directional small antennas which are being widely used in short-range applications, the gain of the antenna is approximately constant in the frequency band of operation leading to the variation of the aperture by  $1/f^2$ . In Figure 4.3a, the frequency variations of the signal power and antenna gain are shown in the receiver and transmitter sides. In the cases where a constant-gain antenna is used in the network, the transmitter power is designed to be constant in the frequency range to meet constant EIRP in the transmitter side, result in the received power rolling off as  $\delta(f)/f^2$  in band. On the other hand, in constant aperture antennas which are large compared to the wavelength of the signal, the gain of the antenna increases by  $f^2$  (Figure 4.3b). Hence, the transmitter gain should change by  $1/f^2$  and the power of the received signal changes by  $\delta(f)$  in this case. In other UWB antennas, the variations of the gain and effective aperture is between these two cases. In resonant-based detection applications, the resonant frequencies of the scatterer are present in the frequency band of operation. These resonances might introduce some variations in the power of the received signal in the desired frequency band.



(a) Omnidirectional antenna in chipless RFID system.



(b) High-gain directional antenna in chipless RFID system.

Figure 4.3 Gain and power considerations in chipless RFID systems.

## 4.2 Time-Domain Signal Link Characterization

As a general case, a bi-static set-up comprised of two UWB antennas is depicted in Figure 4.4. The transmitter antenna, TX, is excited with an incident voltage  $a_{TX}(t)$  and the radiated field from the transmitter at the scatterer position is  $\mathbf{E}^{\text{inc}}(\mathbf{r}, t)$ . The induced current on the surface of the scatterer re-radiates an electric field,  $\mathbf{E}^{\text{s}}(\mathbf{r}_{\text{RX}}, t)$  at the position of the receiving antenna, RX. The scattered field generates a voltage  $v_{\text{oc}}(t)$  across the receiving port. The transmission coefficient

between two antennas is defined as the ratio of the received voltage wave  $b_{RX}(s)$  to the incident voltage wave,  $a_{TX}(s)$ , in the Laplace domain. As the first step, we introduce the impulse response of a scatterer located at the origin as the  $\hat{\mathbf{a}}_2$ -component of the scattered field at  $\mathbf{r}_2$ , in the far zone of the scatterer, for an impulsive incident plane wave of  $\hat{\mathbf{a}}_1\delta\left(t+\frac{\hat{\mathbf{r}}_1\cdot\mathbf{r}}{c}\right)$  as  $\frac{\hat{\mathbf{a}}_1\hat{\mathbf{a}}_2}{r_2}\Gamma(\hat{\mathbf{r}}_1,\hat{\mathbf{r}}_2,t)$ . In the general case,  $\hat{\mathbf{a}}_1$  and  $\hat{\mathbf{a}}_2$  are functions of time. The impulse response of the scatterer is a dyad, which includes all the scatterer information for a particular  $(\hat{\mathbf{r}}_1,\hat{\mathbf{r}}_2,t)$ . The next step is computing the incident field versus the effective length of the transmitting antenna and the input signal. The antenna can be characterized in the far-zone by its equivalent effective length as [54, 55]

$$\mathbf{h}(\hat{\mathbf{r}};t) = -\frac{\hat{\mathbf{r}}\times\hat{\mathbf{r}}\times}{I_a}\int_{S_{ant}}\mathbf{J}(\mathbf{r}';t+\mathbf{r}'\cdot\hat{\mathbf{r}}/c)dS' \quad (4.3)$$

where  $S_{ant}$  indicates the antenna surface,  $\mathbf{J}$  is the electric current on the antenna surface,  $\hat{\mathbf{r}}$  is the unit vector to the observation point,  $I_a$  is the input current, and  $c$  represents the speed of light in free space. The primed and unprimed coordinates indicate the source and observation points, respectively. If the input impedance of the antenna is assumed as  $Z_r$  and  $Z_{TX}$  is the impedance of the matching circuit, then the reflection coefficient at the transmitter,  $S_{TX}$ , in the frequency domain is given by

$$S_{TX} = \frac{Z_{TX} - Z_r^*}{Z_{TX} + Z_r} \quad (4.4)$$

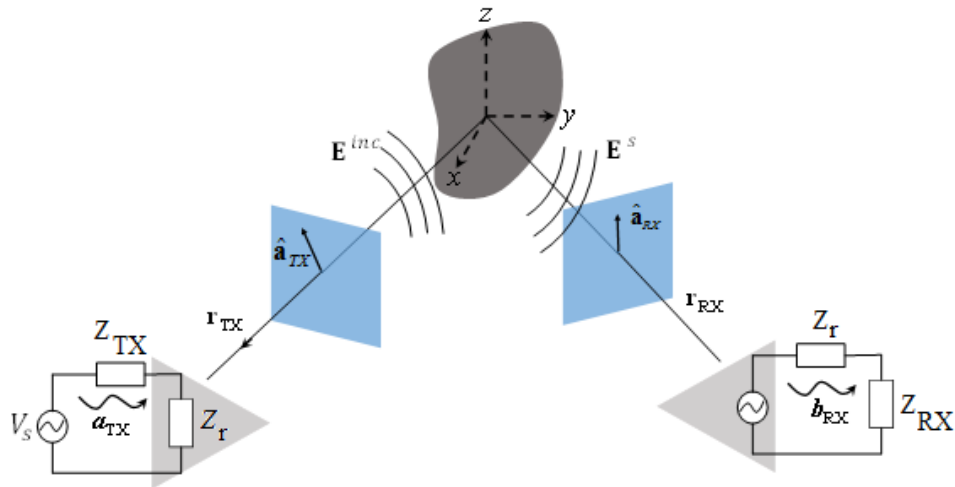


Figure 4.4 Schematic of the bio-static set-up for measuring the impulse response of the tag.

The realized effective length of the antenna is defined in time domain as [55]

$$\mathbf{h}_{\text{TX}}^{\text{R}}(\hat{\mathbf{r}}; t) = \frac{1 - s_{\text{TX}}(t)}{2} * \mathbf{h}_{\text{TX}}(\hat{\mathbf{r}}; t) \quad (4.5)$$

where  $s_{\text{TX}}(t)$  is the inverse Fourier transform of  $S_{\text{TX}}$ . Using the definition of the realized effective length of the transmitting antenna, the incident electric field  $\mathbf{E}^{\text{inc}}$  for an incident voltage wave of  $a_{\text{TX}}(t)$  is computed from

$$\mathbf{E}^{\text{inc}}(\mathbf{r}_{\text{TX}}; t) = -\mu \frac{1}{2\pi r_{\text{TX}}} \frac{\partial}{\partial t} \left[ \frac{a_{\text{TX}}(t)}{\sqrt{R_{\text{TX}}}} * \mathbf{h}_{\text{TX}}^{\text{R}} \left( -\hat{\mathbf{r}}_{\text{TX}}; t - \frac{r_{\text{TX}}}{c} \right) \right] \quad (4.6)$$

where  $R_{\text{TX}}$  is the resistance of the transmitter and  $\mu$  is the permeability of the free space. Using the definition of the impulse response of the scatterer, one can compute the received signal at the receiving antenna port as

$$b_{\text{RX}}(t) = \frac{-\mu}{8\pi^2 r_{\text{TX}} r_{\text{RX}}} \frac{\partial}{\partial t} \left[ \frac{a_{\text{TX}}(t)}{\sqrt{R_{\text{RX}}}\sqrt{R_{\text{TX}}}} * \mathbf{h}_{\text{TX}}^{\text{R}} \left( -\hat{\mathbf{r}}_{\text{TX}}; t - \frac{r_{\text{TX}}}{c} \right) * \hat{\mathbf{a}}_1 \hat{\mathbf{a}}_2 \Gamma \left( \hat{\mathbf{r}}_{\text{TX}}, \hat{\mathbf{r}}_{\text{RX}}; t - \frac{r_{\text{RX}}}{c} \right) * \mathbf{h}_{\text{RX}}^{\text{R}} \left( -\hat{\mathbf{r}}_{\text{RX}}; t \right) \right] \quad (4.7)$$

Equation (4.7) can be simplified if the impulse response of the scatterer is computed for the case where  $\hat{\mathbf{a}}_1$  and  $\hat{\mathbf{a}}_2$  are in the same direction as  $\mathbf{h}_{\text{TX}}^{\text{R}}$  and  $\mathbf{h}_{\text{RX}}^{\text{R}}$ , respectively.

$$b_{\text{RX}}(t) = \frac{-\mu}{8\pi^2 r_{\text{TX}} r_{\text{RX}}} \frac{\partial}{\partial t} \left[ \frac{a_{\text{TX}}(t)}{\sqrt{R_{\text{RX}}}\sqrt{R_{\text{TX}}}} * \mathbf{h}_{\text{TX}}^{\text{R}} \left( -\hat{\mathbf{r}}_{\text{TX}}; t - \frac{r_{\text{TX}}}{c} \right) * \Gamma \left( \hat{\mathbf{r}}_{\text{TX}}, \hat{\mathbf{r}}_{\text{RX}}; t - \frac{r_{\text{RX}}}{c} \right) * \mathbf{h}_{\text{RX}}^{\text{R}} \left( -\hat{\mathbf{r}}_{\text{RX}}; t \right) \right] \quad (4.8)$$

Applying Laplace transform to (4.8), the transmission coefficient is defined as the ratio of  $b_{\text{RX}}(s)$  to  $a_{\text{TX}}(s)$ .

$$S_{\text{RT}}(s) = \frac{s\mu e^{-s(r_{\text{TX}}+r_{\text{RX}})/c}}{8\pi^2 r_{\text{TX}} r_{\text{RX}} \sqrt{R_{\text{TX}} R_{\text{RX}}}} \mathbf{H}_{\text{TX}}^{\text{R}}(-\hat{\mathbf{r}}_{\text{TX}}; s) \cdot \Gamma(\hat{\mathbf{r}}_{\text{TX}}, \hat{\mathbf{r}}_{\text{RX}}; s) \cdot \mathbf{H}_{\text{RX}}^{\text{R}}(\hat{\mathbf{r}}_{\text{RX}}; s) \quad (4.9)$$

For the mono-static case where one antenna is used for both transmitting and receiving, the reflection coefficient is computed from

$$S_{11} = \frac{s\mu e^{-2sr_{\text{RX}}/c}}{8\pi^2 r_{\text{RX}}^2 R_{\text{RX}}} \left( \mathbf{H}_{\text{RX}}^{\text{R}}(\hat{\mathbf{r}}; s) \right)^2 \Gamma(r, r; s) \quad (4.10)$$

The impulse response of the scatterer is obtained as

$$\Gamma(r, r; s) = \frac{8\pi^2 r_{RX}^2 R_{RX} e^{2sr_{RX}/c}}{s\mu(H_{RX}^R(\hat{r}; s))^2} S_{11} \quad (4.11)$$

According to (4.10), the information of the scatterer is included in  $S_{11}$  of the receiving antenna multiplied by the square of impulse response of the antenna. As (4.11) shows, the impulse response of the tag can be calculated by knowing the effective length of the antenna and the distance between the antenna and the scatterer,  $r_{RX}$ .

### 4.3 Antenna Effective Length

As (4.11) shows, one needs to have the effective length of the antenna in order to extract the impulse response of the tag in the measurement set-up. As (4.3) shows, the effective length of the antenna is defined in the far field and is related to the far-field electric field by

$$\mathbf{E}(\hat{\mathbf{r}}) = -j\omega\mu \frac{e^{-jkr}}{4\pi r} I_a \mathbf{H}(\hat{\mathbf{r}}) \quad (4.12)$$

A bi-static set-up, seen in Figure 4.5, can be used in order to measure the effective length of the antenna. It is assumed that both antennas are similar to each other. In bi-static case, the effective length of the antenna can be calculated from

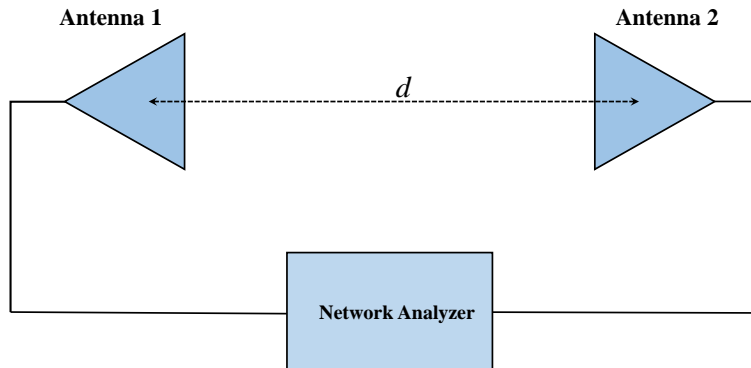


Figure 4.5 Measurement set-up for measuring transfer function of the antenna.

$$\begin{aligned}
S &= \frac{4S_{21}(\omega)}{(1 - S_{11})^2} \\
&= j\omega\mu \mathbf{H}_{\text{TX}}(\omega) \cdot \mathbf{H}_{\text{RX}}(\omega) \frac{e^{-jkd}}{2\pi R_{\text{RX}} d}
\end{aligned} \tag{4.13}$$

where  $S_{21}$  is the transmission coefficient between two antennas,  $S_{11}$  represents the reflection coefficient of the antennas,  $\mathbf{H}_{\text{TX}}$  and  $\mathbf{H}_{\text{RX}}$  are the effective length of the transmitting and receiving antennas, and  $d$  is distance between the antennas. In order to measure the effective length of the antenna, it is necessary to know the distance  $d$  between the antennas. Ultra wideband antennas usually do not have a well-defined phase center and this provides some difficulties in calculating the phase of the antenna effective length. This also might be happen in calculating the phase of the transfer function of the scatterer in (4.11). The phase response of  $S$  in (4.13) can be separated into three terms:  $90^\circ$  due to the  $j\omega$ , twice of the phase of the antenna impulse response, and the phase related to the spherical mode, linearly changes with  $kd$ . Assuming the antenna as a minimum phase system, its phase response can be calculated from the Hilbert transform of its magnitude response [56]. As (4.13) shows, the amplitude of  $S$  is proportional to the amplitude of the square of the transfer function of the antenna with coefficient of  $\omega/(2\pi d)$ . Hence, the minimum phase function  $\phi_m(\omega)$  can be found from

$$\phi_m(\omega) = \frac{2\omega}{\pi} \int_0^{+\infty} \frac{\ln|S(\omega')| - \ln|S(\omega)|}{\omega'^2 - \omega^2} d\omega' \tag{4.14}$$

by assuming a nominal distance  $d = d'$ . The linear part of the phase in  $S_{21}$  is calculated from

$$\phi_L(\omega) = \angle S - \phi_m \tag{4.15}$$

The correction distance can be calculated from the linear phase part as

$$\Delta d = \frac{c_0}{2\pi} \frac{d\phi_L}{df} \tag{4.16}$$

By substituting  $d = d' + \Delta d$  in (4.13), the amplitude of and phase of the transfer function of the antenna is obtained. As an example, two different antennas (circular disk and narrowband monopole) shown in Figure 4.6 are considered. Two circular disks with  $R = 10$  cm are located 40 cm away from each other (face to face) and the reflection and transmission coefficients between

the input ports of the antenna are measured. The  $S_{11}$  and  $S_{21}$  between antennas are depicted in Figure 4.7a. As it shows the antennas are matched ( $S_{11} < -10\text{dB}$ ) for frequencies in the range of 3.1-10.6 GHz. The phase of  $S_{21}$  is seen in Figure 4.7b. According to (4.12), the phase of the  $S_{21}$  is the combination of the three different terms. By assuming the antenna as a minimum phase system, the linear part of the response can be calculated from (4.15). This part is also depicted in Figure 4.7b. By using the equation (4.12) and (4.14), the amplitude and phase response of the antenna effective length are shown in Figure 4.7c and 4.7d. By applying inverse fast Fourier transform (IFFT) to the antenna effective length, its effective length in time domain is seen in Figure 4.7e for  $\theta = 90^\circ$  and  $\varphi = 0^\circ$ . It just represents the angular variation of the pattern of the antenna in the far field. By applying MPM to the late-time response of the radiated field of the antenna, its pole diagram shown in Figure 4.7f.

In narrowband antennas, since the antenna and propagation characteristics are assumed constant over the desired frequency band, they are typically described in the frequency domain. On the other hand, in UWB antennas, not only the frequency-domain characteristics of the antenna and channel should be considered, but their time-domain properties should also be taken into consideration, because they are usually realized in an impulse-based technology.

#### 4.4 Antenna Characteristics in Time Domain

In order to evaluate the performance of an antenna in time domain, some parameters need to be defined as figure of merits. Since the radiation properties of the antenna in the frequency domain

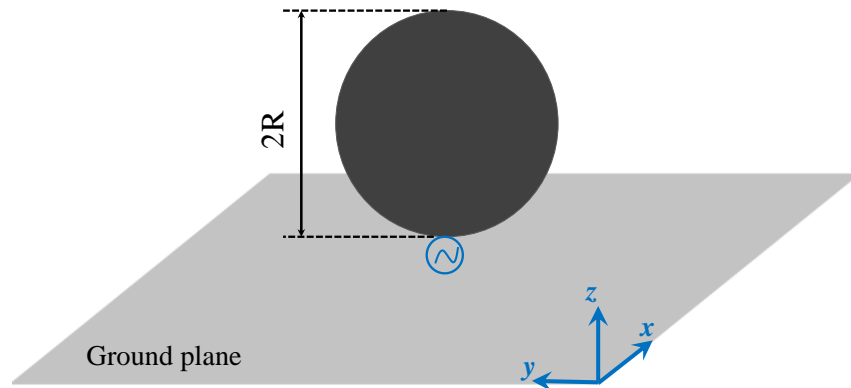


Figure 4.6 (a) UWB Monopole disk and (b) Narrowband monopole antenna.

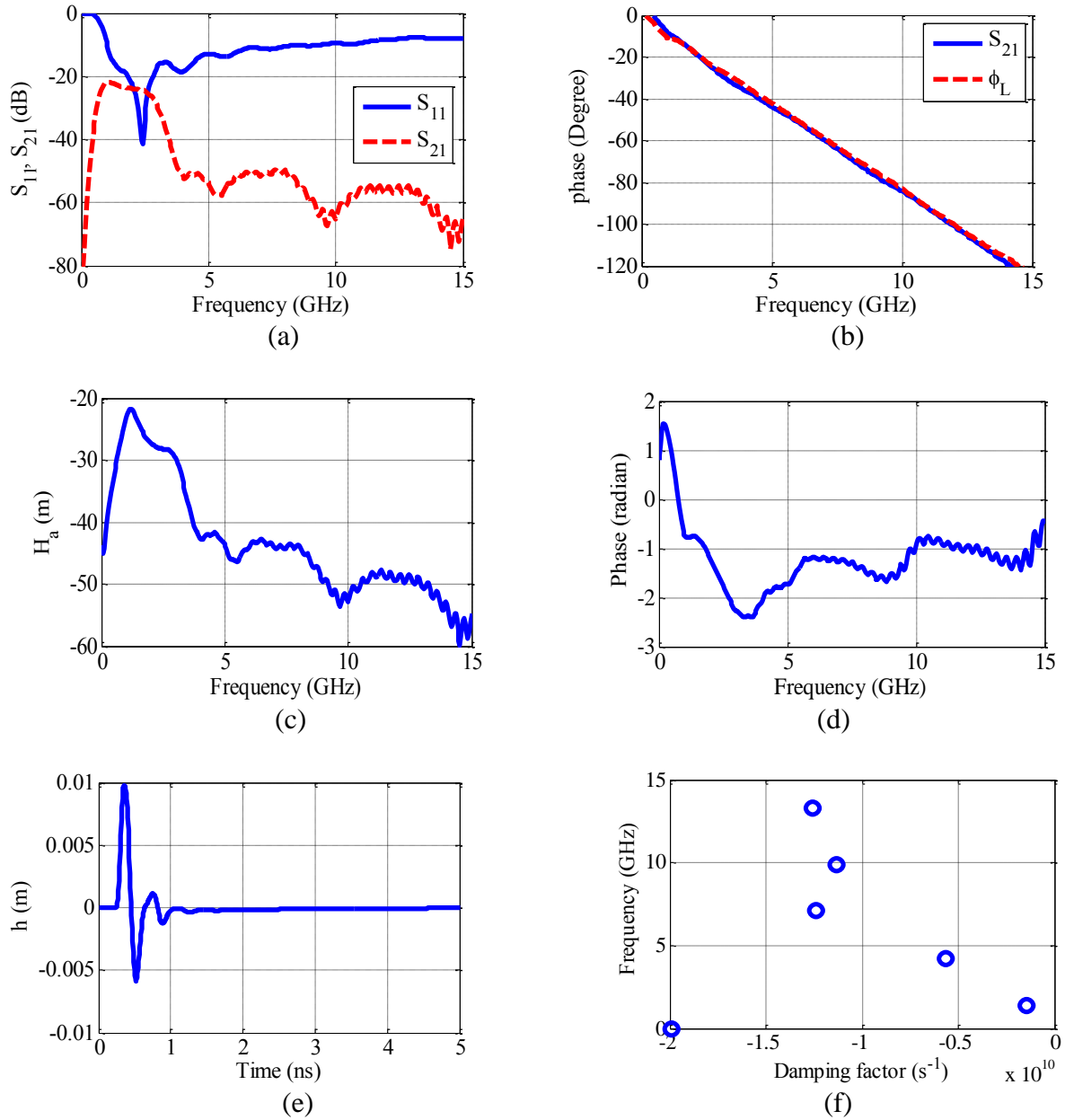


Figure 4.7 (a) Amplitude and (b) phase of the  $S_{21}$  for  $\theta = 0$  and  $\varphi = 0$ , (c) Amplitude and (d) phase of the antenna effective length in frequency domain, (e) antenna effective length in time domain, and (f) pole-diagram of the antenna.

are usually defined in the far-field, it is significantly necessary to translate the concept of far-field into time domain. IEEE defines the far field as “The region of the field where the normalized angular field distribution is essentially independent of the distance from a specified point in the antenna region”. For a narrow band antenna, the far-field distance is defined as the distance from the antenna phase center where the phase shift from the ray originating from antenna maximum

dimension and one from antenna center is  $22.5^\circ$ . In most narrowband antennas, the following range is considered as the far-field [57].

$$R = \frac{2D^2}{\lambda} \quad (4.17)$$

where  $D$  is the maximum antenna dimension in meter and  $\lambda$  is the wavelength of the signal at the desired frequency. As an example, Figure 4.8a shows a narrowband monopole antenna located above a ground plane. Different probes are located at different distances from the antenna. The reflection coefficient of the antenna is seen in Figure 4.8b. The first and third resonances of the antenna are located at  $f = 3.6$  GHz and  $f = 10.8$  GHz. In Figure 4.9, the  $\theta$ -component of the electric field is depicted versus the distance from the antenna at two resonant frequencies. Since the fields in the far field change inversely by distance, the real fields in the far field are approximated by  $A/r$  in Figure 4.9. At the distance where the variations of electric field deflects from  $A/r$ , the near-field of the antenna starts. For example, the far-field region starts from  $R = 4.5$  cm and  $R = 12$  cm at frequencies of  $f = 3.6$  GHz and  $f = 10.8$  GHz, respectively, which are well matched with (4.17). For wideband and UWB antennas, the far field seems frequency-dependent and one needs new definition in time domain. Before defining the far-field region in time domain, it is required to calculate the analytic envelope response of the antenna as

$$h^+(t) = h(t) + jH(h(t)) \quad (4.18)$$

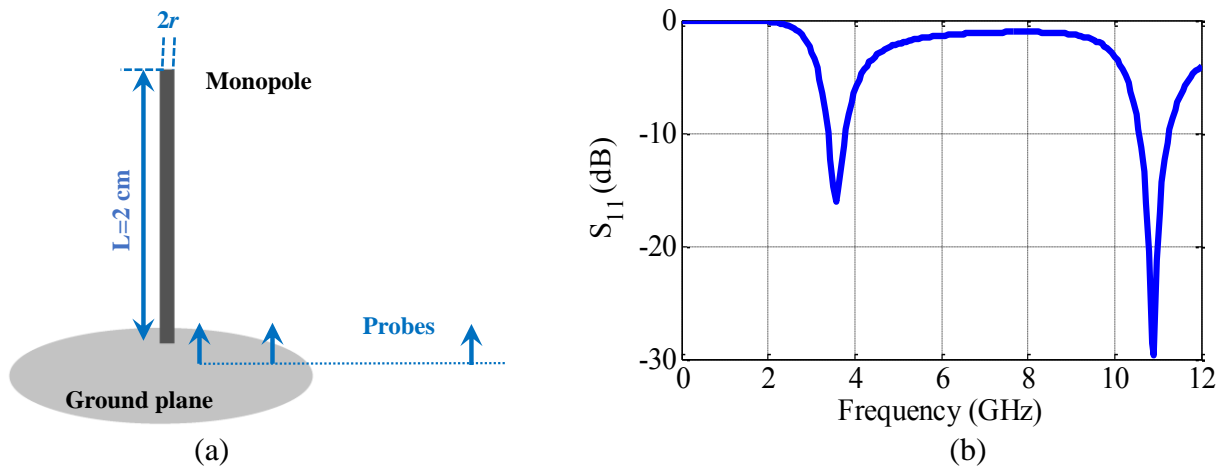


Figure 4.8 (a) Monopole antenna above a ground plane (b) its reflection coefficient.

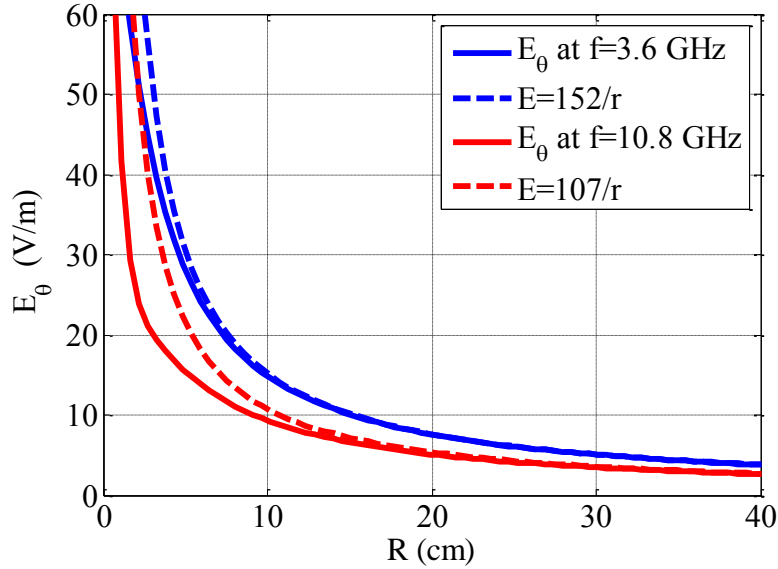


Figure 4.9 Radiated  $E_\theta$  versus the distance from the monopole antenna.

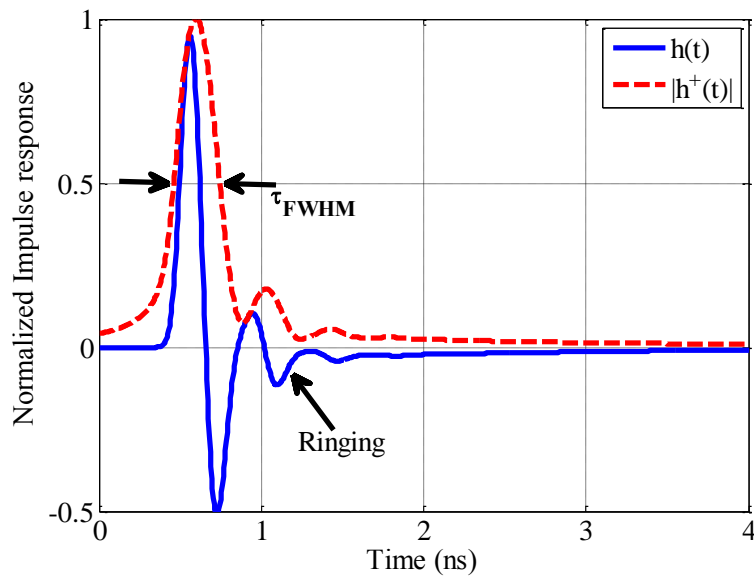


Figure 4.10 Normalized impulse response of the UWB monopole antenna along with analytic envelope.

where  $h(t)$  is the impulse response of the antenna and  $H(\cdot)$  is the Hilbert transform. The dispersion characteristics of the antenna can be studied from the envelope of the analytic impulse response of the antenna,  $|h^+(t)|$  [51].

As an example, Figure 4.10 shows the impulse response and analytic envelope of the UWB monopole antenna at  $\theta = 90^\circ$  and  $\varphi = 0$ . Some of the specific quantities usually used in characterizing the UWB antennas are summarized as following.

1) *Peak Value of the Envelope*: It is defined as the maximum of the antenna transfer function as

$$p(\theta, \varphi) = \max_t |h^+(t, \theta, \varphi)| \quad (4.19)$$

It depends strongly on the directivity of the antenna and its impedance bandwidth [58].

2) *Envelope Width* ( $\tau_{FWHM}$ ): It shows the widening of the radiated impulse from the antenna. It defines as the full width at the half maximum (FWHM) of the analytic envelope of the antenna. This parameter is depicted in Figure 4.10. The lower values of envelope width ensures the transmission of high data rate through the antenna.

In [59], the far-field of the antenna in time domain is defined as the range where the arrival of the closest ray and the arrival of the farthest ray is small compared to envelope width. Assuming  $d_1$  and  $d_2$  as the distances of the closest and farthest dimensions of the antenna to the observation point, the far field of the antenna is the range where [59]

$$\frac{(d_2 - d_1)}{c} \leq \frac{\tau_{FWHM}}{v} \quad (4.20)$$

where  $c$  is the speed of light in free space and  $v$  is a number between 3 to 5 for large antennas. For smaller antennas in the dimensions comparable with  $\lambda$ , larger value of  $v$  must be used. In general, there is not a unique closed-form formula for finding the far-field of UWB antennas in time domain. A reliable way is monitoring the variation of the field from near field to far field. Figure 4.11 shows the variation of the electric fields in the near field and far field of the UWB monopole antenna with  $R = 10$  mm at different distances of the observation point compared to the center of the antenna. In the near field, the shape of the field changes significantly versus distance,  $d$ . As Figure 4.11a shows, for larger distances in the near-field region, not only the fields are shifted, but their shape also changes. On the other hand, the shape of the radiated field does not change versus distance in the far field, as Figure 4.11b shows.

3) *Ringling*: An important parameter which illustrates the dispersion properties of the antenna is ringling,  $\tau_r$ . Ringling originates from the stored energy around the antenna or multiple reflections from the antenna structure. Quantity  $\tau_{r=\alpha}$  is defined as the time until the envelope is fallen in a bound from its peak to  $\alpha.p(\theta, \varphi)$ . For UWB applications such as ranging, one needs to lower the ringling of the antenna less than a few envelope width.

4) *Group Delay*: The frequency dependency of the phase response of the antenna impulse response is defined as the group delay.

$$\tau_g(\omega) = -\frac{d\varphi(\omega)}{d\omega} \quad (4.21)$$

where  $\varphi$  is the phase of the antenna impulse response. In non-distorted antenna, the group delay is constant over the frequency band of operation leading to linearly varying phase with frequency. The nonlinearities of the group delay indicate the resonant behavior of the antenna. In Figure 4.12, the group delay of the UWB antenna seen in Figure 4.6 is depicted.

## 4.5 New Antenna Prototype for Wideband and Ultra-wideband Applications

Different types of wideband antennas have been introduced and employed in practical applications as

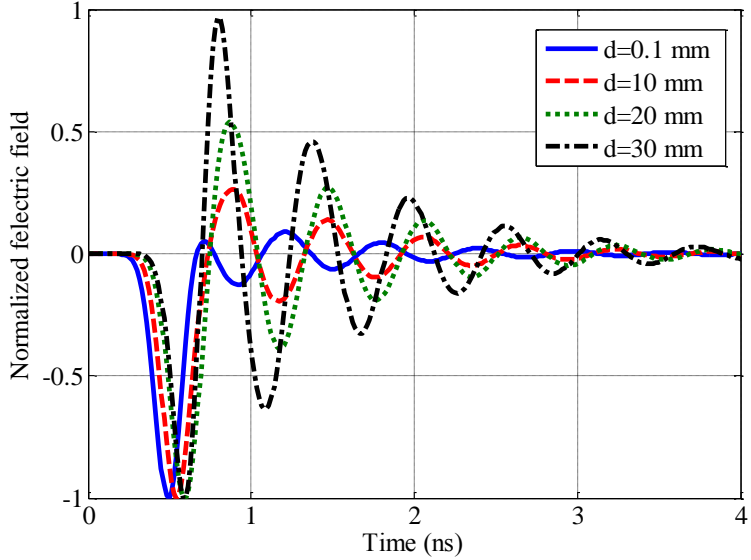
- Frequency-independent antennas;
- Self-complementary antennas;
- Travelling wave antennas;
- Multiple resonance antennas;
- Electrically small antennas;

In frequency-independent antennas, a scaled version of the radiating element is used for scaled wavelength. In practice, one needs to truncate the antenna structure. Bowtie antenna (planar version of Biconical antenna) shown in Figure 4.13a is an example of frequency-independent antennas. It is important to note that independence from frequency refers to the radiation properties of the antenna not its input impedance.

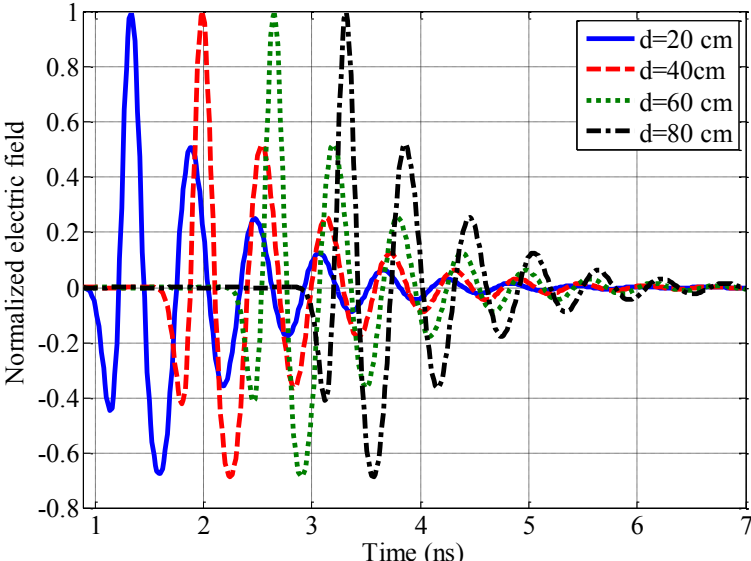
Self-complementary antennas are realized by a self-complementary metallization. In these antennas, the metal and dielectric can be replaced without changing the antenna's configuration. Based on Babine's principle, the input impedance is independent of frequency as

$$Z_{in} = 60\pi \Omega \quad (4.22)$$

It does not mean that the radiation field is independent of frequency as well. The antenna structure seen in Figure 4.13b is an example of the self-complementary antenna. In some applications where both radiation characteristics and input impedance need to be independence of frequency for large bandwidth, both techniques are combined. Two-arm logarithmic spiral antenna is an example of the antenna which combines two aforementioned techniques together.



(a)



(b)

Figure 4.11 Variation of  $E_{\theta}$  versus distance from the antenna in (a) near field and (b) far field of the antenna.

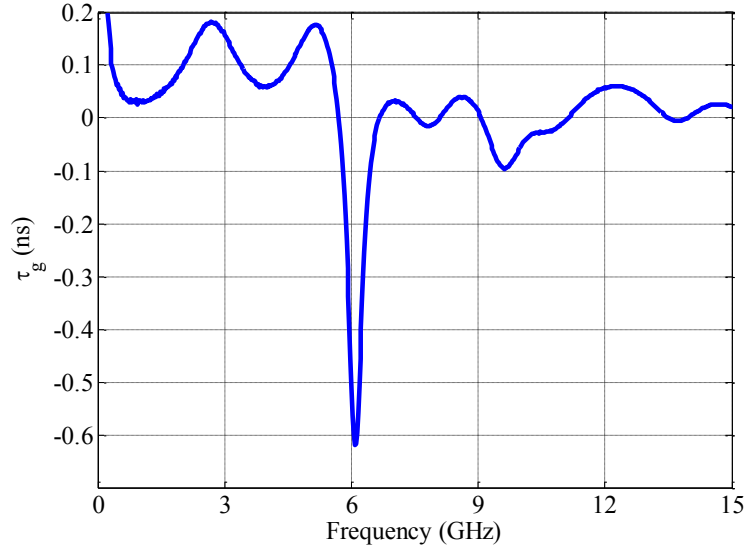


Figure 4.12 Group delay of UWB monopole antenna.

In travelling-wave antennas, a travelling wave along a guiding structure with size much larger than wavelength is used as the radiating element. By travelling the wave along the structure, it radiates progressively and the reflected wave from the antenna end is usually very small compared to the input signal. TEM horn seen in Figure 4.13c is an example of this type of antennas. The antenna structure is tapered to match the antenna impedance to the free space intrinsic impedance for a wide range of frequencies.

Another type of UWB antennas is realized by employing multiple resonances in the antenna structure. These antennas are combinations of multiple and narrow-band radiating elements. Planar log-periodic antenna is a multiple resonance antenna, seen in Figure 4.13d. It includes multiple dipoles with different lengths as  $(l_u/l_{u+1}) = \text{constant}$ . Different narrowband antennas elements can be used as a basis in the design of multi-resonant UWB antennas.

Electrically small antennas are antennas with dimensions far below the resonance region. These antennas are poor in radiation characteristics and impedance matching. Based on the physical limits of the radiation, there is a relationship between the size of the antenna, its quality factor and radiation efficiency [60, 61]. As a result, by decreasing the size of the antenna, its radiation efficiency decreases in order to achieve wider bandwidth. Some efforts have been made in order to miniaturize the antenna structures close to the physical limits. In these antennas the

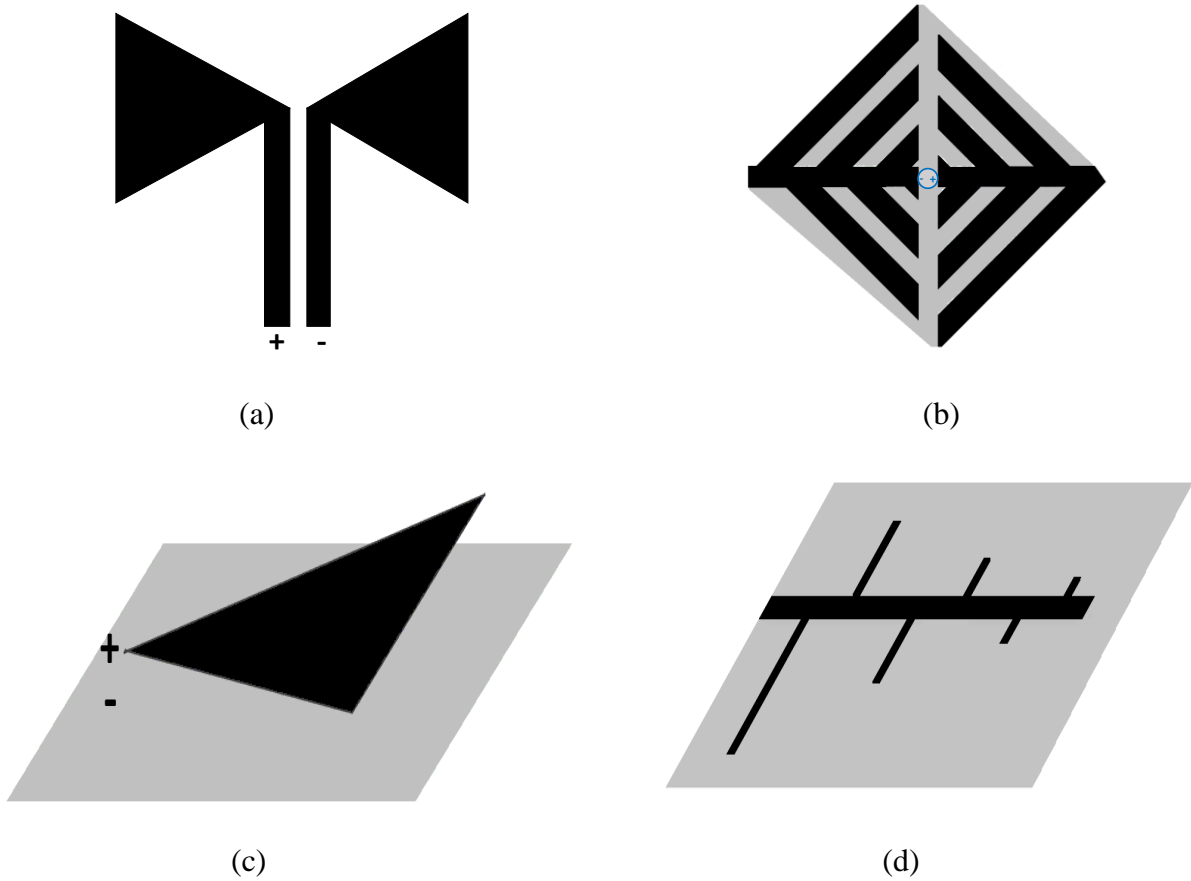


Figure 4.13 (a) Bowtie antenna as a frequency-independent antenna, (b) a self-complementary antenna, (c) TEM horn as a travelling-wave antenna, and (d) Log-periodic antenna as a multiple resonance antenna.



(a)



(b)

Figure 4.14 Two examples of UWB small antennas.

radiation pattern of the antenna is very close to the radiation pattern of  $TM_{01}$  (ideal small dipole) or  $TE_{01}$  (ideal small loop). These antennas are very applicable for low frequency applications (HF, VHF and UHF frequencies) which the size of the antenna is a critical issue. Figure 4.14a shows a typical rotational symmetric UWB monocone antenna with the height of about  $\lambda/5$  [51]. In Figure 4.14b another small antenna of with maximum size of  $\lambda/10$  more than 10:1 bandwidth, and efficiency of more than 95 percent is depicted [62].

The proposed antenna element in this chapter is based on simple monopole antenna above a ground plane. By exciting the antenna through a source terminated in between the ground and antenna, the odd-order resonances can be excited. Figure 4.8 depicts a monopole antenna of length  $L = 20$  mm and its reflection coefficient for a wide range of frequency. The excited resonant frequencies of the antenna are very close to the sharp nulls of the reflection coefficient. Assuming an infinite ground plane, the current distribution and corresponding pattern in the far-field are shown in Figure 4.15 and 4.16. At the first resonance of the antenna,  $f = 3.6$  GHz, the current distribution has its maximum on the feeding point and its null at its end. It produces a radiation pattern with maximum at  $\theta = 90^\circ$  and null at  $\theta = 0^\circ$ . Since the antenna structure is symmetric around z-axis, its radiation pattern is omni-directional. At  $f = 7$  GHz, the current distribution is tapered at the end points which makes the antenna more directive at the broadside direction. At the third resonant modes,  $f = 10.8$  GHz, the current distribution has a null on the antenna length. The current changes its direction at the null point leading to a null in the radiation pattern of the antenna. By increasing the frequency, the location of the null shifts up from the voltage source, corresponding to the frequency of the source. The impedance characteristics of the antennas can be studied by monitoring the variations of the CNRs as a function of structural parameters in the pole diagram. In pole diagram, the resonant frequencies and damping factors of the excited CNRs of the antenna are represented together. In antenna language, the quality factor of the CNRs is usually used in the design procedure, instead of damping factors. For high-Q resonances, the following relation exist between the quality factor and damping factor [19].

$$Q_n = \frac{\omega_n}{2\alpha_n} \quad (4.23)$$

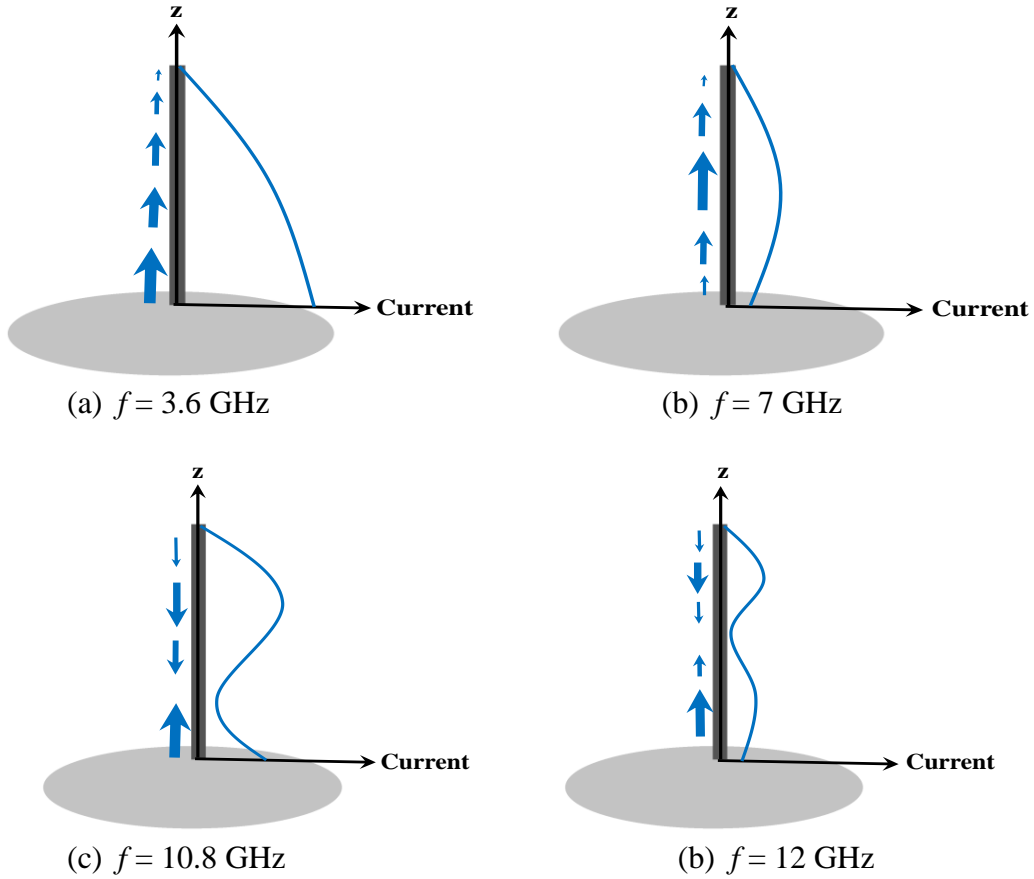


Figure 4.15 Amplitude of the current along the monopole and its direction at different frequencies.

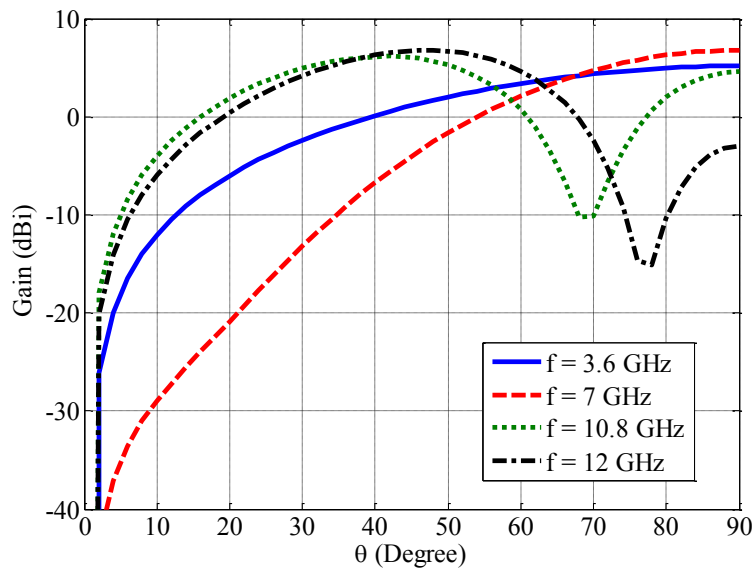


Figure 4.16 Radiation gain of the monopole antenna at different frequencies.

Two structural parameters for changing the resonant frequency and quality factor of the CNRs are the length and width of the monopole antenna. The variations of the CNRs versus the length and width of the monopole are shown in Figure 4.17. As it shows, any increase in the length of the antenna reduces the resonant frequencies with slightly increase in damping factors. On the other hand, by increasing the width of the monopole, the damping factors increase leading to the wider bandwidth of the antenna at the resonant frequencies. The corresponding quality factors of the first three CNRs of the monopole antenna are  $Q_1 = 17.6$ ,  $Q_3 = 27.5$ , and  $Q_5 = 53.3$  in the case of  $r = 0.5$  mm and  $L = 20$  mm. In order to obtain a wide input impedance from the monopole antenna, one needs to lower the quality factors of the CNRs enough and at the same time adjust the resonances of the antenna at appropriate frequencies. Figure 4.18a shows a monopole antenna with simply adjustable length and width as  $r_1$  and  $r_2$ . Assuming  $r_1 = 10$  mm, the variations of CNRs versus  $r_2$  is depicted in Figure 4.18b. For better illustration, the reflection coefficient of the antenna is seen in Figure 4.19a. As the results show, by increasing  $r_2$ , the first resonant frequency of the antenna does not change. While the higher order resonances decrease slightly. Additionally, the quality factors of the CNRs decrease leading to a wideband input impedance. In Figure 2.19b, the radiated electric fields from the antenna in time domain are shown for  $r_2=0.5$  mm and  $r_2=20$  mm. As it shows, the antenna is less dispersive for  $r_2 = 20$  mm. As above mentioned analysis of UWB monopole antenna showed, the resonant frequencies, damping factors and corresponding residues of the CNRs of the antenna can be designed properly in order to have UWB input impedance. The absolute value of the current distribution on the antenna surface for  $r_1 = 20$  mm and  $r_2 = 10$  mm is

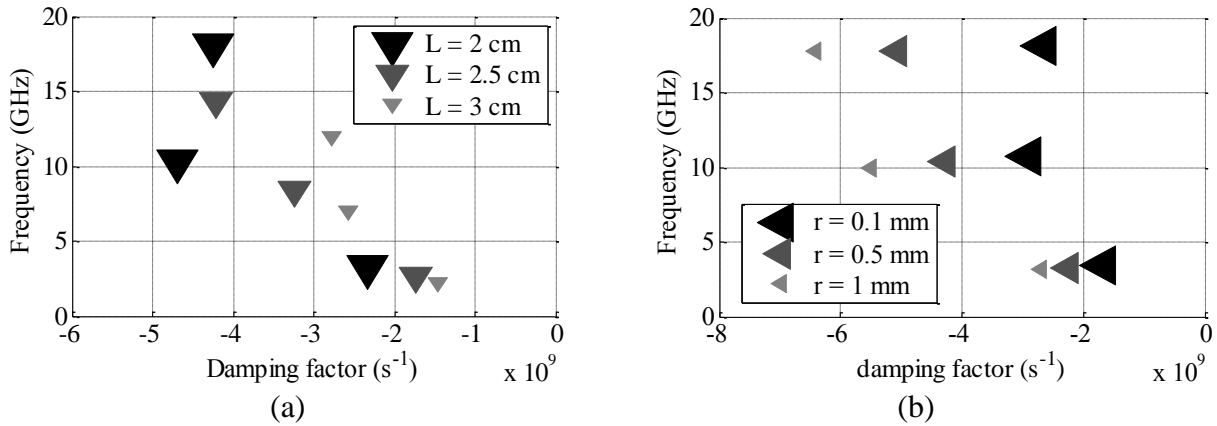
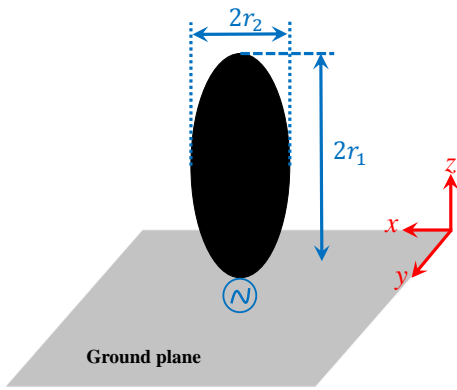
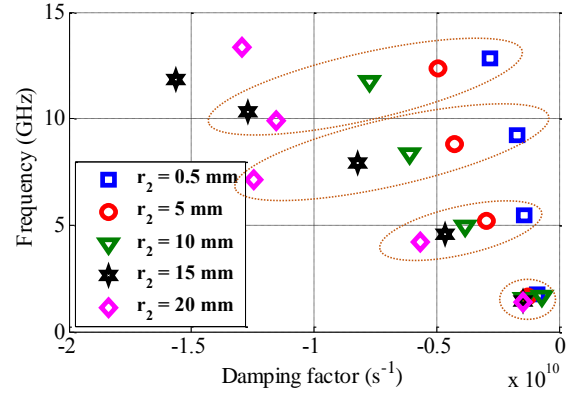


Figure 4.17 Variations of CNRs of the monopole antenna versus (a) antenna length,  $L$  and (b) antenna radius,  $r$ .

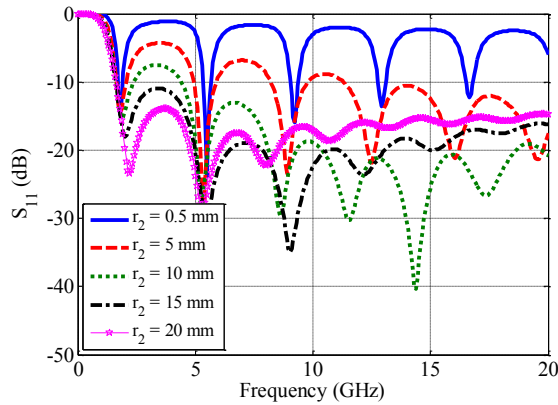


(a)

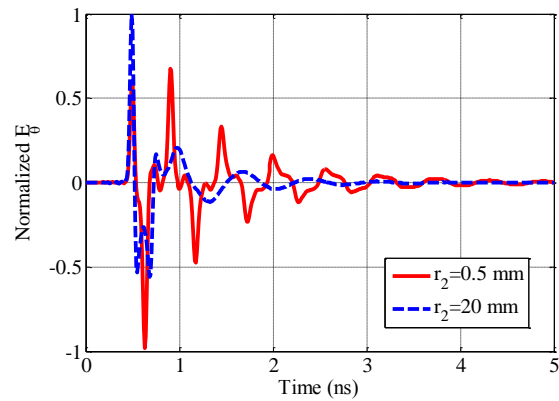


(b)

Figure 4.18 (a) Monopole antenna above a ground plane, (b) its pole diagram for different values of  $r_2$ .



(a)



(b)

Figure 4.19 (a) Reflection coefficient of the monopole antenna, and (b) time-domain radiated field from the antenna.

depicted in Figure 4. 20 at different resonant frequencies of the antenna. At lower frequencies, the current distribution is very close to the current distribution on monopole antenna seen in Figure 4.15. By increasing the frequency, the current is stronger on the edges of the antennas and the standing wave on the antenna edges has more variations which introduces some variations in the far-field radiation fields. At some frequencies, depending on the phase of the current distribution on the tag, some dip null might be introduced in the radiation pattern. For example, the radiation pattern has a dip null at  $\theta = 90^\circ$  and frequency  $f = 6$  GHz. In aforementioned UWB antenna, the quality factors and resonant frequencies of the antenna are adjusted for wide input impedance matching by enlarging the size of the monopole. In following a simple antenna element is

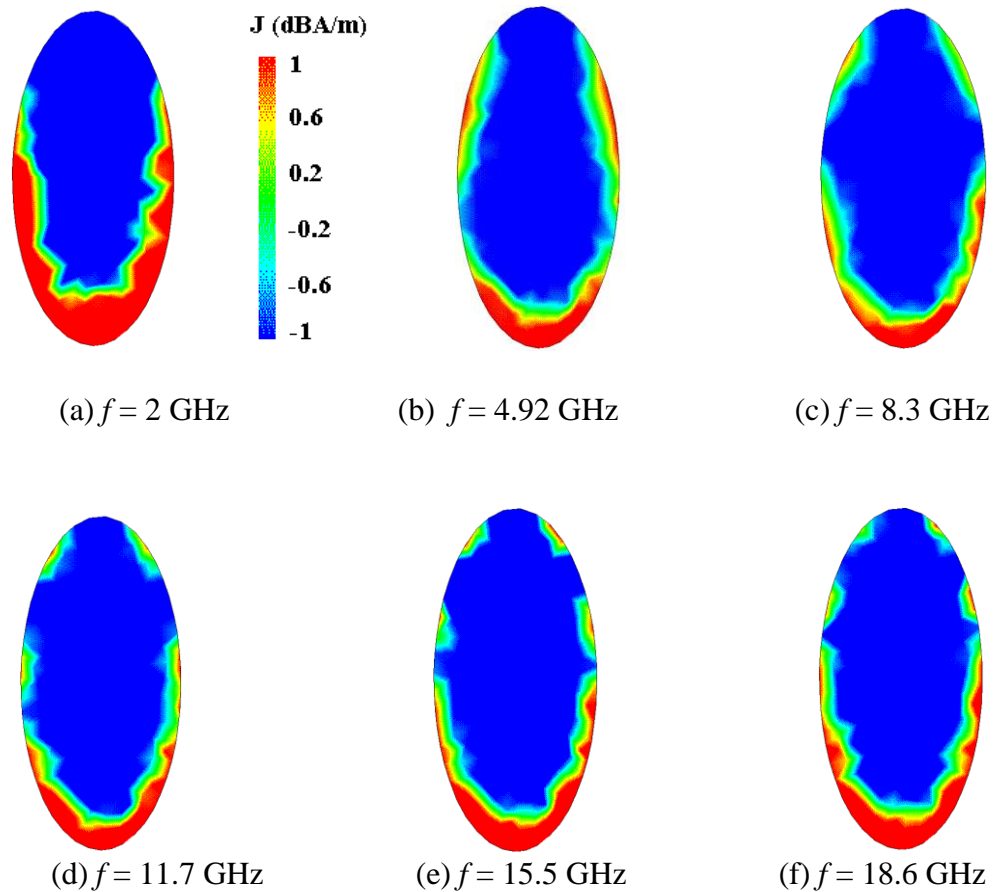


Figure 4.20 Current distribution on the monopole antenna at different resonant frequencies.

introduced useful in wideband and UWB applications. By inserting a short cylinder around the monopole, as seen in Figure 4.22, some new CNRs are added to the antenna structure. The resonant modes of the antenna can be totally categorized by coaxial and monopole modes. The coaxial modes are the TEM resonant modes of the open-ended coaxial line comprised of the monopole as the inner conductor and surrounding cylinder as outer conductor. On the other hand, the monopole modes are the resonant modes of the combination of monopole and the ground plane.

Figure 4.23 shows the reflection coefficient of the antenna for an infinitely thin monopole and  $s=0.4$  mm,  $d=20$  mm and different values of  $h$ . Comparing to the reflection coefficient of the monopole antenna seen in Figure 4.8b, there is a resonant frequency in between the first and third resonances of the monopole. This resonance frequency is strongly dependent on the length ( $h$ ) and the width ( $s$ ) of the cylinder around the monopole. By increasing the length of the coax,  $h$ , its

corresponding resonant frequency decreases. By choosing  $W = 0$  in our simulations, it is possible to study the electric current on the monopole more clearly.

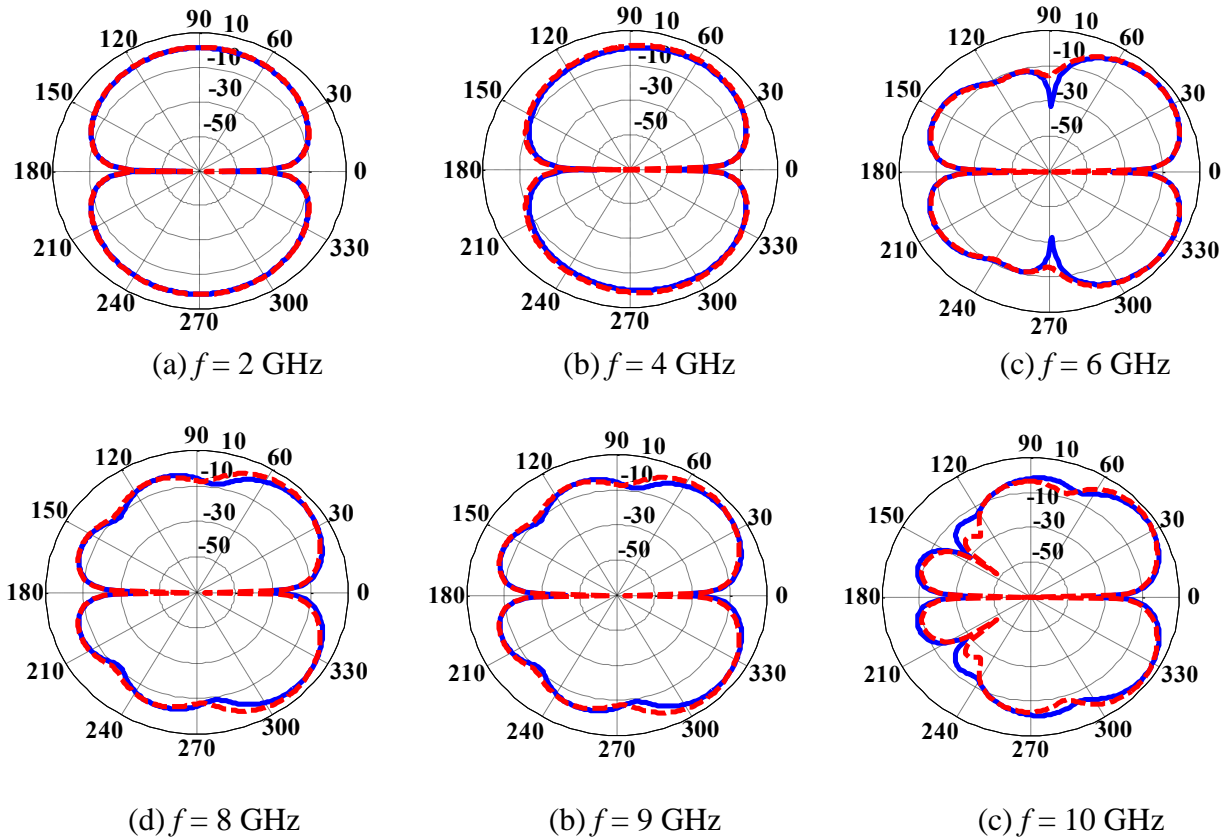


Figure 4.21 Radiation gain of the monopole antenna at different resonant frequencies. (Solid line:  $\varphi = 0$  and dashed line:  $\varphi = 90^\circ$ )

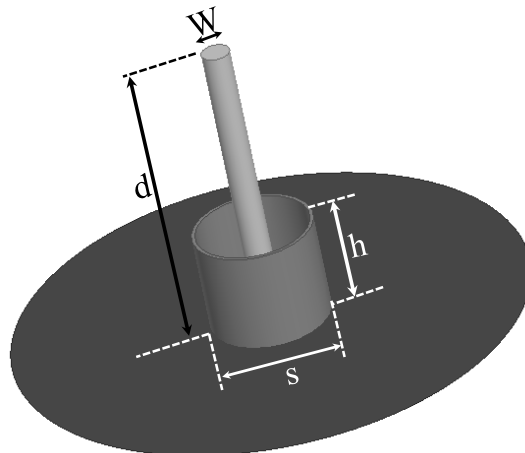


Figure 4.22 A monopole antenna surrounded by short cylinder as a wideband /UWB element.

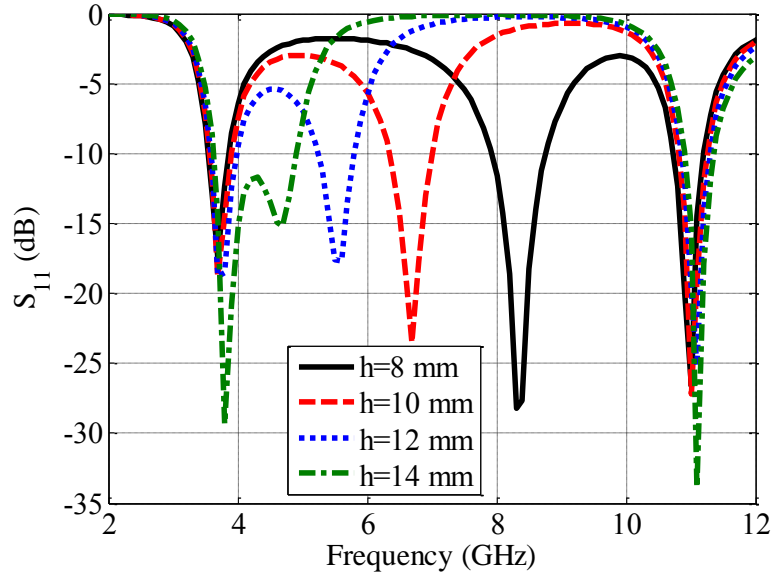


Figure 4.23 Reflection coefficient of the antenna for different values of  $h$ .

In Figure 4.24, the magnitude of the current on the monopole part of the antenna is shown at three resonant frequencies of the antenna. At first and third resonant frequencies,  $f = 3.7$  GHz and  $f = 11.1$  GHz, the current is well-matched with the current distribution on the monopole antenna (without surrounding cylinder). While, the current distribution at  $f = 7.1$  GHz is affected by the presence of the cylinder around it. As can be seen, there is a discontinuity in the current distribution at  $z = 10$  mm, cylinder height. The current on the monopole at the resonant frequency of the coaxial mode of the antenna is depicted in Figure 4.25a for  $h = 8$  mm and  $h = 14$  mm. This current can be separated into two parts: resonant mode and radiation mode. These two modes are shown in Figure 4.25b. The resonant mode is the quarter-wavelength resonance of the coaxial transmission line, as the figure shows. By continuing the current, it crosses the  $z$ -axis at quarter wavelength which is higher than  $h$  due to the parasitic effects at the end of the coax. As an example, the current distribution (Figure 4.25a) for  $h = 8$  mm, has a discontinuity exactly at  $z = 8$  mm and the resonant mode of the current crosses the  $z$ -axis at  $z = 9$  mm, which is associated with the resonant frequency of  $f = 8.33$  GHz. By increasing the length of the cylinder to  $h = 14$  mm, the crossing point of the resonant mode of the current with  $z$ -axis is  $z = 17$  mm, which is associated with  $f = 6.4$  GHz.

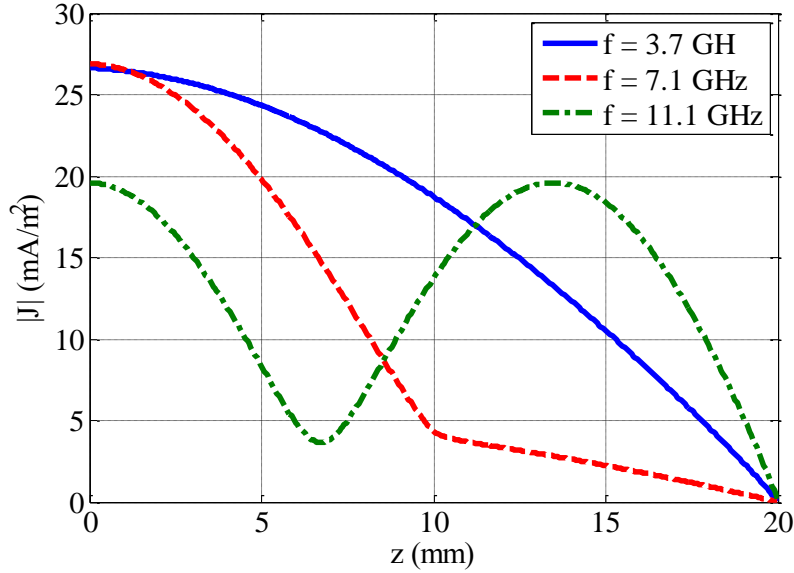


Figure 4.24 The current distribution on the antenna at three resonant frequencies.

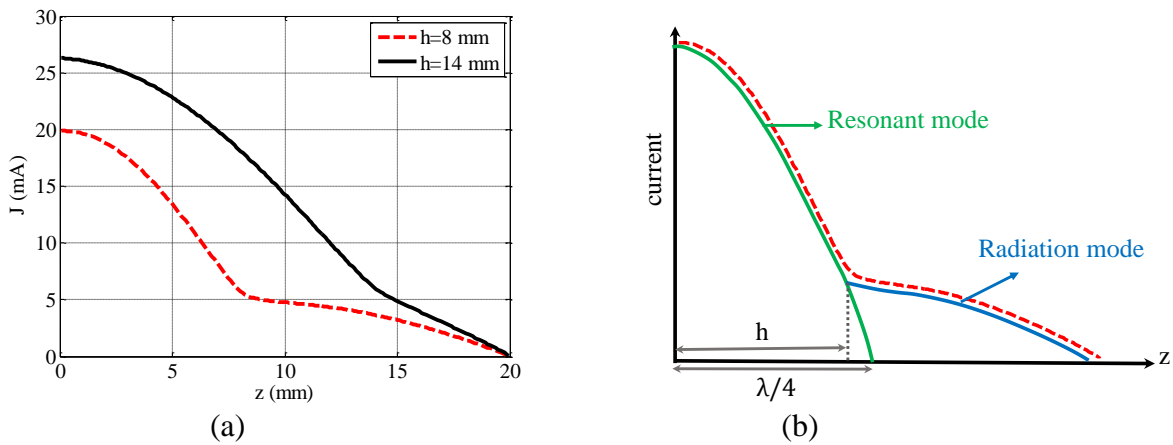


Figure 4.25 The current distribution on the monopole antenna at its coaxial mode resonance for two different values of  $h$ , (b) resonant and radiation modes of current.

According to Figure 4.23, any change in the resonant frequency of the coaxial mode does not change the resonances of the monopole significantly. Figure 4.26 shows the reflection coefficient of the antenna for  $d = 21$  mm,  $h = 12$  mm,  $W = 2$  mm. The calculated  $S_{11}$  is depicted for different values of  $s$ . By changing the value of  $s$ , the intrinsic impedance of the coaxial line changes leading to the change in the input impedance of the antenna and its quality factor at the resonant frequency. As Figure 4.26 shows, the bandwidth of the antenna is 3.5 GHz - 5.5 GHz for  $S_{11} < -10$  dB. The radiation pattern of the antenna is seen in Figure 4.27 at three frequencies for  $s = 12$  mm. As it shows, the radiation pattern changes very slightly in the frequency band. In all cases, the ground

plane is a circular plate of radius 20 mm. By adjusting the resonant frequencies and corresponding damping factors of the CNRs, an ultra-wideband response can be achieved. Figure 4.28 depicts the reflection coefficient of the antenna for two different designs.

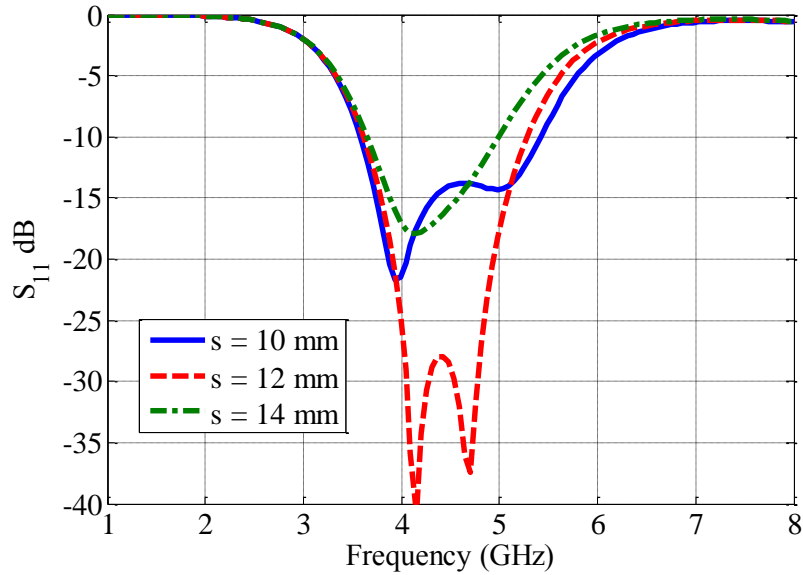


Figure 4.26 Reflection coefficient of the antenna for different values of  $s$ .

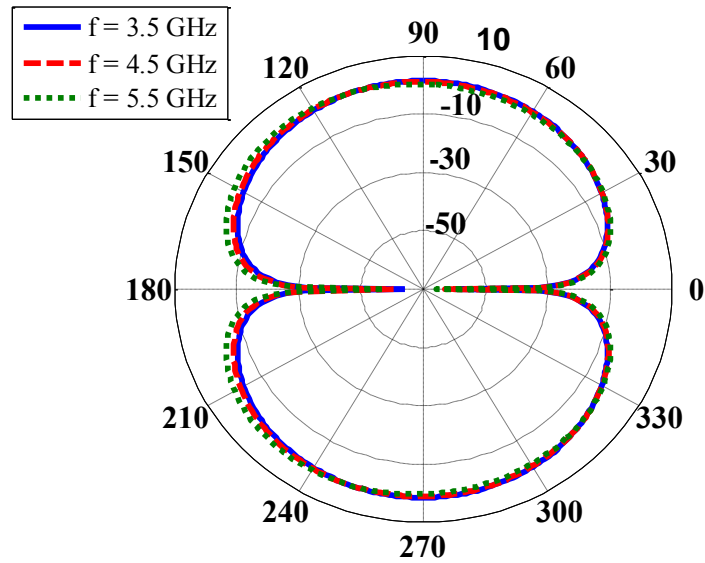


Figure 4.27 The gain of the antenna versus elevation angle at different frequencies for  $h=8$  mm.

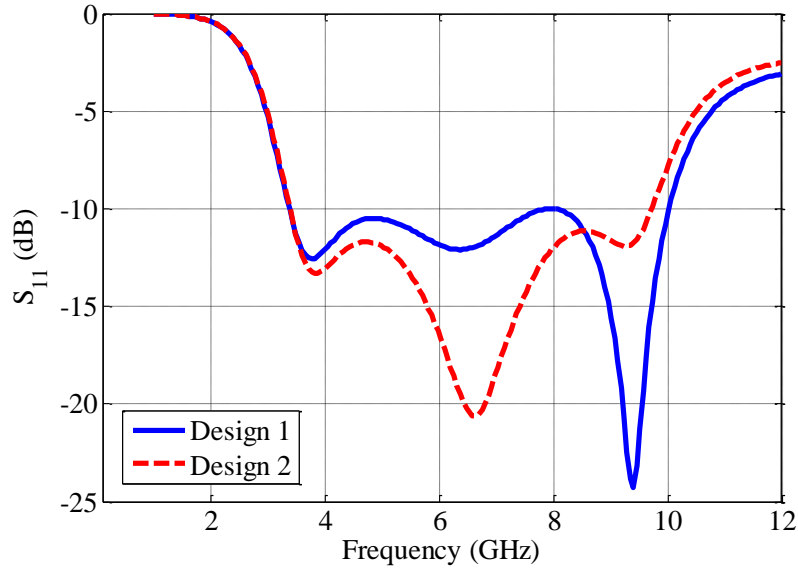


Figure 4.28 Reflection coefficient of the antenna for two different designs. Design 1:  $s = 11$  mm,  $W = 2$  mm,  $h = 5.5$  mm,  $d = 18$  mm, Design 2:  $s = 9$  mm,  $W = 2$  mm,  $h = 5.5$  mm,  $d = 18$  mm

As can be seen, the antenna is matched ( $S_{11} < -10$  dB) for wide range of frequencies. For  $s = 11$  mm, the antenna has wider bandwidth. The far-field gain of the antenna for different frequencies is depicted in Figure 4.29 for design 1. Since the current has some variations in its direction at higher frequencies, there are some nulls in the pattern of the antenna at those frequencies. The pattern of the antenna is omnidirectional because of the symmetry of the antenna structure in  $\varphi$  direction. The radiation field of the antenna in time domain is shown in Figure 4.30a for different directions. The early-time and late-time responses are clearly visible in the time-domain response. For better comparison, the normalized value of the radiated field in far-field is seen in Figure 4.30b for different observation angles. Although the CNRs of the fields do not change with observation angle, but the dispersion characteristics of the antenna change slightly with direction. For higher elevation angles, the antenna is more dispersive. Additionally, there is some ringing originating from the resonant behavior of the antenna. By placing two similar antennas 40 cm away from each other and following the equations (4.13) to (4.16), the amplitude and phase response of  $S_{21}$  are shown in Figure 4.31a and 4.31b. The amplitude and phase of the antenna effective length can be extracted from  $S_{21}$  response for  $\theta = 90^\circ$  and  $\varphi = 0^\circ$ . The effective length of the antenna is useful in calculating the impulse response of the tag in chipless RFID systems. An antenna prototype with dimensions of  $s = 11$  mm,  $W = 2$  mm,  $h = 5.5$  mm,  $d = 18$  mm is fabricated in the VTAG antenna lab.

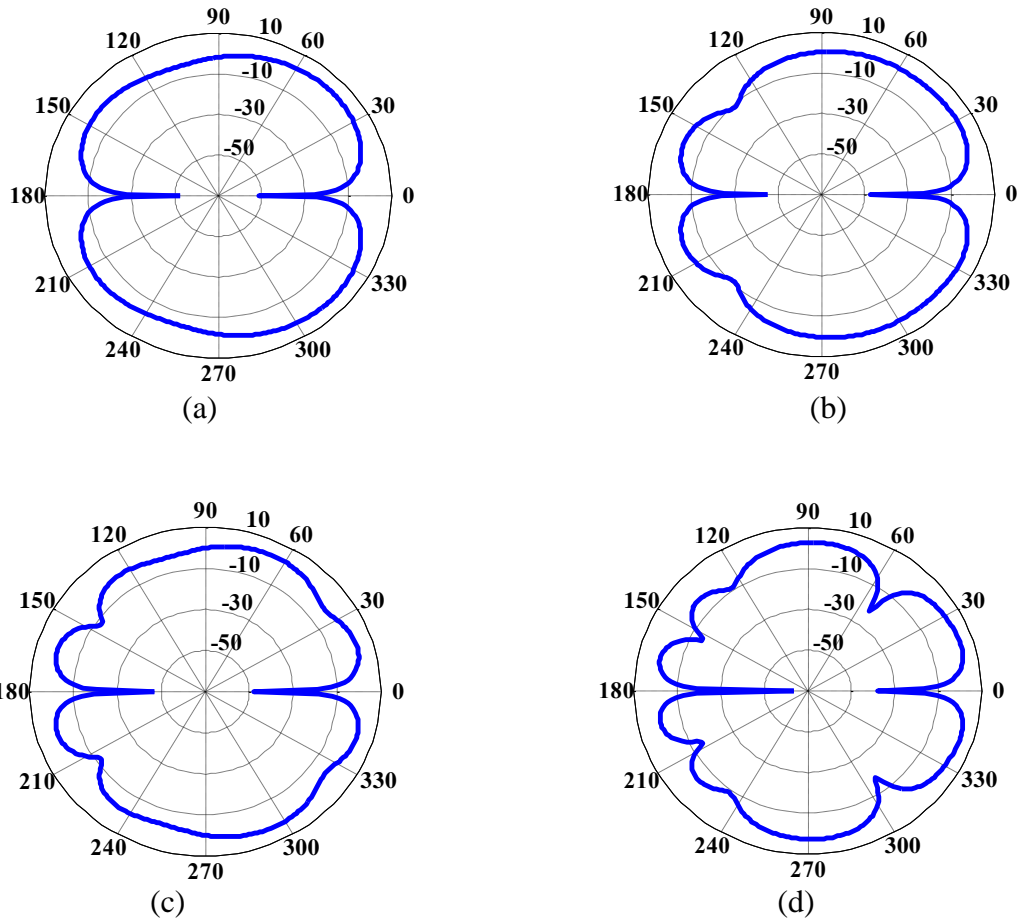


Figure 4.29 Gain of the antenna at (a)  $f = 4$  GHz, (b)  $f = 6$  GHz, (c)  $f = 8$  GHz, and (d)  $f = 10$  GHz.

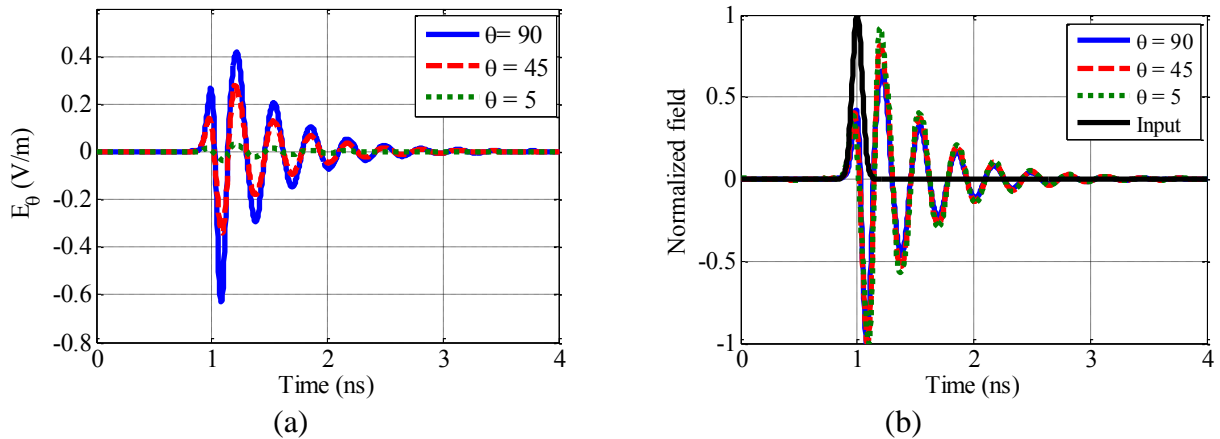


Figure 4.30 (a) The radiation field and (b) normalized radiation field of the antenna in far field.

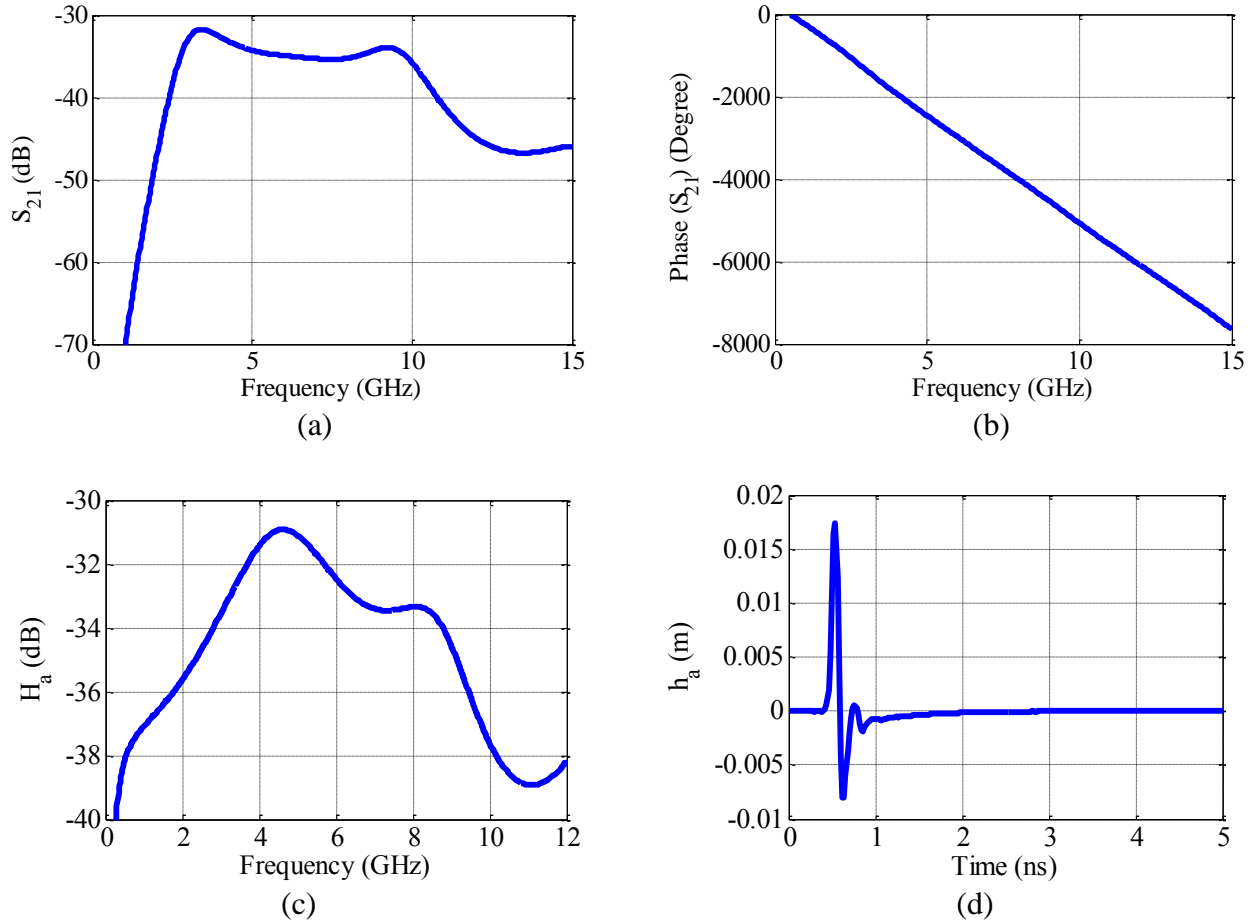


Figure 4.31 (a) amplitude and (b) phase of  $S_{21}$  between two similar antennas when they are spaced 40 cm far from each other, (c) amplitude and (d) phase of the antenna effective length for  $\theta = 90^\circ$  and  $\varphi = 0^\circ$ .

The fabricated antenna is shown in Figure 4.32a. The antenna is connected to Network analyzer (Rohde & Schwarz, ZVA 50-series), as can be seen in Figure 4.32b. The measured reflection coefficient of the antenna is depicted in Figure 4.33. Based on the measured  $S_{11}$ , the antenna shows  $S_{11} < -10$  dB at the desired frequency range of 2.7-10.6 GHz. The radiation pattern of the fabricated antenna is measured in the chamber of Virginia Tech Antenna Group (VTAG). The co-polar and cross-polar radiation pattern of the antenna are shown in Figure 4.34 at different frequencies.

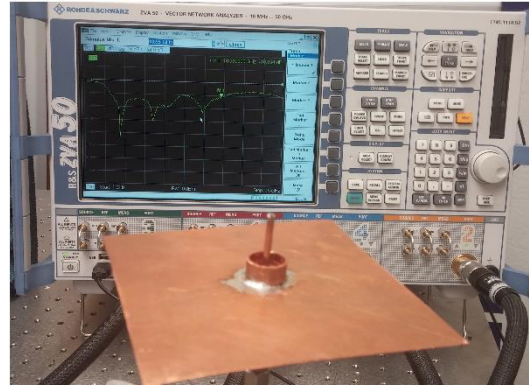


Figure 4.32 (a) Fabricated tag, and (b ) Antenna connected to the network analyzer.

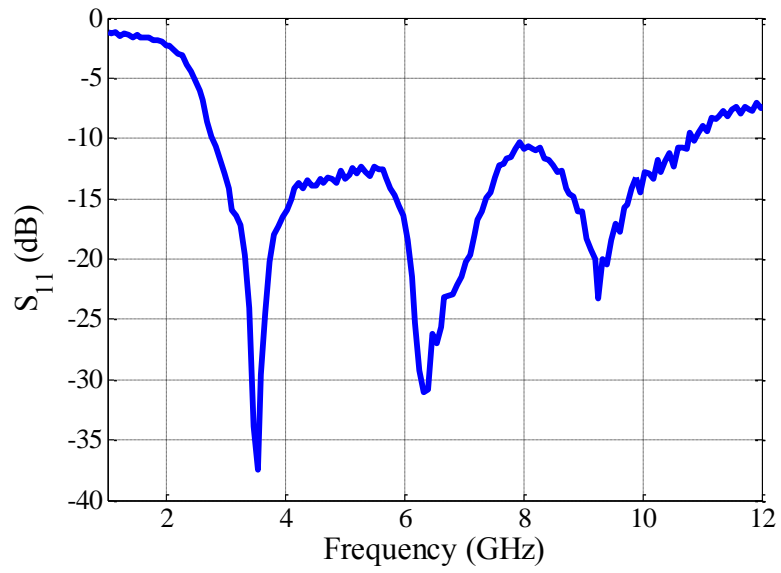


Figure 4.33 Measured reflection coefficient of the antenna.

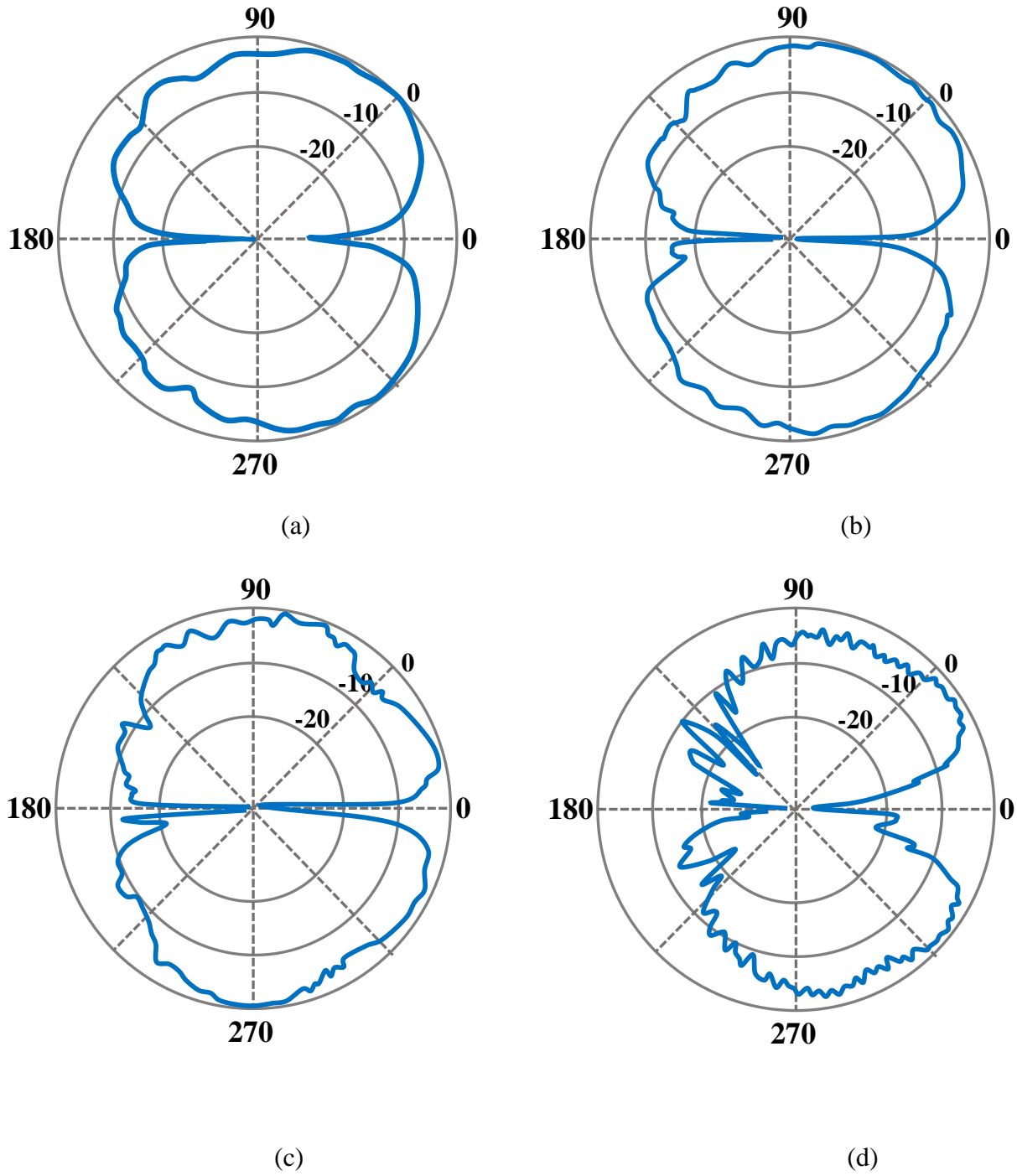


Figure 4.34 Co- and cross polar radiation pattern of the antenna at (a)  $f = 2.7$  GHz, (b)  $f = 4.8$  GHz, (c)  $f = 6.9$  GHz, and (d)  $f = 9$  GHz at  $xz$  and  $yz$  planes.

## 5 Time-Frequency Techniques for Analyzing Transient Scattered Signal from Targets [8] (Chapter used with permission of Springer science and business media, 2015)

Since the scatterer is located at some distances from the receiving antenna, we need a time-frequency analysis technique in order to extract desired spatial and structural information of the target. One important parameter in time-frequency analysis of scattered fields is the resolution of employed technique in time and frequency domains. In circumstances where multiple scatterers or a scatterer with multiple scattering centers is located in the main beam of the receiving antenna, the resolution in time domain is important. While in the cases where the scatterer has multiple resonances in close proximity of each other, the resolution in the frequency domain will be important parameter [63]. Sometimes, we need to employ a time-frequency technique which provides acceptable resolution in both time and frequency domains. As an example, when multiple chipless RFID tags are present in the reader area, good resolution in the time domain improves the accuracy of the localization process and on the other hand, good resolution in the frequency domain enhances the accuracy of the extracted information from the scattered signal. Based on Heisenberg uncertainty principle, there is a restriction on the product of time and frequency resolutions [64]. In this chapter, some practical time-frequency techniques are studied. Starting with most practical one, short-time Fourier transform (STFT), the definitions of time and frequency resolution are presented. Then, the application of wavelet transform in scattering process is presented and its drawbacks are discussed in detail. Re-assigned joint time-frequency (RJTF) method is introduced for improving the frequency resolution. Finally, Short-time matrix pencil method (STMPM) is introduced as an efficient technique and its corresponding resolution in time and frequency is compared with other time-frequency techniques.

### 5.1 Short-Time Fourier Transform (STFT)

Conventional spectral analysis of a signal is based on Fourier transform. The Fourier transform of signal  $x(t)$  is defined as

$$X(f) = \int x(t) e^{-j2\pi ft} dt \quad (5.1)$$

This transformation is useful tool for analyzing the spectral content of the stationary signals and it also simplifies some differential equations by converting the integrations and derivatives to algebraic operations in Fourier domain. The inverse Fourier transform of signal is written by

$$x(t) = \int X(f) e^{j2\pi ft} df \quad (5.2)$$

In practical applications, the signal is unstationary and its spectral contents change with time. The most commonly used time-frequency representation of signal is STFT. In this technique, a sliding window of fixed length is moved along the time axis of the signal and fast Fourier transform (FFT) is applied to each time snapshot. Assuming  $h(t)$  as the window function, the STFT of the signal  $x(t)$  is defined by

$$\begin{aligned} \text{STFT}_x(t, f) &= \int x(\tau) h^*(\tau - t) e^{-j2\pi f\tau} d\tau \\ &= \int X(\nu) H^*(\nu - f) e^{-j2\pi \nu t} d\nu \end{aligned} \quad (5.3)$$

The first equation in (5.3) shows that STFT can be thought of as a local spectral of the windowed signal. The second equation shows that the window can be applied in the frequency domain. In this view, STFT performs as a filter sliding in the frequency domain. One useful window function usually used in practical applications is the Gaussian function defined as

$$h(t) = \frac{1}{\sqrt{\delta}} e^{-\pi(t/\delta)^2} \quad (5.4)$$

where  $\delta$  is related to the standard deviation of the pulse. As an example, time-domain signal in (5.5) is considered.

$$x(t) = \begin{cases} A \sin(2\pi f_1 t) e^{-\alpha_1 t} & t \leq t_0 \\ A \sin(2\pi f_1 t) e^{-\alpha_1 t} + B \sin(2\pi f_2 t) e^{-\alpha_2(t-t_0)} & t_0 \leq t \end{cases} \quad (5.5)$$

This signal can be regarded as the scattered field from two single-resonance scatterers located at different distances from the antenna, regardless of the early-time responses. The signal is shown in Figure 5.1 for  $A = 3$ ,  $\alpha_1 = 0.5e9$ ,  $\alpha_2 = 0.8e9$ ,  $B = 3$ ,  $f_1 = 6$  GHz, and  $f_2 = 7$  GHz. The spectrogram of the signal is depicted in Figure 5.2 by applying Gaussian window defined in (5.4) to (5.5) for two values of  $\delta$ . By changing the variance of the Gaussian window, its width changes, which leads

to the change in the resolution in time and frequency domains. By choosing  $\delta = 1$  (narrower window in time domain), the time resolution is improved and as a result, the turn-on times of the resonant frequencies can be seen in the spectrogram; while the close resonant frequencies are not distinguishable in the spectrogram. On the other hand, by choosing  $\delta = 1$ , the frequency resolution is enhanced at the expense of deterioration of time resolution. Hence, the resolution of the transformed signal is strongly dependent on the window function. For better illustration, the time-domain signal of  $x(t) = \delta(t - t_0) + e^{-j2\pi f_0 t}$  is considered [65]. By applying STFT with the Gaussian function of  $\delta$  to the time-domain signal, the transformed signal is given by

$$\text{STFT}_x(t, f) = \frac{1}{\sqrt{\delta}} e^{-\pi(t-t_0)^2/\delta^2} e^{-j2\pi f t_0} + \sqrt{\delta} e^{-\pi\delta^2(f-f_0)^2} e^{-j2\pi(f-f_0)t} \quad (5.6)$$

The transformed signal seen in (5.6) shows clearly the effect of  $\delta$  on the resolution in time and frequency. It is desirable the STFT to be concentrated around  $t = t_0$  and  $f = f_0$ , because the signal includes an impulse at time  $t_0$  and an impulse at frequency  $f_0$ . But, the STFT of the signal has two pulses around  $t=t_0$  and  $f=f_0$ . As (5.6) shows, any increase in  $\delta$  improves the frequency resolution and deteriorates the time resolution and vice versa. Therefore, by choosing  $\delta$  in between these two limits, one has limited resolution in time and frequency.

### 5.1.1 Resolution

It is more desirable to quantify the concept of the resolution in time and frequency domains. The time resolution,  $\Delta t$  of the window function,  $h(t)$  is defined by

$$\Delta t^2 = \frac{\int t^2 |h(t)|^2 dt}{\int |h(t)|^2 dt} \quad (5.7)$$

It means that two pulses can be distinguished in time domain if they are more than  $\Delta t$  apart [65]. Similarly, the frequency resolution is defined by

$$\Delta \omega^2 = \frac{\int \omega^2 |H(\omega)|^2 d\omega}{\int |H(\omega)|^2 d\omega} \quad (5.8)$$

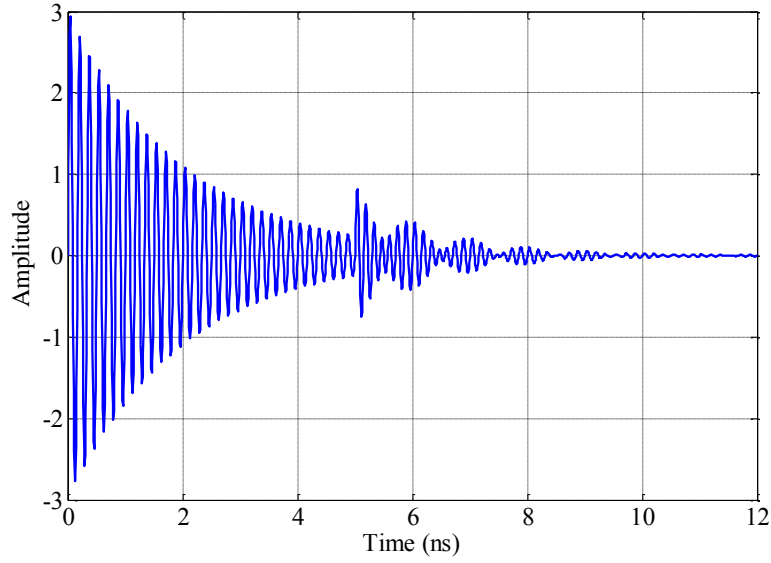


Figure 5.1 Time-domain signal.

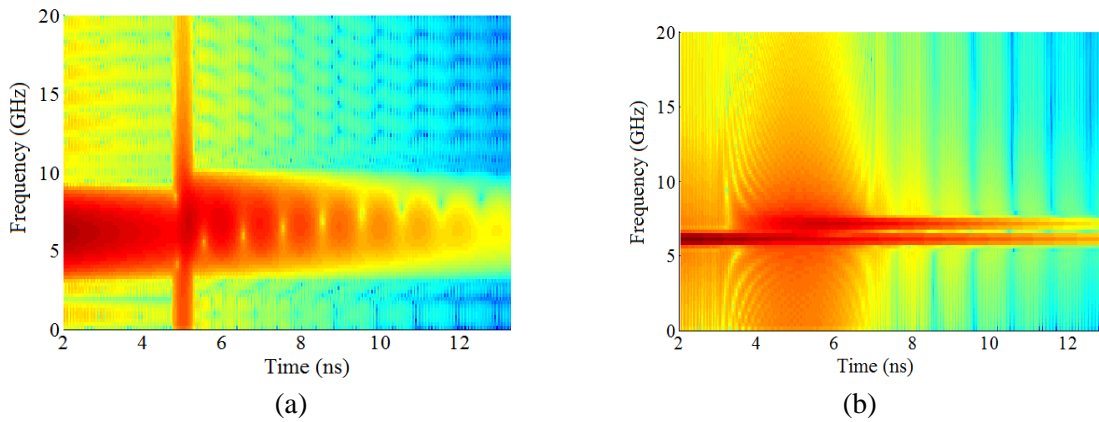


Figure 5.2 Spectrogram of the signal for (a)  $\delta = 0.8e-9$ , and (b)  $\delta = 4e-9$

Two frequencies can be discriminated in the frequency domain if they are more than  $\Delta\omega$  apart. There is an intrinsic limitation on the time and frequency resolutions, which is governed by Heisenberg principle as

$$\Delta t \cdot \Delta\omega \geq \frac{1}{2} \quad (5.9)$$

For Gaussian window defined in (5.4), the time and frequency resolutions are as  $\Delta t^2 = \frac{\delta^2}{2}$  and

$$\Delta\omega^2 = \frac{1}{2\delta^2} .$$

## 5.2 Wavelet Transform

As another time-frequency technique, wavelet transforms are widely being used in signal processing. In STFT analysis of a signal, the length of the window is fixed in whole time-frequency plane leading to fixed time and frequency resolutions. The wavelet transform of  $x(t)$ , a square-integrable function, is defined by

$$W_x(s, \tau) = \int x(t) h_{s, \tau}^*(t) dt \quad (5.10)$$

where asterisk denotes the complex conjugates. The wavelets are generated from a mother wavelet,  $h$ , as

$$h_{s, \tau}(t) = \frac{1}{\sqrt{s}} h\left(\frac{t - \tau}{s}\right) \quad (5.11)$$

where  $s$  and  $\tau$  are the scale and translation factor. The dimension of  $s$  is Hz. The wavelet transform of signal  $x(t)$  is the trajectory of the signal into the wavelet basis functions with different translation and scale factors. The wavelets are dilated as  $s > 1$  and are contracted when  $s < 1$ . By normalizing the wavelet basis as (5.11), their energy is equal to 1 for any translation and scale. The wavelet transform of the signal can also be written versus the Fourier transforms of the signal and window function as

$$W_x(s, \tau) = \frac{\sqrt{s}}{2\pi} \int X(\omega) H^*(s\omega) e^{j\omega\tau} d\omega \quad (5.12)$$

where  $H$  is the Fourier transform of  $h(t)$ . In this view, the wavelet transform can be assumed as a bank of wavelet filters with different scales and shifts corresponding to  $e^{j\omega\tau}$ . As (5.12) shows, the wavelet transform of a signal depends on the wavelet basis,  $h$ . Various wavelet functions are introduced for different applications. There are some conditions which wavelets should satisfy among them admissibility and regulatory properties are the most important. Satisfying these two conditions, one can make his own wavelet for a special application. As an important property, no information should be lost during the transformation. This can be expressed by the following resolution of identity for two arbitrary functions of  $f_1$  and  $f_2$  [65].

$$\int \int \langle f_1, h_{s,\tau} \rangle \langle f_2, h_{s,\tau} \rangle d\tau \cdot d\left(\frac{1}{s}\right) = c \langle f_1, f_2 \rangle \quad (5.13)$$

where  $\langle f, h \rangle$  shows the inner product of function  $f$  and wavelet  $h$  and  $c$  is a constant. It is easy to show that

$$c = -\int |H(\omega)|^2 \frac{d\omega}{|\omega|} \quad (5.14)$$

Relation (5.14) implies that the integration of the inner products of  $h$  with  $f_1$  and  $f_2$  over all the scaling and translation parameters is proportional to the inner of the two functions. By removing  $f_2$  from the two sides of (5.13), the inverse wavelet transform can be written by

$$x(t) = \frac{-1}{c} \int \int \frac{1}{\sqrt{s}} W_x(s, \tau) h\left(\frac{t-\tau}{s}\right) d\tau \cdot d\left(\frac{1}{s}\right) \quad (5.15)$$

Therefore, the time-domain signal can be recovered from its wavelet transform. It implies that no information will be lost during the transformation process. The constant value of  $c$  implies that  $H(0) = 0$ , or equivalently

$$\int h(t) dt = 0 \quad (5.16)$$

The condition (5.16) which guarantees the oscillatory behavior of the wavelet function is called admissibility property. The weaker condition on wavelet is regularity condition, which implies that wavelet should be local in time and frequency domains. Assuming  $\tau = 0$  and expanding signal  $x(t)$  into the Taylor series at  $t = 0$ , one has [65]

$$W_x(s, 0) = \frac{1}{\sqrt{s}} \left[ \sum_{n=0}^N x^{(n)}(0) \int \frac{t^n}{n!} h\left(\frac{t}{s}\right) dt + \int R(t) h\left(\frac{t}{s}\right) dt \right] \quad (5.17)$$

where  $R$  is the reminder of the Taylor series. The  $r$ -order moment of the wavelet is written by

$$M_r = \int t^r h(t) dt \quad (5.18)$$

By change of variables in the integrals in (5.17) and using (5.18), the wavelet transform at  $\tau = 0$  is written by

$$W_x(s,0) = \frac{1}{\sqrt{s}} \left[ x(0)M_0s + \frac{f'(0)}{1!}M_1s^2 + \dots + \frac{f^{(n)}(0)}{n!}M_ns^{n+1} + \mathcal{O}(s^{n+2}) \right] \quad (5.19)$$

Based on the admissibility property,  $M_0 = 0$ . Therefore, the speed of converge of the above series with decreasing  $s$  is determined by the first non-zero term in the series. The  $n$ -order wavelet is one which its first  $n$ -order moments are zero.

$$M_n = \int t^n h(t) dt = 0 \quad (5.20)$$

or equivalently in the Fourier domain, one can write

$$H^{(n)}(0) = 0 \quad (5.21)$$

This condition exhibits the smoothness of the wavelet at  $f = 0$ . For the wavelet of order  $n$ , wavelet transform is decayed by  $s^{n+1/2}$ . Additionally, it has first  $n+1$  vanishing moments decaying by  $t^n$ . Therefore, the wavelet transform is an oscillatory function which is localized in both time and frequency domains. In comparison to STFT, by choosing small value of the scale, the wavelet analysis permits to analyze the discontinuities, singularities and edges in more detail and it gives the global view of the signal for large scales. This property of the wavelet is depicted in Figure 5. 3. As it shows, for larger scales corresponding to low frequencies, the wavelet is dilated and for smaller scales, it contracted. The bandwidth of wavelet at scale  $s$  is

$$(\Delta\omega)_s^2 = \frac{\int \omega |H(s\omega)|^2 d\omega}{\int |H(s\omega)|^2 d\omega} = \frac{(\Delta\omega)^2}{s^2} \quad (5.22)$$

Therefore, its quality factor is defined as

$$Q = \frac{1/s}{(\Delta\omega)_s} = \frac{1}{\Delta\omega} \quad (5.23)$$

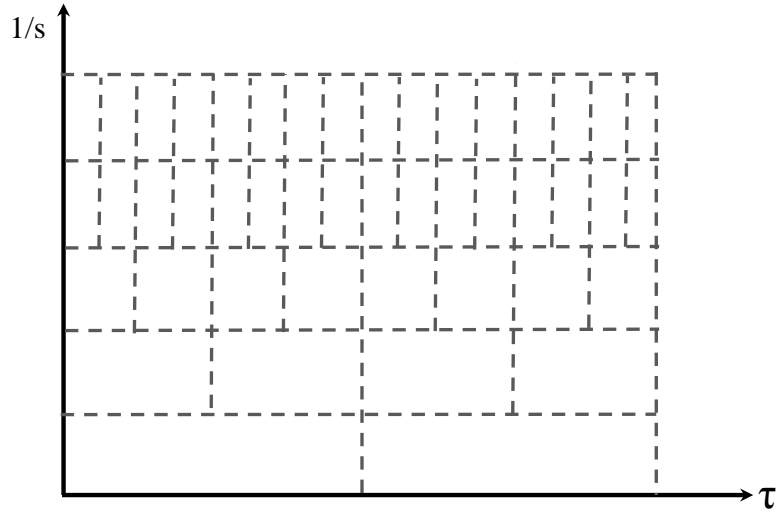


Figure 5.3 Time and frequency resolutions in wavelet transform.

Hence, the wavelet transform is constant-Q analysis. For low frequencies, it has small bandwidth or wider time window. On the other hand, for high frequencies (low scales), it adopts larger bandwidth leading to the smaller time window. As an example, the signal in (5.4) is considered. The wavelet transform of the signal is depicted in Figure 5.4 by using Morlet basis function. It is seen that around  $s = 100$  corresponding to the resonant frequency of the signal, the wavelet transform has stronger value. In multi-resonant signals when the resonances are close to each other, the detection of the resonances using wavelet transform is not easy. However, in the processing of the scattered signals from resonant-based targets, one needs much better resolution in time and frequency in order to extract the required data from the signal. Some wavelet families have been introduced for time-frequency analysis of different types of signals. Figure 5.5 shows some practical wavelets. One can choose the desired wavelet based on the shape of the signal. Some approaches such as Wigner-Vile, adaptive time-frequency representation and so on were introduced for enhancing the resolution in both time and frequency domains [63]. In most of the proposed technique, some interferences presented in the time-frequency which are not suitable for analyzing of scattered signal from resonant-based structures.

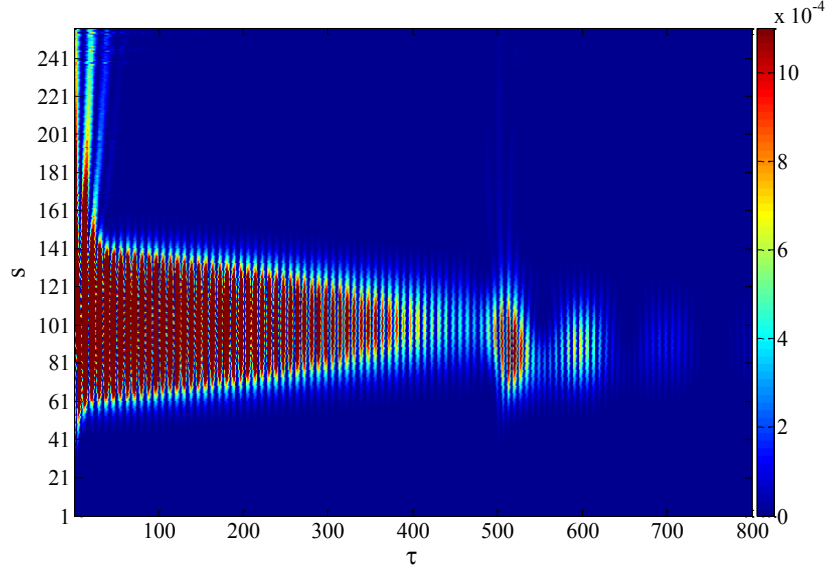


Figure 5.4 Wavelet transform of the signal.

### 5.3 Re-assigned Joint Time-Frequency (RJTF)

In previous sections, two commonly used techniques for time-frequency analysis of time-domain signals were studied. In both techniques, as (5.3) and (5.10) show, the transformed signal depends on the characteristics of the window function. In these approaches, the amplitude of the transformed signal is plotted in a time-frequency plane. In general, each time-varying signal can be expressed in time and frequency by

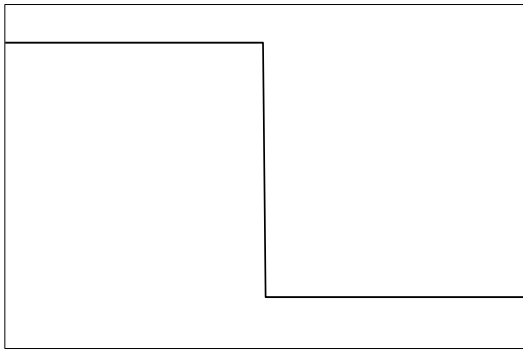
$$x(t) = a(t)\exp(j\phi(t)) \quad (5.24)$$

$$X(f) = A(f)\exp(j\phi(f)) \quad (5.25)$$

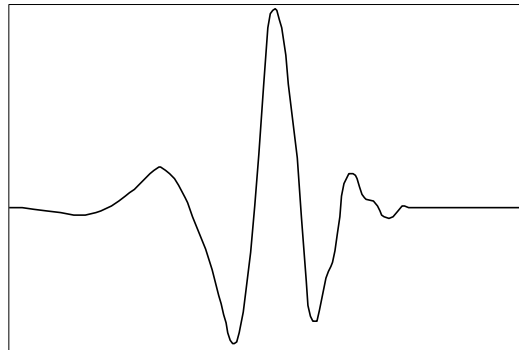
where  $X$  is the Fourier transform of  $x$  and  $a$  and  $A$  are real positive quantities. The instantaneous frequency and the group delay of a signal are one-dimensional transformations trying to represent the temporal and spectral signal characteristics simultaneously. For the signal shown in (4.24) and (2.25), these parameters are calculated as

$$f_i = \frac{1}{2\pi} \frac{d\phi(t)}{dt} \quad (5.26)$$

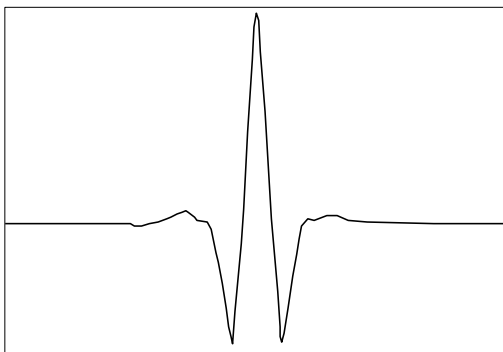
$$t_g = \frac{1}{2\pi} \frac{d\phi(f)}{df} \quad (5.27)$$



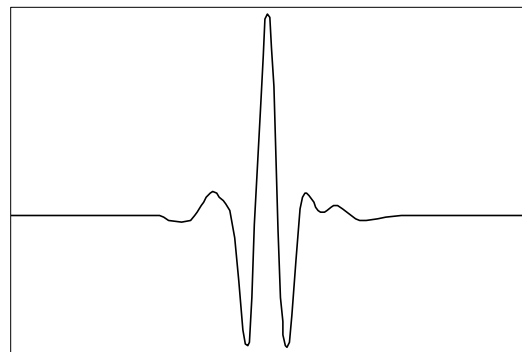
(a) Haar



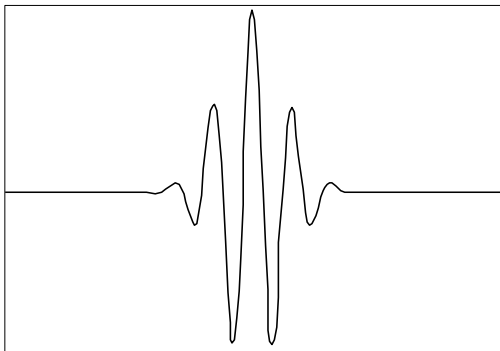
(b) Db4



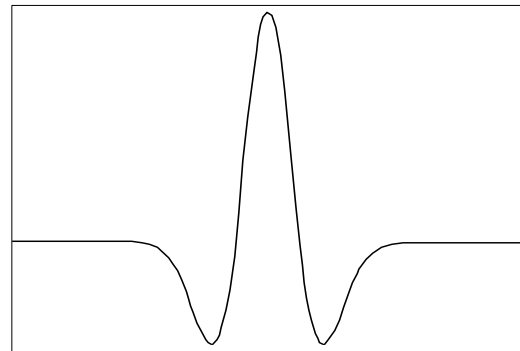
(c) Coeflet2



(d) Sym4



(e) Morlet



(f) Mexican Hat

Figure 5.5 Some practical wavelets.

These time-frequency representations provide some drawbacks for multi-resonant signals. Assuming the following signal [66]

$$x(t) = e^{j2\pi f_1 t} + e^{j2\pi f_2 t} \quad (5.28)$$

With some mathematical manipulations, it is easy to show that the instantaneous frequency of the signal is  $(f_1+f_2)/2$ . One can find so many signals with the same instantaneous frequency.

In order to study the effect of window function, we start with some simple cases. In the first group which is called amplitude maximum of the spectrum (MS), a window of length  $\Delta t$  is moved along the time axis and the spectrum of the widowed signal is calculated versus time index. Assuming the rectangular pulse as the window function located at  $t=t_0$ , then the spectrum of the signal is

$$S(t_0, f) = \int_{t_0-\Delta t/2}^{t_0+\Delta t/2} a(t) \exp[j\varphi(t) - j2\pi f t] dt \quad (5.29)$$

We consider two limits of  $\Delta t$  in the calculation of S. In the first case,  $\Delta t \rightarrow 0$ , then

$$S(t_0, f) = a(t_0) \int_{t_0-\Delta t/2}^{t_0+\Delta t/2} \exp[j\varphi(t) - j2\pi f t] dt \quad (5.30)$$

Therefore, quantity S is maximum at the frequency for which the phase is stationary as

$$f_m = \frac{1}{2\pi} \left. \frac{d\varphi(t)}{dt} \right|_{t_0} \quad (5.31)$$

which is the instantaneous frequency of the signal. For  $\Delta t \rightarrow +\infty$ ,  $S(t_0, f) = X(f)$  which is a line parallel to the time axis in the time-frequency plane.

The second case is related to the second equation seen in (5.3), which is called the maximum envelope method (ME). In this method, a rectangular pulse of width  $f_0-\Delta f/2$  to  $f_0+\Delta f/2$  in the frequency domain moves along the frequency axis and inverse Fourier transform (IFFT) is applied to each windowed signal as

$$S(t, f_0) = \int_{f_0-\Delta f/2}^{f_0+\Delta f/2} X(f) \exp[j2\pi f t] df \quad (5.32)$$

For  $\Delta f \rightarrow 0$ , the time at which S has a maximum is given by

$$t_m = - \left. \frac{1}{2\pi} \frac{d\phi(f)}{df} \right|_{f_0} \quad (5.33)$$

which is the group delay time as a function of frequency. For  $\Delta f \rightarrow +\infty$ ,  $S(t, f_0) = x(t)$  is a line parallel to the frequency axis in the time-frequency plane. Hence, it is seen that in these two cases the transformed signal in the time-frequency axis depends strongly on the length of the window chosen in time or frequency domains. In the third case, the energy distribution can be calculated for  $(t_0, f_0)$ . Assuming

$$S(t_0, f_0) = \int_{f_0 - \Delta f/2}^{f_0 + \Delta f/2} X(f) \exp[j2\pi f t_0] df \quad (5.34)$$

The integrated energy distribution at  $(t_0, f_0)$  is  $|X(f_0)\Delta f|^2$ . It is easy to show that the energy distribution is independent of  $t_0$  for  $\Delta f \rightarrow 0$  and is equal to  $x(t_0)$  for  $\Delta f \rightarrow +\infty$ .

In all above mentioned time-frequency analysis techniques including STFT, the transformed signal is written by

$$X(\tau, f) = \int x(t) h_{\tau, f}^*(t) dt \quad (5.35)$$

The original signal can be recovered from

$$x(t) = \int \int X(\tau, f) h_{\tau, f}(t) d\tau \cdot df \quad (5.36)$$

There is an infinity of manners for defining  $h$ ; here we chose

$$h_{\tau, f}(t) = g(\tau - t) e^{j2\pi f(t - \tau)} \quad (5.37)$$

Assuming

$$\int |g(t)|^2 dt = 1 \quad (5.38)$$

By inserting (5.37) in (5.35), the transformed signal is given by

$$\begin{aligned} X(\tau, f) &= e^{j2\pi f \tau} \int x(t) g(\tau - t) e^{-j2\pi f t} dt \\ &= A(\tau, f) e^{j\phi(\tau, f)} \end{aligned} \quad (5.39)$$

Hence, the original signal can be reconstructed as

$$x(t) = \int \int A(\tau, f) \cdot g(\tau - t) e^{[j\phi(\tau, f) + j2\pi(ft - f\tau)]} d\tau \cdot df \quad (5.40)$$

If the time variations of  $A$  and  $g$  are slow compared to phase variations, the maximum contribution to the integral emanates from the regions close to the stationary conditions as

$$\frac{\partial}{\partial \tau} e^{[j\phi(\tau, f) + j2\pi(ft - f\tau)]} = 0 \quad (5.41)$$

$$\frac{\partial}{\partial f} e^{[j\phi(\tau, f) + j2\pi(ft - f\tau)]} = 0 \quad (5.42)$$

The stationary-phase points are

$$t' = \tau - \frac{1}{2\pi} \frac{\partial \phi(\tau, f)}{\partial f} \quad (5.43)$$

$$f' = \frac{1}{2\pi} \frac{\partial \phi(\tau, f)}{\partial \tau} \quad (5.44)$$

which are related to group delay and instantaneous frequency of the filtered signal. In re-assigned joint time-frequency (RJTF), the energy density  $S(\tau, f)$  is assigned to the point of coordinates  $(t', f')$  instead of  $(\tau, f)$ . Now, the effect of the window length on the transformed signal can be explored with subject to (5.34). For  $\Delta f \rightarrow 0$ , using (5.43) and (5.44), one obtains

$$t' = -\frac{1}{2\pi} \frac{\partial \arg\{X(f_0)\}}{\partial f_0} \quad (5.45)$$

$$f' = f_0 \quad (5.46)$$

which is corresponding to the group delay at the frequency  $f_0$  and for  $\Delta f \rightarrow +\infty$ , one has

$$t' = t_0 \quad (5.47)$$

$$f' = \frac{1}{2\pi} \frac{\partial \arg\{x(t_0)\}}{\partial t_0} \quad (5.48)$$

which is the instantaneous frequency at  $t = t_0$ . In RJTF, the distribution energy changes from group delay to instantaneous frequency curves in the time-frequency plane by changing the window length from 0 to  $+\infty$ . Assuming the STFT of the signal  $x(t)$  as

$$X(\tau, \omega) = \int x(t) e^{-\frac{(\tau-t)^2}{2\sigma^2}} e^{+j2\pi f(\tau-t)} dt \quad (5.49)$$

in which the Gaussian pulse has been used as the window function. The instantaneous time and frequency can be calculated from [67]

$$f_{inc} = f + \frac{1}{2\pi\delta} \text{Im} \left\{ \frac{\eta}{X} \right\} \quad (5.50)$$

$$t_{inc} = t + \delta \text{Im} \left\{ \frac{\eta}{X} \right\} \quad (5.51)$$

In Figure 5.5, the time-frequency representation of the signal seen in (5.4) is depicted for  $A=3$ ,  $\alpha_1 = 0.5e9$ ,  $\alpha_2 = 0.8e9$ ,  $B=3$ ,  $f_1 = 6$  GHz, and  $f_2 = 7$  GHz. As it shows, the resonant frequencies and turn-on times of the resonances can be easily seen from its time-frequency representation.

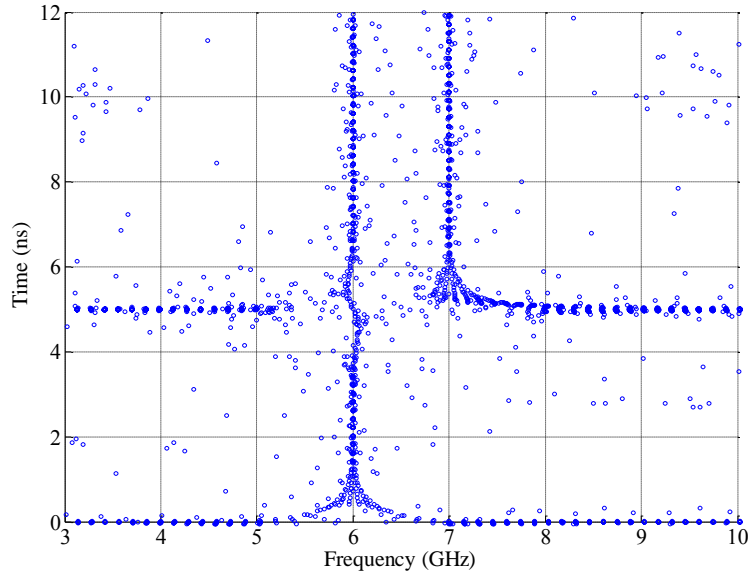


Figure 5.6 Time-frequency representation of signal by RJTF and  $\delta = 0.6e-9$ .

## 5.4 Short-Time Matrix Pencil Method (STMPM)

Based on singularity expansion method (SEM) expressed in section 2.1, the backscattered response from scatterers can be expanded versus the complex natural resonances. For complex scatterers with multiple scattering centers and multiple resonances, different resonant frequencies might have

different turn-on times. Depending on the polarization and the direction of the incident field compared to the scatterer, some resonances might be excited stronger than the others. In these applications, there are two important factors need to be considered in the time-frequency representation of the signal. First as mentioned before, time and frequency resolutions should be improved in order to extract the position of the scatterer and its resonant frequencies. The other factor is the robustness of the employed approach in extracting the weak resonances in the presence of the stronger ones. Recently, another time-frequency method, called short-time matrix pencil method (STMPM), is proposed which shows good performance as a view of resolution and ability to extract low energy resonances. In reality, there is a unique damping factor corresponding to each resonant frequency. Therefore, instead of working on the spectral content of the scattered signal in Fourier domain, it is more informative to work on complex natural resonances (CNRs) in Laplace domain. In some scenarios such as design process of resonant-based scatterers, the knowledge of the damping factors of the resonances give some more information about the structural dimensions and electromagnetic behavior of the scatterer. Taking advantage of STMPM, the damping factors of the CNRs can be obtained from its scattering response. As mentioned in section 2.4, the scattering response from the scatterer is affected by two different phenomena: the early time is due to the specular reflections from the scattering centers of the scatterer and is followed by the-late time response which is the radiation fields from the natural modes of the scatterer. In general, the scattered field can be written as

$$s(t) = e(t) + \sum_{n=1} R_n e^{-\alpha_n t} \cos(\omega_n t + \varphi_n) \quad (5.52)$$

where  $e(t)$  is the early-time response and the late-time response is expanded versus the natural resonances of the scatterer as  $s_n = \alpha_n + j\omega_n$  with corresponding residue,  $s_n$ . In 1992, matrix pencil method (MPM) is employed to extract the complex natural resonances of the damped sinusoidal signals [68]. In this technique, by sampling the time-domain signal, two matrices are introduced, which the CNRs are the generalized eigenvalues of their associated pencil.

#### 5.4.1 Matrix Pencil Method (MPM) [68]

MPM is a technique used for extracting the CNRs of the damped sinusoidal signal. First, the late-time response of the scatterer as the summation over damped sinusoidals is considered as

$$y(t) = \sum_{m=1}^M R_m e^{-s_m t} \quad (5.53)$$

By sampling the signal, the  $k^{\text{th}}$  sample is

$$y(t_k) = \sum_{m=1}^M R_m e^{-s_m t_k} \quad (5.54)$$

where

$$z_n = e^{s_n \Delta t} \quad (5.55)$$

Quantity  $M$  is the number of the poles in the signal,  $k=0, 1, \dots, N-1$  is the sample index and  $\Delta t$  is the sampling interval. Ignoring the noise, two following matrices are formed by sampling data.

$$[Y_1] = \begin{bmatrix} y(0) & y(1) & \dots & y(L-1) \\ y(1) & y(2) & \dots & y(L) \\ \vdots & \vdots & \dots & \vdots \\ y(N-L-1) & y(N-L) & \dots & Y(N-2) \end{bmatrix}_{(N-L) \times L} \quad (5.56)$$

$$[Y_2] = \begin{bmatrix} y(1) & y(2) & \dots & y(L) \\ y(2) & y(3) & \dots & y(L+1) \\ \vdots & \vdots & \dots & \vdots \\ y(N-L) & y(N-L+1) & \dots & Y(N-1) \end{bmatrix}_{(N-L) \times L} \quad (5.57)$$

where  $L$  is a number between  $N/3$  and  $N/2$ . Two matrices in (5.56) and (5.57) can be decomposed for an arbitrary  $L < N-1$  in the following manner

$$[Y_1] = [Z_1][R][Z_2] \quad (5.58)$$

$$[Y_2] = [Z_1][R][Z_0][Z_2] \quad (5.59)$$

where  $[Z_0]$  and  $[R]$  are diagonal matrices

$$[Z_0] = \text{diag}[z_1, z_2, \dots, z_N] \quad (5.60)$$

$$[R] = \text{diag}[R_1, R_2, \dots, R_N] \quad (5.61)$$

and

$$[Z_1] = \begin{bmatrix} 1 & 1 & \dots & 1 \\ z_1 & z_2 & \dots & z_M \\ \vdots & \vdots & & \vdots \\ z_1^{(N-L-1)} & z_2^{(N-L-1)} & & z_N^{(N-L-1)} \end{bmatrix}_{(N-L) \times N} \quad (5.62)$$

$$[Z_2] = \begin{bmatrix} 1 & z_1 & \dots & z_1^{L-1} \\ 1 & z_2 & \dots & z_2^{L-1} \\ \vdots & \vdots & & \vdots \\ 1 & z_M & \dots & z_M^{L-1} \end{bmatrix}_{N \times L} \quad (5.63)$$

By constituting the following matrix pencil as

$$[Y_2] - \lambda[Y_1] = [Z_1][R]\{[Z_0] - \lambda[I]\}[Z_2] \quad (4.64)$$

where  $[I]$  is an  $N \times N$  identity matrix, it is easy to show the  $i^{\text{th}}$  row of  $\{[Z_0] - \lambda[I]\}$  is zero for  $\lambda = z_i$  ( $i = 1, \dots, N$ ). Therefore,  $z_i$  is the generalized eigenvalue of the matrix pair  $[Y_2], [Y_1]$ . Thus, the  $z_i$ s are calculated by solving the following ordinary eigenvalue problem.

$$\{[Y_1]^+ [Y_2] - \lambda[I]\} \quad (5.65)$$

where  $[Y_1]^+$  is the Moore-Penrose pseudo-inverse of  $[Y_1]$ .

For noisy data, some prefiltering must be used in order to remove extra poles resulting from noise. In this case, first the following matrix is formed using sampled data as

$$[Y] = \begin{bmatrix} y(0) & y(1) & \dots & y(L) \\ y(1) & y(2) & \dots & y(L+1) \\ \vdots & \vdots & & \vdots \\ y(N-L-1) & y(N-L) & \dots & y(N-L) \end{bmatrix}_{(N-L) \times (L+1)} \quad (5.66)$$

As can be seen,  $[Y_1]$  and  $[Y_2]$  are obtained from  $[Y]$  by removing the last and the first columns, respectively. A singular-value decomposition (SVD) of the matrix  $[Y]$  can be written as

$$[Y] = [U][\Sigma][V]^H \quad (5.67)$$

where  $[U]$  and  $[V]$  are unitary matrices. The parameter  $M$ , estimated number of CNRs in the signal by MPM, is introduced as a threshold and the singular values beyond  $M$  are set to zero. In theory

and noiseless data,  $M$  is equal to the number of CNRs contained in signal. An appropriate way to choose  $M$  is through looking at the ratio of the maximum singular value to all other singular values in the matrix. Considering  $\sigma_c$  as the singular value such that

$$\frac{\sigma_c}{\sigma_{\max}} \approx 10^{-p} \quad (5.68)$$

where  $p$  is the number of significant decimal digits in the data. For instance, if the measurement data is known to be accurate up to three significant digits, then the singular values for which the ratio in (5.68) are less than  $10^{-3}$  are the singular values of measured noise. The chosen value of  $p$  depends strongly on the strength of the weakest pole compared to the strongest one. For low values of  $p$ , the weak poles can not be detected in the presence of the much stronger poles. By increasing the value of  $p$ , the weak poles can be extracted at the expense of arrival of poles from noise. The next step is to construct the filtered matrix  $[V']$ . It is constructed such that it contains only  $M$  dominant right-singular vectors  $[V]$ .

$$[V'] = [v_1, v_2, \dots, v_M] \quad (5.69)$$

Now, by suppressing the singularities corresponding to the noise,  $[Y_1]$  and  $[Y_2]$  can be constructed.

$$[Y_1] = [U][\Sigma'][V_1']^H \quad (5.70)$$

$$[Y_2] = [U][\Sigma'][V_2']^H \quad (5.71)$$

where  $[V_1']$  and  $[V_2']$  are obtained from  $[V]$  by removing the first and last rows and  $[\Sigma']$  is obtained from the  $M^{\text{th}}$  column of  $[\Sigma]$ , corresponding to the  $M$  dominant singular values. Following the same approach as in (5.64), the poles of the signal can be obtained. Once the poles and  $M$  are known, the residues  $R_i$  are found from the following least squares problem.

$$\begin{bmatrix} y(0) \\ y(1) \\ \vdots \\ y(N-1) \end{bmatrix} = \begin{bmatrix} 1 & 1 & \dots & 1 \\ z_1 & z_2 & \dots & z_M \\ \vdots & \vdots & & \vdots \\ z_1^{N-1} & z_2^{N-1} & \dots & z_M^{N-1} \end{bmatrix} \begin{bmatrix} R_1 \\ R_2 \\ \vdots \\ R_M \end{bmatrix} \quad (5.72)$$

### 5.4.2 STMPM in Late-Time

In STMPM, a sliding window of length  $T_w$  is moved along the time axis and matrix pencil method is applied to each windowed signal [69]. Figure 5.7 shows a time-domain signal along with the sliding window located at  $t = T$ . As a simple scatterer, consider the late-time response of the signal seen in (5.73).

$$L(t) = \sum_{n=1} R_n e^{-\alpha_n t} \cos(\omega_n t + \varphi_n) U(t - t_0) \quad (5.73)$$

where  $U$  is the step function defined as

$$U(t - t_0) = \begin{cases} 1 & t \geq t_0 \\ 0 & t < t_0 \end{cases} \quad (5.74)$$

In (5.73), it is assumed that all CNRs of the scatterer start resonating at the same time,  $t_0$ , called turn-on time. This is valid for simple scatterers such as chipless RFID tag. Meanwhile, for complex scatterers such as airplane and so on, each resonance might have its own turn-on time. The turn-on times give some information about the location of the scattering centers of the scatterer compared to the receiving antenna.

According to Figure 5.7, a time-window of length  $T_w$  is moved along the time axis incrementally by the value of  $T$ . Poles and residues of each sliding window are computed using MPM and they are indexed by  $T$  to realize a time-frequency representation. The windowed signal can be written by

$$e_w(t) = \text{Re} \left\{ \sum_{n=1}^N R_n^T e^{-s_n(t-t_0)} U(t-t_0) \right\} \quad (5.75)$$

in which

$$\begin{aligned} R_n^T &= R_n e^{-s_n T} \\ &= R_n e^{-(\alpha_n + j\omega_n)T} \end{aligned} \quad (5.76)$$

In natural logarithmic scale, (5.76) is expressed by

$$\text{Ln}(|R_n^T|) = \text{Ln}(|R_n|) - \alpha_n T \quad (5.77)$$

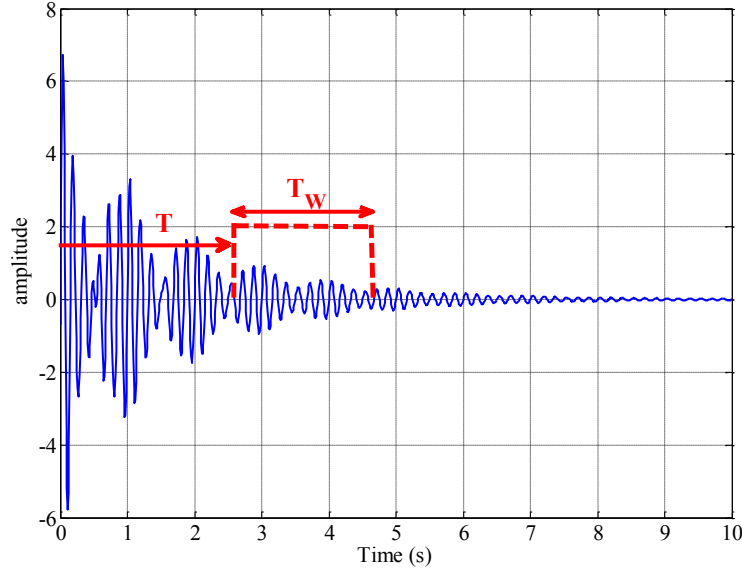
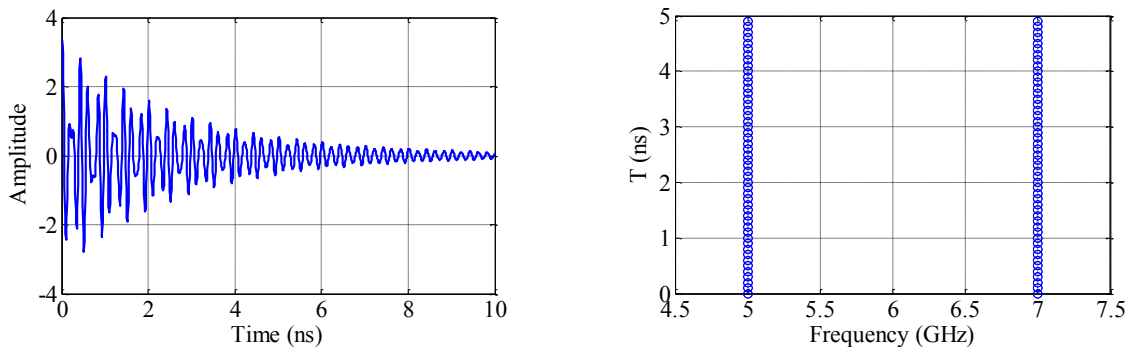


Figure 5.7 Time-domain signal with moving window.

Equation (5.77) indicates that in normal logarithmic scale, residues linearly decrease versus  $T$  with slope  $\alpha_n$ . The real part of the poles,  $\alpha_n$ , calculated from MPM are very sensitive to noise. An alternative way of calculating the damping factors of the CNRs is to find the slopes of the residues versus time in the normal logarithmic scale as (4.76) shows. The simulation results presented in this section will show that the CNRs calculated from STMPM are more accurate than those from MPM. By calculating the poles and residues, three different diagrams (time-frequency, time-damping factor, and time-residue) can be used in detection and localization of scatterers. As a simple case, the following signal is considered.

$$s(t) = R_1 e^{-\alpha_1 t} \cos(2\pi f_1 t + \varphi_1) + R_2 e^{-\alpha_2 t} \cos(2\pi f_2 t + \varphi_2) \quad (5.78)$$

Figure 5. 8a shows signal  $s(t)$  versus time for  $R_1 = 2$ ,  $R_2 = 1.5$ ,  $\alpha_1 = 3e8$ ,  $\alpha_2 = 5e8$ ,  $f_1 = 5e9$ ,  $f_2 = 7e9$ ,  $\varphi_1 = \pi/4$ , and  $\varphi_2 = \pi/3$ . By applying STMPM to the time-domain signal, its time-frequency and



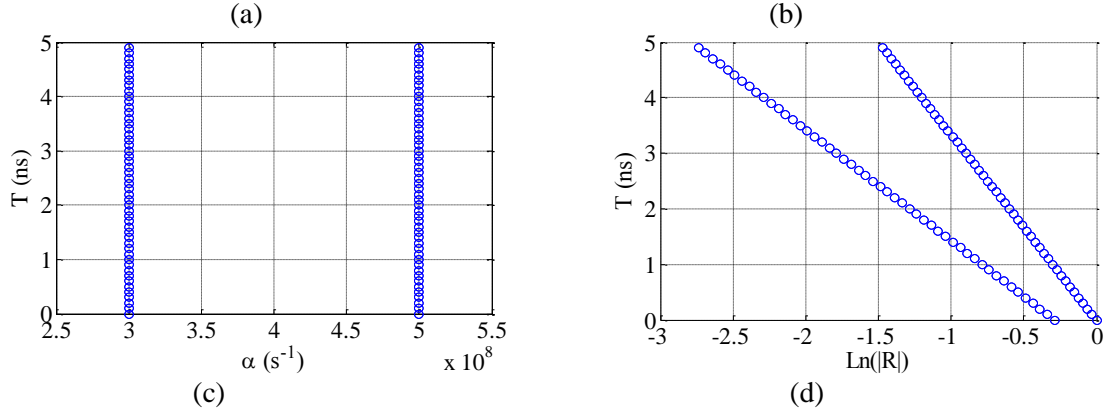


Figure 5.8 (a) Time-domain signal, (b) time-frequency, (c) time-damping factor and (d) time-residue diagrams of the signal.

time-damping plots are depicted in Figure 5.8b, 5.8c, and 5.8d. Two resonant frequencies and their corresponding damping factors are seen clearly in the Figure. Figure 5.8d shows the normal logarithm of the residues of the CNRs versus time. The slope of the lines is associated to the damping factors of the CNRs.

Two important parameters of STMPM are the filtering parameter  $p$  and window length,  $T_w$ . In practical applications, it is very important to choose the optimum values of  $p$  and  $T_w$  to extract the time and frequency information from noisy data. Frequency resolution deals with the minimum distance between two adjacent resonant frequencies of the signal which can be distinguished. Assuming signal seen in (4.77) with  $R_1 = R_2 = 1$ ,  $\alpha_1 = \alpha_2 = 3e8$ ,  $f_1 = 5$  GHz and  $\Delta = f_2 - f_1$ , the minimum window length required for distinguishing two poles of the signal is represented in Figure 5.9 in terms of  $\Delta = f_2 - f_1$  for different values of  $p$ . For lower  $\Delta$ , larger  $T_w$  is required. This is common in all time-frequency approaches. On the other hand, by increasing  $p$ , smaller window need to be used. Employing smaller window length means improving the time resolution. Therefore, it is possible to improve the time and frequency resolutions by applying STMPM with optimum values of  $p$  and  $T_w$ . For better comparison, the time-frequency representation of the signal seen in (5.78) is shown in Figure 5.10 by applying STMPM and RJTF techniques to the time-domain signal. The length of the applied window in both methods is  $T_w = 2.5$ ns. Compared to STMPM result, there are some interferences in between two resonances of the signal when we use RJTF with the same window length. Additionally, there are slight variations in the resonant frequencies of the signal at time instances. Therefore, the proposed technique can be useful when high density of data is places on the tags.

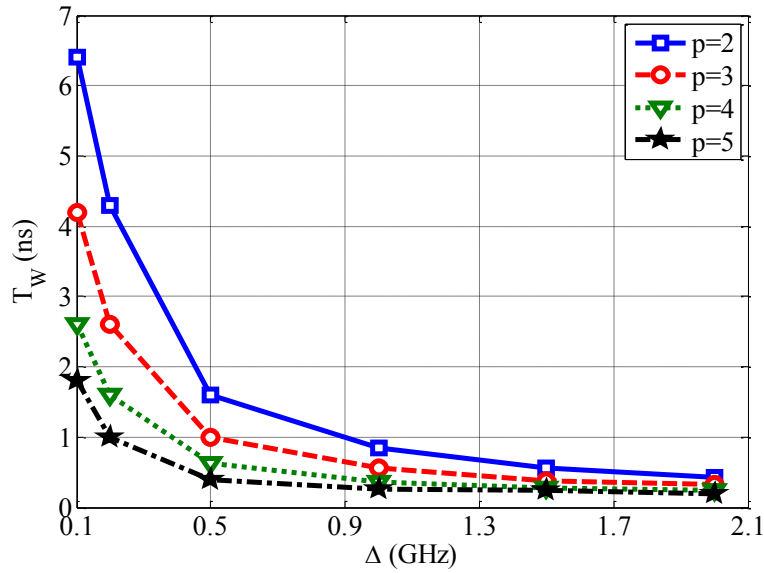


Figure 5.9 Minimum window length for distinguishing two resonances of the signal versus frequency distance [70] (With permission, Copyright© 2015 IEEE).

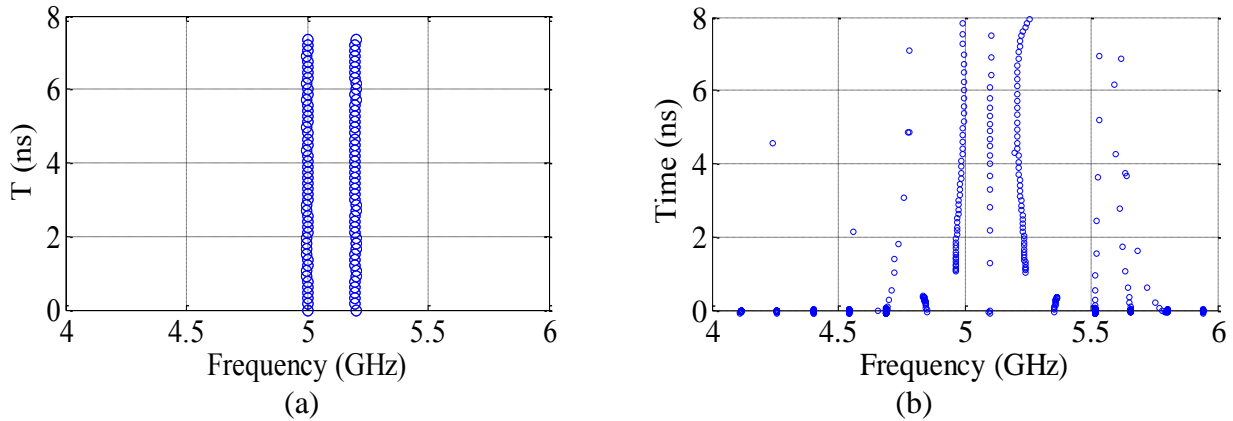


Figure 5.10 Time-frequency representation of the signal by applying (a) STMPM and (b) RJTF.

In order to study the ability of the proposed technique in extracting low power CNRs in the presence of the stronger ones, the signal seen in (5.78) is considered with  $R_1 = 30$ ,  $R_2 = 1$ ,  $\alpha_1 = \alpha_2 = 5e8$ ,  $f_1 = 5e9$ ,  $f_2 = 6e9$ , and  $\varphi_1 = \varphi_2 = 0$ . The signal and its time-frequency representation are depicted in Figure 5.11 for different values of  $T_W$  and  $p$ . The residue of the first pole is 30 times stronger than the first one's. For  $T_W = 1.1$  ns and  $p = 2$ , the stronger resonant frequency is detected by STMPM. By increasing the time window to  $T_W = 4$  ns, again the stronger resonance is detected.

While by increasing filtering parameter to  $p = 4$ , and keeping  $T_w = 1.1$  ns, both resonances are detected. This is very important in scattering processes where some poles are excited stronger than the others. As the results show, by increasing the value of  $p$ , not only is the resolution in time and frequency domains improved, but the weaker CNRs of the signal can be detected in the presence of the stronger ones.

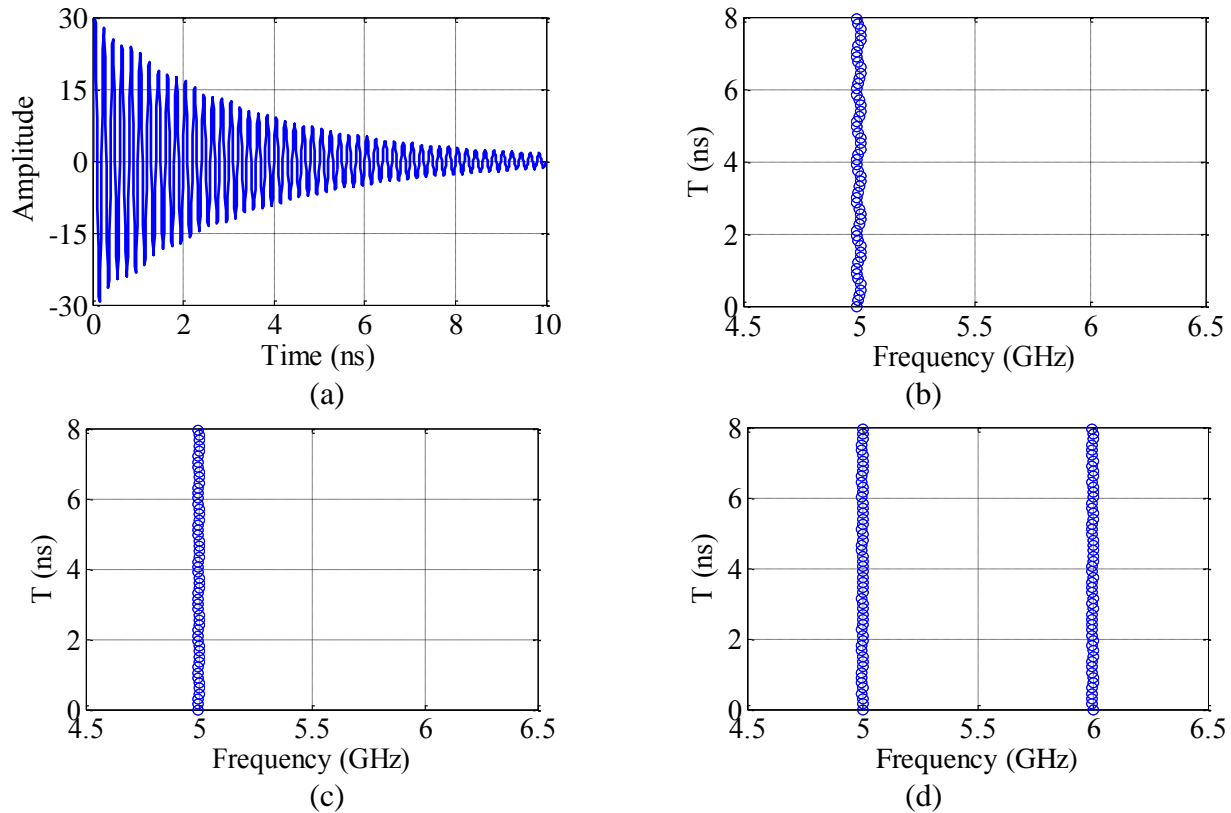


Figure 5.11 (a) Signal in time domain, Time-frequency representation of signal for (a)  $T_w = 1.1$  ns,  $p = 2$ , (b)  $T_w = 4$  ns,  $p = 2$ , and (c)  $T_w = 1.1$  ns,  $p = 4$  [70] (With permission, Copyright© 2015 IEEE).

### 5.4.3 STMPM in Early Time

Matrix pencil method (MPM) was first introduced as a technique to extract the CNRs of the damped sinusoidal signals. According to the discussion in section 2.4, an entire-domain function needs to be added to the series of damped sinusoidals in order to guarantee the convergence of the series. It means that the received signal includes an early-time response followed by the damped sinusoidals in the late time. Now the question is how STMPM works for early-time responses of

the scatterers. In other word if one can expand an impulse signal in terms of damped sinusoidals. Based on Fourier series, each time-limited signal in  $t \in [0, T_w]$  can be expanded versus sinusoidal signals as

$$x(t) = \sum_{n=0}^{+\infty} A_n \cos\left(\frac{2\pi n}{T_w} t + \varphi_n\right) \quad (5.79)$$

In theory, the series has infinite number of terms. But in practical applications, it is truncated to a finite number of sinusoidals to achieve the desirable accuracy.

In UWB application, the early-time response is a pulse-shaped signal covering all the excited frequencies. Depending on the location of the observation point compared to the scatterer, it can be expanded versus the incident field and its integration and derivatives with respect to time [17]. In simple scatterers such as chipless RFID tag where the scatterer is approximated by just one scattering center in the frequency band of operation, the early-time response is approximated by just one term. In the near-field of the scatterer it is very similar to the incident field, while in the far field it inclined to the first time derivative of the incident field. In complex scatterers with multiple scattering centers, more terms need to be considered in the series. As an example, the following Gaussian signal is assumed.

$$x(t) = \exp\left(-\frac{(t - \tau)^2}{2\delta^2}\right) \quad (5.80)$$

The time-domain signal seen in (5.80) and its first derivative with respect to time are depicted in Figure 5.12 for  $\delta = 0.5e-9$  and  $\tau = 0.15$  ns. The derivative of the signal is normalized to its maximum value. By applying STMPM with  $T_w = 2$  ns and  $p = 3$  to the signal, its pole diagram is depicted in Figure 5.13. As it shows, the original pulse is approximated by four damped sinusoidal signals. These four signals are depicted in Figure 5.14. By summing the four damped sinusoidals, the reconstructed signal is depicted in Figure 5.15 along with the reconstructed signal based on Fourier series of the pulse. As it shows, the recovered signal by damped sinusoidals is more accurate than one resulted from Fourier series with the same number of terms,  $M = 4$ . Assuming the length of window as  $T_w = 2$  ns in Figure 5.12, the position of the pulse is changed in the window.

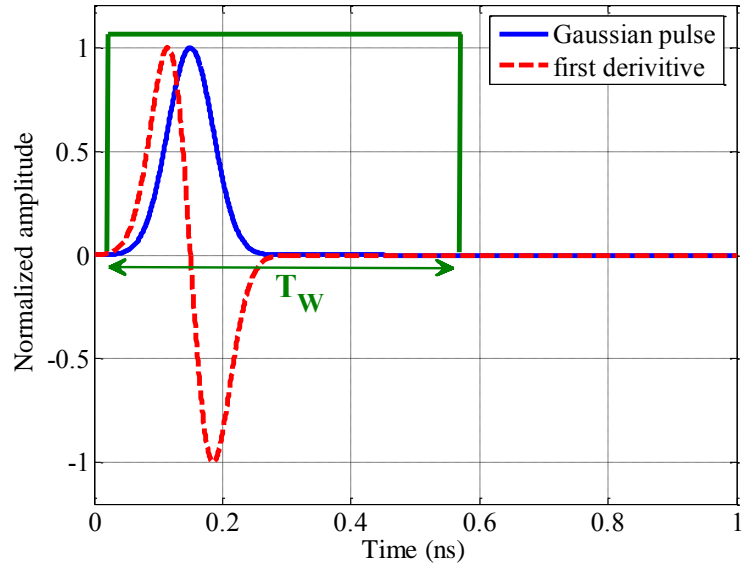


Figure 5.12 Gaussian pulse and its first derivative with respect to time.

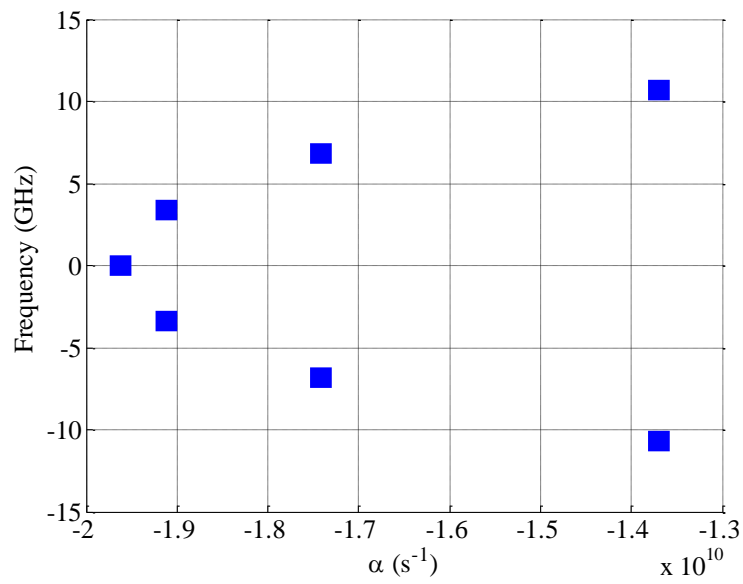


Figure 5.13 Pole diagram of the Gaussian pulse function.

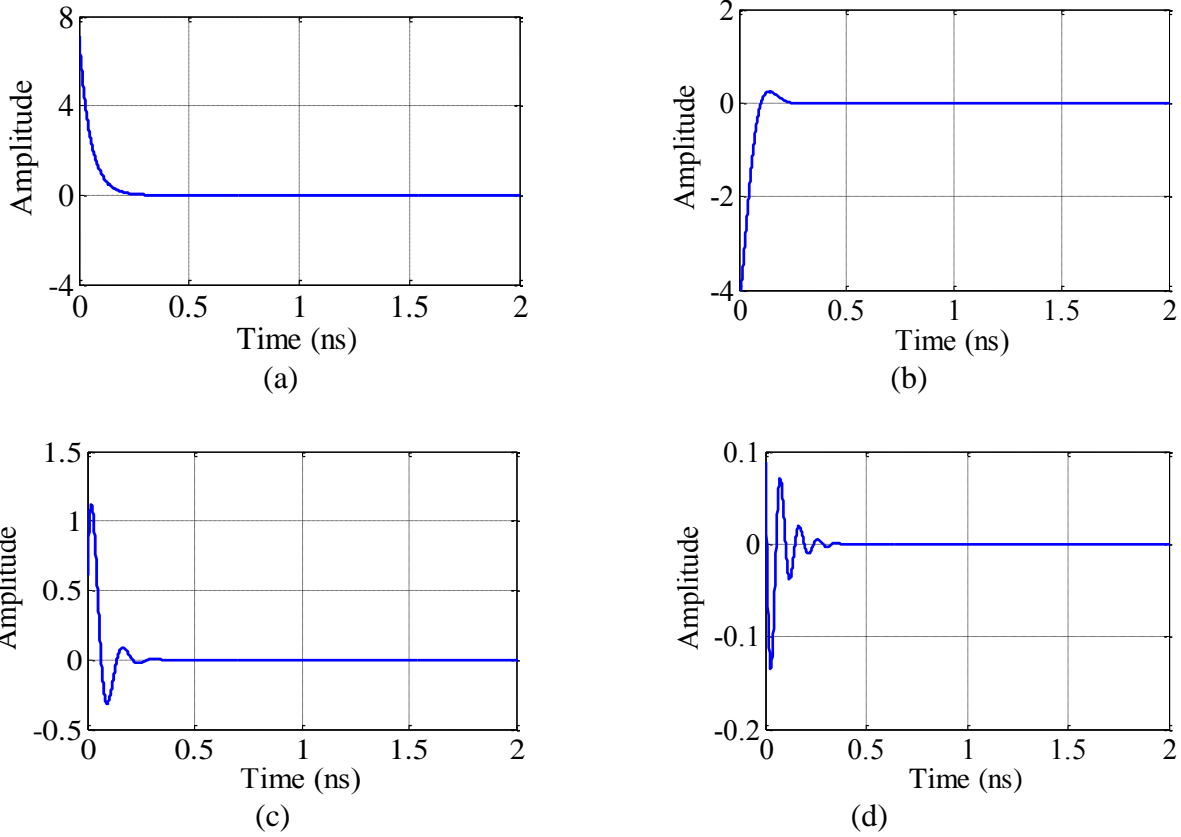


Figure 5.14 Four extracted damped sinusoidal modes by applying STMPM to the Gaussian pulse.

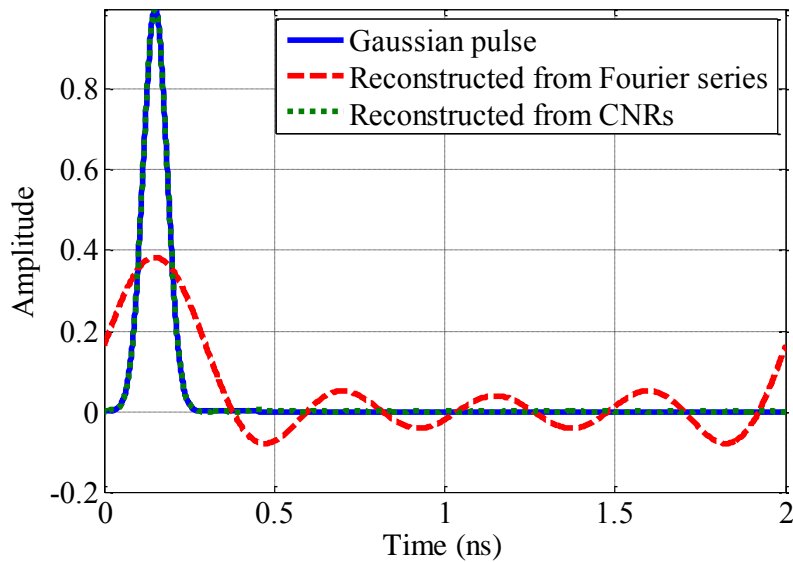


Figure 5.15 Gaussian pulse and reconstruction one from Fourier transform and CNRs.

The pole diagram of the pulse is shown in Figure 5.16 for different values of  $\tau$ . By moving the pulse from left to the right of the window, the extracted CNRs move to the right side of the imaginary axis either. For  $\tau < 1$  ns, the CNRs must be highly damped resonances leading to the poles located at the left hand side of the pole diagram. On the other hand, for  $\tau > 1$  ns, constructive signals must grow with time leading to the CNR located at the right hand side of the pole diagram. For  $\tau = 0.5$  ns and  $\tau = 1.5$  ns when the pulse is located at the same distance from the center, the poles are asymmetrically located at two sides of the imaginary axis. By moving the pulse away from the center of the window, the poles move away from the imaginary axis and when it is at the center, they are on the imaginary axis. When the pulse is located at the center of the window,  $\tau = 1$  ns, the poles are located on the imaginary axis of the pole diagram with more terms. It means that when the pulse is at the center of the window, the series of the CNRs inclines to the Fourier series of the signal. Since the poles are non-damped sinusoidals, more terms are needed to achieve the required accuracy. The reconstructive signals are depicted in Figure 5.17 for different  $\tau$ s and  $T_w = 2$  ns. For  $\tau = .5$  ns, the reconstructed signal is zero for  $t > 2$  ns either. In the case of  $\tau = 1$  ns where the poles are close to the imaginary axis, Gibbs phenomenon is seen at sharp variations of the signal. According to Figure 5. 17c, by increasing  $p$  in STMP, more terms are included in the series and the accuracy of the reconstructed signal is improved. Since the poles are not perfectly located on the imaginary axis, there is a sharp discontinuity at the end of the time window. For  $\tau = 1.5$  ns when the pulse in the RHS of the window, the reconstructed signal is similar to the original one in  $t \in [0, 2e-9]$ . But it has very sharp variations for larger time values. These sharp variations emanate from the growing sinusoidal signal summed together. Based on the presented results in Figures 5.15 to 5.17, it is seen that the reconstructed signal approximates the original one for  $t \in [T, T + T_w]$ . The width of the early-time impulses is related to the bandwidth of the incident field. By increasing the bandwidth, the impulses become narrower. In far-field region, the shape of the scattered field inclines to the derivative of the incident field. Assuming the Gaussian pulse seen in (5.80), its normalized derivative with respect to time is shown in Figure 5.12. By changing the position of the signal in the time window, the extracted poles are shown in Figure 5.18 for different values of  $\tau$ .

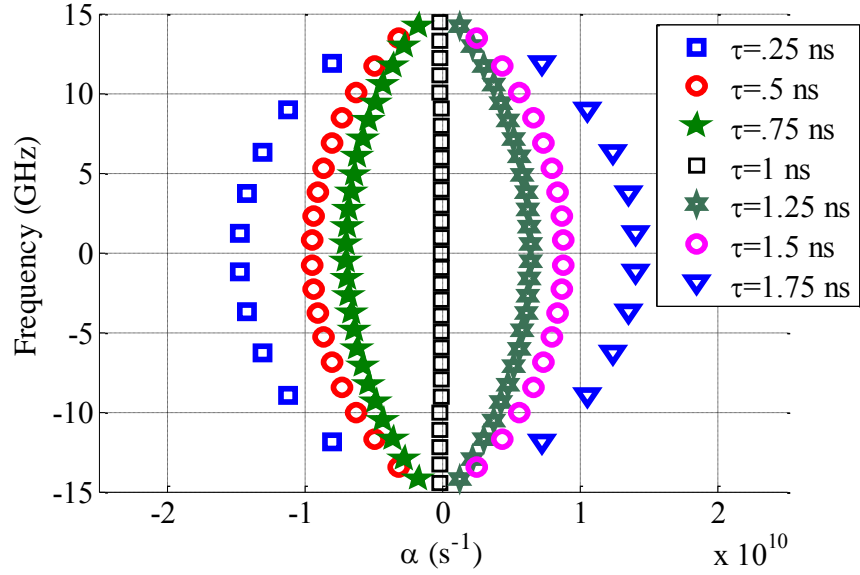


Figure 5.16 Pole diagram of the Gaussian pulse for different values of  $\tau$ .

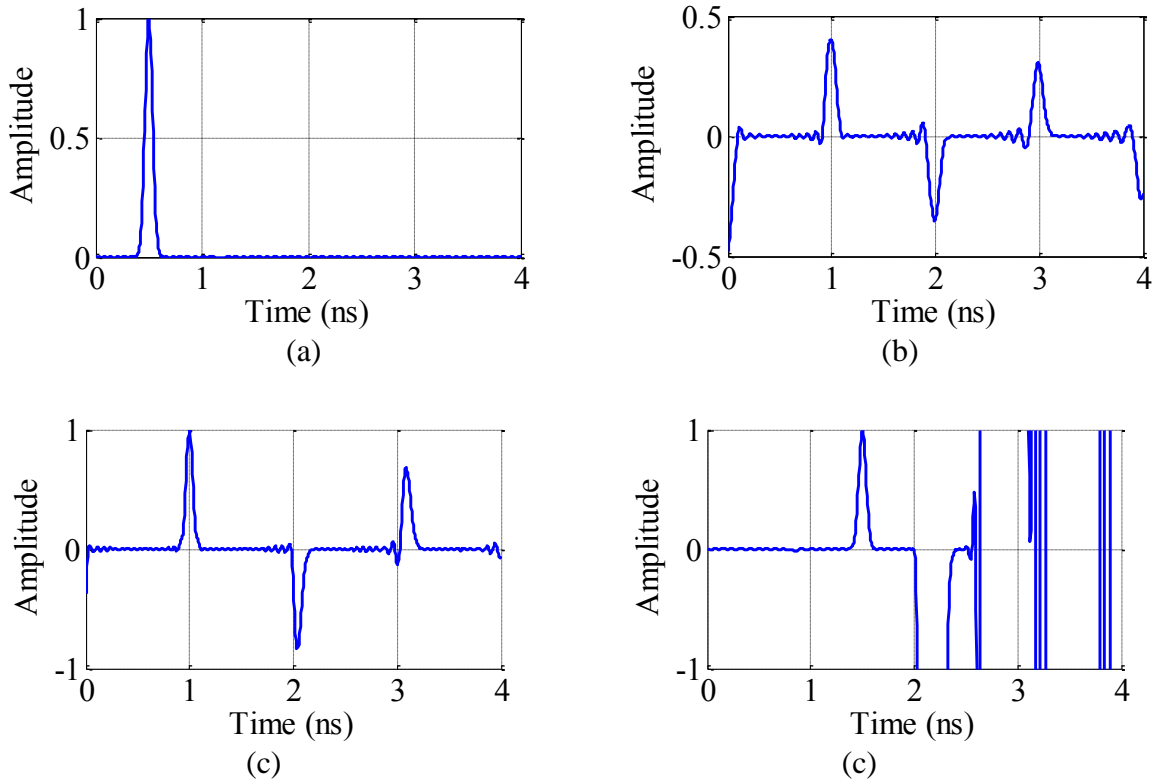


Figure 5.17 Reconstructed pulse signal for (a)  $\tau = .5$  ns,  $p = 4$ , (b)  $\tau = 1$  ns,  $p = 4$ , (c)  $\tau = 1$  ns,  $p = 8$ , (d)  $\tau = 1.5$  ns,  $p = 4$ .

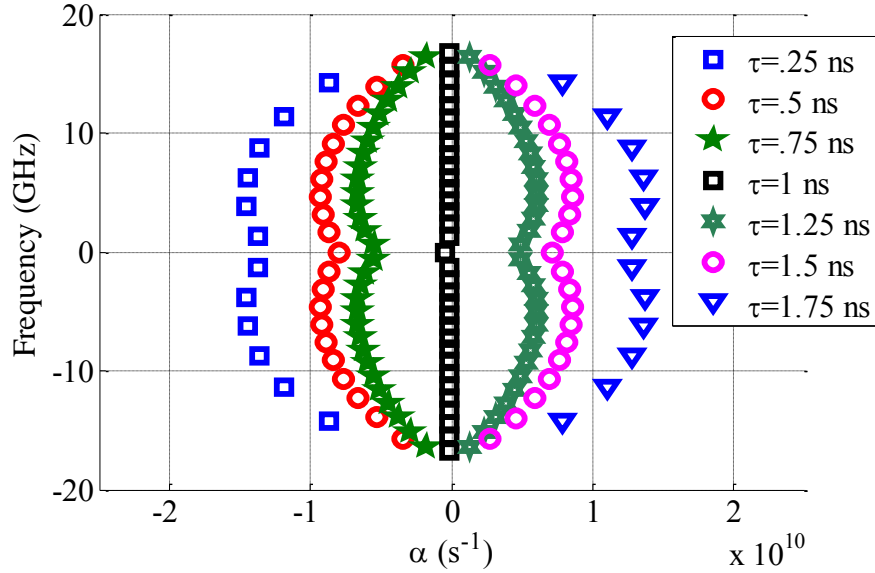


Figure 5.18 Pole diagram of the derivative of Gaussian pulse for different values of  $\tau$ .

Again, by moving the pulse to the RHS of the window, the corresponding poles move to the RHS of the pole diagram. When the pulse is located at the center of the window, the poles are very close to the imaginary axis of the pole diagram. Figure 5.19 shows the reconstructed signal based on Fourier series and summation over CNRs with  $M = 4$  compared to the original signal. As can be seen, the original signal is accurately constructed by summing over CNRs. While it needs more terms in Fourier series to achieve the desired accuracy. According to above mentioned discussion, the CNRs of the early-time response move from the LHS to the RHS of the pole diagram when the window moves along the time axis. This is very useful in detecting the early-time response of the scatterers. In Figure 5.20, the extracted damping factors of the Gaussian pulse and its derivative located at  $\tau = .15$  ns is depicted versus the center of the sliding window by applying STMPM to the time-domain signal. As it shows the damping factors are zero when the pulse is located at the center of the window. For the derivative of the pulse, there are two other zero crossing points coincident with the position of the maximum and minimum points of the signal in addition to the center of the pulse located at  $\tau = .15$  ns. As another example, the scattered signal from a resonant structure is depicted in Figure 5.21a. By applying STMPM with  $T_w = 1$  ns to the signal, the extracted poles of the scatterer is depicted in Figure 5.21b for different sliding times. The early-time response of the scatterer is centered at  $t = 1.55$  ns. As it shows, the extracted poles move from the RHS of the pole diagram to the LHS by sliding the window along the time. The CNRs of

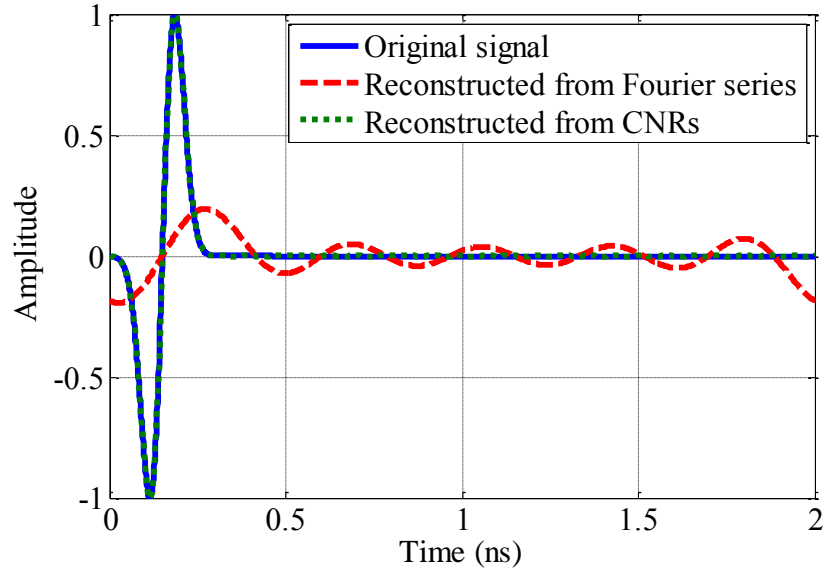


Figure 5.19 Derivative of the Gaussian pulse and reconstruction one from Fourier transform and CNRs.

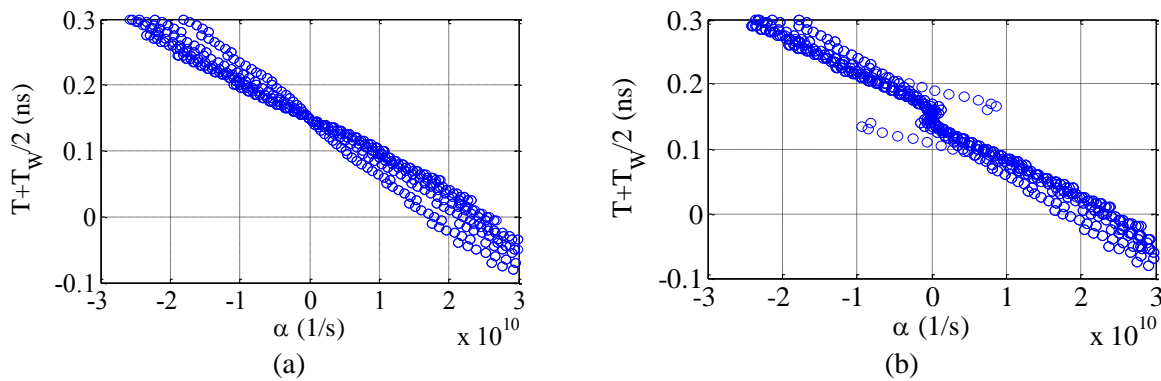


Figure 5.20 Extracted damping factor versus the center of the sliding window for (a) pulse, and (b) its derivative.

the late-time response are shown in the figure. They do not change by sliding window along the late-time signal. On the other hand, the poles of the early-time response vary as a function of  $T$ . This can be helpful in separating the early-time response from the late-time one. In Figure 5.21c, the extracted damping factors are shown as a function of window's center time. The position of the early-time response is clearly seen at  $t = 1.55$  ns where the damping factors are zero. The damping factor of the CNR in the late time response is seen in Figure 4.21c. In second example, two scatterers are assumed 12 cm away from each other. The radar cross-section (RCS) of the second scatterer is considered much smaller than the first scatterer RCS. Figure 5.21d shows the

received scattered signal from the scatterers by illuminating them by an incident electric field. The early-time response of the first scatterer is followed by the late-time response originating from the natural modes of the scatterer. The early-time of the second scatterer is hidden in the late-time of the first target. Since its dimensions are much smaller than the lowest wavelength of the incident field, it does not excite the CNRs of the second target. By applying STMPM to the time-domain signal, the extracted damping factors are shown in Figure 5.21e versus the center of the sliding window. The zero crossing of the damping factors show the position of the early-time responses of the scatterers. By extracting the CNRs of the early-time and late-time responses, the reconstructed early time and late time are depicted in Figure 5.21f. The turn-on time of the resonance and position of the scatterers can be accurately obtained from the proposed technique. The location of the scatterers can be calculated by knowing the centers of the early-time responses.

#### 5.4.4 Performance of STMPM Against Noise

Noise is any unwanted signal which interferes with the desirable signal. Detection in the presence of noise is very challenging when the backscattered signal is not very strong. Because the normal radiation modes of the scatterer are damped sinusoidals, the signal to noise ratio decreases with respect to time. In communication systems, the dominant noise is additive white Gaussian noise (AWGN). White noise is a random signal with a constant power spectral density. Assuming the input noise as AWGN, the received signal is represented as

$$s(t) = e(t) + \sum_{n=1} R_n e^{-\alpha_n t} \cos(\omega_n t + \varphi_n) + n(t) \quad (5.81)$$

where  $e(t)$  is the early-time response and  $n(t)$  is AWGN. The second term is the late-time response including the CNRs of the scatterer. For  $n^{\text{th}}$  CNR, the corresponding signal is

$$\begin{aligned} s(t) &= R_n e^{-\alpha_n t} \cos(\omega_n t + \varphi_n) + n(t) \\ &= x(t) + n(t) \end{aligned} \quad (5.82)$$

With aforementioned assumptions on noise, its power spectral density and correlation function are defined as

$$S_N(f) = \frac{N_0}{2} \quad (5.83)$$

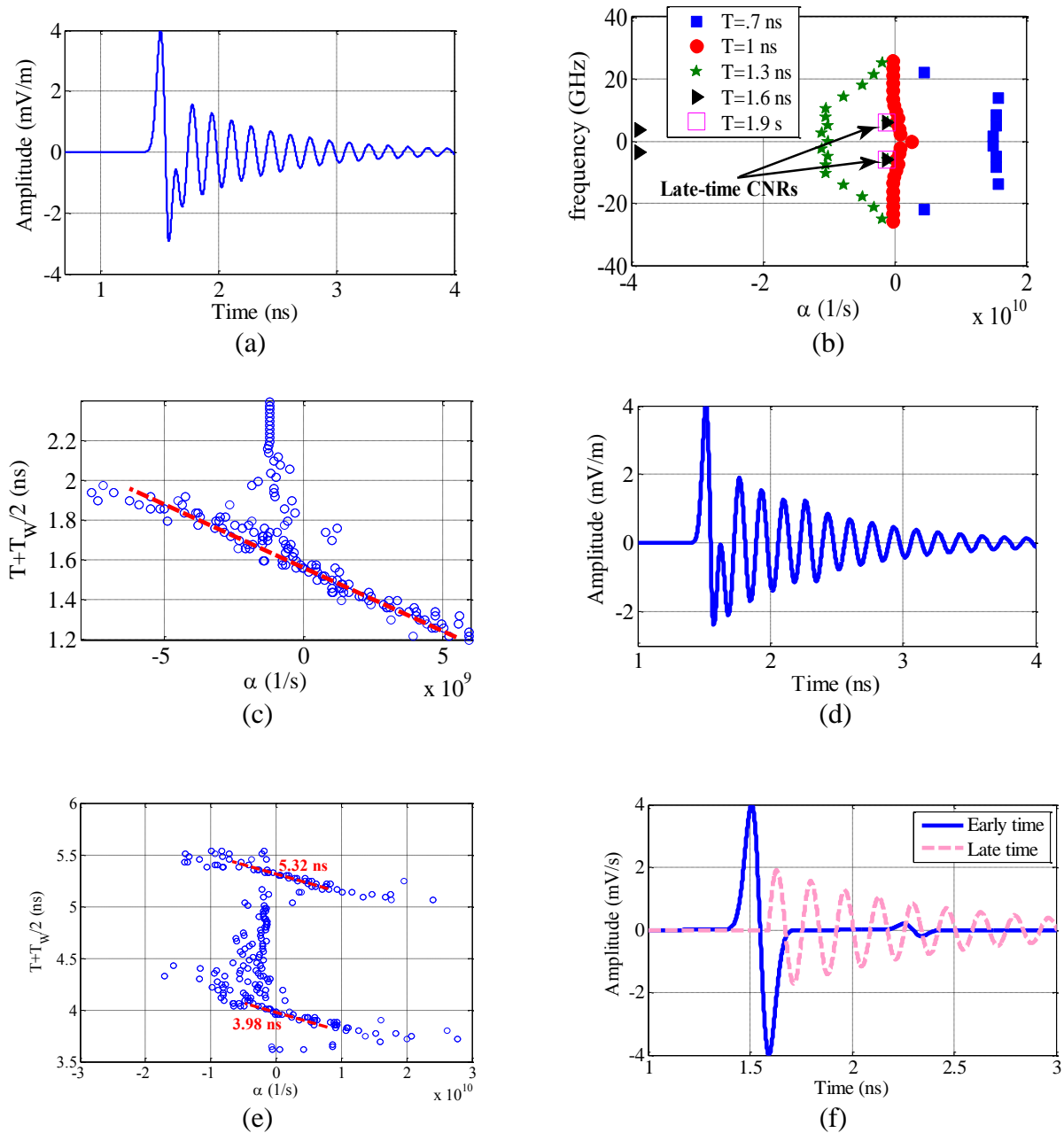


Figure 5.21 (a) Backscattered electric field from the scatterer, (b) pole diagram of the signal for different sliding times, (c) extracted damping factors with respect to the center of the sliding window, (d) backscattered electric field from two scatterers, (e) extracted damping factors with respect to the center of the sliding window, and (f) reconstructed early-time and late-time responses.

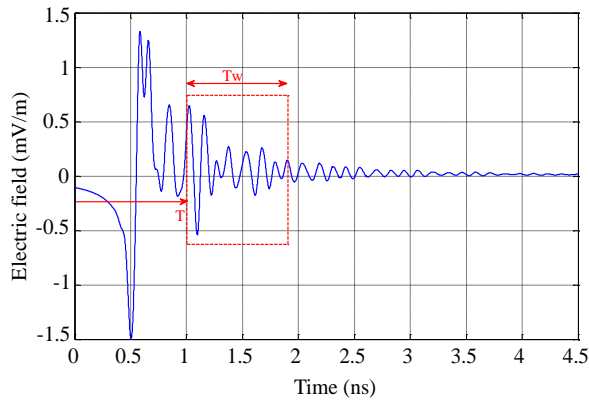
$$\begin{aligned}
SNR &= \frac{S_x}{S_N} \\
&= \frac{\int_T^{T+T_w} x^2(t) dt}{\int_{-\infty}^{+\infty} |H(f)|^2 KT_c df}
\end{aligned} \tag{5.86}$$

where  $K= 1.38 \times 10^{-23}$  ( $\text{m}^2\text{Kg s}^{-2}\text{K}^{-1}$ ) is the Boltzmann constant,  $T_c$  is the temperature in Kelvin, and  $H(f)$  is the sinc function corresponding to the Fourier transform of the rectangular pulse of width  $T_w$  in time domain. After some mathematical manipulations, the SNR in (5.86) is given by

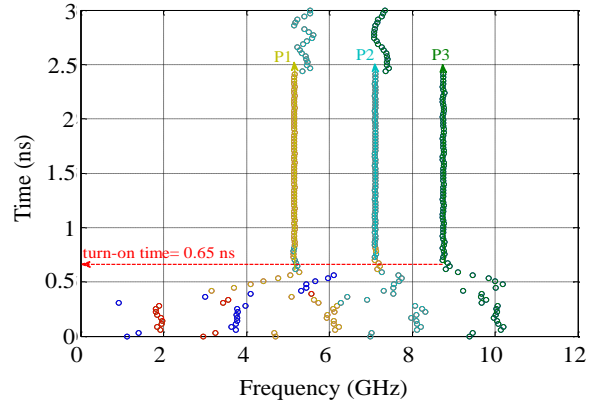
$$\begin{aligned}
SNR &= \frac{e^{-2\alpha_n T} R_n^2}{4KT_c T \alpha_n} \left\{ \left[ 1 + \alpha_n^2 \cos(2\varphi_n + 2T_w) - \alpha_n \omega_n \sin(2\varphi_n + 2T_w) \right] \right. \\
&\quad \left. + e^{-2\alpha_n T_w} \left[ 1 + \alpha_n^2 \cos(2\varphi_n + 2T_w + 2T) - \alpha_n \omega_n \sin(2\varphi_n + 2T_w + 2T) \right] \right\}
\end{aligned} \tag{4.87}$$

According to (5.87), SNR is proportional with the square of the residue of the CNR and decreases with any increase in damping factor. For long-read distances, the residues decrease leading to smaller SNRs. As it shows, by sliding the window along the time, the energy of signal decreases, while the energy of noise does not change. Hence, higher SNR is accessible at the earlier times of the signal. In scattering from multi-resonant structures, one need a few number of cycles in order to detect all the resonances from the scattered signal. On the other hand, in scattering from lossy media, the damping factors of the CNRs might be large enough to attenuate the response very fast. In such cases, the knowledge of the turn-on time of the CNRs is very useful. Because by placing the sliding window just before the turn-on time, some CNRs from the early time response might come into the pole diagram of the signal.

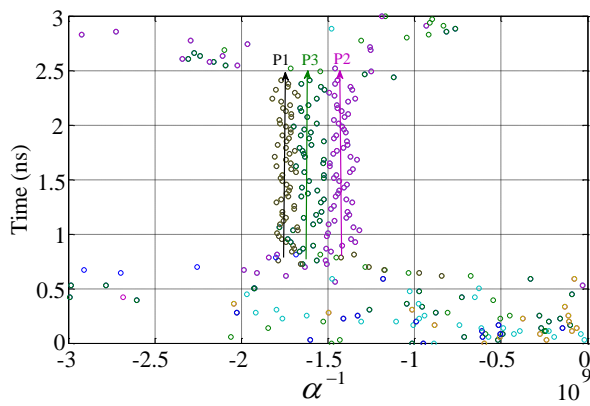
In order to study the effect of noise on STMPM, the backscattered signal from a 3-bit tag is seen in Figure 5.22a. The early-time and late-time responses are clearly seen in the figure. By applying the proposed method to the time-domain signal, the time-frequency, time-damping factor and time-residue of the signal is depicted in Figure 5.22b, 5.22c, and 5.22d for  $T_w = 0.8\text{ns}$  and  $p = 2$ . The poles of the early-time response are converged to the poles of the late time at turn-on times. Compared to resonant frequencies, there are some variations in the extracted damping factors. The turn-on time of the CNRs of the tag is shown in the time-frequency representation of the signal as  $t_0 = 0.65\text{ns}$ . By adding noise to the signal, the time-damping factor and time-residue of the signal are shown in Figure 5.23 for  $SNR = 15\text{dB}$ . As the results show, the damping factor is very sensitive



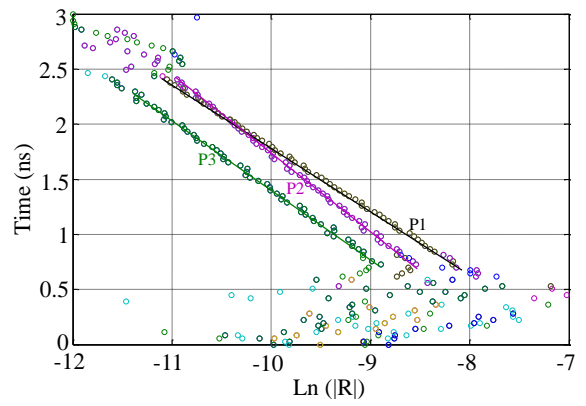
(a)



(b)

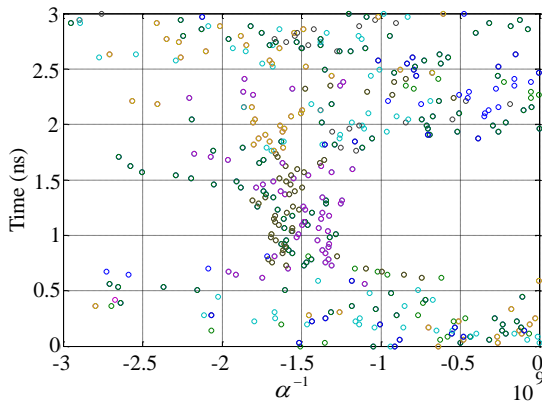


(c)

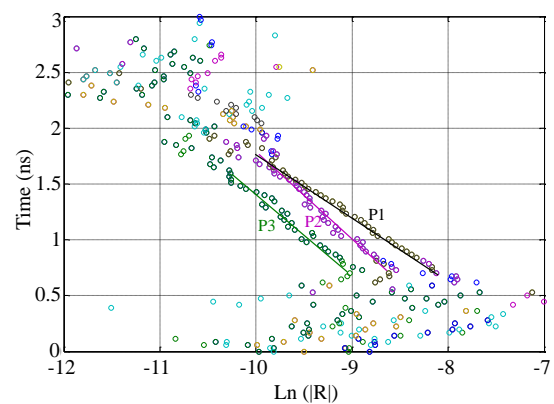


(d)

Figure 5.22 (a) Backscattered electric field, (b) Time-frequency diagram, (c) Time-damping factor, and (d) Time-residue diagram of the signal [69] (With permission, Copyright© 2014 IEEE).



(a)



(b)

Figure 5.23 (a) Time-damping factor of the signal, (b) Time-residue diagram of the signal for SNR = 15 dB [69] (With permission, Copyright© 2013 IEEE).

Table 5-1 Percentage error of estimating of real and imaginary parts of the dominant poles of the tag calculated from direct matrix pencil method (MPM) and short-time-matrix-pencil-method (STMPM) [69] (With permission, Copyright© 2013 IEEE).

SNR	$\omega_1$	$\omega_2$	$\omega_3$	$\alpha_1$		$\alpha_2$		$\alpha_3$	
				MPM	Slope of residues	MPM	Slope of residues	MPM	Slope of residues
15	0.39	0.31	0.36	9.14	7.18	12.7	7.1	11.1	6.78
10	0.71	0.68	0.82	17	15.3	22	15.1	21.6	14.6
5	2.85	2.98	3.2	28.4	24.6	31.5	26.8	48	29

to noise. For later times, by decreasing the SNR, the detection of the CNRs becomes challenging. In Figure 5.23b, the time-residue of the CNRs of the signal are shown. The slop of the lines are equal to the damping factors of the poles. The calculated damping factors in time-residue diagram is more accurate than ones calculated from MPM. Table. 1 presents the average error of estimating the real and imaginary parts of the poles for 50 different sets of noisy data with a specific SNR value. As the table shows, the proposed method gives more accurate results for damping factors than MPM. The reason is that the calculating damping factor from the time-residue diagram is based on the residues of CNRs which is related to the energy.

## 5.5 Application of STMPM in Wideband Scattering from Resonant Structures [70]

As a time-frequency approach, various scattering mechanisms such as resonance, scattering center, and dispersion features of the scatterer can be monitored in the time-frequency diagram obtained from STMPM [70]. In some applications such as radar, the CNRs of the airplane are used as the ID for detection purposes [71]. In these applications, high-Q resonances are more effective for identification purposes. These high-Q resonances are mostly generated by cavity structures embedded on the scatterer. For example, the engine of the airplane makes an open-ended cavity resonator whose corresponding CNRs participate effectively in the late-time backscattered response from the airplane. Hence, the ID of the airplane can be adjusted by changing the resonant modes of the open-ended engine cavity. These CNRs are usually affected by the dispersion characteristics of the structure.

Figure 5.24 indicated various scattering-mechanism representations in the time-frequency diagram [72]. A vertical line represents a reflection from a scattering center while a horizontal line introduces a resonance mechanism in the scattering mode. Any slope in the time-frequency diagram (as Figures 5.24c and 5.24d show) represents a dispersive phenomenon. In order to gather all the above mechanisms into one example, an open-ended cylindrical cavity seen in Figure 5.25a is often considered in literature [21, 22, 73-77]. An incident electric field polarized in  $x$ -direction and propagating in  $-z$  direction illuminates the cavity. The backscattered field contains reflections from the rim and bottom of the cavity and dispersive internal resonant modes of the cavity. As the time-domain response in Figure 5.25b indicates, three pulse-shaped responses at  $t = 1ns$ ,  $t = 4.3ns$  and  $t=5.4ns$  are due to the specular reflections from the rim, and the external and internal back of the cavity, respectively. The time-frequency diagram of the signal is depicted in Figure 5.26 using STMPM and STFT. The parameters of STMPM are chosen as  $T_w = 0.4ns$  and  $p = 2$ . According to figure, there are two scattering centers and three resonant modes. The modes with cut-off

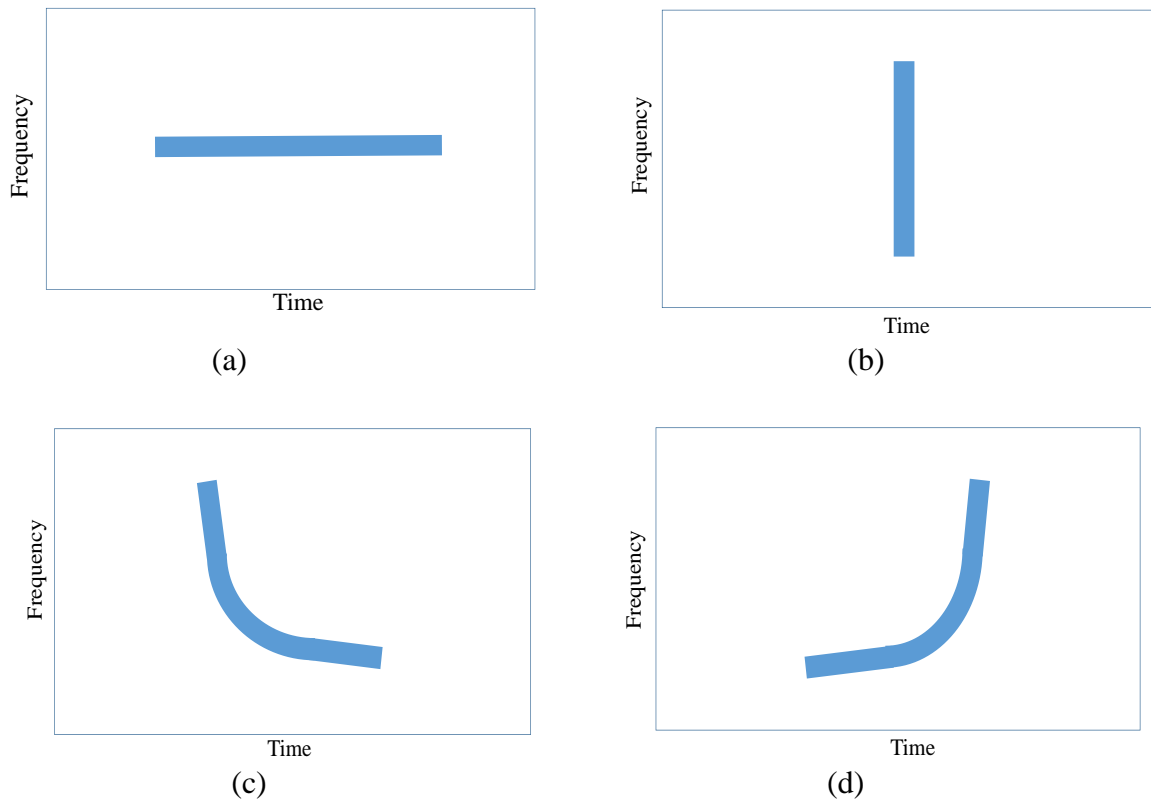


Figure 5.24 Scattering mechanisms in time-frequency analysis. (a) Scattering center. (b) Resonant behavior. (c) Structural dispersion. (d) Material dispersion [70] (With permission, Copyright© 2015 IEEE).

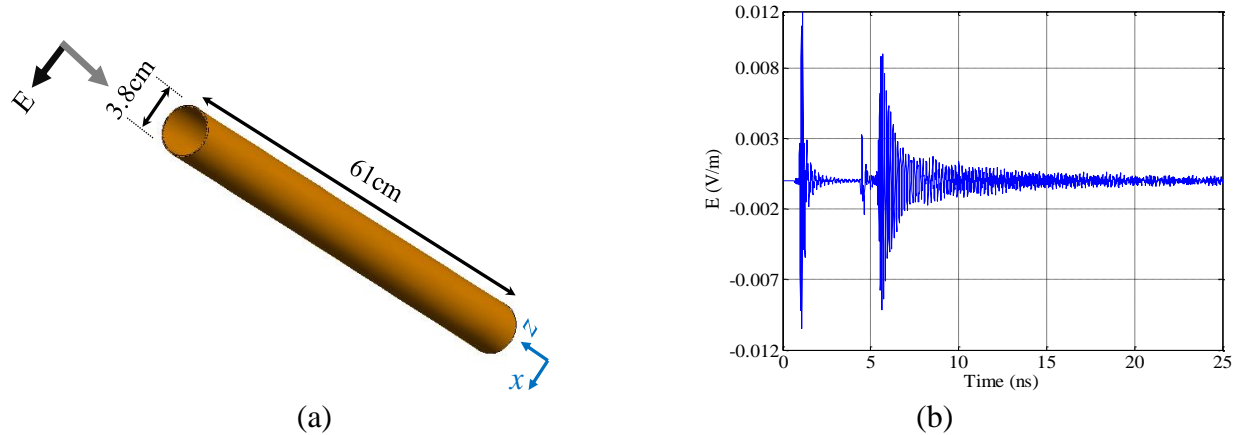


Figure 5.25 (a) Open-ended circular cavity excited by incident plane wave, (b) Backscattered signal in time domain [70] (With permission, Copyright© 2015 IEEE).

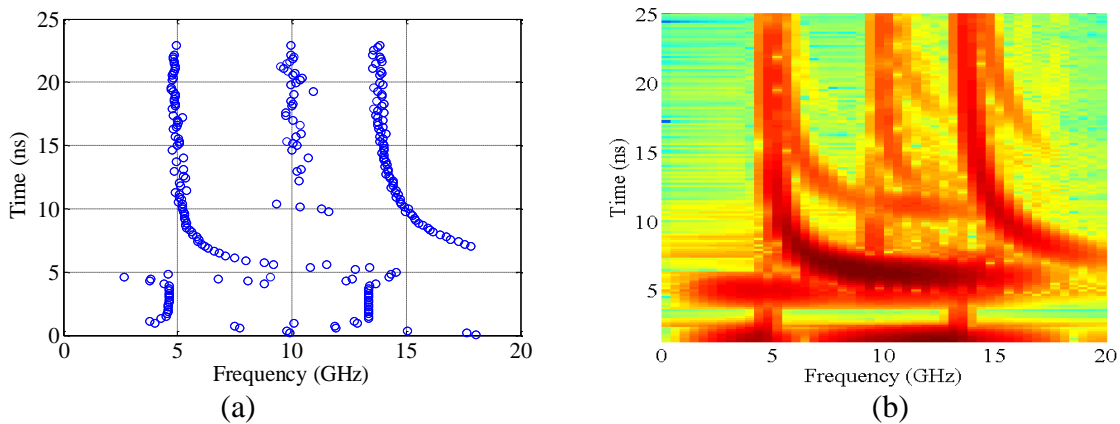


Figure 5.26 (a) Time-frequency diagram of the backscattered signal from the cylinder based on (a) STMPM and (b) STFT [70] (With permission, Copyright© 2015 IEEE).

frequencies  $f = 5$  GHz and  $f = 13.8$  GHz have been excited more strongly than the mode with cut-off resonance at  $f = 9.9$  GHz. There are some poles parallel to the frequency axis located around  $t = 10$  ns which emanate from the second roundtrip travel of the pulse inside the waveguide cavity. The spectrogram of the signal based on STFT is shown in Figure 5.26b. As can be seen, because of the poor resolution of STFT in both frequency and time domains, the scattering centers and resonant frequencies of the cavity cannot be accurately extracted from the spectrogram of the signal. This is especially severe when the resonances are closer to each other. By increasing the length of the window and filtering parameter,  $p$ , and consequently increasing the frequency resolution as seen in Figure 5.27, not only is the second mode clearly visible, but there also exist

some extra resonances higher than 13.8 GHz. These frequencies result from the second roundtrip travel of the pulse inside the cavity, which shows itself at later times. Here, in addition to the dispersive modes of the first roundtrip of the pulse inside the cavity, the modes corresponding to the second roundtrip are visible with different turn-on times which is exactly matched with the electrical length of the cavity. The dispersion characteristics of the modes have been highlighted with dashed lines. In order to extract the accurate times of the reflections from the lid and bottom of the cavity in the time-domain signal, the damping factors of the windowed signal are shown in Figure 5.28 versus the center of the window for two values of  $T_w$ , window length, and  $p$ , filtering parameter. The zero-crossing points in the damping factors versus time are the time instances of the multiples reflections from the structure. Another advantage of the proposed technique is that the local resonant frequencies of the scatterer are illustrated by discrete poles in the time-frequency diagram rather than continuous colors in wavelet and STFT. Figure 5.29 shows the time-frequency diagram of the signal based on the proposed technique for SNRs of 20dB and 10dB. For lower values of SNR, we need to decrease the value of  $p$  in order to avoid the presence of poles originating from noise.

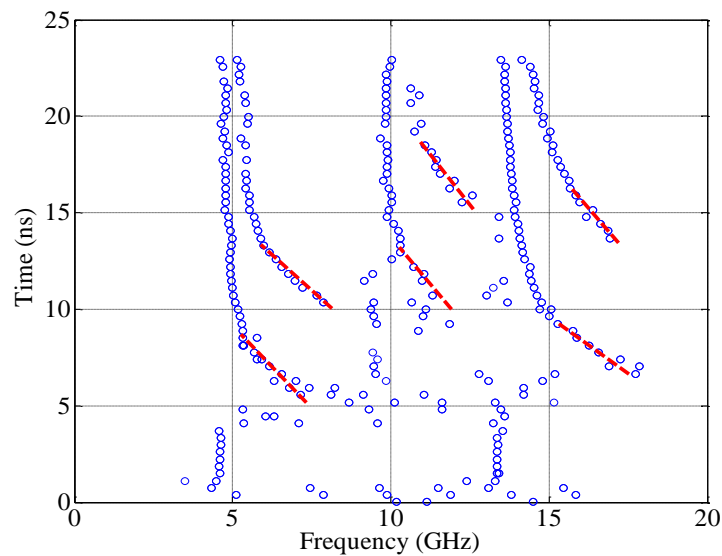


Figure 5.27 Time-frequency diagram of the scattered field for  $T_w = 1$  ns,  $p = 4$  [70] (With permission, Copyright© 2015 IEEE).

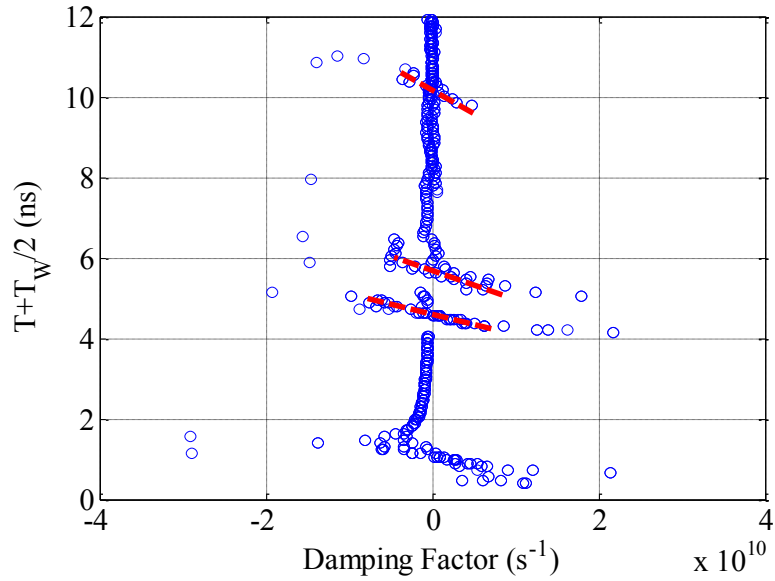


Figure 5.28 Time-damping factor representation of backscattered signal from cavity.

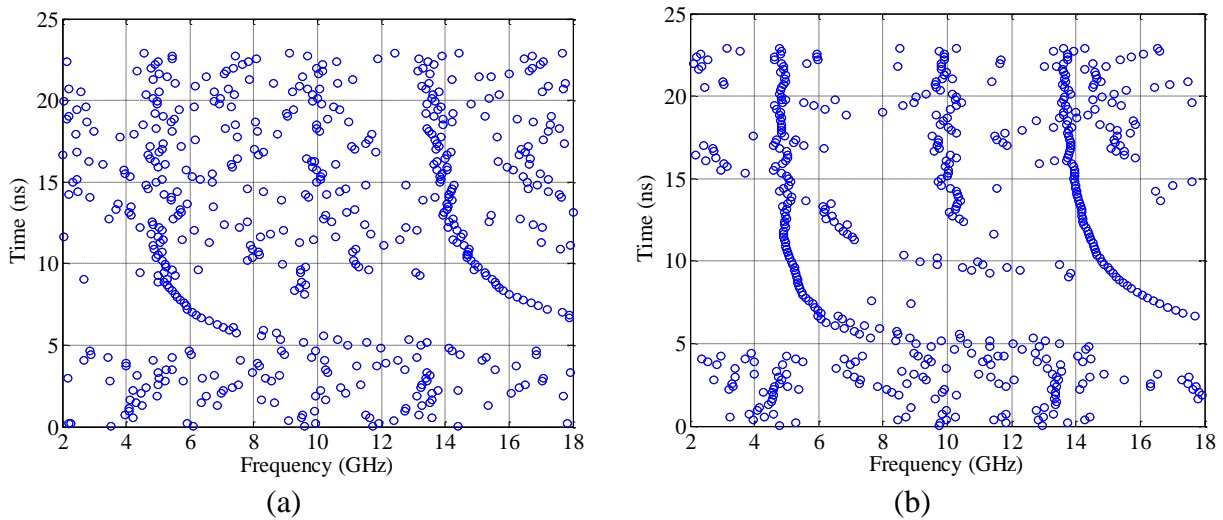


Figure 5.29 Time-frequency diagram of the signal with (a) SNR=10dB,  $T_W = 0.8\text{ns}$ ,  $p=2$  and (b) SNR=20dB,  $T_W = 0.8\text{ns}$ ,  $p=4$  [70] (With permission, Copyright© 2015 IEEE).

## **6 Detection, Identification, and Localization in Chipless RFID Tags [8] (Chapter used with permission of Springer science and business media, 2015)**

In previous chapter, short-time matrix pencil method (STMPM) was introduced as an efficient time-frequency analysis technique. By improving time and frequency resolutions, the resonant frequencies and turn-on times of the CNRs are monitored in time-frequency diagram. The ID of the tag is located in the spectral of the scattered field. The turn-on times of the CNRs are useful in calculating the distance of the tag compared to the antenna. In circumstances where multiple chipless RFID tags are present in the reader area, a space representation of the tags is needed to localize their positions. Hence, one needs a space-time-frequency representation of the signal in order to detect, identify and localize the chipless tags in the reader area. The accuracy of the approach depends on the resolution in space, time and frequency. When multiples tags are in the main beam of the antenna, a collision-avoidance algorithm is required to separates the IDs of the tags

In this chapter, first a space-time-frequency algorithm is introduced by which the IDs and locations of the tags are calculated by applying STMPM and its dual, narrow-frequency matrix pencil method (NFMPM) to time and frequency domain signals, respectively. In some applications, multiple reflections from the antenna structure used in the RFID system or multiple reflections from the dielectric material introduce some impulses in the late-time response of the resonant-based scatterers. In such cases, the impulses limits the sliding of the time window along the signal. This problem can be solved by separating the early-time and late-time responses of the scatterer. As mentioned in section 5.3 and 5.4, by sliding the window along the time-domain signal, the poles originating from the early time can be distinguished from poles of the late-time response, which facilitates the detection, identification and localization of chipless RFID tags.

### **6.1 Detection of Chipless RFID Tags**

The detection process can be performed based on time-domain or frequency-domain signal. In [46, 49, 78, 79], the absolute value of the backscattered signal in the frequency domain and group delay of the received signal are used in detection process. Based on the singularity expansion method

(SEM), the impulse response of the scatterer for the incident and scattered fields directed in the  $\hat{\mathbf{r}}_1$  and  $\hat{\mathbf{r}}_2$  can be expressed by

$$\Gamma(\hat{\mathbf{r}}_1, \hat{\mathbf{r}}_2; s) = \sum_{n=1}^N \frac{R_n(\hat{\mathbf{r}}_1, \hat{\mathbf{r}}_2)}{s - s_n} + \Gamma_e(\hat{\mathbf{r}}_1, \hat{\mathbf{r}}_2; s) \quad (6.1)$$

where the first term is the late-time response, including the complex natural resonances  $s_n$  and corresponding residues  $R_n$ , and the second term is the early-time response of the scatterer. Compared to the early-time response and residues, the complex natural resonances (CNRs) are aspect-independent. Although each scatterer includes an infinite number of CNRs, the series in (6.1) is truncated to  $N$ , the number of fundamental resonances excited by the incident electric field. Compared to the CNRs, the residues  $R_n$  and the early-time response of the tag  $\Gamma_e$  depend strongly on the direction and polarization of the transmitting and receiving antennas. As mentioned in Chapter 2, the embedded CNRs of the tag are high-Q resonances. Assuming the tag is illuminated by an incident pulse  $\delta(t)$ , the scattered field in close proximity of the  $n$ th resonant frequency is written by

$$E(\omega) = \frac{R_n}{(\alpha - \alpha_n) + j(\omega - \omega_n)} + \sum_{\substack{m=1 \\ m \neq n}}^N \frac{R_m}{(\alpha - \alpha_m) + j(\omega - \omega_m)} + \Gamma_e(\omega) \quad (6.2)$$

Although the late-time response has its maximums at the resonant frequencies of the tag, it does not necessarily happen for the total field. The received signal at the  $n^{\text{th}}$  resonant frequency is

$$E(\omega_n) = \frac{R_n}{(\alpha - \alpha_n)} + \sum_{\substack{m=1 \\ m \neq n}}^N \frac{R_m}{(\alpha - \alpha_m) + j(\omega_n - \omega_m)} + \Gamma_e(\omega_n) \quad (6.3)$$

As (6.3) shows, the received signal at  $\omega = \omega_n$  is separated into three terms. The first term in (6.3) is the scattered field from the  $n$ th resonant frequency; the second term is due to the coupling of the other resonators on the  $n$ th resonator resonating at  $\omega = \omega_n$ , and the third term is the early-time response of the tag at  $\omega_n$ . As an important note here, the magnitude of the scattered field at the  $n^{\text{th}}$  resonant frequency is not simply a maximum at  $\omega_n$ . The coupling of the other poles, the second term in (6.3), and early-time response can change the maximum peak of the total field in the frequency domain to a minimum null or may shift it to other frequencies. Since the couplings and

the early-time response of the tag are aspect-dependent, the magnitude of the scattered field in the frequency domain is aspect-dependent as well. The main observation is that the magnitude of the impulse response of the tag in the frequency domain is not sufficient to extract the resonant frequencies of the tag.

Similarly, in detection techniques based on the group delay of the received signal, the group delay is not sufficient for extracting the resonant frequencies of the tag. The group delay is defined as

$$\tau_g = -\frac{d\phi_{s_{11}}(\omega)}{d\omega} \quad (6.4)$$

where  $\phi_{s_{11}}(\omega)$  is the phase response of the tag. Again, assuming high-Q resonances are embedded on the tag and ignoring the effect of the second term in (6.4), the group delay of the received signal can be written by

$$\tau_g = \frac{1}{1 + \left(\frac{\omega - \omega_n}{\alpha - \alpha_n}\right)^2} - \frac{d\phi_{r_e}(\omega)}{d\omega} \quad (6.5)$$

where  $\phi_{r_e}(\omega)$  is the phase of the early-time part of the signal, which is aspect-dependent. Therefore, both the magnitude and phase of the impulse response of the scatterer can vary by changing the source and observation points. Ignoring the early-time part of the signal causes a misleading result where the group delay shows its maximum value at the resonant frequencies of the tag. In the cases where the phase of the early-time part has stronger variations than the phase of the late-time part, the detection of the resonant frequencies from the group delay is not straightforward. As an example, Figure 6.1 shows a single-bit tag, located in the xy plane, illuminated by an incident electric field. The scattered signal in given two different orientations of the receiving antenna is depicted in Figure 6.2a. The resonant frequency of the tag is  $f = 5.09$  GHz, while the peaks and nulls in the scattered signal are slightly shifted around it. Hence, the locations of nulls and peaks in the backscattered response from the tag are not the exact values of the resonant frequencies of the tag. This is very important in the identification of a tag with high density of data, in which case the resonant frequencies are close to each other. In Figure 6.3b, the

group delay of the received signal for two different cases is shown. Although the first peak of the group delay is exactly located at the resonant frequency of the slot, there are some other peaks corresponding to variations in the early-time response. Hence, the absolute value of the scattered signal and its group delay cannot be used to accurately extract the ID of the tag. In contrast to the absolute-value and group-delay response of the scattered field, the detection can be performed based on the time-domain response. As mentioned before, the time-domain response of the tag is the combination of the early-time and late-time responses. The aspect-independent parameters of the tag, the complex natural resonances (CNRs), are included in the late-time response. This part of the response must be separated from the early time, which contains the specular reflections from the tag.

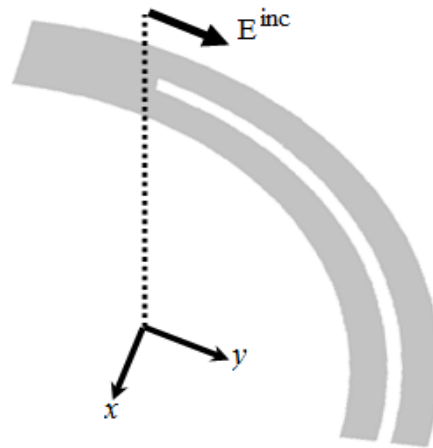


Figure 6.1 Single-bit tag illuminated by a plane incident field.

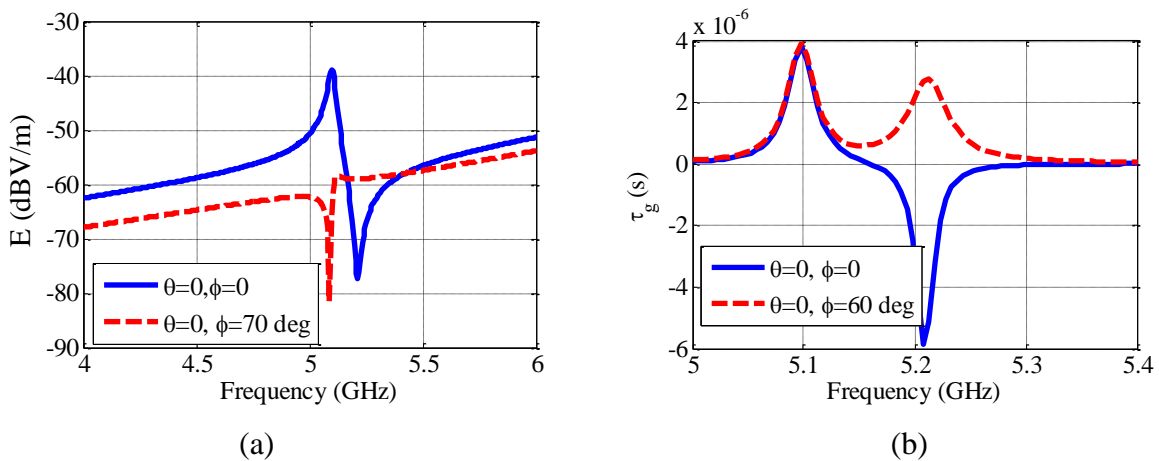


Figure 6.2 (a) Scattered electric field from the tag for two different orientations of receiving antenna, (b) Group delay of the scattered field for two different orientations of receiving antenna.

## 6.2 Space-Time-Frequency Anti-Collision Algorithm for Identifying Chipless RFID Tags [80]

In Figure 6.4, the schematic view of multiple tags presented in the main beam of the reader antenna is depicted. As it shows, the received backscattered signal is composed of the reflected signals from each tag. Assuming the configuration in Figure 6.4, the scattered field can be written in the Laplace-domain as (6.6).

$$\mathbf{E}^s(\mathbf{r}) = \int \bar{\mathbf{G}}_e(\mathbf{r}, \mathbf{r}'; s) \cdot \mathbf{J}_s(\mathbf{r}') ds' \quad (6.6)$$

The source points are presented in the primed coordinate and the observation points are presented using unprimed coordinates. Quantity  $\bar{\mathbf{G}}_e$  is the electric dyadic Green's function [13] and  $\mathbf{J}_s$  is the surface current density induced on the scatterer. Here, the reader area is assumed as a scattering medium with tags as the scattering centers. For the case of multiple tags, the current density can be written as the summation of the currents on the tags as

$$\mathbf{J}_s(\mathbf{r}') = \sum_{m=1}^M \mathbf{J}_{sm}(\mathbf{r}' - \mathbf{r}'_m) \quad (6.7)$$

in which  $M$  is the number of tags, and  $\mathbf{r}'_m$  and  $\mathbf{J}_{sm}$  are the location and induced current on the  $m^{\text{th}}$  tag, respectively. Backscattered fields from the tags can be deduced from the electric field integral equation (EFIE) as

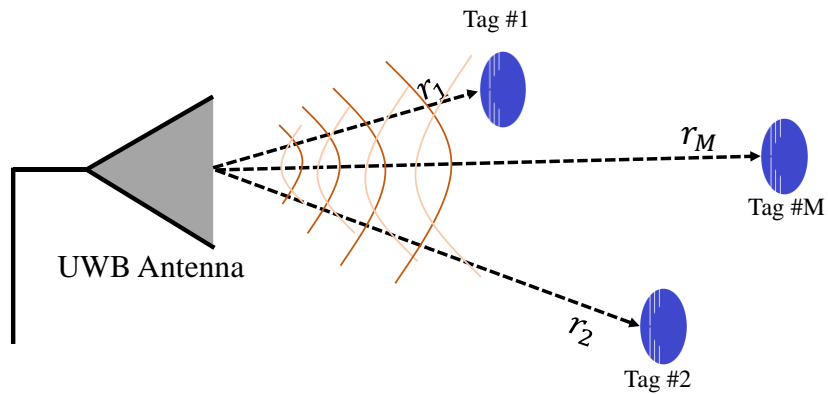


Figure 6.3 Multiple chipless RFID tags present in the reader zone [80] (With permission, Copyright© 2014 IEEE).

$$\int \vec{\mathbf{G}}_e(\mathbf{r}, \mathbf{r}'; s) \cdot \mathbf{J}_s(\mathbf{r} - \mathbf{r}') ds' = -\hat{t} \cdot \mathbf{E}^{\text{inc}}(\mathbf{r}) \quad \forall \mathbf{r} \in S \quad (6.8)$$

in which  $\mathbf{E}^{\text{inc}}$  is the incident electric field which emanates from the antenna,  $\hat{t}$  represents the unit vector tangential to the tag surface, and  $s = \alpha + j\omega$  is the complex frequency. On the other hand, based on singularity expansion method (SEM), the current in (6.7) and (6.8) can be expanded by a series of complex natural resonances as

$$\mathbf{J}_s(\mathbf{r}'; s) = \sum_{m=1}^M \sum_{n=-N_m}^{N_m} \frac{\vec{\mathbf{A}}_m^{(n)} \cdot \mathbf{J}_{sm}^{(n)}(\mathbf{r}' - \mathbf{r}'_m)}{(s - s_m^{(n)})} + \sum_{m=1}^M \mathbf{J}_m(\mathbf{r}' - \mathbf{r}'_m; s) \quad (6.9)$$

where  $\mathbf{J}_{sm}^{(n)}$  and  $s_m^{(n)}$  are the  $n^{\text{th}}$  natural-mode current and pole of the  $m^{\text{th}}$  tag. Compared to complex natural resonances, the residue coefficients,  $\vec{\mathbf{A}}_m^{(n)}$ , are aspect-dependent, depending strongly on the polarization and incident angle. The last summation in (6.9) contains the entire-domain function including the early-time response from the scatterers [81, 82]. The early-time response originates from the scattering centers of the scatterer [81, 83-85]. By inserting (6.9) in (6.8) and applying the method of moments, the induced currents on the tags can be obtained. Assuming the frequency band of operation covers all the natural resonances of the tags, the backscattered signal from induced current on the tags can be written in time domain as

$$\mathbf{e}^s(\mathbf{r}, t) = \sum_{m=1}^M \left[ \mathbf{e}_m(\mathbf{r}, t) + \text{Re} \left( \sum_{n=1}^{N_m} \mathbf{R}_n^{(m)} e^{-s_n^{(m)}(t-t_m)} \right) \right] \quad (6.10)$$

in which  $t_m$  represents the turn-on time of the  $m^{\text{th}}$  tag. It is assumed that CNRs of each tag have the same turn-on time. For complex scatterers, this assumption might not be accurate. According to Altes' model [17] mentioned in Chapter 2, the early-time response can be approximated by a series of pulse responses as

$$\mathbf{e}_m(\mathbf{t}) = \mathbf{e}^{\text{inc}}(\mathbf{r}, t) * \sum_{p=-\infty}^{+\infty} a_{mp} \delta^{(p)}(t - t_m) \quad (6.11)$$

where  $t_m$  is the delay time equal to the roundtrip time between the antenna and the  $m^{\text{th}}$  tag. The impulse response of the  $m^{\text{th}}$  tag in (6.11) is summed over the integrals and derivatives of the Dirac-delta function. Here, the negative and positive value of  $p$  refers to the  $p^{\text{th}}$  integral and derivative of the delta function. Therefore, (6.10) can be written in Laplace-domain as

$$\begin{aligned}\mathbf{E}^s(\mathbf{r}, s) &= \sum_{m=1}^M \left[ \sum_{p=-\infty}^{+\infty} a_{mp} s^p \mathbf{E}^{\text{inc}}(\mathbf{r}, s) e^{-st_m} + \sum_{n=-N_m}^{N_m} \frac{\mathbf{R}_m^{(n)}}{s - s_m^{(n)}} \right] \\ &= \sum_{m=1}^M \left[ \mathbf{A}_m(\mathbf{r}, s) e^{-st_m} + \sum_{n=-N_m}^{N_m} \frac{\mathbf{R}_m^{(n)}}{s - s_m^{(n)}} \right]\end{aligned}\quad (6.12)$$

in which the early-time summation is summarized by  $\mathbf{A}_m$ . Comparing (6.10) with (6.12), there is a duality between late-time response in time domain and the early-time response in Laplace domain [80, 84]. By applying STMPM to (6.10), the complex resonances of the tags and their residues are found at each snapshot of time. By shifting the sliding window by  $T$  in the late-time region, the backscattered signal can be written as

$$\mathbf{e}_{\text{late-time}}^s(\mathbf{r}, t) = \text{Re} \left( \sum_{m=1}^M \sum_{n=1}^{N_m} \mathbf{R}_m^{\text{T},n} e^{-s_m^{(n)}(t-t_m)} \right) \quad (6.13)$$

in which

$$\mathbf{R}_m^{\text{T},n} = \mathbf{R}_m^{(n)} e^{-(\alpha_m^{(n)} + j\omega_m^{(n)})T} \quad (6.14)$$

In normal logarithmic scale, (6.14) can be expressed as

$$\text{Ln}(|\mathbf{R}_m^{\text{T},n}|) = \text{Ln}(|\mathbf{R}_m^{(n)}|) - \alpha_m^{(n)}T \quad (6.15)$$

As can be seen in (6.15), the residues linearly decrease versus  $T$  with slope  $\alpha_m^{(n)}$ . By applying Narrow-frequency matrix pencil method (dual of STMPM) to the frequency response in (6.12), a space-frequency representation is obtained in which the scattering centers (here the tags) of the response are depicted versus frequency. In this diagram, the resonant frequencies of the tags in the late time are converted to some unstable poles. In practical applications limited to the frequency band of 3.1-10.6 GHz, when some dense multi-bit tags exist in the reader zone, the resonances of the tag in the frequency domain perturb the early-time response. In these cases, by inserting the poles and related residues in (6.10), the early-time part of the signal is found as

$$\mathbf{E}_{\text{early-time}}^s(\mathbf{r}, s) = \sum_{m=1}^M \mathbf{A}_m(\mathbf{r}, s) e^{-st_m} \quad (6.16)$$

By applying NFMPM to (6.16), the delay times ( $t_m$ ) are accurately obtained. The flowchart of the proposed algorithm is illustrated in Figure 6.4. The aforementioned technique is generalized and

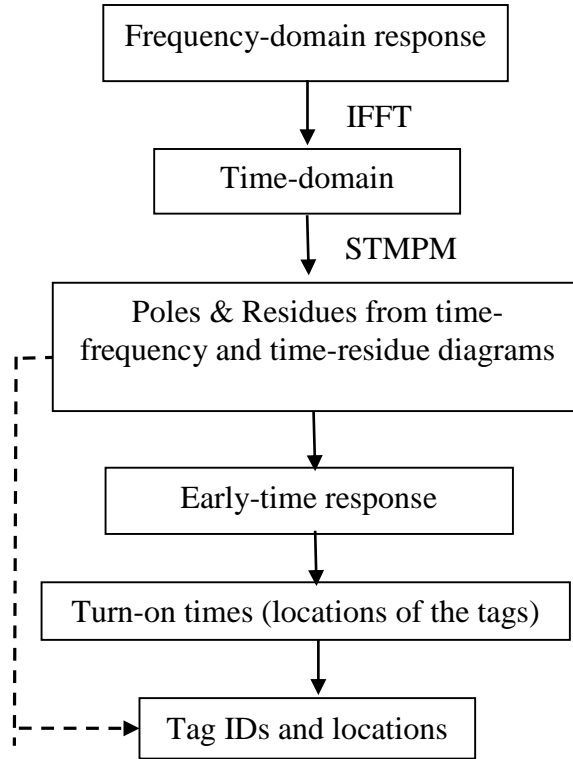


Figure 6.4 Flowchart of the proposed anti-collision algorithm [80] (With permission, Copyright© 2014 IEEE).

can be used for any multi-resonance tag schemes. For better illustration, Figure 6.5a shows a scenario in which two single-bit tags are illuminated by a plane wave. In the first case, the resonant frequencies of the tags are assumed at  $f_1=7.8$  GHz and  $f_2=9.8$  GHz and the tags are located  $R=20$  cm away from each other. Each tag is characterized by a complex natural resonance (CNR) which is created by inserting a quarter-wavelength slot on the tag surface [42, 45]. The approach is applicable for other types of tag including slot, transmission line, or spiral resonators [41, 44-47, 86]. The time-domain response is shown in Figure 6.6a. The early-time and late-time responses of the tags are illustrated by two different lines. The sliding time and window length are shown by  $T$  and  $T_w = 0.5ns$ . The time-frequency representation of the response is shown in Figure 6.6b. According to the figure, the unstable poles in the early-time part converge to the CNRs at turn-on times ( $t_1$  and  $t_2$ ). Then, after  $t_2=2.4ns$ , the response contains the backscattered signal from both tags; whereas before  $t_2$ , the backscattered signal contains just the response from the first tag. In contrast to the time-frequency

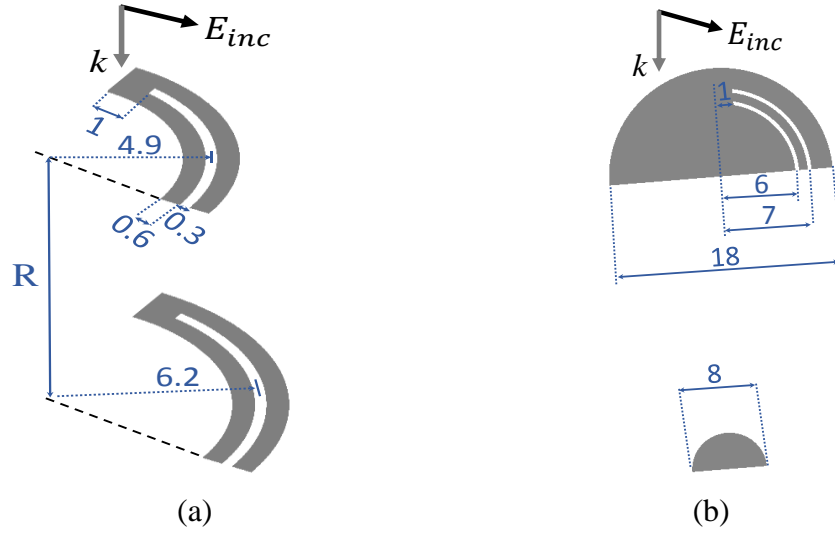


Figure 6.5 (a) Two single-bit tags and (b) two 2-bit tags spaced by  $R$  are illuminated by a plane wave. Units in mm [80] (With permission, Copyright© 2014 IEEE).

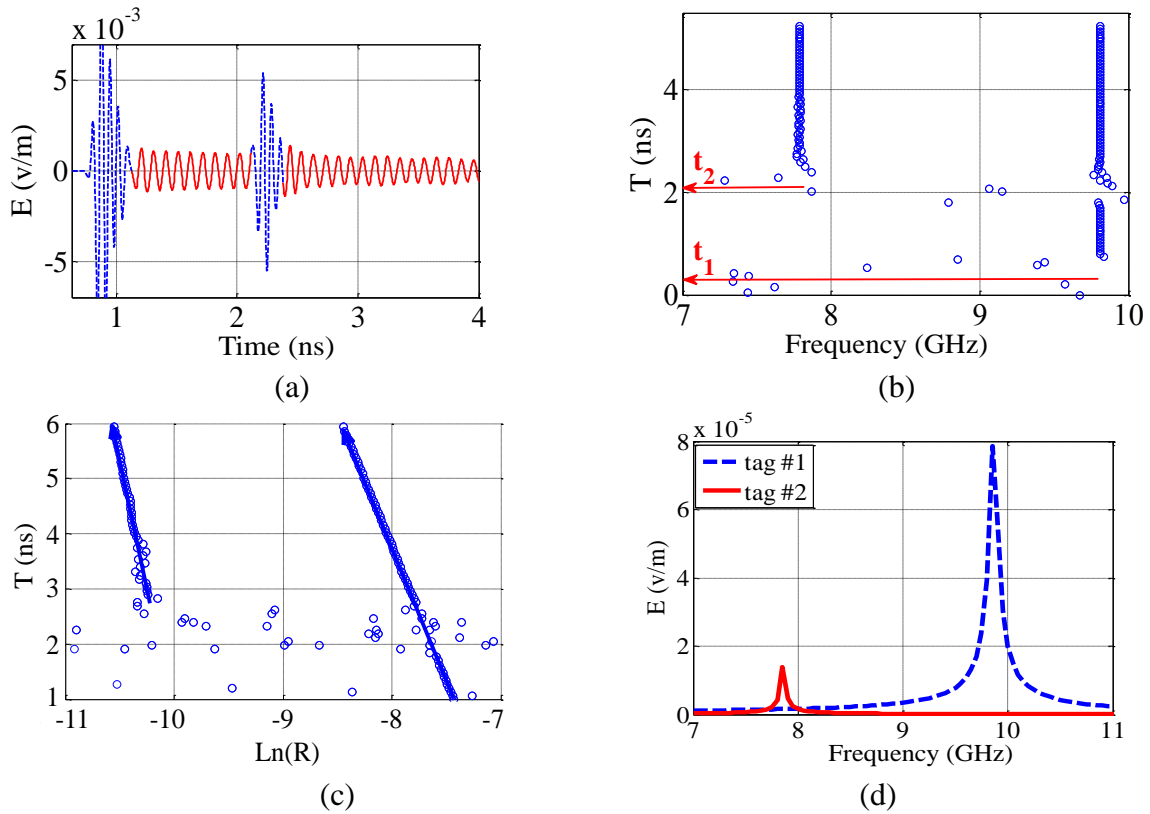


Figure 6.6 (a) Time-domain backscattered signal from two tags spaced by  $R=20\text{cm}$  (b) time-frequency representation of the signal by applying STMPM with  $T = 0.5\text{ns}$ . (c) time-residue diagram of the signal. (d) Separated responses of the tags in frequency-domain [80] (With permission, Copyright© 2014 IEEE).

representation of the signal, in the time-residue diagram of Figure 6.6c, two poles can be easily distinguished. The pole with turn-on time  $t_1=1\text{ns}$  is associated with tag #1 and likewise, the pole with turn-on time  $t_2=2.4\text{ns}$  is related to the second tag. According to (6.15), the slopes of the lines in Figure 6.6c are equal to the damping factor of the poles. By reconstructing the backscattered signal from the tags in the time domain, the contribution of each tag in the late-time response of the received signal is shown in Figure 6.6d. As can be seen, the amplitude of the backscattered signal from the first tag is higher than that of the second tag. The amplitudes at the resonant frequencies are directly proportional to the residues of the poles. In addition, the frequency response of each tag is depicted separately which simplifies the identification process. As another example, two similar single-bit tags are considered in Figure 6.5a resonating at  $f_1=7.7\text{GHz}$ . The time-frequency and time-residue representations of the signal are shown in Figures 6.7a and 6.7b, respectively. Two turn-on times of the resonators are shown in Figure 6.7a. By plotting the residues versus sliding time, there is a jump in the residue at the second turn-on time. This jump comes from the resonant frequency of the second tag. Assuming the pole of the tags as  $s_1=\alpha_1+j\omega_1$  and the residues of the first and second tag's poles as  $R_1$  and  $R_2$ , then the backscattered signal after  $t_2$  can be written as

$$R_1 e^{-(\alpha_1+j\omega_1)(t-t_1)} + R_2 e^{-(\alpha_1+j\omega_1)(t-t_2)} = e^{-(\alpha_1+j\omega_1)t} \left( R_1 e^{(\alpha_1+j\omega_1)t_1} + R_2 e^{(\alpha_1+j\omega_1)t_2} \right) \quad (6.17)$$

Hence, the residue of the single pole  $R_1$  before  $t_2$  becomes the term in the parentheses in right-hand side of (6.17) after  $t_2$ . Since the poles of the tags have the same damping factors, the slopes of the lines are the same. The late-time frequency response of the tags is shown in Figure 6.7c. Although they share the same resonant frequency and quality factor, they have different amplitudes at the resonant frequency. By applying NFMPM to the total frequency-domain response of the tags (without subtracting the late-time response), the locations of the tags are depicted in Figure 6.7d in a space-frequency diagram. There are some unstable poles (between  $R=5\text{cm}$  to  $R=25\text{cm}$ ) associated with the resonances of the tags. These poles can be suppressed by subtracting the late-time response from the total response in (6.12). In Figure 6.8, the time-residue of the backscattered signal from the tags is depicted for different polarizations of tag. As can be seen when the second

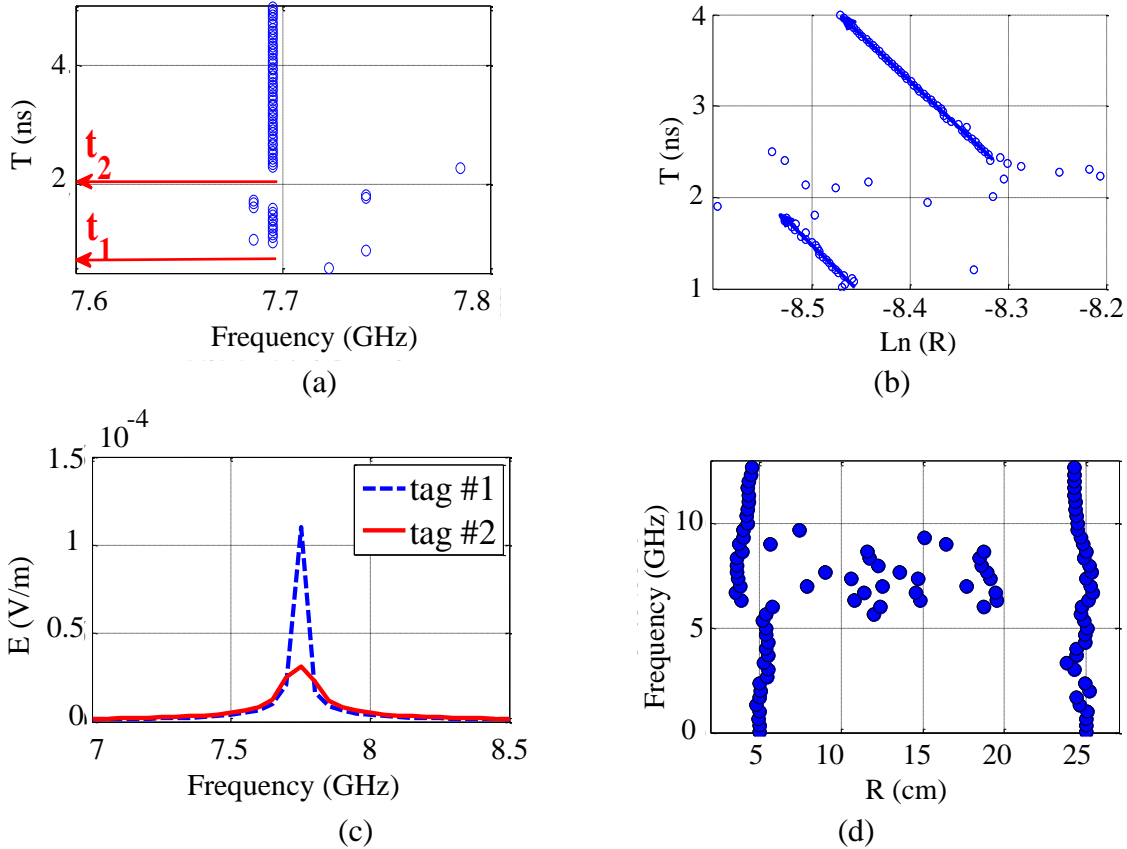


Figure 6.7 (a) Time-frequency and (b) time-residue representation of the signal by applying STMPM with  $T=0.5\text{ns}$ . (c) Separated responses of the tags in frequency-domain (d) space-frequency response after SFMPM [80] (With permission, Copyright© 2014 IEEE).

tag is rotated by  $45^\circ$  along its axis, the electric field of the incident wave is perpendicular to the slot's length and it excites the tag's pole more effectively. According to Figure 6.8, the residue of the first tag does not change while the residue of the second tag shifts proportional to the polarization of the second tag. When the slot's length is in parallel with the incident electric field ( $90^\circ$  rotation), the excited residue of the second tag is small and as can be seen in Figure 6.8, it produces a small shift at the second turn-on time.

In the third example as shown in Figure 6.5b, two 2-bit tags are illuminated by an incident plane wave. The first illuminated tag represents two resonant frequencies at  $f_1 = 5.3\text{GHz}$  and  $f_2 = 7.1\text{GHz}$  (ID = 11) and the second tag has no resonant frequencies (ID = 00). In addition, the RCS of the second tag is much smaller than that of the first. The time-domain and frequency-domain

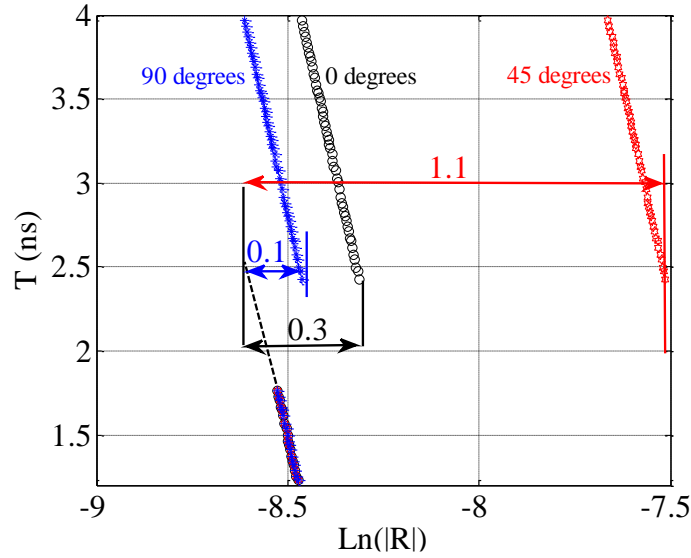


Figure 6.8 6.8. Time-residue diagram for different polarizations [80] (With permission, Copyright© 2014 IEEE).

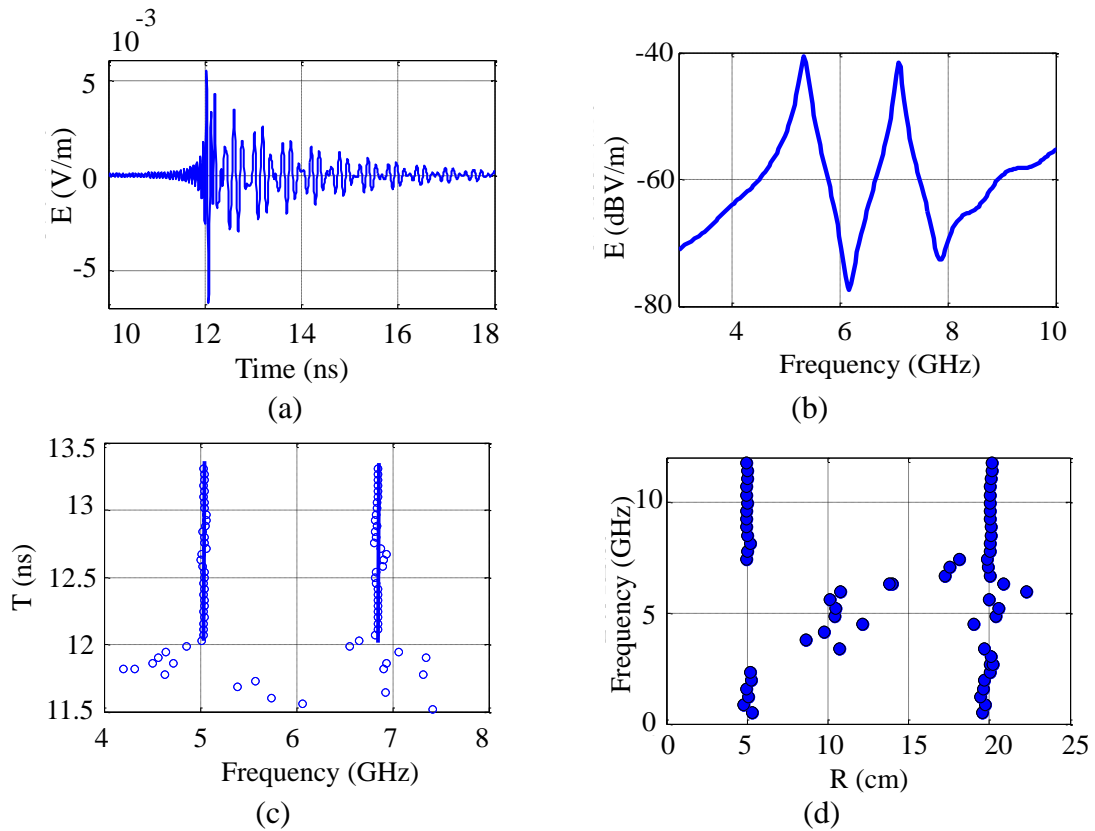


Figure 6.9 (a) Time-domain signal (b) frequency-domain response (c) time-frequency diagram after STMPM (d) space-frequency diagram after SFMPM [80] (With permission, Copyright© 2014 IEEE).

responses are depicted in Figures 6.9a and 6.9b. In this case, the early-time response of the second tag is obscured in the late-time response of the first tag. By applying STMPM and NFMPM to the time-domain and frequency-domain responses, the time-frequency and space-frequency diagrams of the signal are shown in Figures 6.9c and 6.9d. Similar to previous examples, if one knows the turn-on times and poles, the ID of each tag can be found by reconstructing the backscattered signal of each tag. Here, the presence of the second tag cannot be detected without the space-frequency diagram.

As another example, two 3-bit tags are assumed 20cm apart. The configuration and dimensions of the tags are shown in Figure 6.10. The tags represent ID<sub>1</sub>:111 and ID<sub>2</sub>:101. The presence and absence of each assigned resonant frequency represents bits 1 and 0, respectively. The assigned resonances are at  $f_1=6.2\text{GHz}$ ,  $f_2=8.7\text{GHz}$ , and  $f_3=10.9\text{GHz}$ . The simulation is performed in CST Microwave Studio. The pole diagram of the three-bit tag is depicted in Figure 6.11. The illuminating plane wave first hits tag #1 and then tag #2. The time, frequency, time-frequency and time-residue responses of the backscattered field are shown in Figure 6.12. Obviously, the identification process cannot be done perfectly with backscattered frequency-domain response. From the time-frequency response, it can be inferred that the first tag represents three resonant frequencies. At  $t = 1.8\text{ ns}$ , the illuminating wave hits the second tag with ID<sub>2</sub> = 101. According to Figure 6.12c, three resonant frequencies exist in the backscattered signal after  $t = 1.8\text{ ns}$ . In the simulation results, the window length of  $T_w=0.5\text{ns}$  is used. Another important parameter introduced in matrix pencil method (MPM) is  $p$  which is the number of significant decimal digits in the sampled data. It acts as a filtering parameter determining the accuracy of the extracted poles.

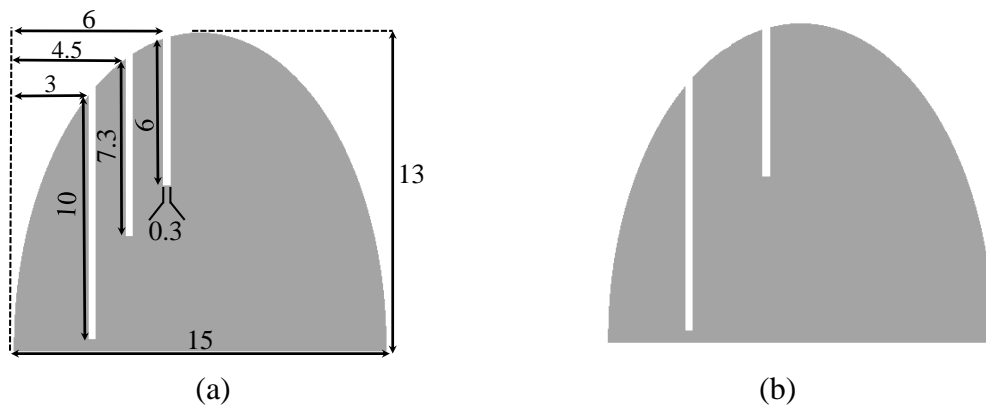


Figure 6.10 Schematic view of the tags. (a) ID<sub>1</sub>:111, (b) ID<sub>2</sub>: 101[80] (With permission, Copyright© 2014 IEEE).

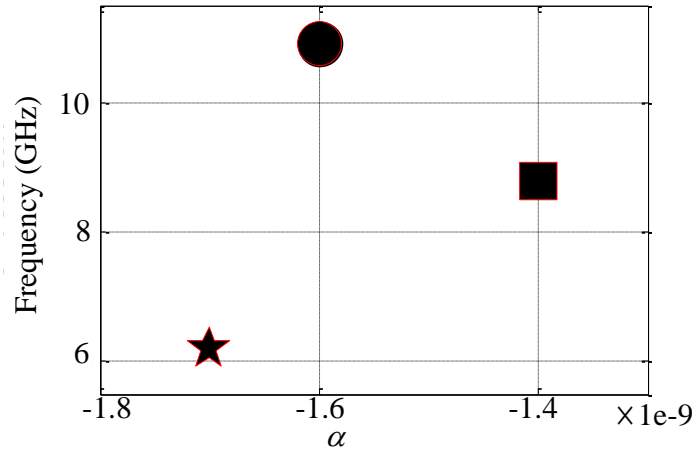


Figure 6.11 Pole diagram of the 3-bit tag [80] (With permission, Copyright© 2014 IEEE).

For noisy data, we usually use  $p \leq 3$ . Here,  $p = 4$  is used for more accuracy. For values less than 4, just two poles of the second tag after  $t = 1.8$  ns are represented in the time-frequency diagram. To identify the ID of the second tag, we use the time-residue diagram shown in Figure 6.12d. As can be predicted by the mathematical formulation in (6.15) and (6.17), the residues of the first and third bits have jumps at the second turn-on time whereas the residues of the second bit are located in a straight line without any jump at the second turn-on time. It confirms that the second resonant frequency after  $t = 1.8$  ns is related to the first tag's response. Therefore the ID of the second tag is  $ID_2 = 101$ . The slopes of the poles in the time-residue diagram are related to the damping factors of the poles in Figure 6.11. As an example, the second pole, which has the lowest damping factor, has the steepest slope in Figure 6.12d.

As a final scenario, the incident wave first illuminates tag #2 with  $ID_2 = 101$ , then second tag with  $ID_1 = 111$ . The time-residue diagram of the backscattered signal is shown in Figure 6.13a. In this case, all the residues have a jump at the second turn-on time. By obtaining the residues and poles of the signal, the contribution of each tag to the backscattered signal is shown in Figure 6.13b.

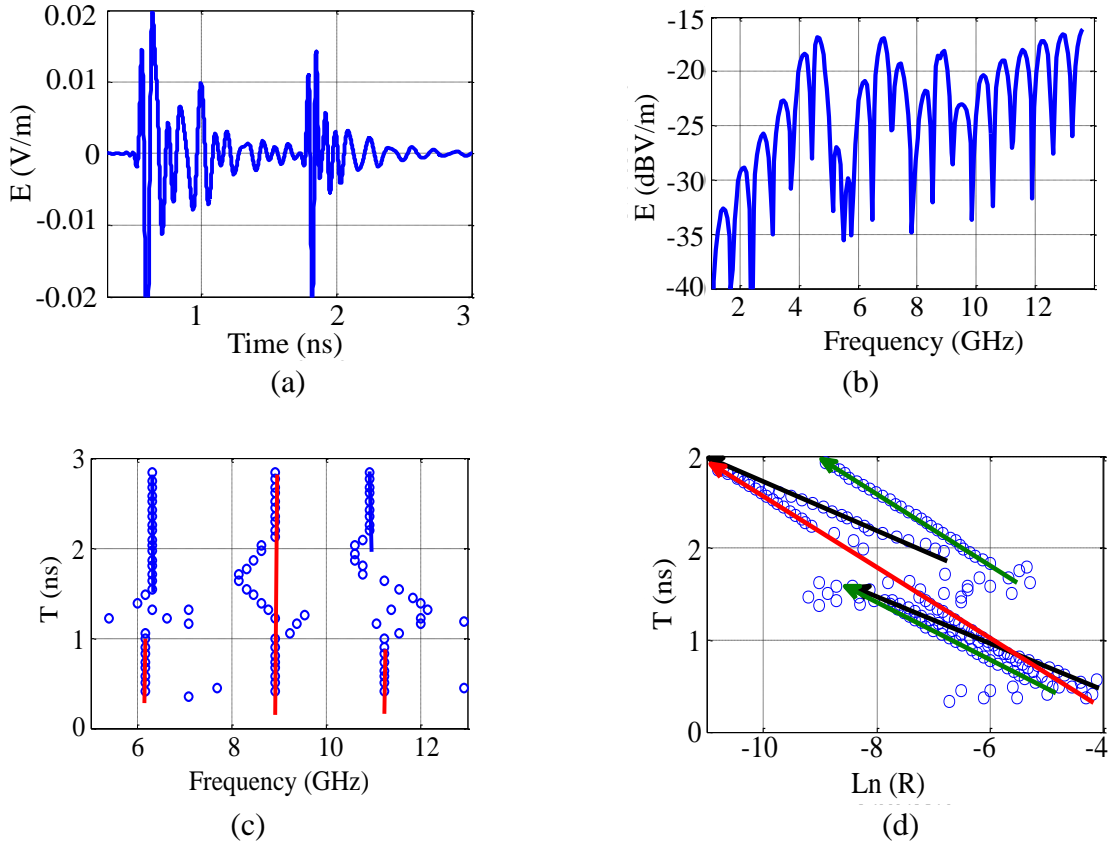


Figure 6.12 (a) Time-domain backscattered signal from two tags spaced by  $R=20\text{cm}$  (b) frequency-domain response (c) time-frequency representation of the signal by applying STMPM with  $T=0.5\text{ns}$ . (d) Time-residue diagram of the signal [80] (With permission, Copyright© 2014 IEEE).

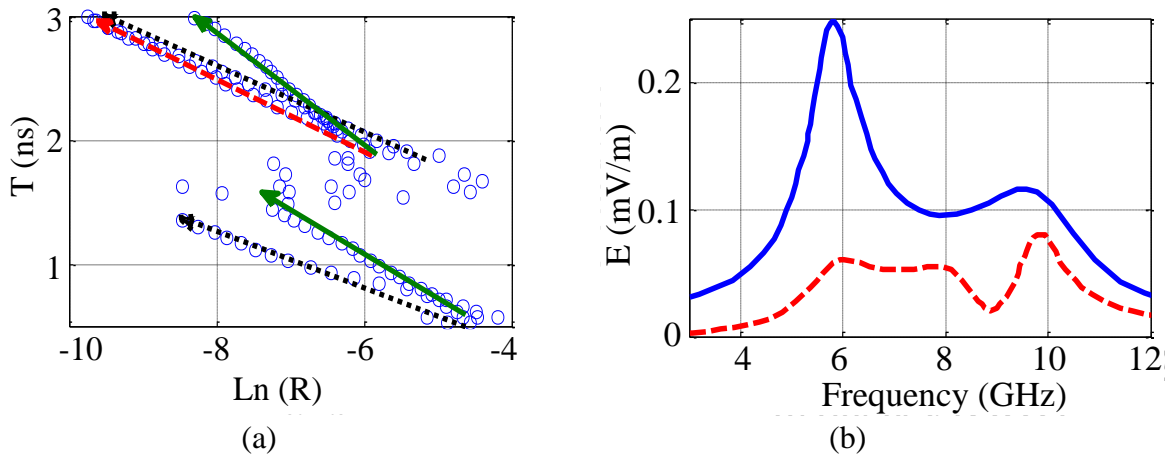


Figure 6.13 (a) Time-residue diagram of the backscattered signal (b) separated responses of the tags in frequency-domain [80] (With permission, Copyright© 2014 IEEE).

### 6.2.1 Space, Time and Frequency Resolutions

Similar to other time-frequency analysis methods such as wavelet transforms, short-time Fourier transform and so on, time and frequency resolutions are key parameters in the proposed method. The resolution in time and frequency domains is strongly dependent upon the length of the sliding window. The frequency resolution is related to the minimum distance in frequency between two adjacent resonant frequencies which can be identified. We discussed about the effect of window length and filtering parameter on the resolution in chapter 5.

Other important parameter affecting the frequency resolution is noise. In order to study the effect of the window length on the frequency resolution, the time-domain signal in (6.18) is considered as the backscattered signal from a two bit tag.

$$s(t) = Ae^{-\alpha t} (\sin(2\pi f_1 t) + \sin(2\pi (f_1 + \Delta)t)) + n(t) \quad (6.18)$$

For more simplicity, the poles are assumed to have the same residue and damping factor and  $n(t)$  is the additive Gaussian white noise. Assuming  $f_1 = 5$  GHz and  $\alpha = 1e8$  (1/s), the minimum required frequency length of window for distinguishing the poles is shown in Figure 6.14 as a function of  $\Delta$  for different SNRs. As it shows, when the resonances of the tag are located closer to each other, we need to increase the window's length to distinguish the resonances. Also, for lower SNR cases, a larger value of  $T_w$  is required to distinguish the poles. The filtering parameter in MPM ( $p$ ) is directly related to SNR. For lower SNRs, a lower value of  $p$  should be employed in the algorithm

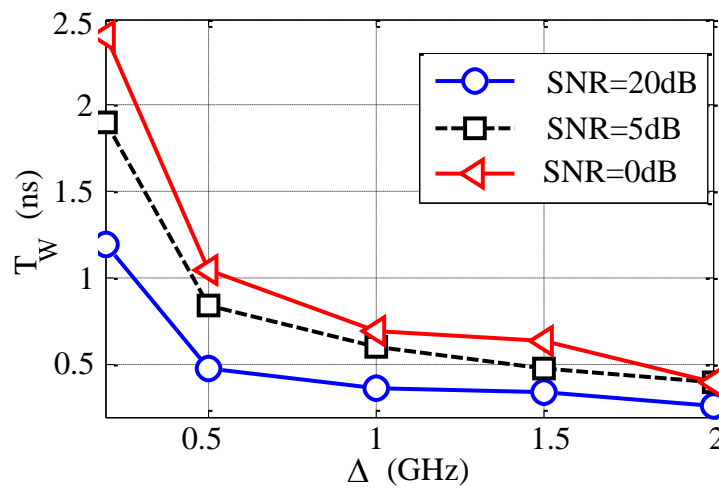


Figure 6.14 Minimum required window length as a function of  $\Delta$  for different SNRs [80] (With permission, Copyright© 2014 IEEE).

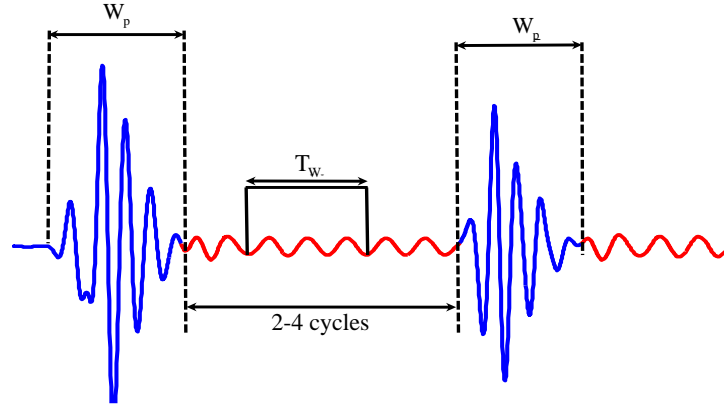


Figure 6.15 6.15. Backscattered signal from two single-bit tags [80] (With permission, Copyright© 2014 IEEE).

so as not to allow the poles due to noise to come into the picture. Here, the value of  $p$  is chosen as 5, 4, and 3 for SNR = 20, 5, and 0 dB, respectively. By increasing the length of time-window, frequency resolution is increased which deteriorates the time resolution. For example, the turn-on time in Figure 6.12c is located in between 1.5ns and 2ns which causes a significant error in calculating locations of the tags. On the other hand, the range resolution depends on the pulse width of the incident wave. Figure 6.15 shows the backscattered signal from two single-bit tags. The early-time response of the tags is a replica of the incident wave whose width can be approximated by [87]

$$W_p = \frac{1}{B} = \frac{1}{(10.6 - 3.1)GHz} = 0.13ns \quad (6.18)$$

where  $B$  is the operational bandwidth of the incident wave (3.1-10.6 GHz). Hence, the range resolution can be calculated as

$$\Delta R = \frac{cW_p}{2} = 2cm \quad (6.20)$$

In practical applications, we usually need a few cycles of the sinusoidal signals in the window to extract the poles. Considering the worst case as  $f_{min} = 3.1$  GHz, the minimum range resolution at which the tags and their IDs can be distinguished using the arrival times of the early-time responses is between 7-15cm.

### 6.3 Separating the Early-Time and Late-Time Responses for Detection, Identification, and Localization of Chipless RFID Tags

In previous section, the turn-on time and IDs of the tags were obtained by applying STMPM and NFMPM to the time-domain and frequency-domain backscattered signal received by the antenna. As mentioned, in multi-tag applications, the resolution in space, time and frequency plays an important role in detection, identification and localization of the tags. A few cycles of the late-time response is required in order to place the sliding window in the late time for extracting the poles of the tag. The detection of the tags is also very challenging when the tags are located less than 10cm away from each other. In such cases, one needs wider bandwidth in order to decrease the resolution in space. Based on the algorithm proposed in Figure 6.4, in multi-bit tags with high quality CNRs, the late-time poles must be removed from the frequency response in order to extract the delay-times of the scatterers accurately by applying NFMPM to the frequency-domain response. The accurate calculation of amplitude and phase of the residues is not easy, especially in low-Q resonances of the tags. By employing an optimization process in the detection procedure, the accuracy of the approach is improved which complicates the processing calculations in the reader. According to section 5.3, by sliding the window along the time-domain signal, the position of the impulses in the received signal can be distinguished by monitoring the zero-crossing points in time-damping factor diagram. This technique is very efficient when multiple reflections exist in the signal.

As an example, Figure 6.16 shows a 4-bit tag located 30 cm away from a TEM horn antenna. The dimension of the antenna is depicted in Figure 6.16. The reflection coefficient of the antenna, in the presence and absence of the tag, is seen in Figure 6.17a. The reflection coefficient of the antenna in time domain is seen in Figure 6.17b. After multiple reflections from the feeding point and antenna aperture, the radiated field interrogates the tag. Since the embedded resonances of the tag have high quality factors, the late-time response from the tag stays for long time. The multiple reflections from the antenna and tag are located in the let-time response of the tag. For better illustration, by applying STMPM to the time-domain reflection coefficient, the extracted damping factors are shown in Figure 6.17c versus the center of window. The location of multiple reflections from the antenna aperture are located at zero-crossing points of the damping factors. The time-

frequency representation of the signal is shown in Figure 6.17d. The resonant frequencies of the tag are stably located at  $f = 4.8$  GHz,  $f = 5.2$  GHz,  $f = 6$ GHz, and  $f = 6.4$  GHz.

The proposed technique can be efficiently used in detecting multiple tags located close to each other. As an example, Figure 6.18 depicts the time-domain and time-damping factor diagrams of the received signal when two 3-bit tags are located in the reader area. Three cases as  $d = 20$  cm,  $d = 10$  cm and  $d = 4$  cm are considered here. Since the early-time responses of the tags are located very close to each other and are followed by the late time responses of the tags, the extraction of the scattering centers (here the tags) from the time-domain response is very challenging; While, by applying the proposed technique, the location of the tags can be obtained from the zero-crossing times in time-damping factor diagram.

## 6.4 Measurement Results

Three 3-bit tags with IDs of  $ID_1 = 101$ ,  $ID_2 = 111$ , and  $ID_3 = 011$  are designed based on the proposed technique in Chapter 3. The second and first bits of tags #1 and #3 are respectively nulled by soldering a stub in the middle of the related slots. This manual soldering causes a small shift in the resonant frequencies which is negligible in our analysis. Two measurements are performed: First, according to Figure 6.19, two tags ( $ID_1$  and  $ID_2$ ) are located 20cm away from each other in front of a UWB quad-ridge horn antenna. Then the third tag is located 15cm from the second tag. The antenna is connected to the network analyzer and the  $S_{11}$  is measured while the frequency is swept from 10 MHz to 25 GHz. This wide frequency range is chosen for better resolution in the time domain. For practical applications, the standard frequency band (3.1-10.6 GHz) can be used for measurement. The data measured by the network analyzer cannot be used directly to extract the poles because it includes undesired components such as the contribution of TEM horns and the scattering from background objects in addition to the tag response. As a result, another measurement is performed without the presence of the tags to subtract the effect of the background objects from the first measured data. The input power is 18dBm. The time-domain backscattered signal for two cases is shown in Figure 6.20a. By applying STMPM to the time-domain response, the time-frequency diagram of the signal is obtained, shown in Figure 6.20b. The optimum values of  $p$  and  $T_w$  are used at each snapshot of time for extracting the poles. Here, we used  $p = 4$  and  $T_w = 0.5$  ns for  $3.5\text{ns} \leq t \leq 5.3\text{ns}$  and  $p = 5$  and  $T_w = 0.6$  ns for  $5.3\text{ns} \leq t$ .

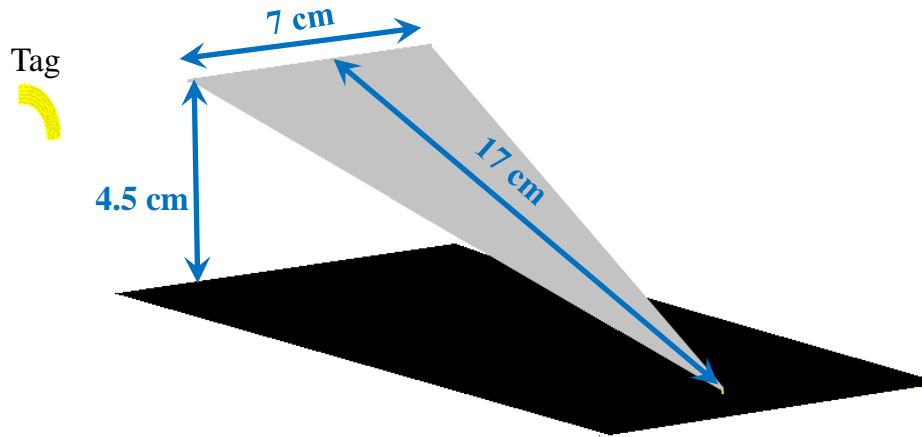


Figure 6.16 A 4-bit chipless RFID tag located 30 cm away from the antenna.

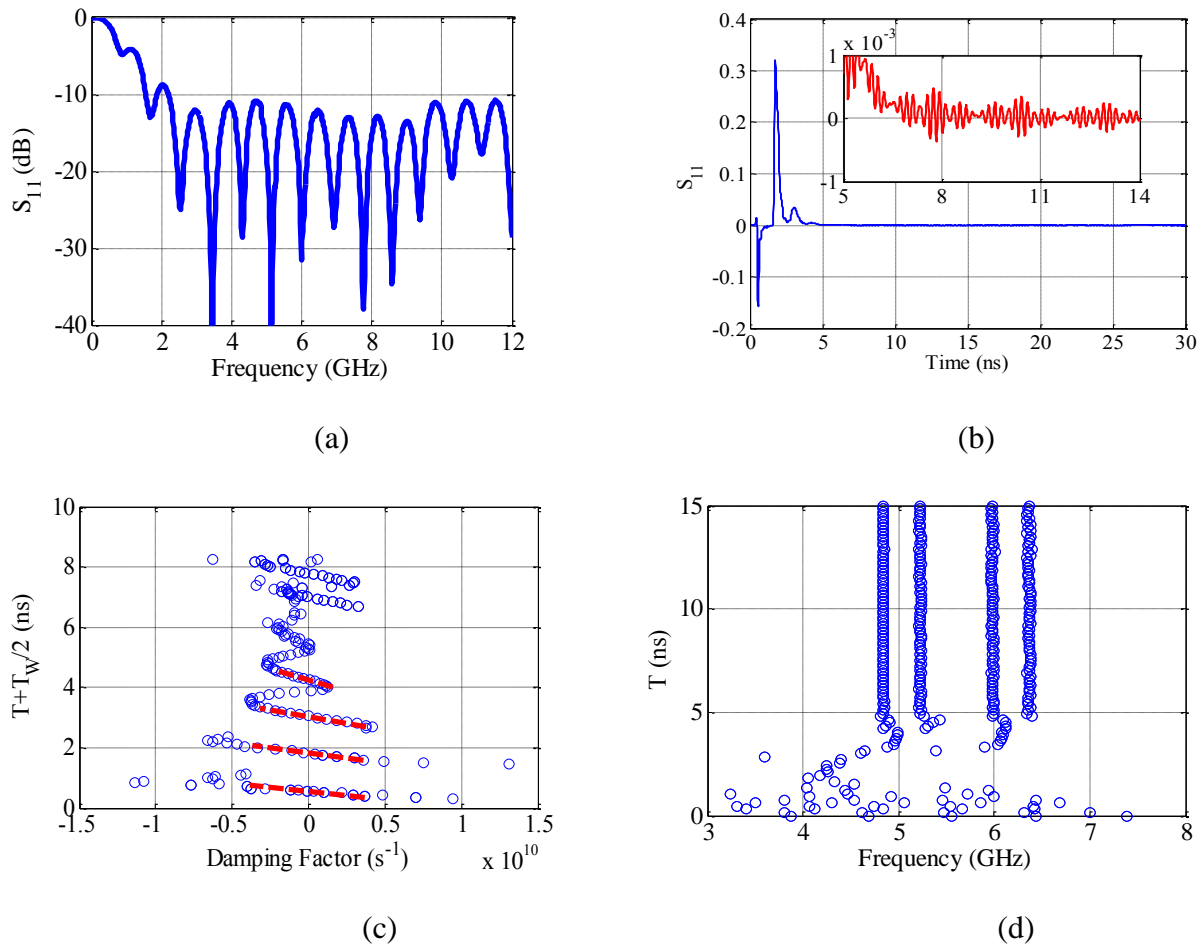
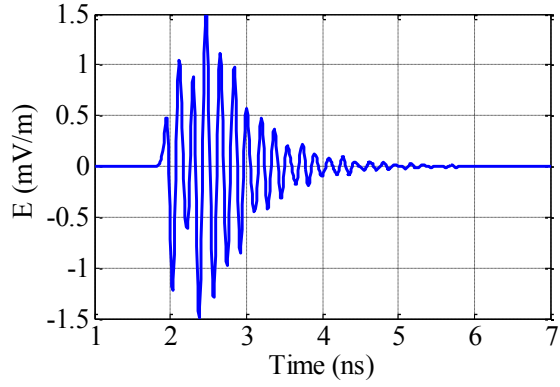
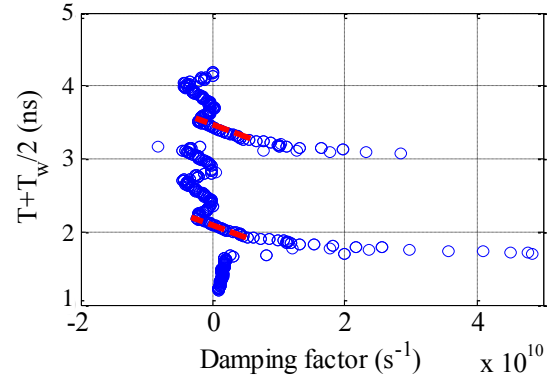


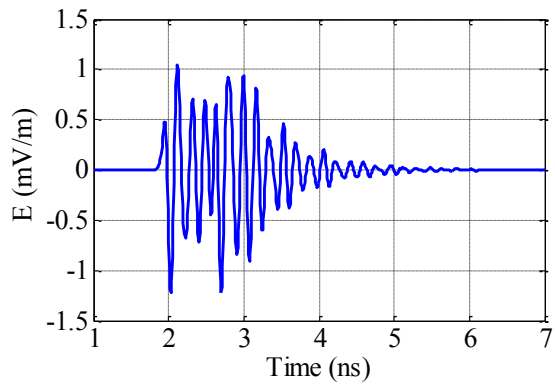
Figure 6.17 Reflection coefficient of the antenna loaded by tag in (a) frequency domain, (b) time domain, (c) Time-damping factor diagram and (d) Time-frequency diagram of the  $S_{11}$ .



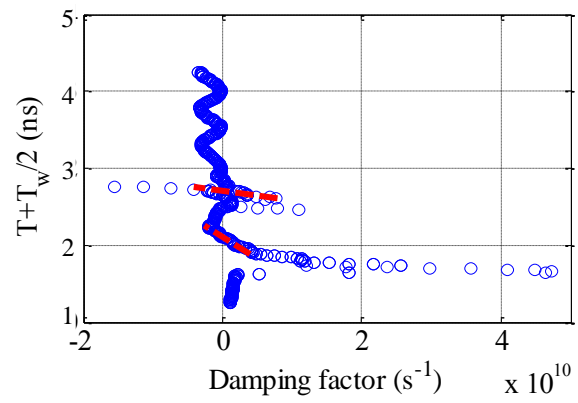
Time-domain signal for  $d = 20$  cm



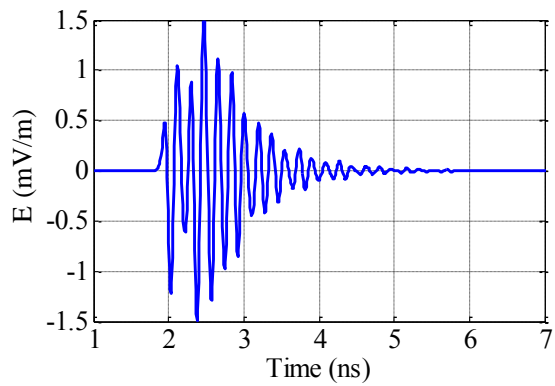
Time-damping factor for  $d = 20$  cm



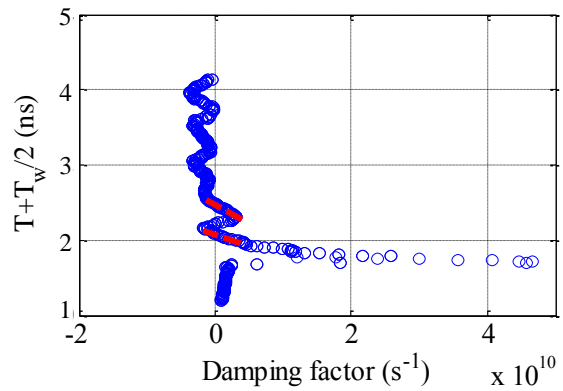
Time-domain signal for  $d = 10$  cm



Time-damping factor for  $d = 10$  cm



Time-domain signal for  $d = 4$  cm



Time-damping factor for  $d = 4$  cm

(a)

(b)

Figure 6.18 (a) Time domains and (b) Time-damping factor diagrams of the backscattered signal from two tags.

These parameters are chosen based on number of resonances in the snapshot of time and SNR. Due to the limited time resolution, the exact turn-on times cannot be obtained from this diagram. The exact turn-on time is crucial in reconstructing the tag responses because the time-domain reconstructed signal is very sensitive to phase (or turn-on times). As can be seen in Figure 6.18, the second set of poles excited at  $t = 5.3\text{ns}$  have different residues than the poles excited at  $t = 3.9\text{ns}$ . Thus, the first and second tags represent two and three resonant frequencies, respectively. At  $t = 6.2\text{ ns}$ , the poles of the third tag are excited. The third tag is rotated  $45^\circ$  with respect to incident electric field. The resonant frequencies and ID of each tag can be identified from the time-frequency and time-residue diagrams. In Figure 6.22a, the real and imaginary parts of the backscattered signal versus frequency are shown. Following the algorithm presented in the flowchart of Figure 6.4, by suppressing the late-time poles of the tags, the space-frequency diagram of the response is shown in Figure 6.22b for two cases. Here, the accurate turn-on times (or equivalently locations of the tags) are depicted in a space-frequency diagram

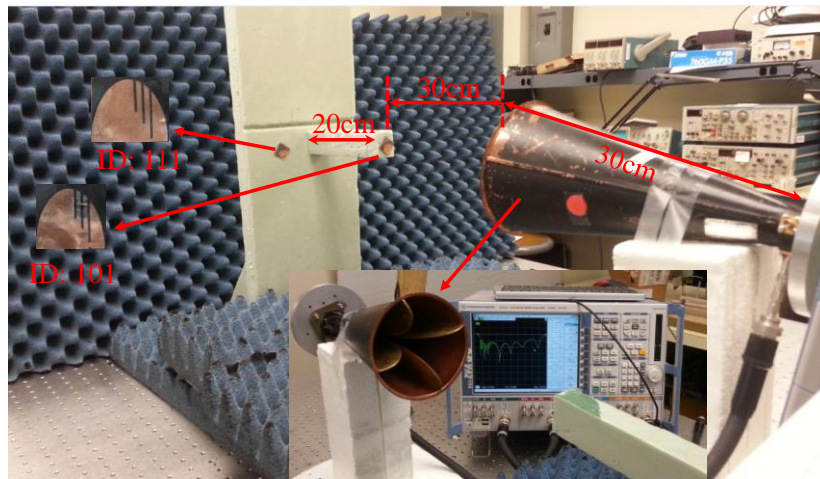


Figure 6.19 Set-up for the measurement of backscattered signal from two tags [80] (With permission, Copyright© 2014 IEEE).

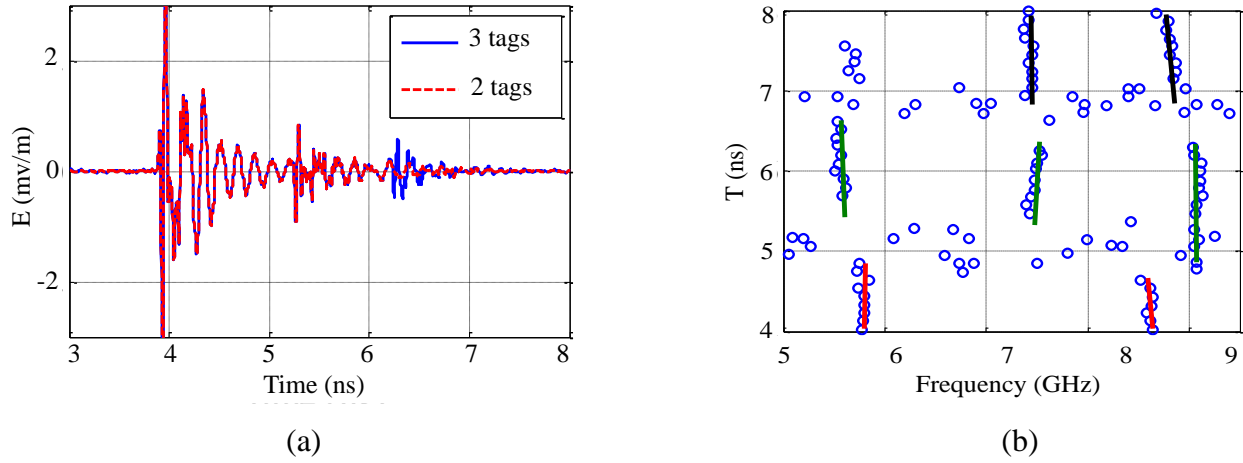


Figure 6.20 (a) Time-domain backscattered signal from the tags, (b) Time-frequency representation of the backscattered signal [80] (With permission, Copyright© 2014 IEEE).

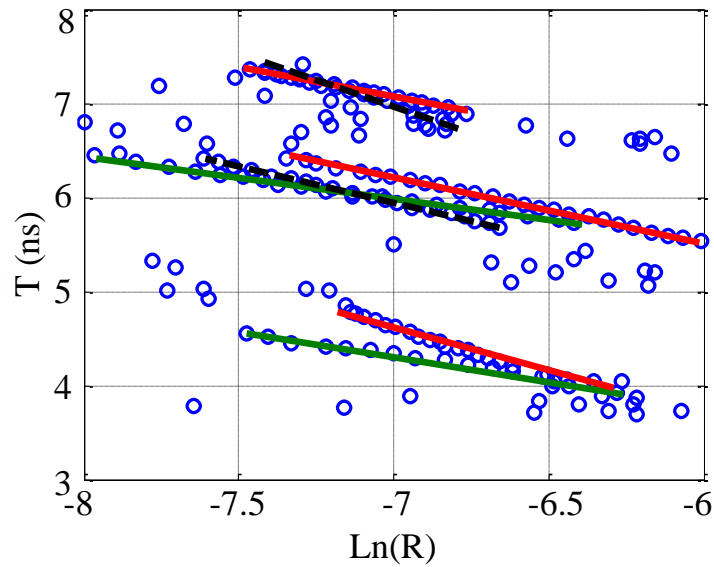


Figure 6.21 Time-residue representation of the backscattered signal [80] (With permission, Copyright© 2014 IEEE).

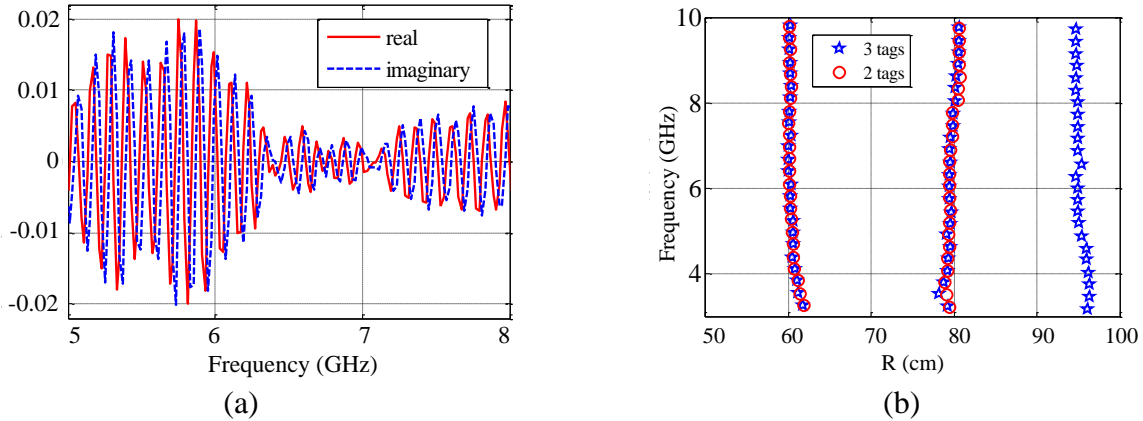


Figure 6.22 (a) Real and imaginary parts of the measured backscattered signal, (b) Space-frequency diagram of the measured response [80] (With permission, Copyright© 2014 IEEE).

## 6.5 Localization of Chipless RFID Tag [88]

In tracking applications, it is desired to know the precise location of the tag in the reader area. For example, by knowing the tag location, the reader antenna can direct the antenna beam to the object, suppressing the interference signals from background objects [89]. In addition, by enabling this capability in conventional chipless RFID systems, it can be used in a wider range of crucial applications such as health-care monitoring in hospitals. For example, in microwave hyperthermia of breast cancer [90], the accurate localization of the tumor is necessary. Additionally, the localization technique is useful in the positioning of chipless RFID sensors placed in different locations of the medium in order to sense the density of a particular gas [91] or the humidity of the medium [78]. In such cases, because of the inhomogeneity of the material under consideration, multiple tags are used in different places. Therefore, the accurate localization and identification of the tags is an essential part of the measurement set-up.

Ranging techniques can be categorized as time-based ranging and received signal strength-based ranging [92]. The former is based on the time of arrival (TOA) of the signal while later is based on the principle that the greater the distance between two nodes, the weaker their relative received signals are. In practical applications, taking advantage of ultra-wideband technology in the detection process, the first method shows better accuracy and precision than the second [92]. However, there are some factors which affect the performance of the ranging process in the reader. In ideal propagation conditions, without considering multipath and interference phenomena in our

discussion, the ranging accuracy for SNR larger than 15dB is limited to the Cramer-Rao (CR) bound as [92, 93]

$$E\{R\} \geq \frac{c^2}{8\pi^2 \beta^2 SNR} \quad (6.21)$$

where  $E\{\cdot\}$  is the mean square error (MSE),  $R$  accounts for the estimation error,  $c$  is speed of light in free space and  $\beta$  represents the effective bandwidth of signal [94]. For lower SNRs, the estimation error is limited to a stricter bound, called the Ziv-Zakai bound [92]. The formulation is more difficult for multipath effects. As the simplest case, we consider the CR bound in (6.21). According to (6.21), the ranging error is strongly dependent on the SNR and the pulse shape. Figure 6.24 shows the ranging error as a function of SNR for CR bound in the presence of AWGN noise. The frequency bandwidth is 3.1-10.6 GHz. For SNRs lower than 10dB, the Ziv-Zakai bound is more accurate which shows worse ranging error than the CR bound. It is seen that by decreasing SNR, the ranging error is increased. This may happen when the tag is located at larger distances from the reader antenna. In addition, the detection technique plays an important role in ranging calculations. In most applications, classical matched filter (MF) TOA estimator is used to find the time when the signal has its maximum peak [92]. This strategy might not be the best method for localizing chipless RFID tags. The backscattered response from the tag includes early-time and late-time responses. In the cases where the early-time response is much stronger than the late-time response, the aforementioned technique works well. However in multi-bit tags, the late-time response of the tag is composed of high-Q sinusoidals corresponding to the embedded poles on the tag. At time instances when some sinusoidals are in-phase, their effect might be constructive enough to strengthen the late-time response at those time instances. Additionally, if two or more tags are located in the reader area, the early-time response of the second tag might be hidden in the late-time response of the first illuminated tag. Also, for bi-static cases, there is no guarantee that the early-time response is stronger than the late-time response.

Although many efforts have been made in the design and implementation of chipless tags, there is a demanding request for improved detection techniques in the reader, especially for localization applications. In [95], a space-time-frequency method has been suggested for the localization of the tags. Later on, the proposed method in [95] was confirmed by experimental results in [89].

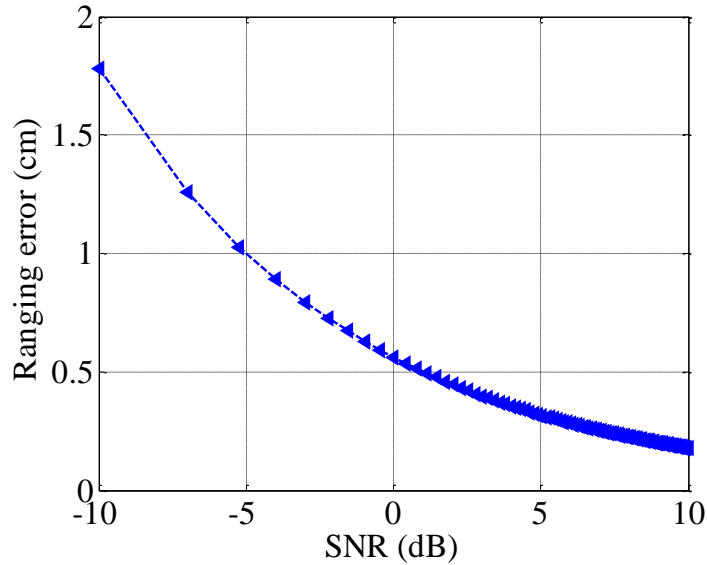


Figure 6.23 Ranging error versus SNR [88] (With permission, Copyright© 2014 IEEE).

The localization is based on the employment of three antennas spaced at different points in the reader area. For larger spaces, the area can be divided into some unit cells covered by some antenna arrangement. Although the authors in [89] did not consider the circumstances where the late-time response is stronger than the early-time part and also when multiple multi-bit tags are present in the reader area, the method performs well within 2.1cm and 3.5° error in distance and angle for a single tag. Here, a new technique is introduced for accurate localization of chipless RFID tags in the reader area. Similar to [95], three antennas are used in the unit cell. Assuming the reader area as the scattering area, the tags can be regarded as the scattering centers of the medium. Based on Altes' model, the early-time response from the reader zone can be expanded versus the localized impulse responses of the scattering centers. By applying NFMPM, which is the dual of the short-time matrix pencil method (STMPM), to the frequency-domain response of the tag at each antenna port, its location can be easily found by some mathematical manipulations. The major advantages of the technique proposed herein are as follows:

- 1) An easy-to-implement approach is proposed to qualitatively improve localization accuracy in chipless RFID systems.
- 2) This technique is applicable for localization of multiple multi-bit tags in the reader zone.
- 3) By obtaining the accurate value of turn-on time of the tag, its ID can be easily found by applying STMPM to the time-domain response.

- 4) By taking advantage of the three-antenna implementation in the unit cell, the effects of noise and polarization issues in the identification can be reduced considerably.
- 5) The interferences from adjacent unit cells can be strongly eliminated from the backscattered signals.

Figure 6.24 illustrates the system configuration arranged for the localization of chipless RFID tags. The area under consideration is subdivided into unit cells. Each unit cell is covered by three ultra wideband antennas spaced by  $120^\circ$  with respect to the center of the unit cell. The frequency of operation is assumed to be 3.1-10.6 GHz compatible with FCC requirements. By employing three antennas at each unit cell and obtaining the turn-on time of the tag (or equivalently the distances from the tag to the antennas), the position of the tag can be calculated easily. In addition, this arrangement has some other benefits which improves the detection and identification capability of the reader. By increasing the distance between tag and antenna, the amplitude of both early-time and late-time responses decrease which leads to a decrease in SNR. This results in two different drawbacks in the localization and identification of the tags. According to (6.21), by degrading SNR of the received signal, the ranging accuracy deteriorates. Also, by increasing the distance and adding extra noise to the signal, the extraction of the embedded poles of the tag becomes extremely challenging. With a three-antenna arrangement and some power considerations, we can ensure that the SNR of the backscattered signal from the tag is above a threshold for at least one of the antenna ports. Hence, we can obtain the signature of the tag by analyzing the strongest backscattered received signal from the tags.

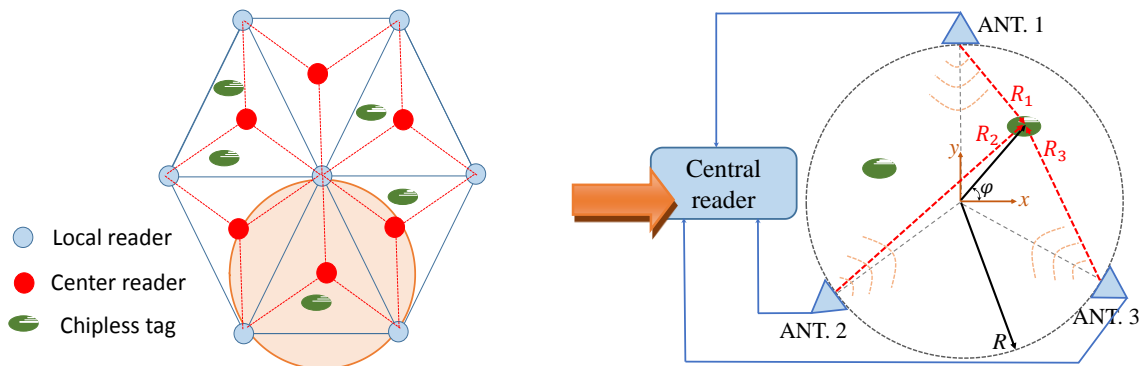


Figure 6.24 System configuration for localizing chipless RFID tags in the reader area [88] (With permission, Copyright© 2014 IEEE).

Furthermore, by receiving the backscattered signal from three different directions, the direction and polarization dependency of the tag can be mitigated. In conclusion, a three-antenna configuration in a unit cell facilitates both localization and identification processes in the reader part. According to Figure 6.24, three antennas in the unit cell are spaced at  $120^\circ$  on a circle of radius  $R$ . Assuming multiple multi-bit chipless RFID tags present in the reader area, the backscattered responses at the antenna ports contain the reflections from the tags, antennas and interferences from the adjacent unit cells. Considering  $s_i(t)$  as the input signal at the  $i^{\text{th}}$  antenna port, the backscattered signal can be written as the combination of early-time and late-time responses of the scattering objects as

$$r_i(t) = e_i(t) + l_i(t) = \sum_{n=1}^{N_t+N_o} \left[ e_{n,i}(t) + \text{Re} \sum_{m=1}^{M_n} R_{n,i}^m e^{-s_n^m t} \right] U(t - t_{n,i}) \quad (6.22)$$

where  $e_{n,i}$  is the early-time response of the  $n^{\text{th}}$  object at the  $i^{\text{th}}$  antenna port. The second part in the bracket contains the late-time responses from the objects which based on singularity expansion method (SEM) is summed over all natural resonances ( $s_n^m$ ) with weighting residues ( $R_n^m$ ).  $U(\cdot)$  is the Heaviside function and  $t_{n,i}$  is the turn-on time of the  $n^{\text{th}}$  scatterer at the  $i^{\text{th}}$  antenna port.  $N_t$  is assumed to be the number of the tags in the cell,  $N_o$  is the number of signals other than the tag's reflections coming from background objects and interferences, and  $M_n$  is the number of bits embedded on the  $n^{\text{th}}$  tag. Based on Altes' model, the early-time response from each scatterer can be expanded versus the impulse response of the localized scattering centers as

$$e_{n,i}(t) = s_i(t) * \sum_{p=-\infty}^{+\infty} a_{n,p,i} \delta^{(p)}(t - t_{n,i}) \quad (6.23)$$

where  $t_{n,i}$  is the delay-time from the  $i^{\text{th}}$  antenna to the  $n^{\text{th}}$  scatterer. The impulse response of the  $n^{\text{th}}$  scatterer in (6.23) is summed over the integrals and derivatives of the Dirac-delta function. Here, the negative and positive values of  $p$  refer to the  $p^{\text{th}}$  integral and derivative of the delta function, respectively. For simple scatterers as in our case, one term of the summation might be enough. By inserting (6.23) in (6.22), the received signal in the Laplace domain can be written as

$$R_i(s) = \sum_{n=1}^N \left[ \sum_{p=-\infty}^{+\infty} A_{n,p,i}(s) e^{-st_{n,i}} + \sum_{m=1}^{M_n} \frac{R_{n,i}^m}{s - s_n^m} \right] \quad (6.24)$$

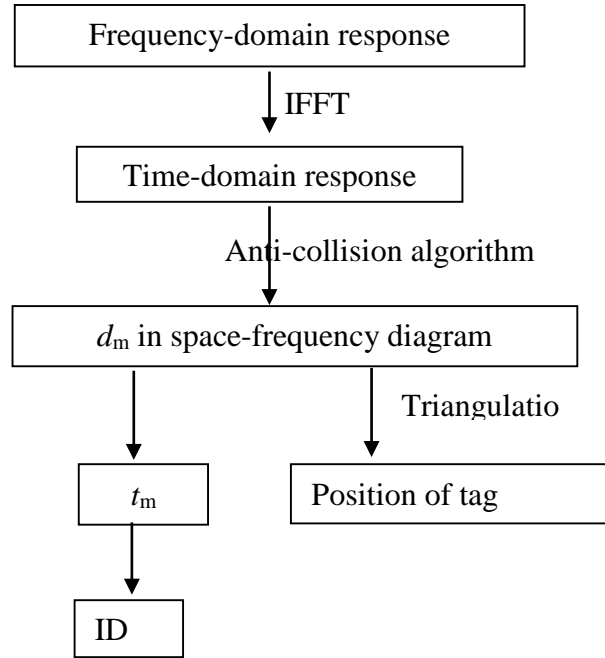


Figure 6.25 Flowchart of proposed localization algorithm [88] (With permission, Copyright© 2014 IEEE).

in which  $A_{n,p,i}(s) = a_{n,p,i} s^p S(s)$ . By employing the method proposed in Section 6.2, suppressing the late-time response and applying the narrow-frequency matrix pencil method (NFMPM) to the frequency-domain of early-time response, the accurate values of roundtrip time of the scattering centers,  $t_{n,i}$ , can be obtained. In this approach, a sliding-frequency window is moved along the frequency axis and the matrix pencil method is applied to each window. By converting the extracted complex times to distance as  $d_m = ct_m/2$  and plotting  $d_m$  versus sliding frequency, the distance from the tags to the antenna can be monitored in the space-frequency diagram. Knowing the distance of a tag from the antennas, its location can be calculated with respect to the reference point at the center of the unit cell. After obtaining the turn-on times of the tags, the time-window can be adjusted in the late-time response of the tag in order to extract the corresponding poles of the tag. The flowchart seen in Figure 6.25 summarizes the proposed localization technique.

As an example, the 3-bit tag under consideration is shown in Figure 6.26. It consists of three quarter-wavelength slots resonating at  $f_1=5.1\text{GHz}$ ,  $f_2=7.1\text{GHz}$ , and  $f_3=8.1\text{GHz}$ . The simulated and measured RCS of the tag is depicted in Figure 25 when the incident electric field is perpendicular to slot length. Based on the RCS of the tag and sensitivity of the receiver, the input power can be adjusted so as to maintain an SNR above a certain threshold. For larger tags, the reflected signal

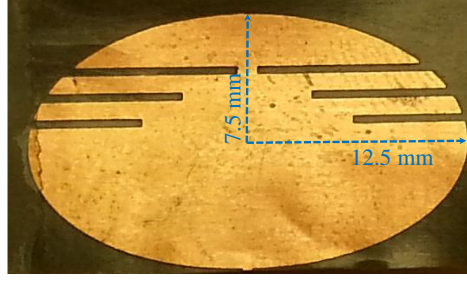


Figure 6.26 Configuration of the 3-bit fabricated tag [88] (With permission, Copyright© 2014 IEEE).

is stronger which results in lower ranging error based on (20). According to [3], the minimum SNR at which the tag's ID can be accurately identified is about 15dB. Assuming the tag is located in the far field of the antenna, the radar budget equation can be written in the frequency domain as

$$\frac{P_r}{P_t} = \frac{A^2 \delta(f) f^2}{4\pi c^2 R^4} \quad (6.25)$$

where  $P_r$  and  $P_t$  are the received and transmitted power at the antenna with the effective area of  $A$ . The quantity  $\delta$  is the frequency-dependent RCS of the tag as shown in Figure 25,  $c$  is the speed of light in free space and  $R$  is distance from tag to antenna. A TEM-horn antenna with a length of 30 cm and effective aperture surface area of 150 cm<sup>2</sup> is connected to a network analyzer to measure the backscattered signal from the tag. Assuming  $R_{\max} = 100\text{cm}$  as the maximum detectable range, the ratio of received to transmitted power at the antenna is shown versus frequency in Figure 6.28. The measured received noise by the antenna in the laboratory environment is about -60 dBm. The peaks of the frequency-domain response in Figure 6.28 are associated with the resonant frequencies of the tag. As it shows, at the first resonant frequency of around  $f = 5\text{GHz}$ , the value of  $P_r/P_t$  is -50dB. This value is the combination of the early-time response and the corresponding residue of the late-time response of the tag at  $f = 5\text{GHz}$ . For high-Q resonances, the late-time residue is effectively dominant. Assuming 10dB for the early-time response and polarization mismatch, transmitted power should be adjusted to have  $P_t > 10\text{dBm}$  in order to keep the SNR above 15 dB. By choosing  $P_t = 20\text{dBm}$ , the backscattered response from the tag is calculated by subtracting the resultant  $S_{11}$  at the antenna port from the off-tag measured  $S_{11}$ . In Figure 6.29, the measured backscattered electric field from the tag is depicted for different distances of the tag from the antenna. For better comparison, the electric fields are shifted up along E-axis. It is seen that by

increasing the distance, the backscattered response becomes noisy. In order to extract the resonances of the tag from the backscattered signal, short-time matrix pencil method (STMPM) is applied to the time-domain signal. As an example, the frequency-domain, time-domain, time-frequency, and time-residue responses of the backscattered signal from the tag located at 30 cm from the antenna are shown in Figure 6.30. From the time-domain response, it is seen that  $t=2\text{ns}$  at which the signal has its maximum amplitude can be considered as the roundtrip time from the

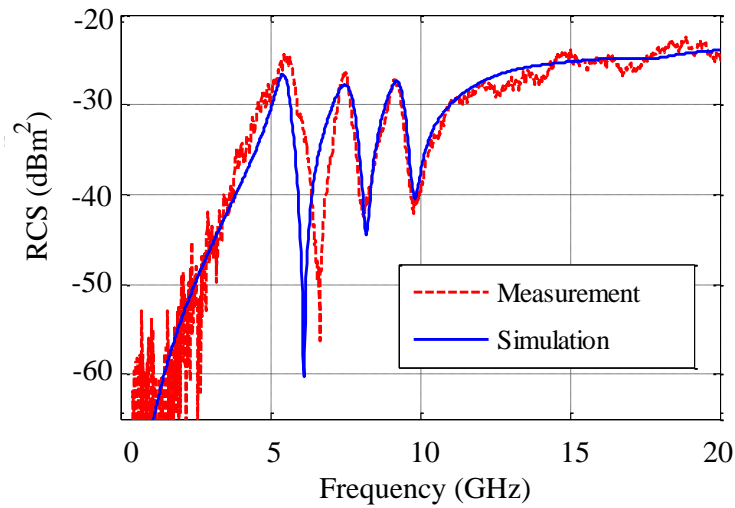


Figure 6.27 Simulated and measured RCS of the tag when the incident electric field is perpendicular to slot length [88] (With permission, Copyright© 2014 IEEE).

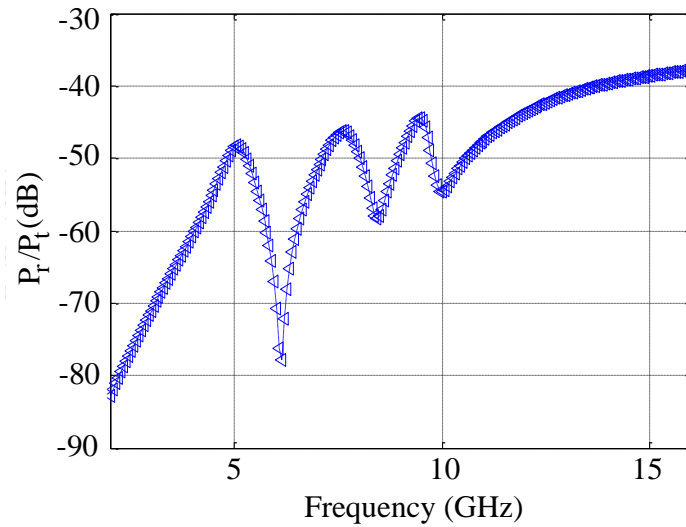


Figure 6.28 Normalized received power at the antenna versus frequency [88] (With permission, Copyright© 2014 IEEE).

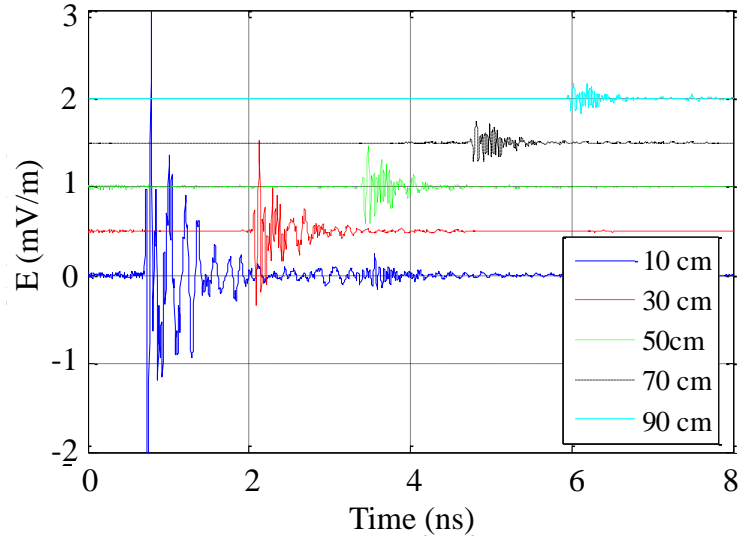


Figure 6.29 Measured time-domain response from the tag for different distances [88] (With permission, Copyright© 2014 IEEE).

tag to the antenna. The time-domain response is composed of early-time and late-time responses. The early-time part emanates from the scattering centers of the tag and depends strongly upon the incident angle and polarization. The late-time response is the summation of damped sinusoids corresponding to the slot poles. All the information embedded on the tag is included in the late-time response. The time-frequency diagram of the response shows the resonant frequencies (frequency-domain data) and also, the turn-on times (time-domain data) of the resonances in time. Because of limited time resolution in time-frequency analysis, the exact turn-on time cannot be extracted, especially when multiple tags are present in the reader area. It also leads to considerable error in ranging calculations. The real and imaginary parts of the backscattered signal are shown in Figure 6.31 versus frequency. By applying NFMPM to the frequency response, the distance of the tag from the antenna is illustrated for different cases in a space-frequency diagram in Figure 6.32. According to this diagram, the scattering centers, which in this case are the tags, reflect the incident pulse. The accuracy of the method is shown for different distances from tag to antenna. The proposed method is applied to the cases where multiple tags are located in the main beam of the antenna.

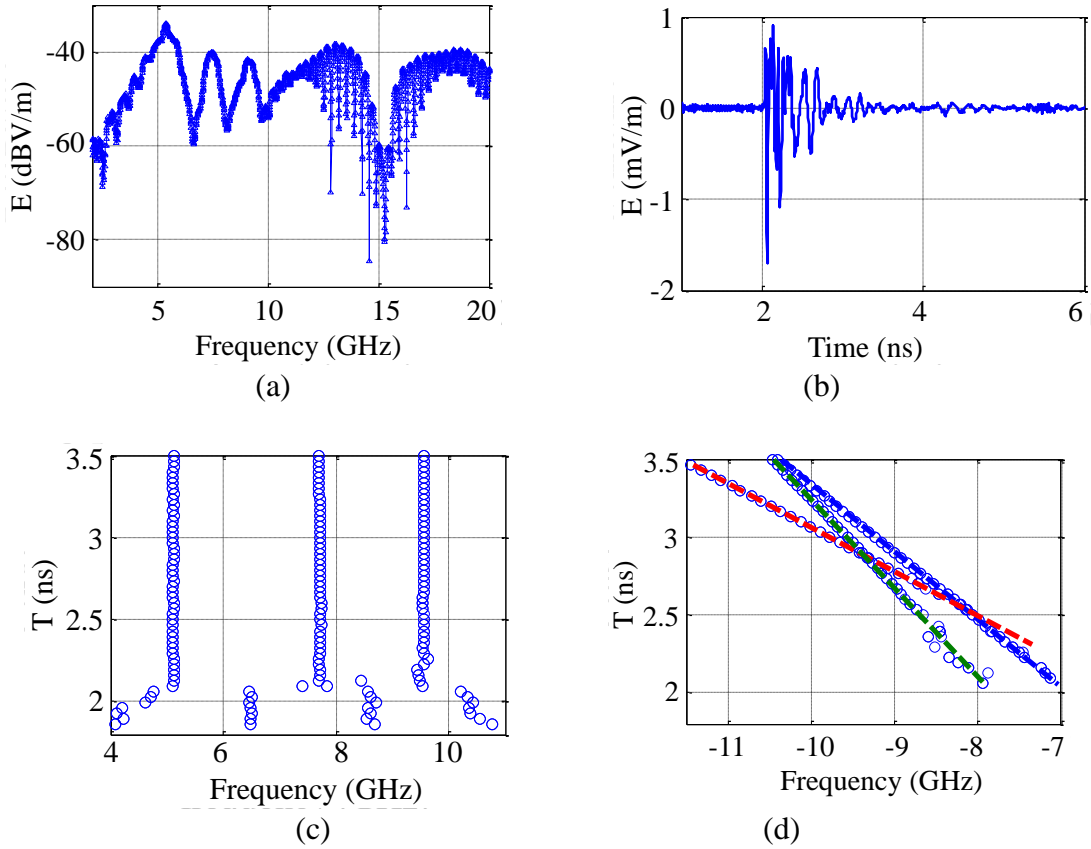


Figure 6.30 (a) Frequency-domain, (b) time-domain, (c) time-frequency and (d) time-residue representation of measured backscattered signal from the tag [88] (With permission, Copyright© 2014 IEEE).

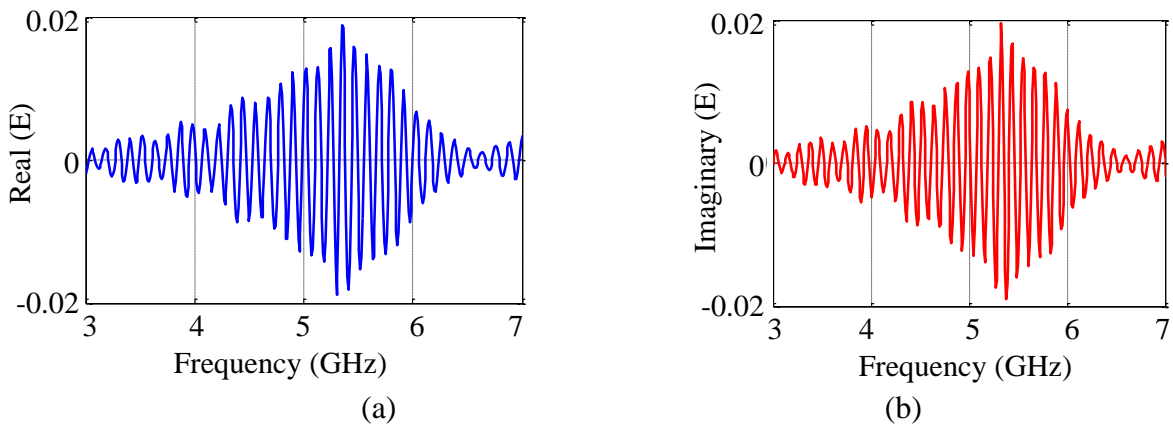


Figure 6.31 (a) Real and (b) imaginary parts of the measured backscattered signal from the tag[88] (With permission, Copyright© 2014 IEEE).

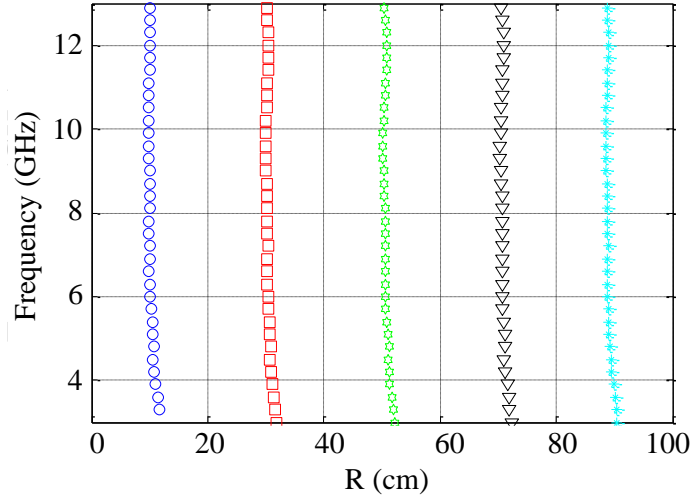


Figure 6.32 Space-frequency diagram of measured backscattered response from the tag for different cases [88] (With permission, Copyright© 2014 IEEE).

As an example, two 2-bit tags with high-Q resonators are spaced 25cm apart. The scenario and dimensions of the tags are depicted in Figure 6.33a. An incident electric field illuminates the tags and the backscattered response is retrieved in the reader. The frequency and time-domain responses are depicted in Figures 6.33b-d for two rotation angles of the second tag. The tags carry two different IDs of 01 and 11, respectively. As the time-domain response shows, for  $\varphi = 0$ , the early-time response of the second tag is hidden in the late-time response of the tags. This phenomenon is more severe when more tags with higher density data are present in the reader zone. In Figure 34, the space-frequency diagram of the backscattered response is shown for  $\varphi=0$ , the worst-case scenario. Compared to the results shown in Figure 6.29, the backscattered signals from the tags are normalized to the impulse response of the antenna. In the cases where the data is embedded in the spectral-domain response of the tags, the localization cannot be efficiently performed based on the time of arrival (TOA) or received signal strength (RSS) [89]. Meanwhile, by employing the proposed algorithm as shown in Figure 6.25, not only can the location of the tags be obtained but their IDs can also be retrieved successfully. The aforementioned algorithm can be employed for finding the positions of the tags in the reader area. Here, we just consider one unit cell covered by three TEM horn antennas as Figure 6.35 depicts. The antennas are interspersed along a circle of radius  $R=65\text{cm}$ . The simulation is performed in FEKO. The measurement set-up

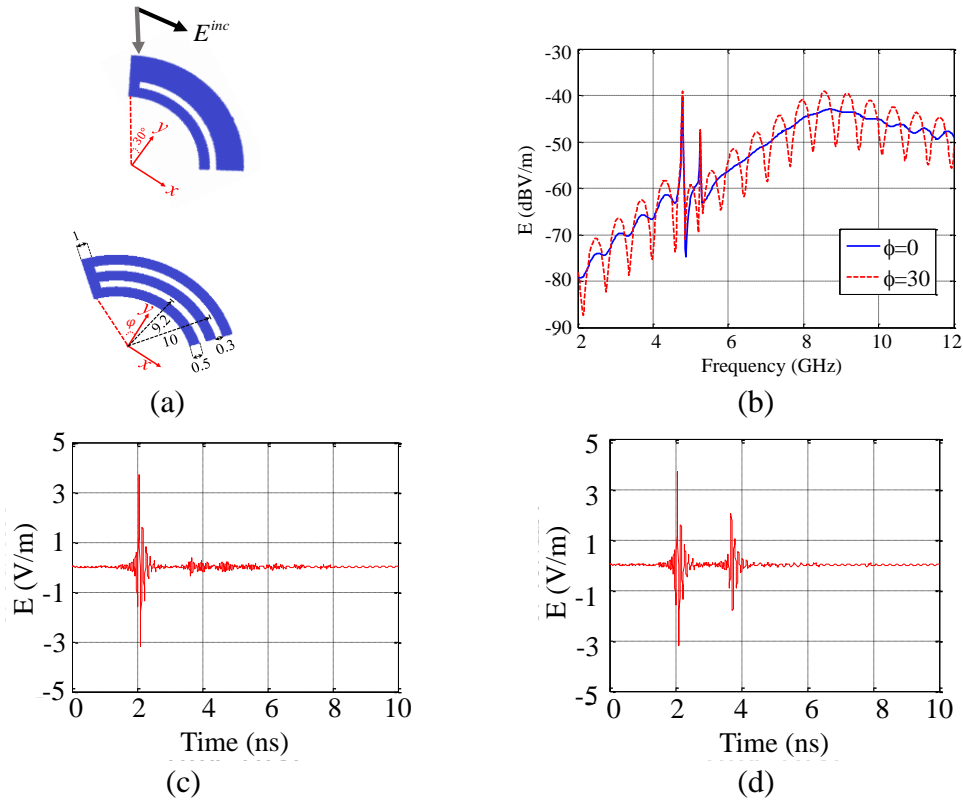


Figure 6.33 (a) Two 2-bit tags illuminated by an incident electric field. (b) Frequency-domain response of the backscattered electric field from two tags, time-domain response from the tags for (c)  $\phi = 0^\circ$  and (d)  $\phi = 30^\circ$  [88] (With permission, Copyright© 2014 IEEE).

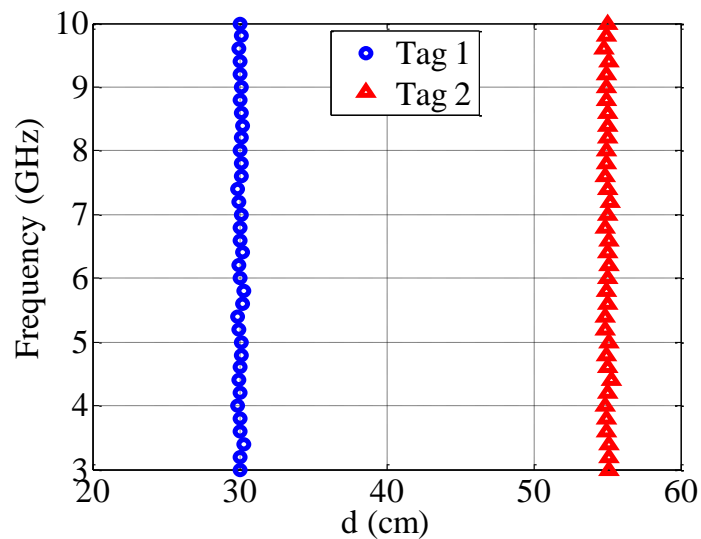


Figure 6.34 Space-frequency diagram of the backscattered response from the tags [88] (With permission, Copyright© 2014 IEEE).

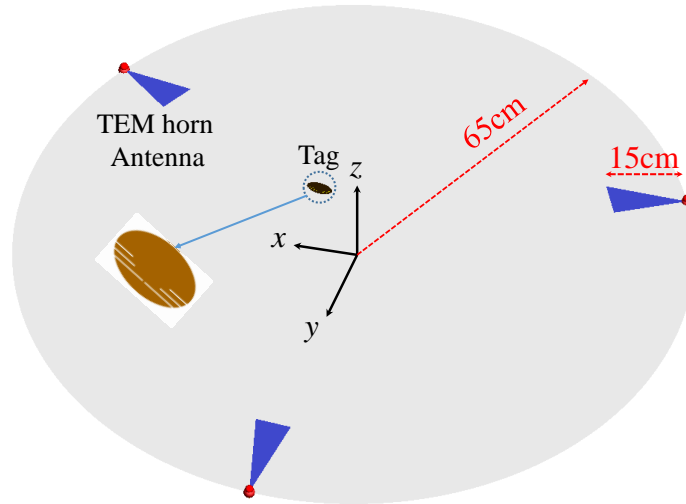


Figure 6.35 Simulation set-up in FEKO [88] (With permission, Copyright© 2014 IEEE).

is shown in Figure 6.36. Three TEM horns are connected to the network analyzer and two measurements in the presence and absence of the tag are performed. By taking the difference between two sets of measurements, the tag response is retrieved at the antenna ports. First, one tag is considered in the reader zone. By receiving the backscattered responses at the antenna ports and applying the proposed technique to the signals, the distances of the tag from three antennas are obtained. The position of the tag can be obtained via triangulation. In the cases where three circles do not intersect at a unit point because of the limited accuracy of the method, the closest point to the circles is considered as the tag position. For simplicity, we express the position of the tag in polar representation by  $(\rho, \varphi)$ .

Figure 6.37a shows the time-domain backscattered signals at the antenna ports when the tag is located at the center of the reader area perpendicular to the y-axis. It is seen that the strength-based positioning is not an accurate technique for localization of chipless RFID tags. Depending on the polarization and direction of the tag with respect to the antenna, the strength of the late-time and early-time responses may change. Hence, at some times the late-time response can be stronger than the early-time response which makes the localization more difficult. Instead, by employing the proposed algorithm shown in Figure 6.25, the positions and IDs of the tags can be extracted. The simulated, measured, and real positions of the tag in the unit cell are depicted in Figure 6.37b

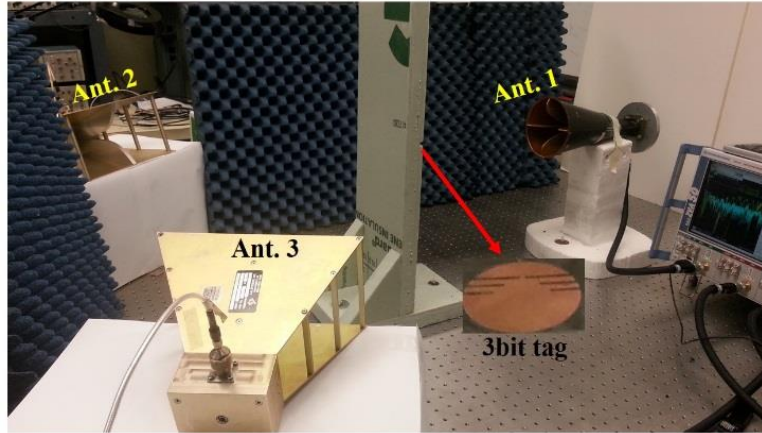


Figure 6.36 Measurement set-up for localizing the chipless RFID tag [88] (With permission, Copyright© 2014 IEEE).

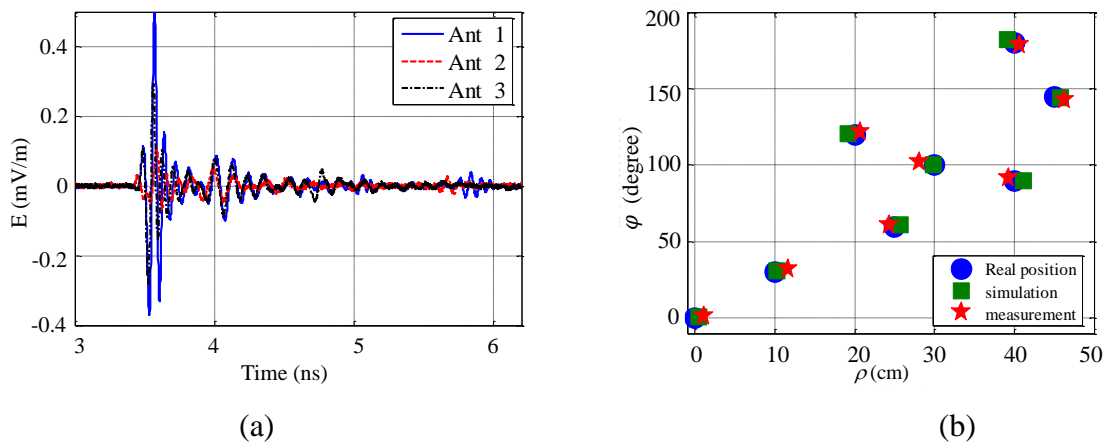


Figure 6.37 (a) Measured time-domain signals from the tag located at the center of the unit cell, (b) Position of the tag extracted from the proposed technique compared to real position [88] (With permission, Copyright© 2014 IEEE).

for different situations. In each situation, the ID of the tag can be extracted from the closest antenna port due to better SNR. As another example, two tags are placed in the unit cell. Figure 6.38 shows the time-domain backscattered signals at the antenna ports when the tags are located at  $(20, 90^\circ)$  and  $(20, 210^\circ)$ . It is seen that for the first and second antennas where the second tag is further from the antenna, the turn-on time is not clearly visible. However, by applying the proposed technique, the positions of the tags can be extracted accurately. By applying short-time matrix pencil method (STMPM) to the time-domain response received at the first antenna port, the time-frequency

response of the tags is shown in Figure 6.38a. The IDs of the tags are visibly indicated in Figure 6.38a as ID<sub>1</sub>:111 and ID<sub>2</sub>:011. The accuracy of the proposed method is compared to the real positions of the tags in three different cases in Figure 6.39. In each case, the locations of the tags are changed to compare the results.

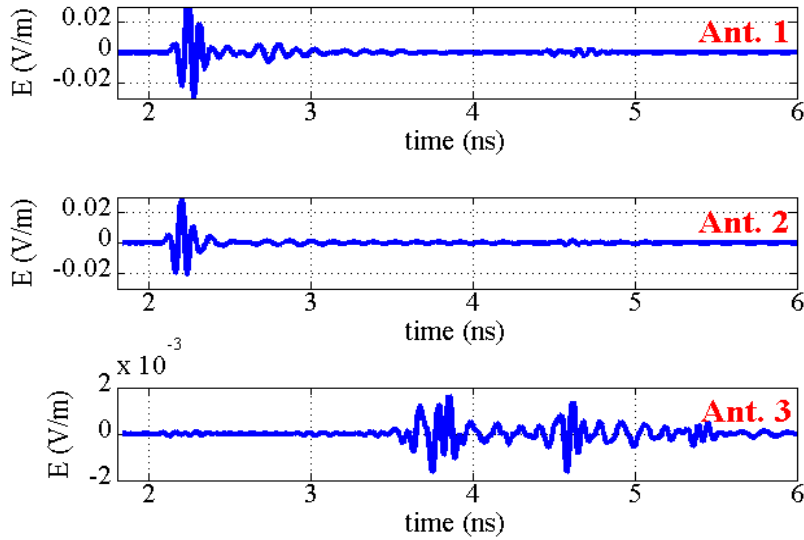


Figure 6.38 Backscattered signals from two tags at the antenna ports [88] (With permission, Copyright© 2014 IEEE).

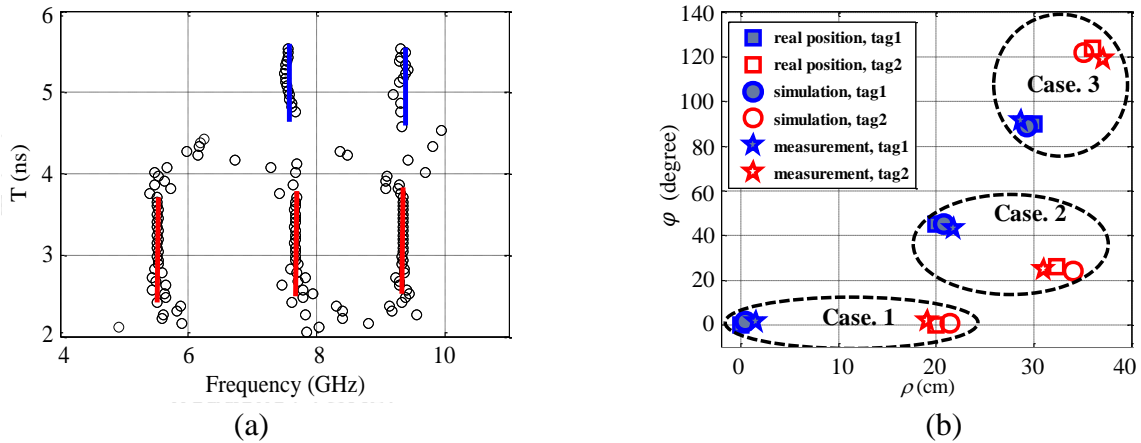


Figure 6.39 (a) Time-frequency response of the received signal at the first antenna, (b) Positions of the tags extracted from the proposed technique compared to real position [88] (With permission, Copyright© 2014 IEEE).

## 7 Conclusion and Future Work

This dissertation provides the design process of chipless RFID systems including tag, antenna, and reader. As a whole communication system, the performance of each component affects strongly the performances of the other parts of the system. In this chapter, a summary of the dissertation is introduced and some conclusion remarks are presented. Suggestions for future work are also outlined.

### 7.1 Summary of Dissertation

The dissertation is can be divided into three different parts: tag design, antenna and detection technique.

In chapter 2, the scattering mechanisms in chipless RFID tags were discussed and modeled. The theoretical and physical interpretations of Singularity expansion method (SEM) and characteristic mode theory (CMT) were studied in this chapter. The reflected signal from chipless RFID tag in time domain is composed of early-time and late-time responses. Altes model was introduced for modeling the early time of the scattered field in the near-field and far-field observation points. Based on SEM, aspect-independence CNRs of the tag are included in the late-time response. An equivalent circuit model was introduced based on SEM in order to represent the electromagnetic behavior of the scatterer illuminated by incident field. Then, CMT was used as a frequency-dependent technique to study the induced current distribution on the tag. It was shown that, by employing some parameters such as eigenvalues, characteristic angle, and modal significance, the resonant and radiation characteristics of the scatterer can be studied.

In chapter 3, the theoretical aspects studied in chapter 2 were utilized in the design of chipless RFID tags. The variations of CNRs of the tag were denoted in pole diagram. A systematic design procedure based on SEM and CMT was introduced for enhancing the resonant and radiation properties of the tag. It was shown that in some cases, a trade-off between these two features needed to be consider in the design procedure. As an example, by increasing the quality factors of the CNRs, the RCS of the tag decreases. Hence, the design procedure enables the designer to choose the minimum size of the tag meeting the desired data density and RCS requirements. The

effect of coupling between resonances and corresponding residues on the quality factor and residues of the excited CNRs were studied.

In chapter 4, the signal link characterization of chipless RFID system in time and frequency domains was represented and some important aspects in measurement setup of chipless RFID tags were proposed. After introducing time and frequency characteristics of UWB antenna, various UWB antennas applicable in chipless RFID systems were studied. Then, an easy-to-fabricate omni-directional antenna element introduced which can be used in the design of wideband and UWB antennas.

In chapter 5, time-frequency representation of the scattered field from chipless RFID tags was introduced. As an important parameter, the resolution in time and frequency was studied. After studying some basic time-frequency approaches such as STFT and wavelet, it was shown that these two techniques do not provide desired resolution in time and frequency domains for detection and identification of tags. Short-time matrix pencil method (STMPM) was introduced and efficiently employed for the time-frequency analysis of scattered field from chipless RFID tags. The performance of matrix pencil method (MPM) in extracting the CNRs of the signal against noise was improved by applying STMPM to the time domain signal. The application of STMPM was expanded to scattered fields from dispersion structures such as open-ended cavity resonators. It was shown that in addition to the resonant frequencies, the scattering centers and dispersion characteristics of the structure can be obtained by employing STMPM. For the first time, the application of STMPM in sliding the window along the early-time response was introduced. According to the results and discussions presented in this chapter, when the early-time response is located in the left hand side (LHS) of the sliding window, the extracted poles of the early time have negative damping factors, located in the LHS of the pole diagram. By shifting the early time towards the right hand side (RHS) of the window, the extracted poles also shift to the RHS of the pole diagram. As an interesting case when the early time is located at the center of the window, all the extracted poles emanating from the early time are located on the imaginary axis of pole diagram. It enables the reader to distinguish the early-time responses of the multiple scatterers or scatterers with multiple scattering centers in the presence of late-time resonances.

In chapter 6, the detection, identification and localization of chipless RFID tags in the reader area was proposed. When multiple multi-bit tags are present in the reader area, the resolution in space, time and frequency is very important. A space-time-frequency algorithm was introduced by

which the number of tags in the reader area, their IDs and location can be obtained. In this approach, the STMPM and its dual, NFMPM are applied to the time-domain and frequency-domain signal received by the antenna. In the cases when the tags are spaced close to each other, the detection is not easy. By monitoring the time instances when the extracted damping factors are zero, the tags can be detected with better resolution.

## 7.2 Suggestions for Future Work

The detection and identification process based on electromagnetic fields has been demanded in various applications, from radar to bio. The research presented in this dissertation can be expanded in different ways. In following, some application of the proposed technique in different scenarios are addressed.

**Breast Cancer.** X-ray mammography is currently the most common method for detecting breast cancer. The application of high frequencies in X-ray imaging provides a very high resolution. However, it is reported that around 30 percent of breast cancers cannot be detected with current X-ray technology. Additionally, ionizing nature of X-rays is of concern [96].

The contrast between the dielectric constants of a breast tumor and environment around it introduces some resonances in the microwave range [96]. These resonances can be detected by loading the antenna with the breast and applying STMPM to the time-domain received signal by the antenna. By studying the variations of the extracted poles during time, the size and location of the tumor can be studied.

**Ground Penetrating Radars (GPR).** The presence of some under-ground metallic targets can be detected based on their CNRs by applying proposed technique in [97]. Multiple reflections from the ground surface, which complicates the extraction of resonant frequencies of the target, can be removed by applying the proposed technique in this dissertation and detecting zero-crossing points of damping factors versus time. In such applications, since the scattering medium is very lossy, the CNRs are highly damped. A few cycles of the sinusoidal needed to be presented in the scattered time-domain response in order to be able to extract the CNRs of the scatterer.

**Through-The-Wall Detection of On-body concealed weapon or cellphone.** Another important issue, especially in security applications, is the detection of on-body concealed weapons or cellphone carried by people. In [98-104], microwave imaging at high frequencies (millimeter-

wave region) is used for detecting the people carrying weapon. The problem is that the scattering medium is very lossy at these frequencies. Each object has unique electromagnetically complex natural resonances depending on its geometry and material. The resonances of the weapons are usually located in microwave frequencies. These CNRs are not very high-Q resonances and detecting their resonant frequencies is very challenging.

As an example, Figure 7.1 shows an incident electric field, covering frequency band of 3.1-10.6 GHz, illuminates a human carrying a cellphone. The antennas located in the cellphone acts as a scatterer possessing high-Q resonances. The received signal by the antenna includes multiple reflections from the wall-air discontinuities, human body and cellphone. Compared to the CNRs of the body which are located at frequencies lower than 100 MHz, the resonances of the antenna cellphone have higher quality factors and are located at microwave frequencies. This scenario is also valid for weapon targets. In [105], wavelet transform is used to extract the resonant frequencies of the gun in the presence of the body. The wavelet and STFT cannot extract weak resonances of the weapon in the presence of strong scatterers.

The time-frequency technique presented in this dissertation was based on short-time matrix pencil method (STMPM). By applying a narrow window in the size of incident pulse along the time-domain signal and monitoring the damping factors of the windowed signal indexed by time, the location of pulse reflections from the wall and objects are discriminated at time instances where the damping factors are crossing the zero point. The thickness and structural parameters of the wall can be calculated based on the pulse locations. Then, by removing the multiple reflections from the received signal, the resonant frequencies of the weapon are calculated by using STMPM. By classifying the resonances, the presence of the weapon can be detected.

Two different cases, as shown in Figure 7.2 are considered here. In Figure 7.2a, a human carrying a cellphone (or any gun) is illuminated by an incident electric pulse. The backscattered signal from the scatterer can be written in time domain as

$$s(t) = e(t) + \sum_n R_n \exp(-\alpha_n t) \cos(\omega_n t + \varphi_n) \quad (7.1)$$

where  $e(t)$  is the early-time response,  $s_n = \alpha_n + j\omega_n$  represents the  $n^{\text{th}}$  complex natural resonance, and  $R_n$  is the corresponding residue. The signal shown in (7.1) contains the reflection from body and

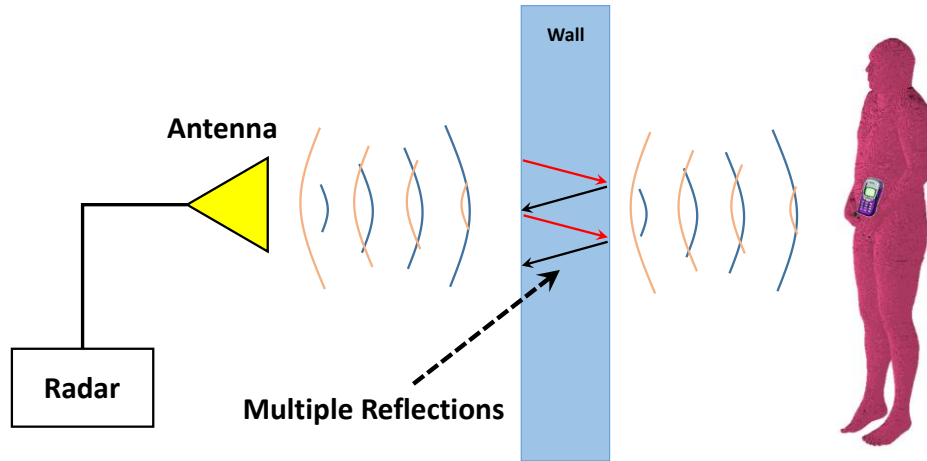


Figure 7.1. Through-the-wall detection of on-body concealed weapon.

cellphone. The early-time response of the human is much stronger than the early time of the cellphone. On the other hand, the CNRs of the human is highly damped and are negligible compared to the CNRs of the cellphone. It means that by proper windowing of the signal, the CNRs of the cellphone can be extracted. Figure 7.3a depicts the time-domain backscattered signal from the body carrying a cellphone. By applying STMPM to the time-domain signal, the presence of the cellphone can be detected by its resonant frequencies in time-frequency diagram (Figure 7.3b). As it shows, second roundtrip reflection from the body occurs at  $t = 12$  ns. This reflection can be detected by the proposed technique in this dissertation. The significant advantage of STMPM compared to other time frequency technique is its ability in extracting low-energy CNRs in the presence of the strongly excited CNRs.

In second example shown in Figure 7.2b, an incident electric pulse impinges the wall surface. The wall is assumed concrete with dielectric constant of  $\epsilon_r = 8$  and loss tangent of  $\tan(\delta) = 0.25$ . Because of the discontinuity of the structure at air-dielectric interferences, multiple reflections occur at the wall surfaces. The time-domain signal is depicted in Figure 7.4a. The multiple reflections from the wall are clearly seen in the time domain signal which located successively along the signal. The location of the pulses can be accurately extracted by applying STMPM to the time-domain signal and monitoring the damping factors versus time index. When the pulse is located at the center of the sliding window, the extracted damping factors passes through the zero, as can be seen in Figure 7.4b.

In Figure 7.1, a complicated case is assumed. A human with cellphone is located behind the wall. The incident pulse illuminated the reader area from the other side of the wall. The reflected signal can be written by

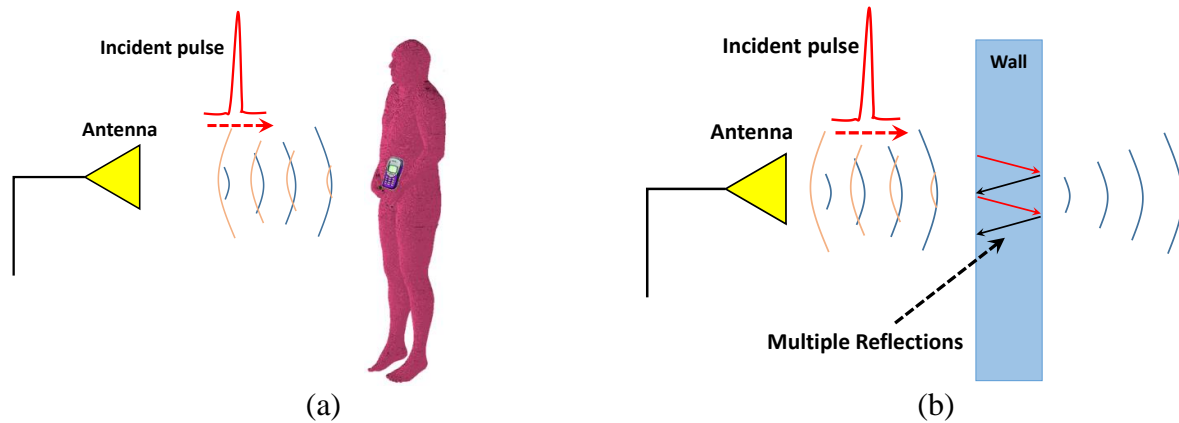


Figure 7.2. (a) Human carrying cellphone in the reader area, (b) A thick wall illuminated by an incident pulse.

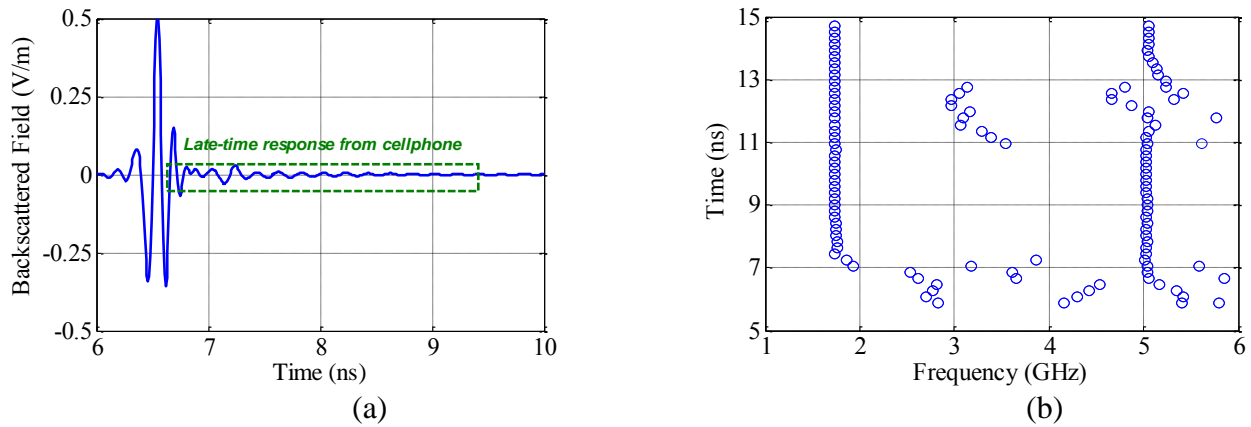


Figure 7.3. (a) Time-domain return signal from body carrying cellphone (b) Time-frequency of the signal.

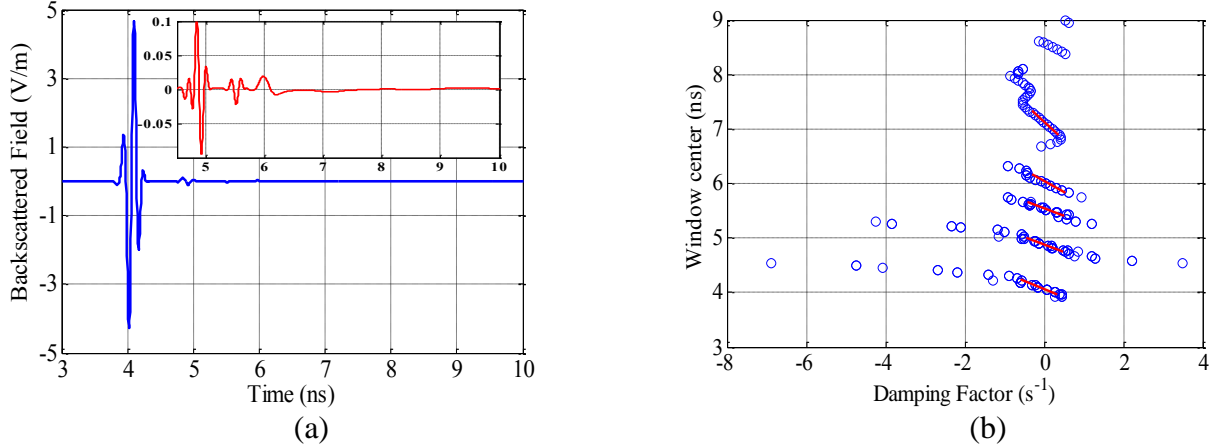


Figure 7.4. (a) Time-domain return signal from body carrying cellphone (b) Time-damping factor diagram of the signal.

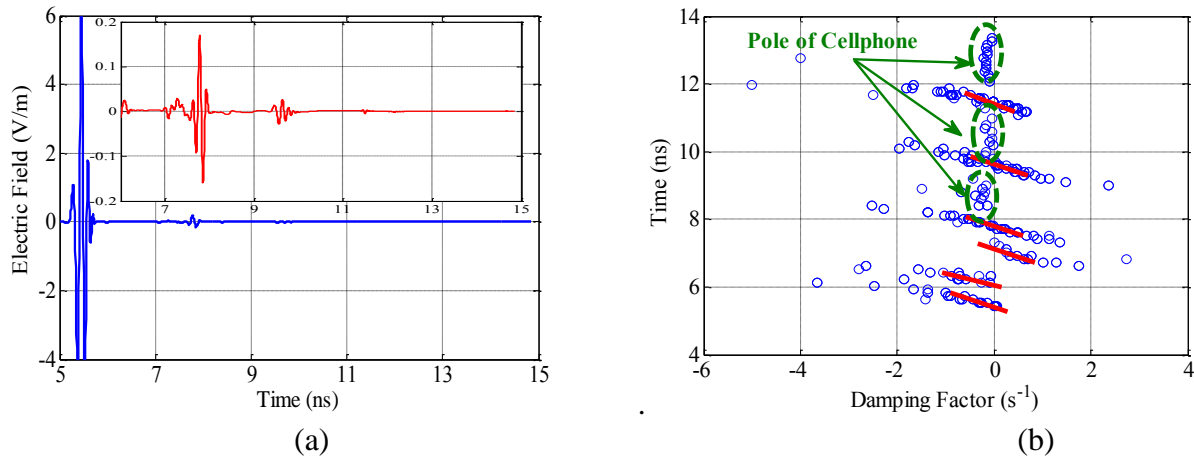


Figure 7.5. (a) Time-domain signal reflected from a human carrying cellphone behind the wall, (b) Damping factors of the extracted poles versus time.

$$s(t) = \sum_{m=1} A_m p(t - t_m) + e_b + \sum_n R_n \exp(-\alpha_n t) \cos(\omega_n t + \varphi_n) \quad (7.2)$$

in which the first term includes multiple reflections from the wall occur at  $t_m$  with different amplitudes ( $A_1 > A_2 > \dots$ ). Second term is the early-time response from the human body and the third term is the damped sinusoidal signals corresponding to the CNRs of the cellphone. By separating three terms of (7.2), the detection process can be easily performed. Figure 7.5a shows the backscattered signal from the human carrying cellphone behind the wall. By applying STMPM

to the time-domain signal, the time-damping factor of the signal is seen in Figure 7.5b. The zero crossing points show the position of multiple pulses in the response. In between the zero crossing pole, there are some poles emanating from the cellphone. As the Figure shows, the small reflections from the wall and human can be monitored in this diagram.

**Multipath mitigation in pattern measurement of antennas-** In some antenna measurements, the multipath effects and reflections from background objects and ground plane limits the accurate measurement of the antenna pattern at some directions. In [106], a time gating approach based on MPM is used for suppressing the undesired reflections in time-domain signal. In some cases, the undesired reflections are very small and hidden in the late-time of the antenna response. The proposed technique can be used for detecting the small reflections from background objects.

## References

- [1] K. Finkelzeller, *The RFID Handbook*. London, UK: John Wiley & Sons Ltd, 2003.
- [2] J. Landt, "The history of RFID," *Potentials, IEEE*, vol. 24, pp. 8-11, 2005.
- [3] H. Stockman, "Communication by Means of Reflected Power," *Proceedings of the IRE*, vol. 36, pp. 1196-1204, 1948.
- [4] A. R. Koelle, S. W. Depp, and R. W. Freyman, "Short-range radio-telemetry for electronic identification, using modulated RF backscatter," *Proceedings of the IEEE*, vol. 63, pp. 1260-1261, 1975.
- [5] V. Chawla and H. Dong Sam, "An overview of passive RFID," *Communications Magazine, IEEE*, vol. 45, pp. 11-17, 2007.
- [6] U. Karthaus and M. Fischer, "Fully integrated passive UHF RFID transponder IC with 16.7- $\mu$ W minimum RF input power," *Solid-State Circuits, IEEE Journal of*, vol. 38, pp. 1602-1608, 2003.
- [7] R. Want, "An introduction to RFID technology," *Pervasive Computing, IEEE*, vol. 5, pp. 25-33, 2006.
- [8] R. Rezaiesarlak, M. Manteghi, *Chipless RFID Tags: Design Procedure and Detection Technique*: Springer, 2015.
- [9] P. V. Nikitin, K. V. S. Rao, and S. Lazar, "An Overview of Near Field UHF RFID," in *RFID, 2007. IEEE International Conference on, 2007*, pp. 167-174.
- [10] J. D. Griffin and G. D. Durgin, "Complete Link Budgets for Backscatter-Radio and RFID Systems," *Antennas and Propagation Magazine, IEEE*, vol. 51, pp. 11-25, 2009.
- [11] a. U.S. Federal Communication Commission (FCC) 47 U.S.C. Section 154, 303, 304, 307, 336, and 544A, ed.
- [12] B. C. E, *The Singularity Expansion Method, in Transient Electromagnetic Fields*. New York: Springer-Verlag, 1976.
- [13] J. Jian-Ming, *Theory and computation of electromagnetic fields*: Wiley, 2010.
- [14] C. E. Baum, *The Singularity Expansion Method in Electromagnetics*: SUMMA foundation, 2012.
- [15] M. K. G. Carrier, C. Pearson, *Functions of a Complex Variable*. New York: McGraw Hill, 1966.
- [16] P. L. W. Baum. C. E, "on the Convergence and numerical Sensitivity of the SEM Pole-Series in Early-Time Scattering Response," *Electromagnetics*, vol. 1, p. 20, 1981.
- [17] R. A. Altes, "Sonar for generalized target description and its similarity to animal echolocation systems," *J Acoust Soc Am*, vol. 59, p. 10, 1976.
- [18] B. C. A, *Antenna Theory: Analysis and Design*: John Wiley and Sons, 2005.
- [19] M. Salehi and M. Manteghi, "Transient Characteristics of Small Antennas," *Antennas and Propagation, IEEE Transactions on*, vol. 62, pp. 2418-2429, 2014.
- [20] L. Lin, A. E. C. Tan, K. Jhamb, and K. Rambabu, "Characteristics of Ultra-Wideband Pulse Scattered From Metal Planar Objects," *Antennas and Propagation, IEEE Transactions on*, vol. 61, pp. 3197-3206, 2013.
- [21] L. B. Felsen, "Progressing and oscillatory waves for hybrid synthesis of source excited propagation and diffraction," *Antennas and Propagation, IEEE Transactions on*, vol. 32, pp. 775-796, 1984.
- [22] E. Heyman and L. B. Felsen, "Creeping waves and resonances in transient scattering by smooth convex objects," *Antennas and Propagation, IEEE Transactions on*, vol. 31, pp. 426-437, 1983.
- [23] E. Heyman and L. B. Felsen, "A wavefront interpretation of the singularity expansion method," *Antennas and Propagation, IEEE Transactions on*, vol. 33, pp. 706-718, 1985.
- [24] F. Tesche, "On the analysis of scattering and antenna problems using the singularity expansion technique," *Antennas and Propagation, IEEE Transactions on*, vol. 21, pp. 53-62, 1973.

- [25] C. E. Baum, "On the Eigenmode Expansion Method for Electromagnetic Scattering and Antenna Problems, Part 1: Some Basic Relations for Eigenmode Expansion, and Their Relation to the Singularity Expansion," *Interaction Note 229*, p. 94, 1975.
- [26] R. H. T. R. J. Garbacz, "A Generalized Expansion for Radiation and Scattered Fields," *Antennas and Propagation, IEEE Transactions on*, vol. 19, p. 11.
- [27] R. F. Harrington and J. R. Mautz, "Theory of characteristic modes for conducting bodies," *Antennas and Propagation, IEEE Transactions on*, vol. 19, pp. 622-628, 1971.
- [28] J. J. Adams and J. T. Bernhard, "Broadband Equivalent Circuit Models for Antenna Impedances and Fields Using Characteristic Modes," *Antennas and Propagation, IEEE Transactions on*, vol. 61, pp. 3985-3994, 2013.
- [29] N. L. Bohannon and J. T. Bernhard, "Design Guidelines Using Characteristic Mode Theory for Improving the Bandwidth of PIFAs," *Antennas and Propagation, IEEE Transactions on*, vol. 63, pp. 459-465, 2015.
- [30] M. Cabedo-Fabres, E. Antonino-Daviu, A. Valero-Nogueira, and M. F. Bataller, "The Theory of Characteristic Modes Revisited: A Contribution to the Design of Antennas for Modern Applications," *Antennas and Propagation Magazine, IEEE*, vol. 49, pp. 52-68, 2007.
- [31] E. A. Elghannai, B. D. Raines, and R. G. Rojas, "Multiport Reactive Loading Matching Technique for Wide Band Antenna Applications Using the Theory of Characteristic Modes," *Antennas and Propagation, IEEE Transactions on*, vol. 63, pp. 261-268, 2015.
- [32] D. Liu, R. J. Garbacz, and D. M. Pozar, "Antenna synthesis and optimization using generalized characteristic modes," *Antennas and Propagation, IEEE Transactions on*, vol. 38, pp. 862-868, 1990.
- [33] R. Rezaiesarlak and M. Manteghi, "Design of Chipless RFID Tags Based on Characteristic Mode Theory (CMT)," *Antennas and Propagation, IEEE Transactions on*, vol. 63, pp. 711-718, 2015.
- [34] R. F. Harrington and J. R. Mautz, "Control of radar scattering by reactive loading," *Antennas and Propagation, IEEE Transactions on*, vol. 20, pp. 446-454, 1972.
- [35] S. Preradovic and N. C. Karmakar, "Chipless RFID: Bar Code of the Future," *Microwave Magazine, IEEE*, vol. 11, pp. 87-97, 2010.
- [36] C. S. Hartmann, "A global SAW ID tag with large data capacity," in *Ultrasonics Symposium, 2002. Proceedings. 2002 IEEE*, 2002, pp. 65-69 vol.1.
- [37] A. T. Blischak and M. Manteghi, "Embedded Singularity Chipless RFID Tags," *Antennas and Propagation, IEEE Transactions on*, vol. 59, pp. 3961-3968, 2011.
- [38] A. Chamarti and K. Varahramyan, "Transmission Delay Line Based ID Generation Circuit for RFID Applications," *Microwave and Wireless Components Letters, IEEE*, vol. 16, pp. 588-590, 2006.
- [39] G. Zhi-xiang, C. Zhi-jun, H. Xin, T. Rui, and W. Meng-yang, "Design and implementation of SAW reader receiving circuit," in *Piezoelectricity, Acoustic Waves and Device Applications (SPAWDA), 2013 Symposium on*, 2013, pp. 1-4.
- [40] S. Gupta, B. Nikfal, and C. Caloz, "Chipless RFID System Based on Group Delay Engineered Dispersive Delay Structures," *Antennas and Wireless Propagation Letters, IEEE*, vol. 10, pp. 1366-1368, 2011.
- [41] R. Rezaiesarlak and M. Manteghi, "A low profile multi-bit chipless RFID tag," in *Radio Science Meeting (USNC-URSI NRS), 2013 US National Committee of URSI National*, 2013, pp. 1-1.
- [42] R. Rezaiesarlak and M. Manteghi, "Complex-Natural-Resonance-Based Design of Chipless RFID Tag for High-Density Data," *Antennas and Propagation, IEEE Transactions on*, vol. 62, pp. 898-904, 2014.
- [43] I. Jalaly and I. D. Robertson, "Capacitively-tuned split microstrip resonators for RFID barcodes," in *Microwave Conference, 2005 European*, 2005, p. 4 pp.

- [44] J. McVay, A. Hoorfar, and N. Engheta, "Space-filling curve RFID tags," in *Radio and Wireless Symposium, 2006 IEEE*, 2006, pp. 199-202.
- [45] M. Manteghi and Y. Rahmat-Samii, "Frequency notched UWB elliptical dipole tag with multi-bit data scattering properties," in *Antennas and Propagation Society International Symposium, 2007 IEEE*, 2007, pp. 789-792.
- [46] S. Preradovic, I. Balbin, N. C. Karmakar, and G. F. Swiegers, "Multiresonator-Based Chipless RFID System for Low-Cost Item Tracking," *Microwave Theory and Techniques, IEEE Transactions on*, vol. 57, pp. 1411-1419, 2009.
- [47] F. Costa, S. Genovesi, and A. Monorchio, "A Chipless RFID Based on Multiresonant High-Impedance Surfaces," *Microwave Theory and Techniques, IEEE Transactions on*, vol. 61, pp. 146-153, 2013.
- [48] R. Rezaiesarlak and M. Manteghi, "On the application of characteristic modes for the design of chipless RFID tags," in *Antennas and Propagation Society International Symposium (APSURSI), 2014 IEEE*, 2014, pp. 1304-1305.
- [49] A. Vena, E. Perret, and S. Tedjini, "Design of Compact and Auto-Compensated Single-Layer Chipless RFID Tag," *Microwave Theory and Techniques, IEEE Transactions on*, vol. 60, pp. 2913-2924, 2012.
- [50] C. E. Baum, *Detection and Identification of Visually Obscured Targets*: Taylor & Francis, 1997.
- [51] W. Wiesbeck, G. Adamiuk, and C. Sturm, "Basic Properties and Design Principles of UWB Antennas," *Proceedings of the IEEE*, vol. 97, pp. 372-385, 2009.
- [52] H. G. Schantz, "Introduction to ultra-wideband antennas," in *Ultra Wideband Systems and Technologies, 2003 IEEE Conference on*, 2003, pp. 1-9.
- [53] S. H, *The Art and Science of Ultra-Wideband Antennas*: Artech House, 2005.
- [54] S. Licul and W. A. Davis, "Unified frequency and time-domain antenna modeling and characterization," *Antennas and Propagation, IEEE Transactions on*, vol. 53, pp. 2882-2888, 2005.
- [55] J. H. Reed, *An introduction to ultra wideband communication systems*. Upper Saddle River, NJ: Prentice Hall PTR, 2005.
- [56] H. Foltz, J. McLean, A. Medina, L. Junfei, and R. Sutton, "UWB antenna transfer functions using minimum phase functions," in *Antennas and Propagation Society International Symposium, 2007 IEEE*, 2007, pp. 1413-1416.
- [57] W. L. S. a. G. A. Thiele, *Antenna Theory and Design*. Hoboken, NJ: Wiley, 1998.
- [58] H. Foltz and J. McLean, "Limits on the Amplitude of the Antenna Impulse Response," *Antennas and Propagation, IEEE Transactions on*, vol. 58, pp. 1414-1417, 2010.
- [59] B. C. E. Farr. E. G, "Extending the Definitions of Antenna Gain and Radiation Pattern Into the Time Domain," *Sensiq and Simulation Notes* 350.
- [60] W. A. Davis, T. Yang, E. D. Caswell, and W. L. Stutzman, "Fundamental limits on antenna size: a new limit," *Microwaves, Antennas & Propagation, IET*, vol. 5, pp. 1297-1302, 2011.
- [61] J. S. McLean, "A re-examination of the fundamental limits on the radiation Q of electrically small antennas," *Antennas and Propagation, IEEE Transactions on*, vol. 44, p. 672, 1996.
- [62] D. W. A. Yang. T, Stutzman. W. L, "The Design of Ultra-wideband Antennas with Performance Close to the Fundamental Limit " *Virginia Tech Antenna Group (VTAG)*, 2008.
- [63] L. H. Chen. V. C, *Time-Frequency Transforms for Radar Imaging and Signal Analysis*: Artech House, 2002.
- [64] G. Kaiser, *A Friendly Guide to Wavelets*: Birkhäuser; 2011 edition, 2010.
- [65] A. D. Poularikas, *Transforms and Applications Handbook*: CRC Press 2000.
- [66] K. Kodera, R. Gendrin, and C. Villedary, "Analysis of time-varying signals with small BT values," *Acoustics, Speech and Signal Processing, IEEE Transactions on*, vol. 26, pp. 64-76, 1978.

- [67] S. S. Ram and L. Hao, "Application of the Reassigned Joint Time-Frequency Transform to Wideband Scattering From Waveguide Cavities," *Antennas and Wireless Propagation Letters, IEEE*, vol. 6, pp. 580-583, 2007.
- [68] T. K. Sarkar and O. Pereira, "Using the matrix pencil method to estimate the parameters of a sum of complex exponentials," *Antennas and Propagation Magazine, IEEE*, vol. 37, pp. 48-55, 1995.
- [69] R. Rezaiesarlak and M. Manteghi, "Short-Time Matrix Pencil Method for Chipless RFID Detection Applications," *Antennas and Propagation, IEEE Transactions on*, vol. 61, pp. 2801-2806, 2013.
- [70] R. Rezaiesarlak and M. Manteghi, "On the Application of Short-Time Matrix Pencil Method for Wideband Scattering From Resonant Structures," *Antennas and Propagation, IEEE Transactions on*, vol. 63, pp. 328-335, 2015.
- [71] J. Chauveau, N. de Beaucoudrey, and J. Saillard, "Resonance Behavior of Radar Targets With Aperture: Example of an Open Rectangular Cavity," *Antennas and Propagation, IEEE Transactions on*, vol. 58, pp. 2060-2068, 2010.
- [72] L. Hoi-Shun, M. Persson, and N. V. Z. Shuley, "Joint Time-Frequency Analysis of Transient Electromagnetic Scattering from a Subsurface Target," *Antennas and Propagation Magazine, IEEE*, vol. 54, pp. 109-130, 2012.
- [73] H. a. G. Friedlander, "Hybrid wavefront-resonance representation for transient scattering by an open cavity. Part III: Analytical models for the late time oscillations," *Journal of Electromagnetic Waves and Applications*, vol. 7, p. 13, 1993.
- [74] E. Heyman, G. Friedlander, and L. B. Felsen, "Ray-mode analysis of complex resonances of an open cavity [radar targets]," *Proceedings of the IEEE*, vol. 77, pp. 780-787, 1989.
- [75] G. F. a. E. Heyman, "Hybrid wavefront-resonance representation for transient scattering by an open cavity. Part I: Formulation," *Journal of Electromagnetic Waves and Applications*, vol. 7, p. 18, 1993.
- [76] G. F. a. E. Heyman, "Hybrid wavefront-resonance representation for transient scattering by an open cavity. Part II: Numerical results and interpretation," *Journal of Electromagnetic Waves and Applications*, vol. 7, p. 16, 1993.
- [77] H. Ling, R. Chou, and S. Lee, "Shooting and bouncing rays: Calculating RCS of an arbitrary cavity," in *Antennas and Propagation Society International Symposium, 1986*, 1986, pp. 293-296.
- [78] R. S. Nair, E. Perret, S. Tedjini, and T. Baron, "A Group-Delay-Based Chipless RFID Humidity Tag Sensor Using Silicon Nanowires," *Antennas and Wireless Propagation Letters, IEEE*, vol. 12, pp. 729-732, 2013.
- [79] A. Vena, E. Perret, and S. Tedjini, "Chipless RFID Tag Using Hybrid Coding Technique," *Microwave Theory and Techniques, IEEE Transactions on*, vol. 59, pp. 3356-3364, 2011.
- [80] R. Rezaiesarlak and M. Manteghi, "A Space-Time-Frequency Anticollision Algorithm for Identifying Chipless RFID Tags," *Antennas and Propagation, IEEE Transactions on*, vol. 62, pp. 1425-1432, 2014.
- [81] C. Baum, "The singularity expansion method: Background and developments," *Antennas and Propagation Society Newsletter, IEEE*, vol. 28, pp. 14-23, 1986.
- [82] D. W. A. Riley. D. J, Besieris. I. M, "The Singularity Expansion Method and Multiple Scattering," *Radio science*, vol. 20, p. 5, 1985.
- [83] W. W. S. Hong. S. K, Andreadis, Davis. W. A, "Practical Implementation of Pole Series Convergence and the Early-time in Transient Backscatter," *Naval research laboratory*, vol. NRL/MR/5740-12-9411, 2012.
- [84] Q. Li, P. Ilavarasan, J. E. Ross, E. J. Rothwell, Y. F. Chen, and D. P. Nyquist, "Radar target identification using a combined early-time/late-time E-pulse technique," *Antennas and Propagation, IEEE Transactions on*, vol. 46, pp. 1272-1278, 1998.

- [85] Q. Li, E. J. Rothwell, K. M. Chen, D. P. Nyquist, J. Ross, and R. Bebermeyer, "Determination of radar target scattering center transfer functions from measured data," in *Antennas and Propagation Society International Symposium, 1994. AP-S. Digest, 1994*, pp. 2006-2009 vol.3.
- [86] C. M. Nijas, R. Dinesh, U. Deepak, A. Rasheed, S. Mridula, K. Vasudevan, *et al.*, "Chipless RFID Tag Using Multiple Microstrip Open Stub Resonators," *Antennas and Propagation, IEEE Transactions on*, vol. 60, pp. 4429-4432, 2012.
- [87] S. M, *Introduction to Radar Systems*: McGraw-Hill, 2001.
- [88] R. Rezaiesarlak and M. Manteghi, "A Space-Frequency Technique for Chipless RFID Tag Localization," *Antennas and Propagation, IEEE Transactions on*, vol. 62, pp. 5790-5797, 2014.
- [89] R. Anee and N. C. Karmakar, "Chipless RFID Tag Localization," *Microwave Theory and Techniques, IEEE Transactions on*, vol. 61, pp. 4008-4017, 2013.
- [90] D. W. A. Hong. S. K, "Use of tumor-specific resonances for more efficient microwave hyperthermia of breast cancer," vol. 55, p. 7, 2013.
- [91] A. Vena, L. Sydanheimo, M. M. Tentzeris, and L. Ukkonen, "A novel inkjet printed carbon nanotube-based chipless RFID sensor for gas detection," in *Microwave Conference (EuMC), 2013 European*, 2013, pp. 9-12.
- [92] D. Dardari, A. Conti, U. Ferner, A. Giorgetti, and M. Z. Win, "Ranging With Ultrawide Bandwidth Signals in Multipath Environments," *Proceedings of the IEEE*, vol. 97, pp. 404-426, 2009.
- [93] C. Woo Cheol and H. Dong Sam, "An accurate ultra wideband (UWB) ranging for precision asset location," in *Ultra Wideband Systems and Technologies, 2003 IEEE Conference on*, 2003, pp. 389-393.
- [94] D. Dardari, R. D'Errico, C. Roblin, A. Sibille, and M. Z. Win, "Ultrawide Bandwidth RFID: The Next Generation?," *Proceedings of the IEEE*, vol. 98, pp. 1570-1582, 2010.
- [95] M. Manteghi, "A space-time-frequency target identification technique for chipless RFID applications," in *Antennas and Propagation (APSURSI), 2011 IEEE International Symposium on*, 2011, pp. 3350-3351.
- [96] S. K. Hong, "Resonance-Based Techniques for Microwave Breast Cancer Applications " PhD, Department of Electrical and Computer Engineering, Virginia Polytechnic Institute and State University (Virginia Tech), 2012.
- [97] M. P. Kolba and I. I. Jouny, "Buried land mine detection using complex natural resonances on GPR data," in *Geoscience and Remote Sensing Symposium, 2003. IGARSS '03. Proceedings. 2003 IEEE International*, 2003, pp. 761-763 vol.2.
- [98] M. Dehmollaian and K. Sarabandi, "Refocusing Through Building Walls Using Synthetic Aperture Radar," *Geoscience and Remote Sensing, IEEE Transactions on*, vol. 46, pp. 1589-1599, 2008.
- [99] E. Ertin and R. L. Moses, "Through-the-Wall SAR Attributed Scattering Center Feature Estimation," *Geoscience and Remote Sensing, IEEE Transactions on*, vol. 47, pp. 1338-1348, 2009.
- [100] L.-j. Kong, C. Guo-long, Y. Jian-yu, and Y. Xiao-bo, "Wall parameters estimation method for through-the-wall radar imaging," in *Radar, 2008 International Conference on*, 2008, pp. 297-301.
- [101] L. Lianlin, Z. Wenji, and L. Fang, "A Novel Autofocusing Approach for Real-Time Through-Wall Imaging Under Unknown Wall Characteristics," *Geoscience and Remote Sensing, IEEE Transactions on*, vol. 48, pp. 423-431, 2010.
- [102] F. H. C. Tivive, A. Bouzerdoum, and M. G. Amin, "A Subspace Projection Approach for Wall Clutter Mitigation in Through-the-Wall Radar Imaging," *Geoscience and Remote Sensing, IEEE Transactions on*, vol. 53, pp. 2108-2122, 2015.
- [103] L. Xiaoxiang, H. Leung, and G. A. Lampropoulos, "Effect of Wall Parameters on Ultra-Wideband Synthetic Aperture Through-the-Wall Radar Imaging," *Aerospace and Electronic Systems, IEEE Transactions on*, vol. 48, pp. 3435-3449, 2012.

- [104] W. Zhang and A. Hoorfar, "A Generalized Approach for SAR and MIMO Radar Imaging of Building Interior Targets with Compressive Sensing," *Antennas and Wireless Propagation Letters, IEEE*, vol. PP, pp. 1-1, 2015.
- [105] B. N. J. Atiah. A, "An Approach for on Body Concealed Weapon Detection Using Continuous Wavelet Transform," *Progress In Electromagnetics Research Symposium Proceedings*, p. 4, 2013
- [106] Y. Taeyoung, W. A. Davis, and W. L. Stutzman, "Multipath mitigation in pattern measurement of small directive antennas based on the singularity expansion method (SEM)," in *Antenna Technology, 2009. iWAT 2009. IEEE International Workshop on*, 2009, pp. 1-4.